GEOLOGY, GEOCHEMISTRY AND GEOCHRONOLOGY OF GRANITIC GNEISSES AND LEUCOCRATIC ORTHOGNEISSES AT THE EASTERN PART OF ÖDEMİŞ-KİRAZ SUBMASSIF, MENDERES MASSIF: PAN-AFRICAN AND TRIASSIC MAGMATIC ACTIVITIES

109543

DOKÜMANTASYON MERKEZİ

109543

by

Osman Ersin KORALAY

November, 2001

İZMİR

Sevgili
Babaannem,
Ailem,
ve
Duygu'ya

GEOLOGY, GEOCHEMISTRY AND GEOCHRONOLOGY OF GRANITIC GNEISSES AND LEUCOCRATIC ORTHOGNEISSES AT THE EASTERN PART OF ÖDEMİŞ-KİRAZ SUBMASSIF, MENDERES MASSIF: PAN-AFRICAN AND TRIASSIC MAGMATIC ACTIVITIES

A Thesis Submitted to the
Graduate School of Natural and Applied Sciences of
Dokuz Eylül University
In Partial Fulfillement of the Requirements for
The Doctor of Phylosophy Degree
in Geology Engineering, Mineralogy-Petrography Programme

by

Osman Ersin KORALAY

November, 2001

İZMİR

Ph.D. THESIS EXAMINATION RESULT FORM

We certify that we have read the thesis, entitled **"GEOLOGY, GEOCHEMISTRY AND GEOCHRONOLOGY OF GRANITIC GNEISSES AND LEUCOCRATIC ORTHOGNEISSES AT THE EASTERN PART OF ÖDEMİŞ-KİRAZ SUBMASSIF, MENDERES MASSIF: PAN-AFRICAN AND CIMMERIAN MAGMATIC ACTIVITIES"** completed by Osman Ersin KORALAY and supervision of Prof. Dr. O.Özcan DORA and that in our opinion it is fully adequate, in scope and in quality, as a thesis for the degree of Doctor of Philosophy.

Prof.Dr. O. Özcan DORA
Supervisor

Prof. Dr. Yücel YILMAZ
Committee Member

Prof. Dr. Cahit Helvacı
Committee Member

Approved by the
Graduate School of Natural and Applied Sciences

Prof.Dr. Cahit HELVACI
Director

ACKNOWLEDGEMENTS

I wish to express his gratitude to Prof.Dr. O.Özcan DORA for his guidance, continuous interest and constructive discussions during my research. I also owe him my warmest thanks and recognition for his understanding, good will and patience.

I feel obliged to Prof.Dr. Osman CANDAN who helped me in many ways during the elaboration of this study. For the numerous discussions we had and the constructive criticism he gave, I express my innermost gratitude.

I sincerely thank Prof. Muharrem SATIR providing me facilities for geochemical and geochronological analysis in University Tübingen.

In particular, I sincerely thank Dr. Fukun CHEN who carried out the radiometric dating, Gisela BARTHOLOMAE, Marcella SCHUMAN, Bernd STEINHILBER, Gabriele STOSCHECK, A.Nalan YILMAZER, Yılmaz GÜLTEKİN and Nedim TATARİ for XRF analysis, J. MAELLICH for preparation of samples for cathodoluminescence analysis and H. HUTTEMANN for help with cathodoluminescence analysis for zircons. Discussions with Dr. G. VAVRA about cathodoluminescence analysis of zircons is gratefully acknowledged.

Numerous friendly help from colleagues at Department of Geology in Dokuz Eylül University are gratefully acknowledged. My best thanks go to my friends Dr. Cüneyt AKAL and Serdar MAYDA for valuable help. I sincerely thank Assoc. Prof. Doğan YAŞAR for the printing of the maps.

This study was limited finantially supported by Research Fund of Dokuz Eylül University (project no: 0922.95.01.17). I sincerely thank DAAD for a fellowship during 1998-1999 in Tübingen.

ABSTRACT

Geological evidence, geochemical compositions and geochronological constraints for a variety rock types from the eastern part of the Ödemiş-Kiraz Submassif of the Menderes Massif are presented and interpreted for the geotectonic evolution of the Menderes Massif.

The rock succession of the Derbent and Demirhan areas, in the eastern part of the Ödemiş-Kiraz Submassif of the Menderes Massif is made up of nappe stack. In the vicinity of Derbent, the rock succession of metamorphic series can be divided into four nappe units. In ascending order, the lower, middle and upper nappe units are represented by internal imbrication of the Pan-African basement series. The uppermost nappe units belonging to the Paleozoic-Mesozoic cover series rests tectonically upon the upper nappe units of the Pan-African basement. These metamorphic rocks of the Menderes Massif displaying typical nappe structure, tectonically overlain by unmetamorphosed ophiolitic rocks. Furthermore, in the Demirhan area, metapelites of cover series are overlain by a nappe unit which completely consists of Pan-African orthogneisses.

Pan-African basement series consisting of metapelites and phyllites were intruded by the granitic protoliths of orthogneisses. Furthermore, the Pan-African basement rocks and the Paleozoic cover series were also intruded by the granitic precurser of leucocratic orthogneisses. The geological evidences prove the granitic origin of these both orthogneisses. They show original intrusive contact relationship with the country rocks. Geochemical compositions indicate that the protoliths of Pan-African orthogneisses were calc-alkaline, peraluminous, S-type, syn- to post-tectonic granites and granodiorites. Geochemical data also reveal that the crustully derived leucocratic orthogneisses were peraluminous, S-type granites with calc-alkaline affinity.

The SEM and CL photomicrographs demonstrate that the analysed zircon populations in Pan-African orthogneisses have distinct magmatic zoning and typical igneous morphology. The $^{207}Pb/^{206}Pb$ ages of 561.5±1.8 and 570.5±2.2 Ma are interpreted as the intrusion ages of protoliths of the Pan-African orthogneiss. The geological and geochronological data suggest that the granitic protoliths of these orthogneisses were emplaced in a period following a high grade metamorphic event related to the Pan-African orogeny.

Zircon grains of leucocratic orthogneisses which are identified as euhedral crystals with typical igneous morphology by SEM and CL studies were dated by the single zircon $^{207}Pb/^{206}Pb$ evaporation method. Single zircon dating of three leucocratic orthogneiss samples yielded mean ages of 234.9±5.8, 241.1±5.2 and 245.7±4.6 Ma. The geological and geochronological evidence indicate that the leucocratic orthogneisses were intruded into the Pan-African basement and Paleozoic cover series during the Early-Middle Triassic time most probably related to the closure of Paleotethys. Based on the tectonic setting and ages of the syn- to post-tectonic leucocratic orthogneiss, it can be suggested that the closure of the Paleotethys at around Eastern Mediterranean might be taken place during the Latest Permian time. Intrusion of protoliths of the Triassic leucocratic orthogneisses into both of the Pan-African basement and Paleozoic cover units reveals that these two units were tectonically juxtaposed prior to Triassic time.

ÖZET

Bu çalışmada Ödemiş-Kiraz Asmasifi'nin doğusundaki çalışma alanlarından elde edilen jeolojik, jeokimyasal ve jeokronolojik veriler Menderes Masifi'nin jeotektonik evrimine açıklık getirmek amacıyla ele alınmış ve yorumlanmışlardır.

Menderes Masifi'nin, Ödemiş-Kiraz Asmasifi doğusunda yer alan Derbent ve Demirhan bölgelerindeki kaya istifi nap yığınları meydana şeklindedir. Derbent çevresinde gözlenen kaya istifi dört nap paketinden yapılıdır. Pan-Afrikan temele ait birimler, kendi içerisinde gelişen bindirmeler yoluyla, alttan üste alt, orta ve üst nap paketlerinden oluşturmaktadır. Paleozoyik-Mesozoyik örtü serilerinden meydana gelen en üstte yer alan nap paketi tektonik bir dokanakla Pan-Afrikan temele ait üst nap paketini üstlemektedir. Bununla beraber, tipik nap yapısı sunan Menderes Masifi'nin metamorfik kayaları, metamorfik olmayan ofiyolitik kayalar tarafından da tektonik olarak üstlenmektedir. Aynı şekilde, Demirhan bölgesinde, Pan-Afrikan ortognayslardan oluşan bir nap paketi örtü serisine ait metapelitik kayalar üzerine tektonik bir dokanakla gelmektedir.

Ortognaysların granitik ilksel kayaları metapelit ve fillitlerden meydana gelen Pan-Afrikan temel içerisine sokulum yapmışlardır. Ayrıca, Pan-Afrikan temel kayaları ve Paleozoyik seriler, lökokratik ortognaysların granitik ilksel kayaları tarafından da kesilmektedir. Elde edilen jeolojik veriler her iki ortognaysın granitik kökenli ve çevre kaya ile ilksel intrüzif dokanaklara sahip olduklarını göstermektedir. Jeokimyasal bileşim Pan-Afrikan ortognaysların ilksel magmatiklerinin kalkalkalen, peralumino, S-tip, sin- ve/veya post-tektonik granit ve granodiyoritler olduklarına işaret etmektedir. Lökokratik ortognayslardan elde edilen jeokimyasal veriler ise, bunların kıtasal kabuktan türeme, S- tip, peralumino ve kalkalkalen karakterli granitler olduğunu göstermektedir.

Pan-Afrikan ortognayslardan analiz edilen zircon popülasyonlarının düzgün magmatik zonlanmalı ve tipik magmatik özşekilli zirkonlardan oluştukları SEM ve CL fotoğrafları ile saptanmıştır. Bu gibi özşekilli tanelerden elde edilen 561.5±1.8 ve 570.5±2.2 my'lık $^{207}Pb/^{206}Pb$ yaşları, ortognaysların ilksel kayalarının sokulum yaşları olarak yorumlanmıştır. Jeolojik ve jeokronolojik veriler bu ortognaysların granitik ilksel kayalarının Pan-Afrikan orojenezi ile ilişkili yüksek dereceli bir metamorfizmayı izleyen evrede sokulum yaptıklarını göstermektedir.

Lökokratik ortognayslardan elde edilen ve SEM ve CL çalışmalarıyla tipik magmatik morfolojiye sahip ve özşekilli oldukları saptanan zirkon tanelerinden $^{207}Pb/^{206}Pb$ tek zirkon evaporasyon yöntemiyle yaşlar elde edilmiştir. Bu yöntemle, üç lökokratik ortognays örneği ortalama 234.9±5.8, 241.1±5.2 ve 245.7±4.6 my yaşları vermiştir. Jeolojik ve jeokronolojik veriler lökokratik ortognaysların ilksel kayalarının Pan-Afrikan temel ve Paleozoyik yaşlı örtü serileri içerisine sokulum yaptığını göstermektedir. Erken-Orta Triyas'ta meydana gelen bu olay olasılıkla Paleotetis'in kapanmasıyla bağlantılıdır. Sin- ve/veya post-tektonik lökokratik ortognaysların tektonik ortamlarına ve elde edilen yaşlara dayanılarak, Doğu Akdeniz çevresinde Paleotetis'in Engeç Permiyen'de kapanmış olabileceği önerilmektedir. Triyas yaşlı lökokratik ortognaysların ilksel kayalarının Pan-Afrikan temel ve Paleozoyik örtü serilerinin her ikisinede sokulum yapmış olmaları, Pan-Afrikan temel ve Paleozoyik örtü serilerinin Triyas öncesinde tektonik olarak biraraya geldiklerini göstermektedir.

CONTENTS

Page

Acknowledgements..... iii

Abstracts..... iv

Özet..... vi

List of Figures..... xii

List of Table..... xxiv

List of Abbreviations..... xxvi

Chapter One

INTRODUCTION

1.1. Previous studies and aims of the study..... 1

1.2. Location of the study areas..... 5

Chapter Two

TECTONOSTRATIGRAPHY

..... 7

Chapter Three

GEOLOGY AND PETROGRAPHY OF THE ROCK UNITS

3.1.Introduction..... 13

3.2. Pan-African Basement Units 15

3.2.1. Paragneiss..... 15
3.2.2. Metapelites (schists and phyllites) 25
3.2.3. Marbles..... 38
3.2.4. Metabasites..... 41
3.2.5. Orthogneiss..... 47
3.3. Paleozoic-Mesozoic cover units..... 54
3.3.1. Metapelites (phyllite-schist-quartzite intercalation)..... 55
3.3.2. Marble..... 62
3.3.3. Metabasites..... 63
3.3.4. Leucocratic orthogneiss..... 65
3.4. The rocks of İzmir-Ankara Zone..... 75

Chapter Four
GEOCHEMISTRY

4.1. Introduction..... 78
4.2. Preparation of the samples for XRF..... 78
4.3. Geochemistry of augen/granitic gneisses..... 81
4.3.1. Whole rock analyses..... 81
4.3.1.1. Major elements..... 81
4.3.1.2. Trace elements..... 81
4.3.2. Element Mobility..... 87
4.3.3. Protoliths of augen/granitic gneisses..... 91
4.3.4. Chemical classification..... 93
4.3.4.1. Normative classification..... 93
4.3.4.2. Multicationic classification..... 94
4.3.4.3. Major element classification..... 94
4.3.4.4. Trace element classification..... 96
4.3.5. Alkaline/Subalkaline affinity..... 97
4.3.6. Magmatic suite determinations..... 98
4.3.7. Shand's index..... 99

4.3.8. Tectonic setting discrimination..... 99
4.3.9. S-type affinity..... 101
4.4. Geochemistry of leucocratic orthogneisses..... 102
4.4.1. Whole rock analyses..... 102
4.4.1.1. Major elements..... 102
4.4.1.2. Trace elements..... 107
4.4.2. Element Mobility..... 107
4.4.3. Protoliths of leucocratic orthogneisses..... 107
4.4.4. Chemical classification..... 112
4.4.4.1. Normative classification..... 112
4.4.4.2. Multicationic classification..... 112
4.4.4.3. Major element classification..... 115
4.4.4.4. Trace element classification..... 115
4.4.5. Alkaline/Subalkaline affinity..... 116
4.4.6. Magmatic suite determinations..... 116
4.4.7. Shand's index..... 116
4.4.8. Tectonic setting discrimination..... 117
4.4.9. S-type affinitiy..... 119

Chapter Five

GEOCHRONOLOGY

5.1. Sampling and preparation of the samples..... 121
5.2. Analytical Techniques..... 123
5.2.1. Cathodoluminescence studies of zircons..... 123
5.2.2. Principles of single zircon $^{207}Pb/^{206}Pb$ evaporation technique.. 125
5.3. Dating of metamagmatic rocks..... 128
5.3.1. Augen gneiss..... 128
5.3.1.1. Previous geochronological studies..... 128
5.3.1.2. Zircon morphology..... 129
5.3.1.3. Description of the samples and $^{207}Pb/^{206}Pb$ ages..... 135

5.3.2. Leucocratic orthogneiss..... 139
5.3.2.1. Previous geochronological studies..... 139
5.3.2.2. Zircon morphology..... 139
5.3.2.3. Description of the samples and $^{207}Pb/^{206}Pb$ ages..... 146

Chapter Six
DISCUSSION

✓ **Tectonostratigraphy of the study areas**..... 154
✓ **Distribution of the leucocratic orthogneisses**..... 156
✓ **Geochemistry and tectonic setting of the Pan-African orthogneisses**.. 157
✓ **Geochemistry and tectonic setting of the Triassic leucocratic orthogneisses**.. 159
✓ **Geochronology of the Pan-African orthogneisses**..... 160
✓ **Geochronology of the Triassic leucocratic orthogneisses**..... 163
✓ **Latest Proterozoic-Early Paleozoic evolution of the Pan-African basement** 165
✓ **Tectonic setting of the Menderes Massif during the evolution of the Paleotethys and Neotethys** 167

Chapter Seven
CONCLUSIONS

..... 173

REFERENCES..... 176

LIST OF FIGURES

Figure		Page
	Chapter One **INTRODUCTION**	
1.1.	a) Tectonic map of the western Turkey and surrounding regions showing major continental blocks and tectonic zones (modified after Okay et al. 1996). b) Simplified geological map of the Menderes Massif and locations of the study areas (modified after Candan 1994).....	6
	Chapter Two **TECTONOSTATIGRAPHY**	
2.1.	Geological map Derbent region located in the eastern part of the Ödemiş-Kiraz Submassif of the Menderes Massif. National grids: İzmir L20-b3, İzmir L20-c2, İzmir L20-c3, İzmir L20-c4, Uşak L21-a4, Uşak L21-d1, Uşak L21-d4.....	8
2.2.	Geological map of Demirhan region located in the southern part of the Ödemiş-Kiraz Submassif of the Menderes Massif. National grid: Aydın M20 a2	9
2.3.	Generalised columnar section of Derbent area located in the easthern part of the Ödemiş-Kiraz Submassif of the Menderes Massif. (without scale).....	11
2.4.	Generalised columnar section of Demirhan region located in the southern part of the Ödemiş-Kiraz Submassif of the Menderes Massif. (without scale).....	12
	Chapter Three **GEOLOGY AND PETROGRAPHY OF THE ROCK UNITS**	
3.1.	a) Tectonic map of the western Turkey and surrounding regions showing major continental blocks and tectonic zones (modified after Okay et al. 1996), b) The simplified geological map of the Menderes Massif and distribution of Early Triassic leucocratic orthogneiss (modified after Candan 1994).....	14

3.2. Nappe units of Derbent area, southern part of Alaşehir, Ödemiş-Kiraz Submassif..... 16

3.3. Geological map Derbent region located in the eastern part of the Ödemiş-Kiraz Submassif of the Menderes Massif. National grids: İzmir L20-b3, İzmir L20-c2, İzmir L20-c3, İzmir L20-c4, Uşak L21-a4, Uşak L21-d1, Uşak L21-d4. 18

3.4. Pytigmatic structures in paragneisses, 650 m southeast of Eğrektaş hill, 30500:34625..... 19

3.5. Paragneisses displaying well-developed granoblastic texture, CPL.. 19

3.6. Small subhedral young garnets overgrowth around garnet porphyroblasts, PPL..... 20

3.7. Sillimanite fibers replacing biotites and garnets. Note that the sillimanite fibrolites are also growth at the quartz and orthoclase grain boundaries, PPL..... 21

3.8. Granoblastic texture in migmatitic paragneisses, CPL..... 22

3.9. The probably cordierite porphyroblasts related to the former granulite facies metamorphism are replaced by sillimanite, quartz, muscovite, biotite, garnet and kyanite in migmatitic paragneisses, PPL..... 23

3.10. Granoblastic texture in charnockitic paragneisses. Biotite shows symplectic overgrowth with quartz. Sillimanite fibrolites are growth at the orthoclase grain boundaries, PPL..... 24

3.11. Quartzite budinages in schist of lower nappe unit display top to SSW movement, 1.5 km southwest of Palamutçuk village, 10600:13375..... 26

3.12. The thrust contact relationships between lower and middle nappe units a) east of Palamutçuk village (12250:14750), b) south west of Aksu village, 15910:14700..... 26

3.13. Photomicrograph of foliation in garnet-mica schist. Long strings of mica minerals show parallelism and define the very remarkable lepidoblastic texture. Garnet and albite porphyroblasts cause also porphyroblastic texture in garnet-mica schists. a) CPL b) PPL..... 30

3.14. Syntectonic albite porphyroblast in garnet-mica schist show about 45° of dextral rotation with respect to S_e during growth. CPL..... 30

3.15. a) Post-tectonic biotite crystal overgrowing a lepidoblastic texture. Quartz ribbons are parallel to the main foliation., CPL. b)

subidioblastic laths of muscovite showing parallel alignment to the foliation, CPL..... 31

3.16. a) Garnet porphyroblasts display by well developed spiral-shaped inclusion trails composing mainly of quartz, PPL, b) Garnet porphyroblasts have a sharply defined inclusion free rim, indicating changing conditions during its growth, PPL..... 32

3.17. Subidioblastic hornblende crystals showing light green pleochroism colour are parallel to the main foliation, PPL..... 33

3.18. The contact relationship of phyllite with marble and schist, northeast of Marmarli village, 34500:21375..... 33

3.19. Quartz rich domains alternating with sericite rich domains in phyllites, CPL. 36

3.20. Aligned subidioblastic prismatic chloritoid crystals show remarkable parallelism with the main foliation, PPL..... 37

3.21. a) Syn-tectonic garnets show 45□ dextral rotation with respect to external foliation during the growing, CPL, b) Euhedral post-tectonic garnet crystals overgrow the former foliation, Note that the cleavage structure trap into the garnets as passive inclusions and perfectly continue without any deflection and development of strain shadow, CPL..... 37

3.22. Staurolites showing remarkable yellow pleochroism colour are produced by a reaction from chloritoid crystals, PPL..... 38

3.23. a) Prismatic kyanite porphyroblasts, and b) fascicular bundle type kyanite crystals in phyllites, CPL..... 39

3.24. a) Granoblastic texture due to the common occurrence of equigranular calcite crystals, CPL. b) Foliated marbles with a fabric defined by aligned muscovite laths alternating with calcite and quartz rich layers, CPL..... 40

3.25. General appearance of metagabbro within orthogneisses, 2 km soutwest of Eğrektaş hill, 30875:32275..... 42

3.26. Corona structures between olivine and plagioclase in metagabbro. Three zones are distinguished around olivine crystals; orthopyroxene in inner part, amphibole + spinel which display symplectic growing in middle part and amphibole in outer part, CPL..... 44

3.27. Boudinaged amphibolite pods in garnet-mica schist, 1.5 km east of Palamutcuk village, 13600:15075..... 44

3.28. a) General appearance of garnet amphibolite showing nematoblastic texture, PPL, b) photomicrograph of epidote amphibolite. Note that, prismatic zoisite crystal are parrallel to the foliation with hornblende and biotite, CPL..... 46

3.29. General appearence of a) granitc gneiss and b) augen gneiss..... 48

3.30. The contact relationship between orthogneiss of middle nape unit and schist of lower nappe unit, a) east of Aksu village, 16925/15450; b) around Kahvedere village, 28550:14075..... 49

3.31. The contact relationship between orthogneiss and schist and amphibolite, a) 3 km NW of Kahvedere village (26400:16475), b) 5 km SW of Sarıpınar village (24650:19850) and c) 1.5 SW of Karaca Ali village, 38525:20625..... 50

3.32. The contact relationship between orthogneiss and schist. Sills and dykes of orthogneiss occur in the schists close to the orthogneiss bodies, 2 km norteast of Derbent, 35500:29675..... 51

3.33. The contact relationship between orthogneiss (granitic gneiss) and schist. The boundary of orthogneiss cut across the main schistosity indicate the intrusive contact relationship, 2 km southeast of Derbent, 35500:29675..... 51

3.34. Photomicrograph showing lepidoblastic and porphyroblastic texture in orthogneisses, CPL..... 52

3.35. Subhedral to euhedral small garnet crystals overgrowth around biotites as a corona structure, CPL..... 53

3.36. The contact relationship between cover series and Pan-African basement, west of Bahadır village (see Figure 3.3)..... 55

3.37. Geological map of Demirhan region located in the southern part of the Ödemiş-Kiraz Submassif of the Menderes Massif. National grid: Aydın M20-a2..... 56

3.38. a) Photomicrograph showing lepidoblastic texture in garnet-mica schist, b) General appearance of mica schists which display parallel alignment of mica flakes, c) Photomicrograph showing lepidoblastic texture in calc-schist, CPL..... 58

3.39. Aligned subidioblastic prismatic chloritoid crystals showing remarkable parallelism with the main foliation, PPL..... 60

3.40. Syn-tectonic garnet crystal showing well-developed inclusion trails, PPL..... 61

3.41. Photomicrograph showing staurolite in the rim of syn-tectonic garnet porphyroblast as inclusions. Note that, inclusions in garnets pass into staurolite and perfectly continue on the right side of the crystal, PPL..... 61

3.42. The contact relationship between schist and marble, west of Eğrektaş hill, 29575:34775..... 62

3.43. An amphibolite bodie in garnet-mica schist of cover series, 2 km southwest of Eğrektaş hill, 28975:32050..... 63

3.44. Subidioblastic to idioblastic aligned hornblende crystals defining well developed nematoblastic texture, PPL..... 64

3.45. The panoramic view of leucocratic orthogneisses in the Derbent area, Dededağı, 34500:31300..... 65

3.46. a) General appearance of the muscovite rich leucocratic orthogneiss., b) general appearance of magnetite bearing leucocratic orthogneisses..... 66

3.47. The intrusive contact relationship between leucocratic orthogneiss and schist a) 35200:29200, b) 34125:27525..... 66

3.48. The dykes of leucocratic orthogneisses cut across the foliation of the schistosity of schist (a, 22125:17125) and the foliation of the augen gneisses (b, 28400:20450)..... 67

3.49. The contact relationship between leucocratic orthogneisses and schists. Sills of the leucocratic orthogneisses are observed close to the contact, a) 35125:28725, b) 29300:18650, c) 29250:18600, d) 28375:21100, e) 31100:24850.. 68

3.50. The contact relationship between sills of the leucocratic orthogneisses and the orthogneisses, 31875:17000.. 69

3.51. The contact relationship between leucocratic orthogneisses and phyllites of the cover series, 07175:03725..... 69

3.52. a) and b) Muscovites showing remarkable parallelism cause lepidoblastic texure in leucocratic orthogneisses. Note that, they have light green pleochroism, CPL, PPL (muscovite±biotite leucocratic orthogneiss), c) granoblastic texture in undeformed parts of the leucocratic orthogneisses, PPL (magnetite± biotite±muscovite leucocratic orthogneiss and biotite leucocratic orthogneiss respectively)..... 71

3.53. Photomicrograph of orthoclase showing common perthitic structure, mainly roded and braided type, CPL. 73

3.54. Photomicrograph showing orthoclase crystal mantled by plagioclase rims in leucocratic orthogneisses, CPL..... 73

3.55. a), b) Photomicrograph showing magnetite crystals in magnetite bearing lecocratic orthogneisses, PPL. 74

3.56. The contact relationship between leucocratic orthogneiss and marble, contact metamorphic assemblage occur in marble 40375/20325..... 75

3.57. Photomicrograph showing grossular and idocrase in the contact metamorphic rocks. Note that, idocrase display typical dark blue interference colour, CPL..... 75

3.58. Contact relationship of İzmir-Ankara Zone rocks with phyllite of cover series, 1 km SW of Bahadır village, 37100:32750..... 76

3.59. Serpentinites of İzmir-Ankara Zone rocks. Pyroxene crystal are visible in some samples..... 76

3.60. Photomicrograph illustrating the general apperance of serpentinites. Serpentinisation of the ultrabasic rock is common, CPL..... 77

Chapter Four
GEOCHEMISTRY

4.1. Location map of the samples for geochemical analyses of the augen/granitic gneisses, south of Alaşehir..... 79

4.2. Major oxides variation diagrams TiO_2, Al_2O_3, $Fe_2O_3^T$, MgO, CaO, Na_2O, K_2O, and P_2O_5 against SiO_2 (wt %) for augen/granitic gneiss from different submassifs of the Menderes Massif 82

4.3. Major oxides variation diagrams, TiO_2, Al_2O_3, $Fe_2O_3^T$, MgO, CaO, Na_2O, K_2O, and P_2O_5 against SiO_2 (wt %) for augen/granitic gneiss of the study area..... 83

4.4. Selected trace element variation diagrams Ba, Cr, Ga, Nb, Ni, Rb, Sr, V, Y, Zn, and Zr (ppm) against SiO_2 (wt %) for augen/granitic gneiss from different submassifs of the Menderes Massif..... 84,85

4.5. Selected trace element variation diagrams, Ba, Cr, Ga, Nb, Ni, Rb, Sr, V, Y, Zn, Zr, and Th (ppm) against SiO_2 (wt %) for augen/granitic gneiss of the study area. 85,86

4.6. Graphical comparison of major oxides, , Al_2O_3, $Fe_2O_3^T$, MgO, CaO, Na_2O, K_2O, and P_2O_5 versus TiO_2 (wt %) for augen/granitic gneiss from different submassifs of the Menderes Massif. 88

4.7. Graphical comparison of major oxides, Al_2O_3, $Fe_2O_3^T$, MgO, CaO, Na_2O, K_2O, and P_2O_5 versus TiO_2 (wt %) for augen/granitic gneiss of the study area. 89

4.8 Graphical comparison of trace elements, Ba, Cr, Ga, Nb, Ni, Rb, Sr, V, Y, Zn, and Zr (ppm) versus TiO_2 (wt %) for augen/granitic gneisses from different submassifs of the Menderes Massif..... 90,91

4.9. Graphical comparison of trace elements, Ba, Cr, Ga, Nb, Ni, Rb, Sr, V, Y, Zn, and Zr (ppm) versus TiO_2 (wt %) for augen/granitic gneiss of the study area..... 92,93

4.10. a) Na_2O/Al_2O_3 vs K_2O/Al_2O_3 (after Garrels &Mackhenzie, 1971) and b) P_2O_5/TiO_2 vs MgO/CaO (after Werner, 1987) discrimination diagrams suggesting an igneous origin for the augen/granitic gneisses of the study area. c) The samples from study area are concentrated in the orthogneiss field of the Al_2O_3 vs MgO discrimination diagram (after Marc, 1992)..... 94

4.11. Chemical classification of the protoliths of the augen/granitic gneiss on a normative An-Ab-Or ternary diagram after Barker (1979)..... 95

4.12. Multicationic classification of the protoliths of the augen/granitic gneiss on Q = [Si/3 - (K+Na+2Ca/3)] vs P= K-(Na+Ca), (after Debon and Le Fort, 1983)..... 95

4.13. The chemical classfication and nomenclature of plutonic rocks using the total alkalis ($Na_2O + K_2O$) versus SiO_2 (TAS) diagram after Cox et al., (1979) adapted by Wilson (1989) for plutonic rocks..... 96

4.14. Classification of the protolith of the augen/granitic gneisses on a) SiO_2 vs Nb/Y and b) SiO_2 vs Zr/TiO_2 binary plots (adapted from Winchester and Floyd, 1977)..... 97

4.15. a) (Na_2O+K_2O) vs SiO_2 binary plot after Cox et al. (1979). The dividing line between alkali and subalkali granite fields is after Miyashiro (1978); b) Zr/TiO_2 vs Nb/Y binary plot after Pearce and Cann (1973), and c) K_2O vs Na_2O binary plot after Middlemost (1975) showing the subdivision of the alkaline field into high K-, K-, and Na- sub series..... 98

4.16. AFM ternary diagram with the dividing line after Kuno (1968) and Irvine and Baragar (1971)..... 99

4.17. Shand's index. $Al_2O_3/(Na_2O+K_2O)$ vs $Al_2O_3/(CaO+Na_2O+K_2O)$ binary plot for the granitic protolith after Maniar and Piccoli (1989)..... 100

T.C. YÜKSEKÖĞRETİM KURULU
DOKÜMANTASYON MERKEZİ

4.18. SiO_2 variation diagrams for tectonic discrimination of the protolith of the augen/granitic gneisses; a) Y vs SiO_2; b) Nb vs SiO_2; and c) Rb vs SiO_2, and d) Nb vs Y, e) Rb vs Y+Nb (after Pearce et al., 1984)..... 101

4.19. Geochemical classification of the granitic protolith on a) a normative corundum vs molar A/CNK binary plot (field boundaries are from Chappel and White (1974) and b) molar A/CNK vs $Fe_2O_3^T$ (after Marc, 1992)..... 102

4.20.a. Sample location map for geochemical analyses of the leucocratic orthogneisses, south of Alaşehir/Manisa..... 103

4.20.b. Sample location map for geochemical analyses of the leucocratic orthogneiss, northeast of Atça/Aydın..... 104

4.21. Major oxides variation diagrams of TiO_2, Al_2O_3, $Fe_2O_3^T$, MgO, CaO, Na_2O, K_2O, and P_2O_5 versus SiO_2 (wt %) for the leucocratic orthogneiss..... 108

4.22. Selected trace element variation diagrams of Ba, Ga, Nb, Rb, Sr, Y, Zn and Zr (ppm) versus SiO_2 (wt %) for the leucocratic orthogneiss. 109

4.23. Graphical comparison of major oxides of Al_2O_3, $Fe_2O_3^T$, MgO, MnO, CaO, Na_2O, K_2O and P_2O_5 versus TiO_2 (wt %) for leucocratic orthogneiss. 110

4.24. Graphical comparison of trace elements of Ba, Ga, Nb, Rb, Sr, Y, Zn, and Zr (ppm) versus TiO_2 (wt %) for leucocratic orthogneiss..... 111

4.25. a) TiO_2 versus SiO_2 discrimination diagram suggesting an igneous origin for the leucocratic orthogneisses after Tarney (1976), b) Na-K relationships for the three groups of leucocratic orthogneisses shown in the igneous spectrum of Hughes (1972) and c) Al_2O_3 versus MgO discrimination diagram after Marc (1992) suggesting orthogneiss series for the leucocratic orthogneiss..... 113

4.26. Chemical classification of the protoliths of the leucocratic orthogneiss on a normative An-Ab-Or ternary diagram after Barker (1979). 112

4.27. Multicationic classification of the protoliths of the leucocratic orthogneisses on a) Q = [Si/3 - (K+Na+2Ca/3)] vs P= K-(Na+Ca) and b) A=Al-(K+Na+2Ca) vs B=(Fe+Mg+Ti) after Debon and Le Fort (1983).... 114

4.28. The chemical classfication and nomenclature of plutonic rocks using the total alkalis (Na_2O+K_2O) versus SiO_2 (TAS) diagram after Cox et al., (1979) adapted by Wilson (1989) for plutonic rocks..... 115

4.29. Classification of the protolith of the leucocratic orthogneisses on a) SiO_2 vs Nb/Y; and b) SiO_2 vs Zr/TiO_2 binary plots adapted from Winchester and Floyd (1977)..... 116

4.30. a) (Na_2O+K_2O) vs SiO_2 binary plot after Cox et al. (1979). The dividing line between alkaline and subalkaline granite fields is from Miyashiro (1978); and b) K_2O vs Na_2O binary plot after Middlemost (1975) showing the subdivision of the alkaline field into high K-, K-, and Na- sub series..... 117

4.31. AFM ternary diagram with the dividing line of Kuno (1968) and Irvine and Baragar (1971); b) $Fe_2O_3^T$ vs Fe_2O_3/MgO, diagram after Miyashiro (1974) 118

4.32. Shand's index. a) $Al_2O_3/(Na_2O+K_2O)$ vs $Al_2O_3/(CaO+Na_2O+K_2O)$ and b) $Al_2O_3/(CaO+Na_2O+K_2O)$ vs $(Na_2O+K_2O)/Al_2O_3$ binary plots for the granitic protolith of the leucocratic orthogneisses after Maniar and Piccoli (1989) 118

4.33. SiO_2 variation diagrams for the tectonic discrimination of the protolith of the augen/granitic gneisses; a) Y vs SiO_2; b) Nb vs SiO_2 and c) Rb vs SiO_2, and d) Nb vs Y, e) Rb vs Y+Nb after Pearce et al., (1984)..... 119

4.34. Geochemical classification of the granitic protolith on a) A/CNK vs $Fe_2O_3^T$ (after Marc, 1992), b) normative corundum vs molar A/CNK and c) molar A/CNK vs molar NK/A binary plots (field boundaries are from Chappel and White, (1974)..... 120

Chapter Five
GEOCHRONOLOGY

5.1. Scheme for the extraction of the common minerals from hard-rock samples..... 122

5.2. Procedure to fix zircon grains for cothodoluminescence analysis, modified after Chen, (1999)..... 124

5.3. Rhenium-doble filament configuration used for Pb evaporation analysis, after Kober, (1986)..... 126

5.4. Main types and subtypes of the typologic classification and corresponding geothermometric scale, after Pupin and Turco, (1972)..... 130

5.5. SEM images of typical zircons of augen/granitic gneisses. a and b: clear, colourless, long prismatic, clustering around L1; c and d: clear, colourless, long prismatic, clustering around S12, e and f: clear, colourless and slightly pink, long prismatic, clustering around S7; g and h: clear, colourless and slightly pink, long prismatic clustering around S17, i and j: clear,colourless, slightly pink andbrown, short and long prismatic, clustering around S7; k: clear, colourless and slightly pink, clustering around S17; l: clear, colourless, long prismatic, clustering around S2..... 131,132,133

5.6. Cathodoluminescence images of characteristic zircon populations in augen/granitic gneisses. Zircons with older core are shown from a to d and i to l. A characteristic feature for zircons is oscillatory zoning indicating a magmatic origin, e to h and m to p. ZCA zoning-controlled alteration, SCA surface-controlled alteration, C the sharp boundary (resorption surface) between cores and overgrowths..... 134,135

5.7. Sample location map for geochronological analysis of augen/granitic gneisses, south of Alaşehir..... 136

5.8. Zircon age for augen gneiss, 96-34. Histogram of radiogenic $^{207}Pb/^{206}Pb$ ratios for evaporated zircons indicating age of 561.5±0.8 Ma ($2\sigma_{mean}$). 137

5.9. Zircon age for augen gneiss, 97-58. Histogram of radiogenic $^{207}Pb/^{206}Pb$ ratios for evaporated zircons indicating age of 570.5±2.2 Ma ($2\sigma_{mean}$). 138

5.10. SEM images of typical zircons of leucocratic orthogneisses. a and b: colorless, turbid, short and long prismatic, clustering around D, c and d: colourless, turbid, short and long prismatic, clustering around P4 and P5 respectively; e: colourless, turbid, short prismatic, clustering around D; f: colourless, clustering around P2; g and h: clear, colourles and slightly pink, short and long prismatic, clustering around S7 and S12 respectively; i and j: colourless, turbid, short prismatic, clustering around P3 and P1 respectively; k and m: colourles, pink, clear to turbid, short prismatic, clusteringaround P4; l, m and n: colourles, pink, clear to turbid, short prismatic, clustering around D; o: pink, colourles, clear to turbid, long prismatic; clustering around T11, p: clear, colourless, short prismatic, clustering around S7..... 140,141,142 143,144

T.C. YÜKSEKÖĞRETİM KURULU DOKÜMANTASYON MERKEZİ

5.11. Cathodoluminescence (CL) images of characteristic zircon populations in leucocratic orthogneisses. A characteristic feature for zircons is oscillatory zoninig indicating a magmatic origin, a to c; d to h show oscillatory zoninig indicating a magmatic origin; i to k show magmatic growth zonation only along outer-most rim of the grain; Zircons with older core are shown from l to o; p to t show oscillatory zonnig indicating a magmatic origin. ZCA zoning-controlled alteration, SCA surface-controlled alteration, C the sharp boundary (resorption surface) between cores and overgrowths..... 144,145,146

5.12. Sample location map for geochronological analyses of leucocratic orthogneisses, south of Alaşehir..... 147

5.13. Sample location map for geochronological analysis of leucocratic orthogneisses, Demirhan village..... 148

5.14. Zircon age for leucocratic orthogneiss. Histogram of radiogenic $^{207}Pb/^{206}Pb$ ratios for evaporated zircons indicating age of 245.7±4.6 Ma ($2\sigma_{mean}$). 150

5.15. Single zircon evaporation data in a plot showing evaporation temperature versus apparent $^{207}Pb/^{206}Pb$ ages (weighted mean values). Error is 2σ of the mean..... 150

5.16. Zircon age for leucocratic orthogneiss. Histogram of radiogenic $^{207}Pb/^{206}Pb$ ratios for evaporated zircons indicating age of 241.1±5.2 Ma ($2\sigma_{mean}$)..... 151

5.17. Single zircon evaporation data in a plot showing evaporation temperature versus apparent $^{207}Pb/^{206}Pb$ ages (weighted mean values). Error is 2σ of the mean. 151

5.18. Zircon age for leucocratic orthogneiss. Histogram of radiogenic $^{207}Pb/^{206}Pb$ ratios for evaporated zircons indicating age of 234.9±5.8 Ma ($2\sigma_{mean}$)..... 152

5.19. Single zircon evaporation data in a plot showing evaporation temperature versus apparent $^{207}Pb/^{206}Pb$ ages (weighted mean values). Error is 2σ of the mean..... 153

Chapter Six
DISCUSSION

6.1. Simplified columnar section of Eğrikavak area, northeast of Aydın, and Derbent area, south of Alaşehir in the Ödemiş-Kiraz Submassif..... 156

6.2. Simplified geological map of the Menderes Massif showing the distribution of leuccocratic orthogneisses, modified from Candan and Dora (1998)..... 158

6.3. Simplified geological map of the Menderes Massif showing geochronological age data obtained from orthogneisses, after Candan and Dora (1998). Data from Hetzel and Reischmann (1996); Dannat (1997), Hetzel et al. (1998); Loos and Reischmann, (1999), Gessner et al. (2001)..... 162

6.4. Simplified geological map of the Menderes Massif. and the Cyclades showing geochronological age data obtained from leucocratic orthogneisses, modified after Candan and Dora (1998). Data from Dannat and Reischmann (1996, 1997) and Reischmann (1998)..... 164

6.5. Geologically constrained reconstraction of the Pannotia supercontinent at the Precambrian-Cambrian boundary, after Dalziel (1997). Thick lines: incipient mid-Iapetus ridges; horizontal lines: East African collisional orogen involving East and West Gondwana. AM: Amazonian craton; B: Baltica (Russian cnaton); C: Congo craton; DRA: Delamerian Ross arc; EA: east Avalonia (southern British Isles); ESMT: hypothetical Ellsworth-Sonora-Mojave transform; F: Florida; F/MP: Falkland-Malvinas Plateau; MAOT: hypothetical Malvinas-Alabama transform; R: Rockall Plateau; RP: Rio de la Plata craton; S: Siberia (Angara craton); SF: São Francisco craton; SV: Svalbard Block; TxP: hypothetical Texas Plateau; WA: West African craton; Wa: west Avalonia..... 166

6.6. Simplified tectonic map of East and West Gondwana including Pan-African suture at Late Paleozoic time. Data after Şengör et al. (1984); Dalziel (1997) and Piper (2000)..... 168

6.7. Reconstruction of Eastern Mediterranean at Latest Permian time, modified from Stampfli et al., (1998). Green coloured elipsoidal area represets the locality of the Menderes Massif proposed by this study. AG: Agh-Darband; BD: Beydağları; KA: Karakaya; ME: Menderes and Taurides; MM: Menderes Massif..... 170

6.8. Schematized sequential cross section showing the pre-Triassic tectonic evolution of the Menderes Massif. Discussions is in the text..... 171

LIST OF TABLES

Table **Page**

Chapter Three

GEOLOGY AND PETROGRAPHY OF THE ROCK UNITS

3.1. Modal mineralogical composition and mineral percentage of the representatitve paragneiss samples..... 20

3.2 Modal mineralogical composition and mineral percentage of the representative paragneiss samples 22

3.3. Modal mineralogical composition and mineral percentage of the representative charnockitic paragneiss samples..... 24

3.4. The modal mineralogical composition and mineral percentage of the representative schist samples..... 29

3.5. Modal mineralogical composition and mineral percentage of the selected phyllite samples 35

3.6. Modal mineralogical composition and mineral percentage of the representative marble samples..... 40

3.7. Modal mineralogical composition and mineral percentage of the representative metagabbro samples..... 43

3.8. Modal mineralogical composition and mineral percentage of the selected amphibolite samples 45

3.9. The modal mineralogical composition and mineral percentage of the representative orthogneiss samples..... 52

3.10. Modal mineralogical composition and mineral percentage of the representatitve schist samples 57

3.11. Modal mineralogical composition and mineral percentage of the representatitve phyllite samples..... 60

3.12. Modal mineralogical composition and mineral percentage of the representative marble samples. 62

3.13. Modal mineralogical composition and mineral percentage of the representative amphibolite samples..... 64

3.14. Modal mineralogical composition and mineral percentages of the representative leucocratic orthogneiss samples..... 72

3.15. Modal mineralogical composition and mineral percentage of representative serpentinite samples..... 77

Chapter Four

GEOCHEMISTRY

4.1. Chemical and normative data of augen/granitic gneisses, na: not analysed..... 80

4.2. Chemical and normative data for leucocratic orthogneisses, na: not analysed..... 105,106

Chapter Five

GEOCHRONOLOGY

5.1. Radiogenic $^{207}Pb/^{206}Pb$ ratios of evaporated zircon grains and corresponding ages 137

5.2. Radiogenic $^{207}Pb/^{206}Pb$ ratios of evaporated zircon grains and corresponding ages..... 149

Chapter Six

DISCUSSION

6.1. Age data of orthogneissic rocks from the Menderes Massif..... 161

Geological, petrographical, geochemical and petrological studies in the Menderes Massif have been carried out for more than 160 years (e.g. Hamilton and Strickland, 1840; Tchihatcheff , 1869; Philippson, 1911; Önay, 1949; Nebert and Ronner, 1956; Schulling, 1958, 1962, 1973; Wippern, 1964; Graciansky, 1965; Scottford, 1969; Başarır, 1970; Dora, 1976; Dora et al., 2001).

The Menderes Massif is commonly interpreted as the eastward continuation of Attic-Cycladic Massif in the Aegean Sea (Dürr et al., 1978; Jacobshagen, 1986; Oberhänsli et al., 1998). However, recently it has been suggested that two massifs are in all aspects not related (Ring et al., 1999). It has been regarded that the Menderes Massif composed of a Pan-African basement rock and an overlying Early Paleozoic-Early Tertiary cover series. The Pan-African basement rocks consist of Late Proterozoic clastic metasediments; i.e. paragneisses, migmatitic paragneisses and mica schists which were intruded by the protoliths of Precambrian eclogitic gabbros and post-Pan-African orthogneisses. The covers can be separated into two units that comprise Palezoic and Mesozoic-Early Tertiary rocks. The Paleozoic series is made up predominantly of a sequence of quartzite, phyllite and marble. The Mesozoic-Early Tertiary series comprises a sequence of metaconglomerate, schist, dolomite, platform type metacarbonate which contain emery deposits, pelagic marble and metaolistostrome.

In the previous studies, paragneisses were regarded as metavolcanic rocks, leptite-gneiss, based on geochemical and geological evidences. Recent studies, new evidences revealed that they are of sedimentary origin (Dora et al., 1995, 2001) and are one of the main units of the basement of the Menderes Massif. Paragneisses and schists are intruded by most probably Precambrian metagabbro and Pan-African granitic gneisses.

It is commonly agreed that the Menderes Massif has a complex and polyphase metamorphic history. The basement rocks of the Menderes Massif were subjected to polyphase metamorphism at granulite-, eclogite- and amphibolite facies conditions which were related to Pan-African orogenesis (Dora et al., 1995; Oberhänsli et al.,

LIST OF ABBREVIATIONS

Ab	: Albite
AG	: Agh-Darband
ALCAF	: Alumino-cafemic
ALUM	: Aluminous
AM	: Amazonian Craton
B	: Baltica (Russian Craton)
BD	: Bey Dağları
Bt	: Biotite
C	: Congo Craton
Cal	: Calcite
Chl	: Chlorite
CL	: Cathodolumiscence
Cld	: Chloritoid
COLG	: Collisional granitoids
CPL	: Cross polarised light
Cpx	: Clinopyroxene
DRA	: Delamerian Ross Arc
EA	: East Avalonia (southern British Isles)
ESMT	: hypotetical Ellsworth-Sonora-Mojave transform
F	: Florida
F/MP	: Falkland-Malvinas Plateau
Gr	: Garnet
Hbl	: Hornblende
Id	: Idocrase
KA	: Karakaya
Ky	: Kyanite
Mag	: Magnetite
MAOT	: hypothetical Malvinas-Alabama transform
ME	: Menderes and Taurides
MM	: Menderes Massif
Ms	: Muscovite
Ol	: Olivine
Opq	: Opaque
Oprx	: Orthopyroxene
Or	: Orthoclase
ORG	: Ocean ridge granitoids
Pl	: Plagioclase
Post-COLG	: Post collisional granitoids
PPL	: Plane polarised light

T.C. YÜKSEKÖĞRETİM KURULU
DOKÜMANTASYON MERKEZİ

Px	: Pyroxene
Qtz	: Quartz
R	: Rockall Plateau
RP	: Rio de la Plata Craton
S	: Siberia (Angara Craton)
SCA	: Surface controled alteration
S_e	: external foliation with respect to a porphyroblast with inclusions
SEM	: Scanning electron microscope
Ser	: Sericite
SF	: Sao Francisco Craton
S_i	: internal foliation in a porphyroblast with inclusions
Sil	: Sillimanite
Sp	: Spinel
Srp	: Serpentine
St	: Staurolite
SV	: Svalbard Block
Syn-COLG	: Syn-collisional granitoids
TxP	: hypotetical Texas Plateau
VAG	: Volcanic arc granitoids
WA	: West African Craton
Wa	: West Avalonia
WPG	: Within plate granitoids
ZCA	: Zonning controled alteration
Zo	: Zoisite

CHAPTER ONE
INTRODUCTION

The Menderes Massif, which occupies a vast area in western Turkey, is part of the Alpine-Himalayan Orogenic Belt. It forms a large (200 x 300 km) culmination of metamorphic rocks. In early studies, it was accepted that the Menderes Massif had a simple internal structure, made up of a Precambrian basement and an Early Paleozoic to Early Tertiary cover series (Schulling, 1962). Recent studies show that this massif does not have a simple structure, but is made up from a nappe stack related to the Alpin compressional tectonics (Konak et al., 1994; Dora et al., 1994; Partzsch et al., 1998; Gessner et al., 1998). Furthermore, the geologic and geochronologic evidence suggests that there have been three distinct magmatic activities in the Menderes Massif: i) Precambrian/Cambrian, ii) Triassic and iii) Tertiary. Major magmatic activity, the granitic protoliths of orthogneiss, took place during Late Precambrian /Early Cambrian. The granitic protoliths of the leucocratic orthogneisses represent the second pulse of magmatic phase, Triassic, in the Menderes Massif. The third phase of magmatic activity, which is unmetamorphosed, yielded 25 to 12 Ma.

1.1. Previous studies and aims of the study

The Menderes Massif, which is of north-easterly oriented and elliptical shaped, has significant imprint on the geological evolution of western Anatolia. It is tectonically overlain by the nappes of İzmir-Ankara Zone including the Bornova Flysch Zone of olistostromal character, in the northwest, the Afyon Zone consisting of low-grade metapelite and metacarbonate in the north, and the Lycian Nappes comprising shales and carbonate and thick ophiolite slices in the south (Şengör and Yılmaz, 1981; Dora et al., 1995).

1997; Candan and Dora, 1998; Candan et al., 1998, 2001). The protoliths of orthogneisses have not experienced this Pan-African metamorphism, which resulted over thrusting and consequent crustal thickening during Pan-African orogeny, and completely lack any mineral assemblages of this poly-phase first event. The metamorphic phases, which have affected the basement rocks, metagabbro paragneisses, migmatitic paragneisses and schists, of the Menderes Massif have not yet been dated radiometricaly.

The origin of the orthogneiss has been controversial for many years. Although, in previous studies, most of researchers suggest a sedimentary protolith of the orthogneisses (Schulling, 1962; Başarır, 1970, 1975; Dora, 1975; Şengör et al., 1984; Satır and Friedrichsen, 1986). Also, a granitic protolith were suggested by some researchers (Graciansky, 1965; Konak, 1985; Konak et al., 1987; Erdoğan; 1992; Bozkurt, 1994, 1995; Bozkurt et al., 1993; Hetzel and Reischmann, 1996; Loos and Reischmann, 1999). Beside this, the intrusion ages for the protoliths of the orthogneisses, which were emplaced in the period following Pan-African metamorphism, have been dated geochronologicaly by many researchers. In previous studies, Şengör et al. (1984) and Satır and Friedrichsen (1986) suggested an intrusion age of 470±9 Ma based on Rb/Sr-whole rock isochron for the protoliths of the orthogneisses. Recent geochronological studies on orthogneisses from the different parts of the Menderes Massif also yielded ages of 546.2±1.2 Ma (Hetzel and Reischmann, 1996), 528±4.3 to 544.1±4.3 Ma (Dannat, 1997; Dannat and Reischmann, 1997) and 521±8 to 572±7 Ma (Loos and Reischmann, 1999). These data were obtained from zircons by the $^{207}Pb/^{206}Pb$ single-grain evaporation method. A metagranite from the Ödemiş-Kiraz Submassif, which has been dated by conventional U-Pb dating, also revealed a Late Precambrian intrusion age of 551.5±1.4 Ma (Hetzel et al., 1998). Consequently, all these geochronological zircon investigations prove strong evidence for a major magmatic episode in the latest Precambrian to early Cambrian.

In previous studies, it was accepted that there is an unconformity between the Pan-African basement rocks and the Early Paleozoic - Early Tertiary cover series

(Schulling, 1962; Graciansky, 1965; Başarır, 1970, 1975; Şengör et al., 1984; Konak, 1985; Satır and Friedrichsen, 1986; Konak et al., 1987) and later this contact was defined as the "main supra-Pan-African unconformity" by Şengör et al., (1984). The granite pebbles from a metaconglomerate in lower horizons of the Paleozoic series have yielded an age of 550 Ma by single zircon evaporation method requires that the basement - cover contact can be interpreted as unconformable (Dora et al., 1995). Furthermore, some authors suggest that the contact between orthogneisses and cover series is intrusive (Bozkurt et al., 1992, 1993, 1995; Erdoğan, 1992; 1993). Orthogneisses display locally preserved intrusive contact relationship with the cover schists. However, in recent years, it has begun to be accepted that the contact between these units is tectonic (Bozkurt and Park, 1994; 1997a, 1997b; Partzsch et et al., 1998; Ring et al., 1999; Bozkurt and Satır, 2000; Gessner et al., 2001).

The second metamorphic event, which affected the Menderes Massif, is controversial. Schulling (1962) was the first researcher suggested a Hercinian metamorphism in the Menderes Massif. Akkök (1983) report a late Triassic metamorphism, which reflects the closure of Karakaya marginal basin of Paleotethys. Granitic intrusions followed this metamorphic event which occurred at greenschist-facies conditions. Although, Şengör et al. (1984) suggested a similar conception, but they did not proposed any clear idea, whether this phase belongs to the Hercinian or Early Alpine orogenesis. The protoliths of the leucocratic orthogneisses represent the second pulse of significant magmatic activity in the Menderes Massif (Koralay and Dora, 1999; Koralay et al., 2001). Limited number of geological and geochronological studies was carried out on the leucocratic orthogneisses. Dannat (1997) and Dannat and Reischmann (1998) give an intrusion age of 227-240 Ma based on $^{207}Pb/^{206}Pb$ single zircon evaporation method for the protoliths of the leucocratic orthogneisses in the Ödemiş-Kiraz and Gördes Submassif. Koralay and Dora (1999) and Koralay et al. (2001) suggest that the protoliths of the leucocratic orthogneisses were metamorphosed during the Alpine orogenesis and transformed into orthogneisses.

The main aims of this study were to (a) document the geological, mineralogical and petrographical characteristics of the rock units; (b) document the geochemical characteristics of the orthogneisses, augen/granitic gneisses, and correlate with the other orthogneisses in different submassif of the Menderes Massif; (c) document the geochemical characteristics of the leucocratic orthogneisses; (d) thereby discuss the possible source and tectonic environment of magma generation both orthogneisses and leucocratic orthogneisses; and (e) discuss the possible relationship of these magmatic events to the metamorphic history of the Menderes Massif.

1.2. Location of the study areas

The study areas are located within the Ödemiş-Kiraz Submassif of the Menderes Massif in western Anatolia. First study area locates in eastern part of the Ödemiş-Kiraz Submassif south of Alaşehir between latitudes 13-43 and longitudes 10-42 (Figure 1.1). The main settlement within this study area is Derbent. This study area covers an area of approximately 630 km^2. It is included on 1/25000 scale Turkish topographic map sheets İzmir L20-b3, İzmir L20-c2, İzmir L20 c3, İzmir L20-c4, Uşak L 21-a4, Uşak L 21-d1, Uşak L 21-d4 (Figure 1.1). Second study area locates in southern part of the Ödemiş-Kiraz Submassif north of Atça between latitudes 02-06 and longitudes 06-09 (Figure 1.1). The main settlement within this area is Demirhan village. This study area covers an area of approximately 12 km^2. It is about 3 km wide in an E-W direction and 4 km long in a N-S direction. It is included on 1/25000 scale Turkish topographic map sheet Aydın M 20-a2 (Figure 1.1).

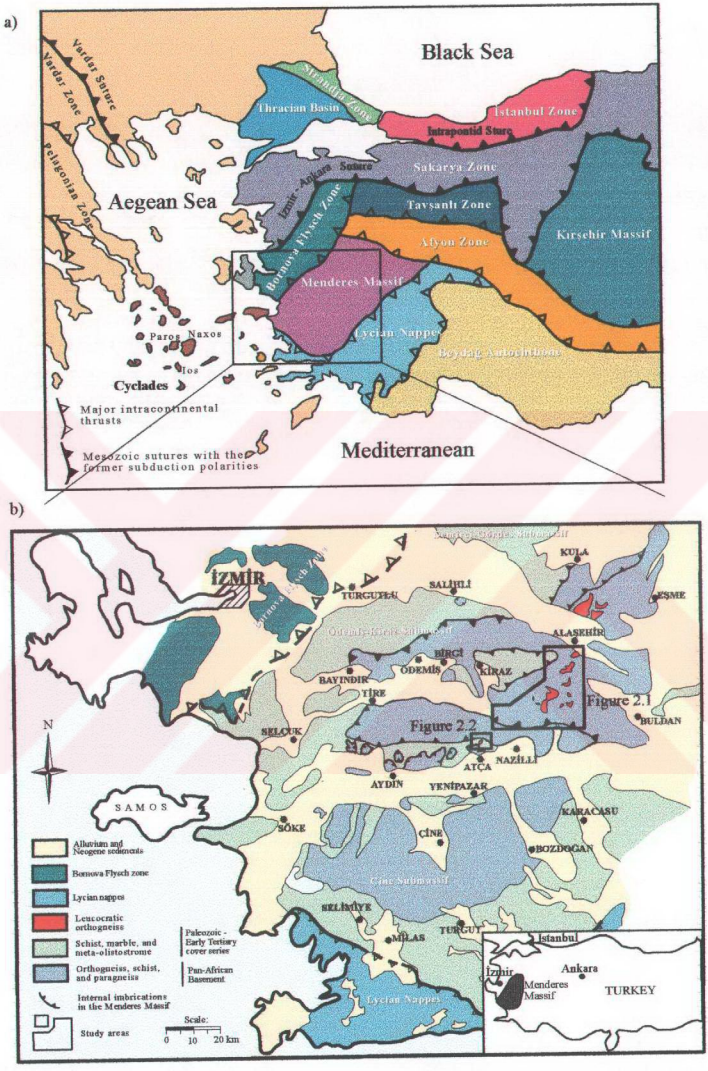


Figure 1.1. a) Tectonic map of the western Turkey and surrounding regions showing major continental blocks and tectonic zones (modified after Okay et al. 1996). **b)** Simplified geological map of the Menderes Massif and locations of the study areas (modified after Candan 1994).

CHAPTER TWO
TECTONOSTRATIGRAPHY

2.1. Tectonostratigraphy

The rock succession of the Derbent and Demirhan areas occuring in the eastern part of the Ödemiş-Kiraz Submassif is made up of nappe stack (Figure 2.1, 2.2). In the eastern part of the Ödemiş-Kiraz Submassif, in the vicinity of Derbent, the rock succession of metamorphic series can be divided into four nappe units (Figure 2.3). In ascending order, the first three-nappe units are represented by the internal imbrication of the Pan-African basement series, whereas the uppermost nappe unit belongs to Palaeozoic-Mesozoic cover series. The metamorphic rocks of the Menderes Massif, which display a typical nappe stacking tectonically overlain by unmetamorphosed ophiolitic rocks which are, most probably, related to İzmir-Ankara Zone. The metamorphic rocks of the Menderes Massif and ophiolite related rocks of the İzmir-Ankara Zone, are unconformably overlain by Neogene sedimentary rocks.

The lower nappe unit of the Pan-African basement series is made up of predominantly schists, e.i. mica schists and garnet-mica schists. The schists include numerous garnet amphibolites bodies as sills and pods. Middle nappe unit predominantly comprises metapelites which minor contain carbonate and phyllite horizons. The metapelites are composed of predominantly garnet-mica schist and subordinately mica schist, hornblende-garnet schist and muscovite-quartz schist. Phyllite levels which are associated with marbles occur in the schists as interlayers and lenses. The phyllites are composed of predominantly biotite phyllite, chloritoid phyllite, garnet phyllite and chloritoid-garnet phyllite and subordinately chloritoid-staurolite-kyanite phyllite. The metapelites in the middle nappe unit are intruded by the protoliths of 562-571 Ma syn- to post-Pan-African orthogneisses and

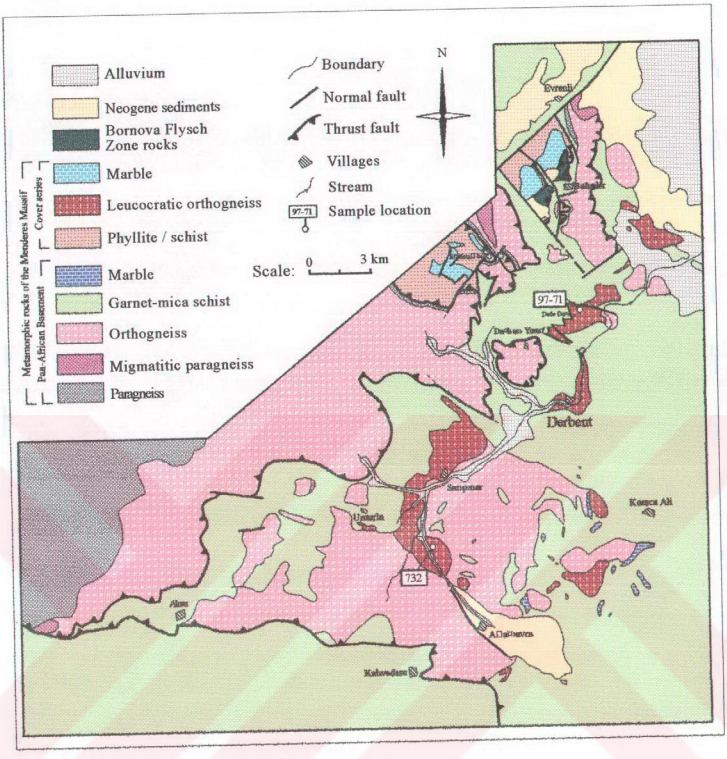


Figure 2.1. Geological map of Derbent region located in the eastern part of the Ödemiş-Kiraz Submassif of the Menderes Massif. National grids: İzmir L20-b3, İzmir L20-c2, İzmir L20-c3, İzmir L20-c4, Uşak L21-a4, Uşak L21-d1, Uşak L21-d4, (for location see Figure 1.1).

Precambrian metabasites. Orthogneisses, both internaly and peripherally, include numerous schist enclaves which are particularly concentrated close to the margins. Furthermore, numerous sills and dykes of orthogneisses are observed in the schists close to the margins of orthogneiss. Schist enclaves in orthogneisses and sills and dykes of orthogneisses in country rocks, e.i.schists, prove the original intrusive contact rocks, e.i. schists, prove the original intrusive contact relationship between schist and orthogneiss. Precambrian metagabbros and amphibolites are found in

schist as sills and pods. Furthermore, the schists are also intruded by the protoliths of 235-246 Ma aged, Triassic, leucocratic orthogneisses which occur only in middle nappe unit. The leucocratic orthogneisses also include peripheraly numerous schist enclaves which are particularly common close to the contact. Moreover, numerous sills of leucocratic orthogneiss are found in the schist and orthogneiss of Pan-African basement close to the margins of leucocratic orthogneiss.

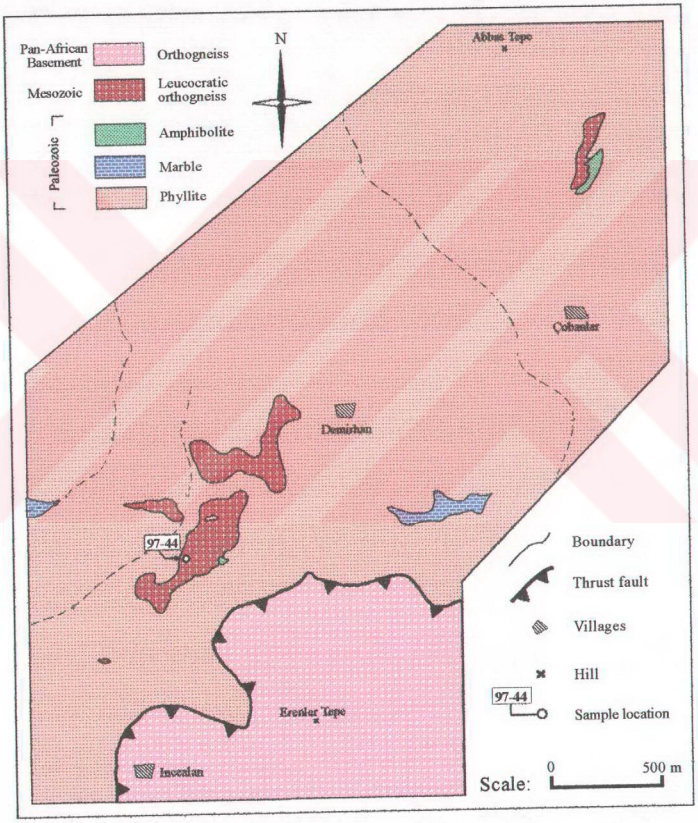


Figure 2.2. Geological map of Demirhan region located in the southern part of the Ödemiş-Kiraz Submassif of the Menderes Massif. National grid: Aydın M20-a2, (for location see Figure 1.1)

Middle nappe unit is tectonically overlain by the upper nappe unit of the Pan-African basement. The upper nappe slice is made up of predominantly orthogneiss and subordinately paragneiss, migmatitic paragneiss and metapelite. The orthogneisses have intrusive contact relationship with paragneiss which is mostly obliterated by the later metemorphic and tectonic events.

The Pan-African nappe units are overlain by the cover series, the upper most nappe unit, with a tectonic contact. In ascending order, the cover series can be divided into two units; i) Paleozoic (Permo-Carboniferous) unit which is made up of phyllite-quartzite-marble intercalation and ii) Mesozoic (Cretaceous) sequence consisting mainly of massive marbles. Phyllites are composed of predominantly chloritoid, garnet and garnet-chloritoid phyllites and subordinately staurolite-garnet phyllites. Schist are made up predominantly of garnet-mica schists and subordinate mica schists and calc-schists. Paleozoic series are overlain by the thick marble sequence with conformable contact relationship.

The metamorphic rocks of the Menderes Massif are tectonicaly overlain by the unmetamorphosed ophiolitic rocks of the İzmir-Ankara Zone. The unmetamorphosed rocks are composed of serpentinites.

In the Demirhan area, low-grade metapelites of cover series known as Permo-Carboniferous phyllites from the other part of the Menderes Massif (Çağlayan et al., 1980; Konak et al., 1987), which contain minor intercalations of quartzite and marble, are observed at the lowest level of the metamorphic series (Figure 2.4). The protoliths of leucocratic orthogneisses reaching up to 600 m in dimension, and many related aplitic veins reaching up to a few meter in thickness, intruded into metasediments of these Late Paleozoic cover series. The cover series are tectonically overlain by the Pan-African orthogneisses.

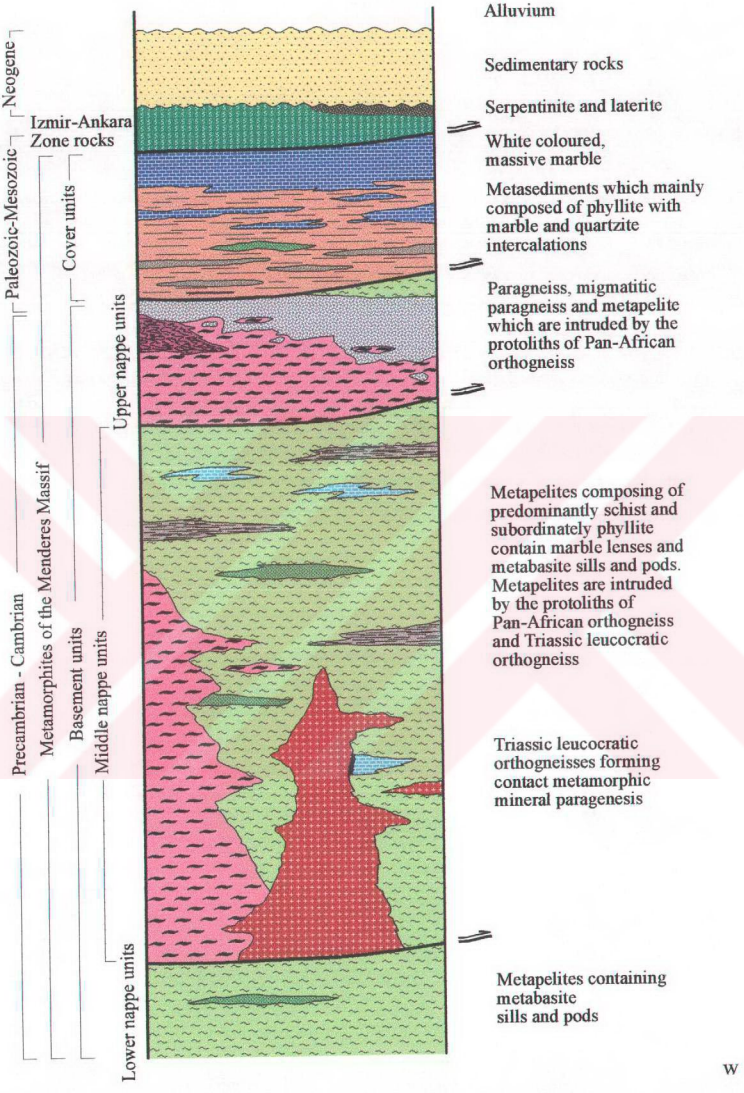


Figure 2.3. Generalised columnar section of Derbent area located in the easthern part of the Ödemiş-Kiraz Submassif of the Menderes Massif.

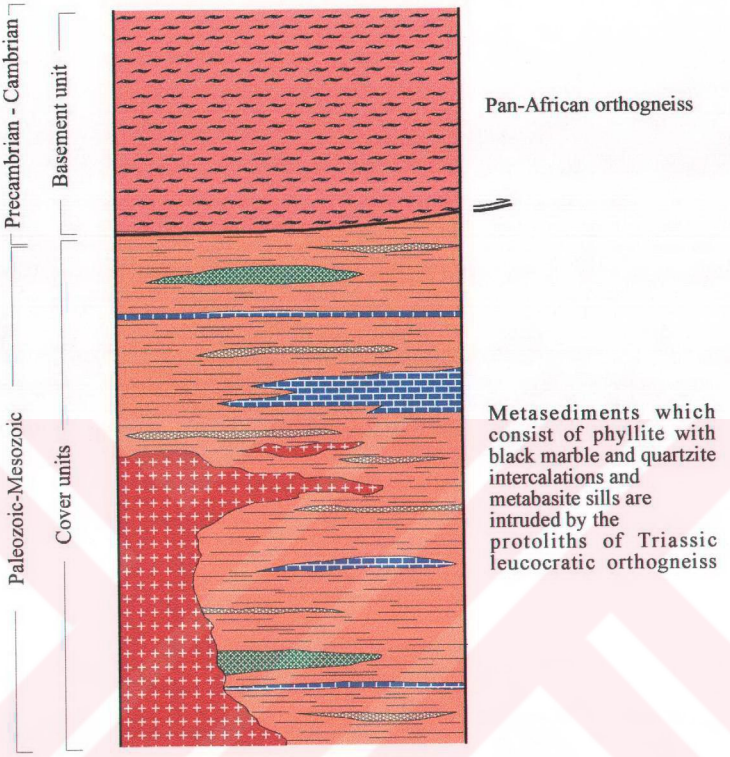


Figure 2.4. Generalized columnar section of Demirhan region located in the southern part of the Ödemiş-Kiraz Submassif of the Menderes Massif.(without scale)

T.C. YÜKSEKÖĞRETİM KURULU
DOKÜMANTASYON MERKEZİ

CHAPTER THREE

GEOLOGY AND PETROGRAPHY OF THE ROCK UNITS

3.1. Introduction

This chapter describes the geological relationship and petrography of the rock units occurring in two distinct areas. They are located within the Ödemiş-Kiraz Submassif of the Menderes Massif (Figure 3.1). First area, Derbent area, is situated in eastern part of the Ödemiş-Kiraz Submassif, south of Alaşehir. Second area, Demirhan area, locates the northern part of Atça occurring at the southern part of the Ödemiş-Kiraz Submassif.

Despite its complex tectonic structure, the metamorphic rock in the stuy areas can be separated into two main rock associations (Dora et al. 1995): Pan-African basement units and Paleozoic to Mesozoic cover units. The Pan-African basement comprises clastic metasediments, i.e. Late Proterozoic paragneisses and metapelites, which were intruded by the protoliths of Precambrian metabasites and syn- to post-Pan-African orthogneisses. The cover series is divisible into three separate units which comprise Paleozoic and Mesozoic rocks. The Paleozoic series is made up predominantly of a sequence of quartzite, phyllite and marble. The Mesozoic series comprises predominantly schist and marble.

Unmetamorphosed remnants of the ophiolitic rocks and related laterites of the İzmir-Ankara Zone tectonically overlie the metamorphic rocks of the Menderes Massif.

Metamorphic rocks and overlying unmetamorphosed rocks of the İzmir-Ankara Zone are unconformably overlain by Neogene sedimentary rocks.

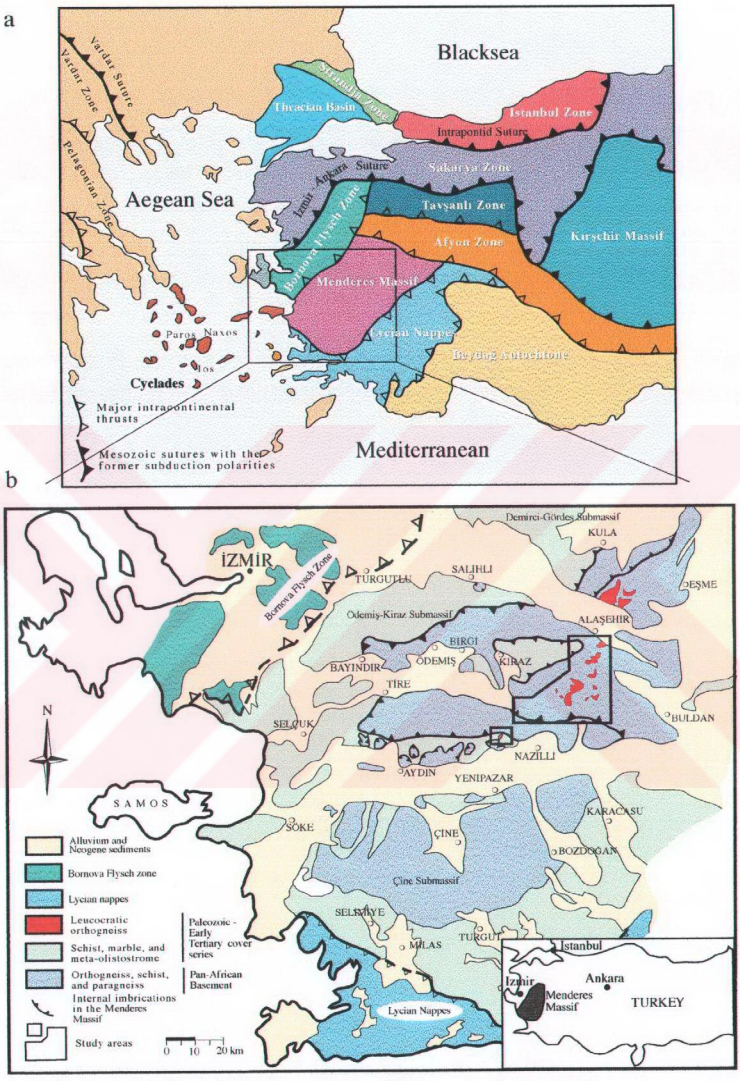


Figure 3.1. a) Tectonic map of the western Turkey and surrounding regions showing major continental blocks and tectonic zones (modified after Okay et al. 1996), b) The simplified geological map of the Menderes Massif and distribution of Early Triassic leucocratic orthogneiss (modified after Candan 1994).

3.2. Pan-African Basement Units

In early studies, it was generally accepted that the Menderes Massif had a simple internal structure, made up of a Precambrian core series and Early Paleozoic-Early Tertiary cover series (Schuiling, 1962; Dora et al., 1990; Dora et al., 1992). Recent studies show that the Massif does not have a simple structure, and it is made up of a nappe stack related to the Alpine compressional tectonics (Konak et al., 1994; Dora et al., 1994; Partzsch et al., 1998; Gessner et al., 1998). The rock succession of the Derbent and Demirhan area occurring in the eastern part of the Ödemiş-Kiraz Submassif is made up of nappe stack.

In the Derbent area, Pan-African basement is divided into three internal nappe units; lower, middle and upper nappe units (Figure 3.2). In these nappe units, the Pan-African basement comprises clastic metasediments, i.e. Late Proterozoic paragneisses and metapelites, which were intruded by the protoliths of Precambrian metabasites and syn- to post-Pan-African orthogneisses.

3.2.1. Paragneiss

Paragneisses are recognised only in upper nappe pile occurring in northern part of the Derbent area (Figure 3.3). They cover an area about 17 km^2. The paragneisses are well exposed around northwest of Aksu in the west and around Eğrektaş hill and Bahadır village in the north (Figure 3.3). They can be easily distinguished by their greyish purple, purple colours, strong, massive and homogenous structures. Furthermore, migmatitic type paragneisses are also observed in the northern part of Eğrektaş hill and eastern part of Evrenli village. These types of paragneisses are obviously differed from homogeneous paragneisses by their well-developed part of paleosome and neosome. Pytigmatic structures, which constitute felsic mineral aggregates, are commonly observed (Figure 3.4).

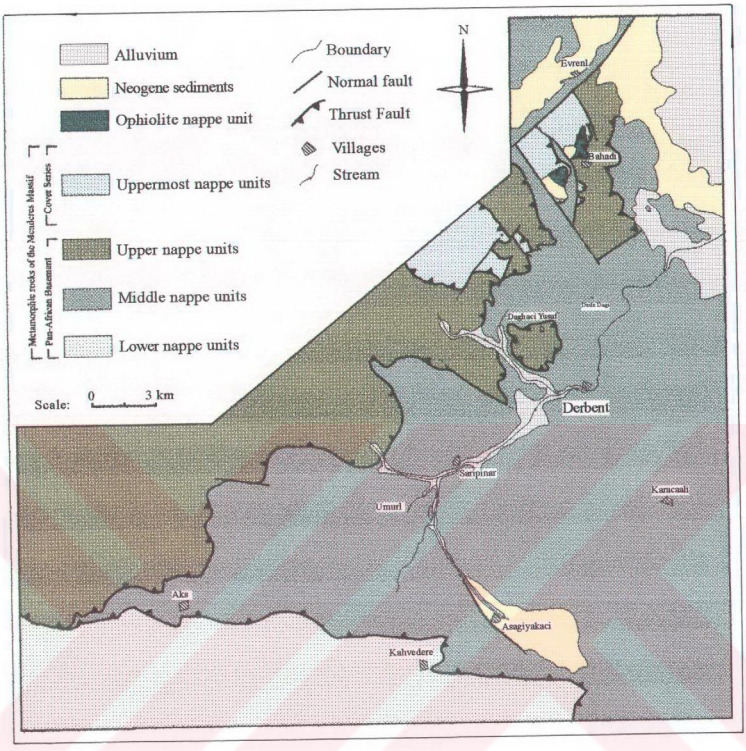


Figure 3.2. Nappe units of Derbent area, southern part of Alaşehir, in the Ödemiş-Kiraz Submassif.

Paragneiss was first time recognised as a distinct rock, fine-grained basic gneiss within the Pan-African basement, in the Çine submassif by Schulling (1962). In the following years these rocks, which are commonly exposed in the Çine (Kun, 1983), Ödemiş-Kiraz (Candan and Kun, 1991) and Demirci-Gördes (Candan, 1994) submassifs, were named as leptite and leptite-gneiss. It was proposed that their protoliths were rhyolitic-andesitic volcanic rocks by Dora et al, 1988; Dora et al. 1990. In recent years, new findings, contrary to the previous view, revealed that paragneisses are of sedimentary origin (Dora et al., 1995; Dora et al., 2001). They are intruded by the granitic protoliths of the Pan-African augen/granitic gneisses dated at

about 550 Ma (Hetzel and Reischmann, 1996) and the protolith of probably Precambrian metagabbro (Candan, 1996). Based on these intrusive contact relationships, it is suggested that these clastic metasediments are Late Proterozoic in age (Dora et al., 2001). Paragneisses were metamorphosed under the granulite facies conditions which affected the basement rock of the Menderes Massif about during the Pan African orogeny (Candan, 1995). Some preserved relict paragneisses belonging to the granulite facies metamorphism were determined in the basement rocks consisting of migmatite, gneiss, metagabbro and metatonalite/metagranodiorite in many places of the Menderes Massif. These rocks which have charnockitic composition contain common hypersthene, perthitic orthoclase and antiperthitic plagioclase (Candan, 1995).

Intrusive contact relationship between paragneiss and augen/granitic gneiss is mostly obscured by the later metamorphic and tectonic events. For this reason, the crosscut contact relationship can not be observed in the study area. In general, the gneisses have a strong foliation along the contact zone. However, the augen/granitic gneisses include common xenoliths of paragneisses, which are particularly concentrating close to the margins. The sizes of xenoliths reach up from a few cm to metres. These xenolites supports the original intrusive contact relationship between paragneiss and augen gneiss. In north of Eğrektaş hill, huge migmatitic paragneiss which seems to be xenolite in augen gneisses is exposed. Paragneisses are tectonically overlain by Mesozoic cover series around Eğrektaş hill in the northern part of Derbent area (Figure 3.2).

The general mineral assemblage of **paragneisses** is quartz + plagioclase + orthoclase + muscovite + biotite + garnet ± kyanite ± sillimanite ± tourmaline ± apatite ± zircon ± opaque oxides. The model analyses of the representative samples of paragneisses are given in Table 3.1.

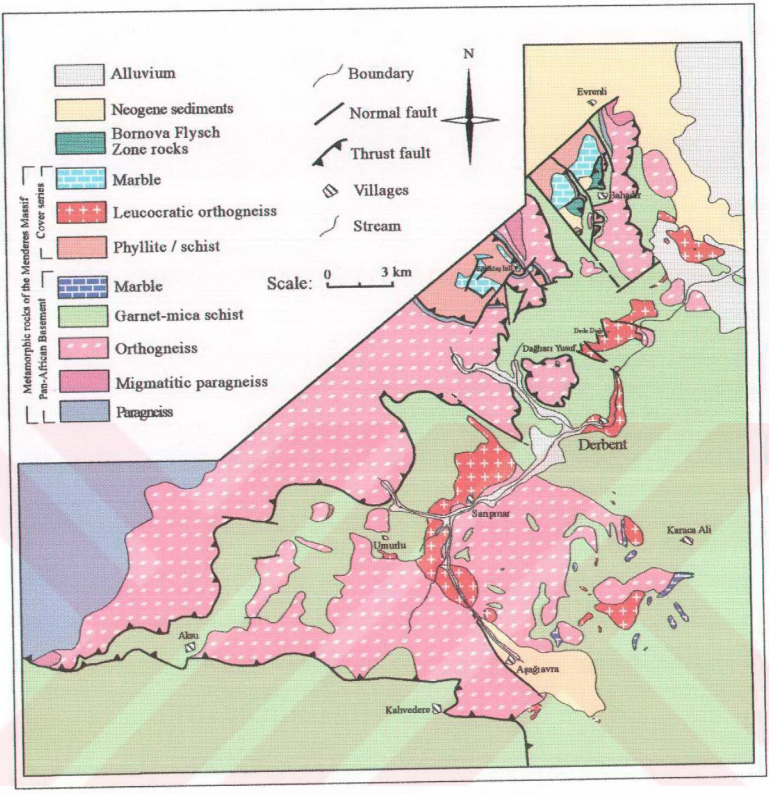


Figure 3.3. Geological map of Derbent region located in the eastern part of the Ödemiş-Kiraz Submassif of the Menderes Massif. National grids: İzmir L20-b3, İzmir L20-c2, İzmir L20-c3, İzmir L20-c4, Uşak L21-a4, Uşak L21-d1, Uşak L21-d4.

Paragneisses which are fine-grained rocks have generally granobalstic to polygonal textures (Figure 3.5) but some display lepidoblastic texture. Quartz usually occur anhedral equigranular grains. They tend to show polygonal texture where the polygonal crystals meet at triple points with interfacial angles of about 120°. Orthoclase and plagioclase are commonly intergrown with quartz and characterized by subhedral to anhedral crystals. Plagioclase show generally lamellar twinning. Orthoclase grains display typical microperthitic texture.



Figure 3.4. Pytigmatic structures in paragneisses, 650 m southeast of Eğrektaş hill (30500/34625).

Garnets are observed mainly as small anhedral crystals. Furthermore, they also occur as porphyroblasts and small subhedral crystals which surround the older garnet porphyroblasts (Figure 3.6).

Kyanite is recognised only in one sample as small prismatic crystals which show remarkable parallelism with the orientatiton of mica minerals. They have high relief and show low interference colours.

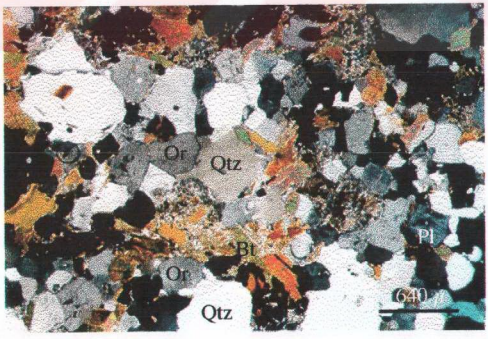


Figure 3.5. Paragneisses displaying well-developed granoblastic texture, CPL.

Table 3.1. Modal mineralogical composition and mineral percentage of the representative paragneiss samples. t: trace

	263	281/A	391	96-96/C	242	405	96-95
Quartz	▬	▬	▬	▬	▬	▬	▬
Plagioclase	▪	▪	▪	▪	▪	▪	▪
Orthoclase	▪	▪	▪	▪	▪	▪	▪
Muscovite	▬	▪	▪	▪	▪	▪	▪
Biotite	▬	▬	▬	▬	▬	▬	▬
Garnet	▪	▪	t	▪	▪	▪	▪
Kyanite							▪
Sillimanite					▪	▬	t
Tourmaline					t	t	t
Apatite				t	t		
Zircon	t	t	t	t	t		t
Opaque oxide	t	t		t	t	t	t

▬ 10 %

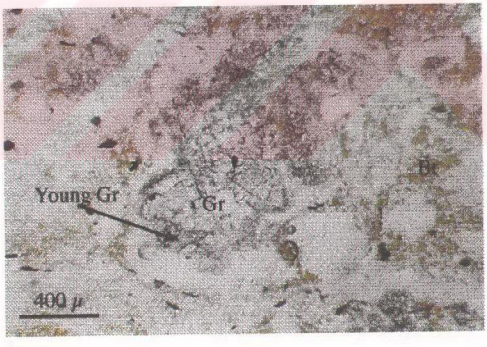


Figure 3.6. Small subhedral young garnets overgrowth around garnet porphyroblasts, PPL.

Sillimanites can be divided into two groups. In the first group sillimanites are formed along two feldspar and/or feldspar/quartz boundaries as small fibrolitic crystals. Second group is formed by sillimanite fibers replacing biotite and garnet (Figure 3.7).

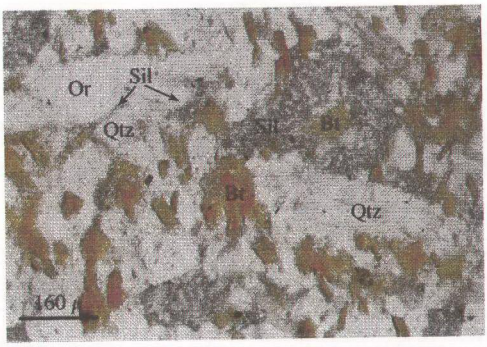


Figure 3.7. Sillimanite fibers replacing biotites and garnets. Note that the sillimanite fibrolites are also growth at the quartz and orthoclase grain boundaries, PPL.

Biotite is usually the most dominant mica in paragneisses. It occurs commonly subidoblastic to ksenoblastic crystals. Some subidioblastic biotites show remarkable parallelism which define lepidoblastic texture (Figure 3.5) Muscovites usually occur as small flakes which accompany to biotites. But, younger muscovites occur as big subidioblastic flakes contaning many inclusions of quartz.

The general mineral assemblage of **migmatitic paragneiss** which is closely similar to the homogeneous paragneisses is quartz + plagioclase + orthoclase + muscovite + biotite + garnet ± kyanite + sillimanite ± tourmaline ± apatite ± zircon ± opaque oxides. The modal analyses of the representative migmatitic paragneisses samples are given in Table 3.2.

Migmatitic paragneiss is fine- to medium-grained rocks and display generally granoblastic texture (Figure 3.8). Quartz and plagioclase have similar properties those of homogeneous paragneisses. Orthoclase grains show typical widespread string type perthitic structure and rarely myrmekitic structures.

Table 3.2. Modal mineralogical composition and mineral percentage of the representative migmatitic paragneiss samples. t: trace

	North of Bahadır		Around Eğrektaş hill		West of Aksu	
	374	**399**	**208**	**293/A**	**96-96/A**	**96-129**
Quartz	▬	▬	▬	▬	▬	▬
Plagioclase	▪	▪	▪	▬	▮	▮
Orthoclase	▬	▬	▬	▬	▬	▬
Muscovite	▪	▪	▪	▮	▪	▬
Biotite	▬	▬	▬	▬	▬	▬
Garnet	▮	▮	▮	▮	▪	▪
Kyanite	t	t	t	▮	t	t
Sillimanite	t	t	t	▮	t	▮
Tourmaline					t	
Apatite	t		t			
Zircon	t	t	t	t	t	t
Opaque oxide	t	t	t	t	t	t

▬ 10 %



Figure 3.8. Granoblastic texture in migmatitic paragneisses, CPL.

Two types of garnets are distinguished; anhedral to subhedral older porphyroblasts and subhedral small crystals overgrowing of older garnet porphyroblasts. Some small subhedral garnets occur around biotites as a corona structure. Sillimanites are commonly observed at the contact of two feldspar as small

fibrolites. On the other hand, some porphyroblasts most probably after cordierites, which are envisaged to have been related to the former granulite facies metamorphism by Dora et al., 2001, were completely pseudomorphosed by a high temperature assemblage such as sillimanite, biotite, garnet, quartz, kyanite and muscovite (Figure 3.9).

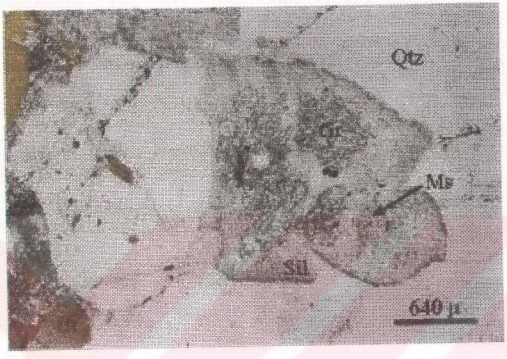


Figure 3.9. The probably cordierite porphyroblasts related to the former granulite facies metamorphism are replaced by sillimanite, quartz, muscovite, biotite, garnet and kyanite in migmatitic paragneisses, PPL.

The general mineral assemblage of the orthopyroxene bearing **charnockitic paragneisses** is quartz + plagioclase + orthoclase + biotite + garnet + sillimanite + orthopyroxene (hypersthene) ± zircon ± opaque oxide phases. The modal analyses of the representative samples of the charnockitic paragneisses are given in Table 3.3.

Charnockitic paragneiss is fine- to medium-grained rock showing granoblastic texture (Figure 3.10). Plagioclase are oligoclase-andezine (An_{29-31}) in composition. Biotite is the dominant mica phases in charnockitic paragneisses and shows remarkable symplectic intergrowth with quartz. Some young biotites are observed around garnet and opaque minerals as corona structure. Orthopyroxenes are observed anhedral to subhedral crystals. They have high relief and show pale brownish pleochroism. Orthopyroxenes are typical hypersthene (En_{50-56}) in composition

(Candan, 1995). Their value of Al_2O_3 is very high (3.75 %) which is typical for granulite facies rocks (Candan, 1995).

Table 3.3. Modal mineralogical composition and mineral percentage of the representative charnockitic paragneiss samples. t: trace

	North of Bahadır		
	431/A1	**431/A2**	**431/A2**
Quartz	▬	▬	▬
Plagioclase	▮	t	▮
Orthoclase	▬	▬	▬
Biotite	▬	▬	▬
Garnet	▬	▬	▬
Sillimanite	▬	▬	▬
Orthopyroxene	▮	▮	▮
Zircon	t	t	
Opaque oxide	t	▮	t

▬ 10 %

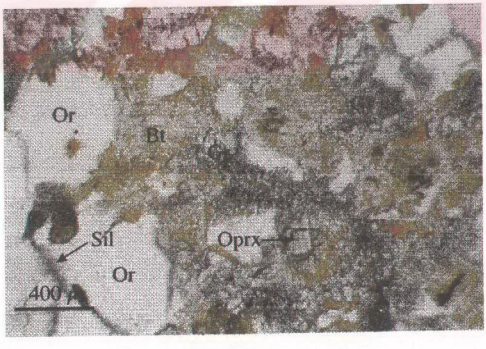


Figure 3.10. Granoblastic texture in charnockitic paragneisses. Biotite shows symplectic overgrowth with quartz. Sillimanite fibrolites are growth at the orthoclase grain boundaries, PPL.

3.2.2. Metapelites (schists and phyllites)

Metapelitic rocks are recognised only in lower, middle and upper nappe units in the Derbent area (Figure 3.3). They cover an area about 210 km^2. Metapelites are predominantly composed of schists and subordinately phyllites. Lower nappe unit is completely made up of schists. Schists are widespread in northeast of Aksu, northeast of Umurlu, north of Karacaali and around of Derbent villages in the middle nappe unit. Whereas, phyllites are common relatively in around of Kokuludede hill (southeast of Karacaali village) in the south. They are intercalating with marbles in different thickness. Furthermore, metapelites contain thin metapsammite (muscovite-quartz schist) levels as interlayers in the middle nappe unit.

Colours of the schists vary from dark brown to yellowish brown and dark to light grey and they display a rusty brown weathering colours. They commonly display pronounced penetrative schistosity, which is defined by the parallel alignment of mica flakes. At some layers, they contain black albite spots reaching up to 1 mm in diameter and black to reddish garnet porphyroblasts within fine-grained mica reach matrix. The maximum grain size of garnet ranges from 1 to 3 mm in diameter and in some samples they reach up to 1 cm.

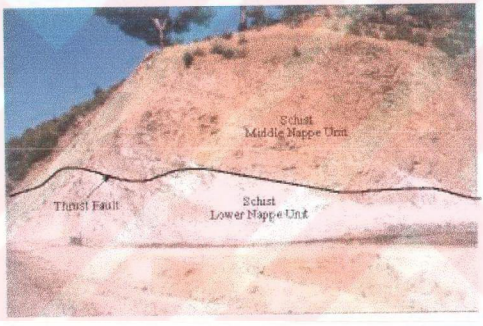
The schists include lenses, ribbons and budins of quartz veins ranging in thickness from 1 cm to 10 cm. Some asymmetric quartz ribbons with Z shape in albite rich schists in lower nappe unit indicate top to the SSW sense of shear (Figure 3.11).

In the southern part of Derbent lower nappe unit, which is made up of completely homogenous metapelites, is tectonically overlain by the schists of middle nappe unit (Figure 3.8). The thrust contact relationship of the same Pan-African schists between lower and middle nappe unit are well exposed at several localities along the road cuts between Aksu and Kahvedere villages (Figure 3.12).



Figure 3.11. Quartzite budinages in schist of lower nappe unit display top to SSW movement, 1.5 km southwest of Palamutçuk village, 10600:13375.

a)



b)

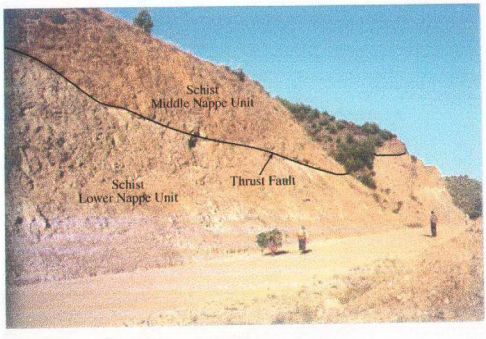


Figure 3.12. The thrust contact relationships between lower and middle nappe units a) east of Palamutçuk village, 12250:14750, b) south west of Aksu village, 15910:14700.

Cataclastic rocks, approximately 6-10 metres in thickness, occur along the thrust fault between schists and/or gneisses of middle nappe unit and schists of lower nappe unit. Clay zone, reaching up 10 cm to 1 m in thickness, is observed along the lower part of the thrust fault.

Schists are composed of predominantly garnet-mica schists and subordinately mica schists. The following assemblages are observed;

⇒ quartz - muscovite - biotite - garnet
⇒ quartz - muscovite - biotite - garnet - hornblende
⇒ quartz - muscovite - biotite
⇒ quartz - muscovite

The general mineral assemblage of schists is quartz + plagioclase + muscovite + biotite ± chlorite ± garnet ± hornblende ± tourmaline ± zoisite ± apatite ± zircon ± rutile ± calcite ± graphite and opaque oxide phases The model analyses of the representative schist samples from lower and middle nappe unit are given in Table 3.4.

The mica schists have a well-developed lepidoblastic texture characterised by the alignment of biotites and muscovites and have a porphyroblastic texture characterised by porphyroblasts of garnet and albite (Figure 3.13.a.b).

Quartz is the one of the major constituents of the schists. They usually occur as anhedral equigranular crystals in the form of aggregates within matrix. However, in the ductile deformed samples they display ribbon structure. In muscovite-quartz schist, they exhibit granoblastic texture with a typical undulatory extinction resulted from the deformation under low temperature conditions.

Table 3.4. The modal mineralogical composition and mineral percentage of the representative schist samples. t: trace, continue.

	Lower Nappe Unit (garnet-mica schist)			Middle Nappe Unit (garnet-mica schist)		
	630	**96-75**	**96-99/A**	**709**	**95-59**	**97-81**
Quartz	▬	▬	▬	▬	▬	▬
Plagioclase	▬	▬	▬	▬	▪	▬
Muscovite	▬	▬	▬	▬	▬	▪
Biotite	▬	▪	▪	▪	▬	▬
Chlorite	▬	▪	▬	▪	t	t
Garnet	▪	▬	▪	▬	▬	▬
Tourmaline	t		t	t		t
Zoisite						
Apatite		t			t	
Zircon						t
Graphite				▪		
Calcite			▪			
Opaque oxide	▪	t	t	t	▪	t

▬ 10 %

	Lower Nappe Unit (mica schist)			Middle Nappe Unit (mica schist)		
	641/A	**96-71**	**96-94**	**527**	**667**	**95-30**
Quartz	▬	▬	▬	▬	▬	▬
Plagioclase	▪	▬	▬	▬	▬	▬
Muscovite	▬	▬	▬	▬	▪	▬
Biotite	▪	▪	▬	▪	▬	▪
Chlorite	▬	▬		▬	▬	▬
Tourmaline	t	t			t	t
Epidote				▪		
Apatite					t	t
Zircon			t	t		t
Rutile			t		t	t
Opaque oxide	▪	▪	t	▪	t	▪

▬ 10 %

T.C. YÜKSEKÖĞRETİM KURULU
DOKÜMANTASYON MERKEZİ

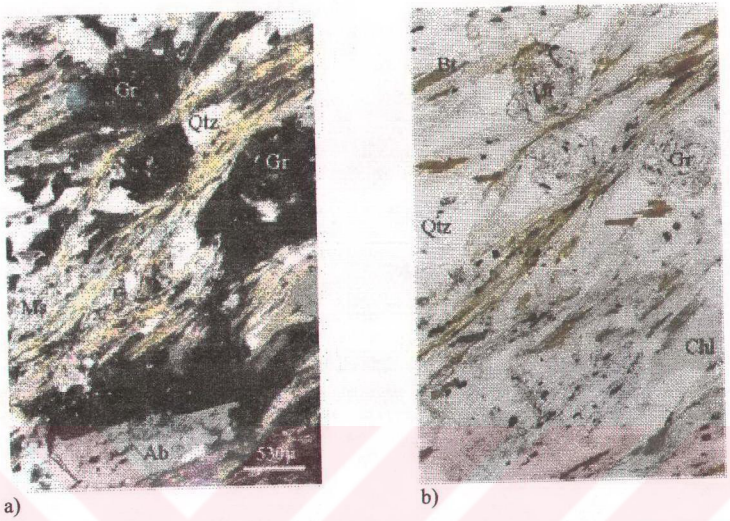
Table 3.4. The modal mineralogical composition and mineral percentage of the representative schist samples. t: trace

	Middle Nappe Unit (hornblende-garnet schist)		Middle Nappe Unit (muscovite-quartz schist)		
	95-48	**97-80**	**110/A**	**681**	**96-17**
Quartz	▬	▬	▬	▬	▬
Plagioclase	▬	▬	▬	▬	▬
Muscovite	▬		▬	▬	▬
Biotite	▬	▬		t	
Chlorite	▮				
Garnet	▬	▬			
Hornblende	▮	▮			
Tourmaline				▮	
Zoisite		t			
Apatite		t	t	t	
Zircon	t	t	t	t	t
Rutile	t	t		t	
Opaque oxide	t	▮	t	▮	t

▬ 10 %

Two type of plagioclase is discriminated in the schists; i) small anhedral crystals intergrowth with quartz in matrix, showing rarely lamellar twinning and ii) albite porphyroblasts which show characteristic albite twinning. In some samples, albite porphyroblasts display internal foliation with inclusions (S_i) passing into the external foliation (S_e) which characterise syn-tectonic crystal growth (Figure 3.14). These syn-tectonic crystals show typical chemical zonation.

Biotite and muscovite most commonly occur as aligned subidioblastic flakes. They tend to define and dominate microstructure in the rock and show remarkable parallelism, which define a strong lepidoblastic texture. Biotite is generally the dominant mica phase in schists occurring as long laths.



a) b)

Figure 3.13. Photomicrograph of foliation in garnet-mica schist. Long strings of mica minerals show parallelism and define the very remarkable lepidoblastic texture. Garnet and albite porphyroblasts cause also porphyroblastic texture in garnet-mica schists. a) CPL b) PPL.

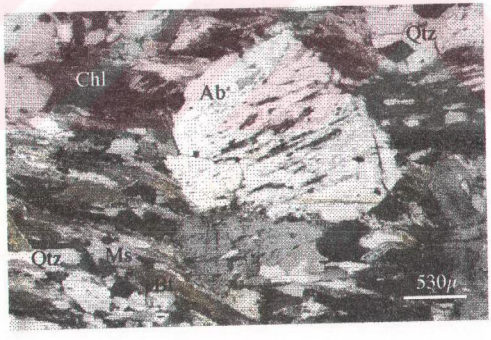


Figure 3.14. Syntectonic albite porphyroblast in garnet-mica schist show about 45° of dextral rotation with respect to S_e during growth. CPL

In plane polarised light (PPL), biotite is pleochroic from light to dark reddish brown and from pale to dark green depending upon whether they are Fe or Mg-rich, whereas muscovite do not show any pleochroism In some thin sections, biotite occur

as large porphyroblasts and young flakes which are found as perpendicular to the main foliation (Figure 3.15.a). Replacement by chlorite and iron oxides are common retrogressive features. They were grown after cessation of deformation, which cause the main foliation. Muscovite occurs as subidioblastic laths and shows alignment parallel to the foliation where the muscovite become dominant, the foliation becomes more distinct (Figure 3.15.b). Chlorites occur either as retrograde product after biotites or as post-tectonic crystals overprinting the main foliation.

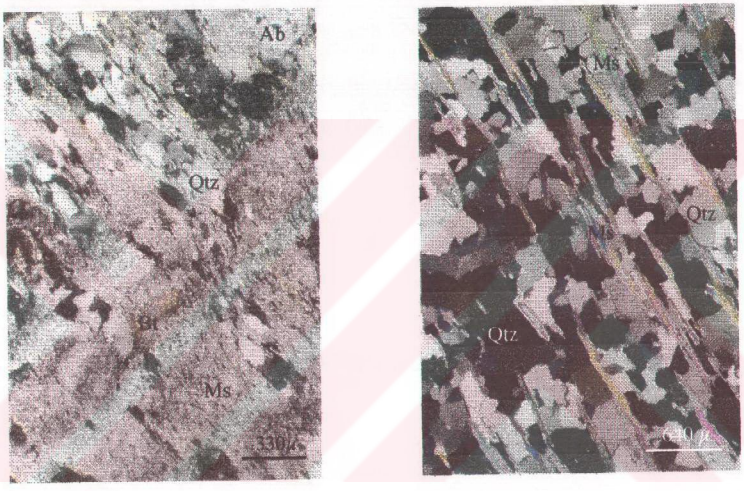


Figure 3.15. a) Post-tectonic biotite crystal overgrowing a lepidoblastic texture. Quartz ribbons are parallel to the main foliation, CPL. b) subidioblastic laths of muscovite showing parallel alignment to the foliation, CPL.

Garnet occurs as euhedral to subhedral porphyroblasts characterised by well-developed spiral-shaped inclusion trails composing mainly of quartz (Figure 3.16.a). Some garnets show no internal fabric and are free of inclusions. Furthermore, garnet

Oxidation and retrograde chlorite replacement around the edges of garnet grains are common features.

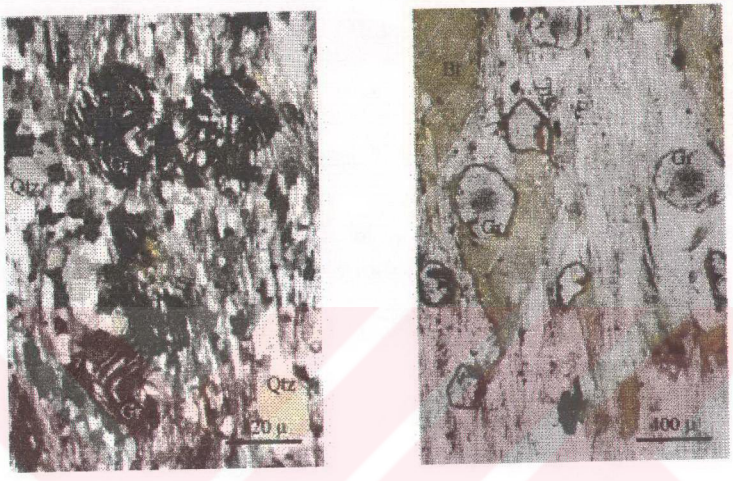


Figure 3.16. a) Garnet porphyroblasts display by well developed spiral-shaped inclusion trails composing mainly of quartz, PPL, b) Garnet porphyroblasts have a sharply defined inclusion free rim, indicating changing conditions during its growth, PPL.

Hornblende occurs as subidioblastic small and prismatic crystals (Figure 3.17). They display typical light green to green coloured pleochroism. They display parallel alignment to the main foliation defined by muscovite and biotite.

Phyllites levels occur in the schists as interlayers and lensess in different thickness. Furthermore, intercalate with marbles around Kokuludede hill and Bahadır village. Phyllites display conformable contact relationship with both schist and marble (Figure 3.18). They are dark gray, greenish gray colours and fine grained rocks. They have a well-developped foliation which is defined by the parallel alignment of micas. Garnet and kyanite crystals reaching up to 1-1.5 cm and 0.5-1 cm respectively can be recognised by the naked eyes. They cause porphyroblastic texture in these rocks .

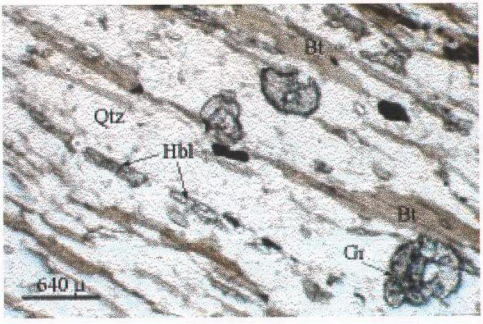


Figure 3.17. Subidioblastic hornblende crystals showing light green pleochroism colour are parallel to the main foliation, PPL.

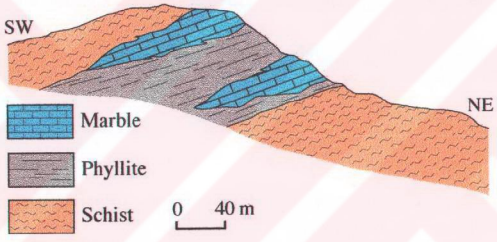


Figure 3.18. The contact relationship of phyllite with marble and schist, northeast of Marmarli village (34500/21375).

The following assemblages are observed in phyllites;

⇒ quartz - sericite - chloritoid - staurolite - kyanite

⇒ quartz - sericite - chloritoid - garnet

⇒ quartz - sericite - garnet

⇒ quartz - sericite - biotite - chloritoid

⇒ quartz - sericite – biotite

The general mineral assemblage of phyllites is quartz ± plagioclase (albite) + sericite ± biotite ± chlorite ± chloritoid ± garnet ± staurolite ± kyanite ± tourmaline ± zoisite ± epidote ± apatite ± zircon ± calcite ± graphite and opaque oxide phases. Modal analyses of representative phyllite samples from middle nappe unit are given in Table 3.5.

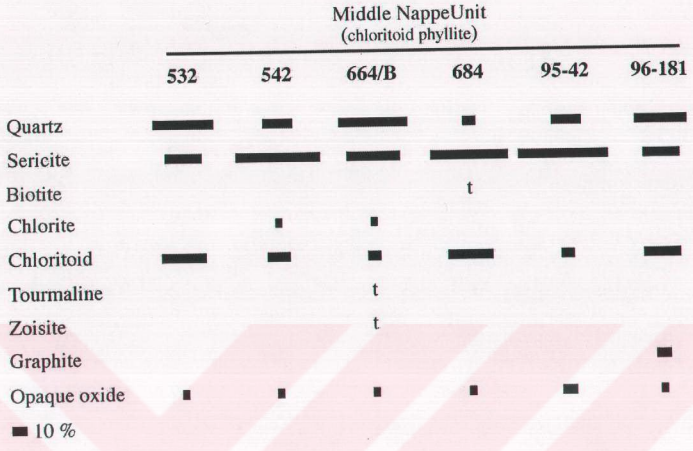
Quartz and fine-grained muscovite mainly form the matrix of the phyllites. Furthermore, they occur as ribbons made up of small anhedral crystals, which display undulatory extinction. In some samples, they occur as quartz rich domains alternating with sericite rich domains (Figure 3.19). Two different foliations can be recognised in phyllites. Sericites within quartz-rich domains mark old schistosity, which differ from main foliation caused by last deformation.

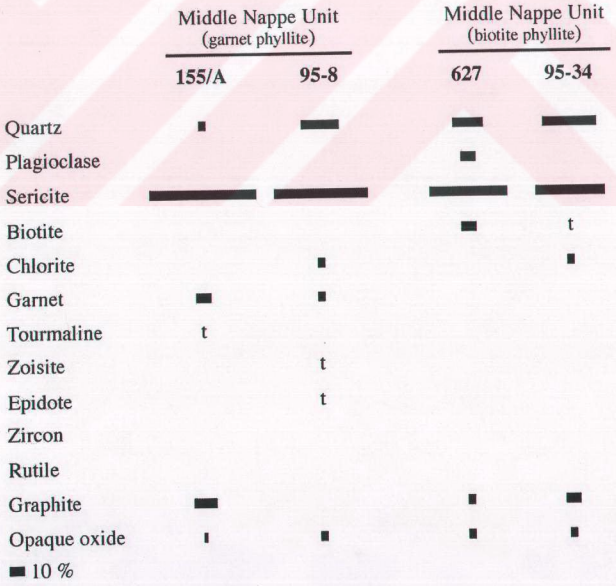
Table 3.5. Modal mineralogical composition and mineral percentage of the selected phyllite samples. t:trace, continue.

	Middle Nappe Unit (staurolite-chloritoid-kyanite phyllite)			Middle Nappe Unit (garnet-chloritoid phyllite)		
	685/A	**685/B**	**685/C**	**550**	**706**	**723/A**
Quartz	▬	▬	▬	▬	▬	▬
Sericite	▬	▬	▪	▬	▬	▬
Biotite			t		▪	
Chlorite			t		▪	▪
Chloritoid	▪	▪	▬	▪	▪	▪
Garnet				▮	t	▬
Staurolite		▮	t			
Kyanite	▬	▬	▪			
Tourmaline			t	t		t
Zoisite					▮	
Zircon	t					
Calcite			t			
Graphite					▪	▬
Opaque oxide	▪	▮	▪	▮	▪	t

▬ 10 %

Table 3.5. Modal mineralogical composition and mineral percentage of the selected phyllite samples. t:trace





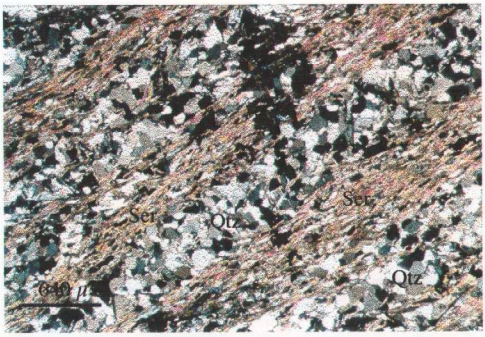


Figure 3.19. Quartz-rich domains alternating with sericite-rich domains in phyllites, CPL.

Albite crystals in some sample display internal inclusion fabric parallel to and passing into the main foliation, which characterise syn-tectonic crystal growth.

Sericites are usually the dominant mica phase in phyllites. They occur as aligned subidioblastic small flakes, which define crenulation cleavage. They produce the intense penetrative cleavage in the rock. Biotites as post-tectonic crystals occur rarely as long laths crosscutting the main foliation. They are commonly retrogressed chlorite and Fe-oxidation.

Chloritoids are commonly found as aligned subidioblastic prismatic crystals, which show remarkable parallelism with the main foliation (Figure 3.20). They display high relief, pale greenish to bluish pleochroism and dark bluish interference colours. Some crystals show typical lamellar twinning.

Garnets are very common and found as syn- and post-tectonic crystals. They occur as subhedral and euhedral porphyroblasts The crystal size of garnets reach up to 1-1.5 cm. Syn-tectonic garnet porphyroblasts display well developed inclusion trails. They show 45° dextral rotation with respect to external foliation during the growing (Figure 3.21.a). The inclusions in garnet porphyroblasts are mainly composed of quartz and plagioclase, sericite, graphite, tourmaline and opaque oxide phases. Post-tectonic garnets are generally euhedral crystals and overgrow the former foliation (Figure 3.21.b). The cleavage structure, which is trapped into the garnets as

passive inclusions, is perfectly continuous without any deflection and development of strain shadow.

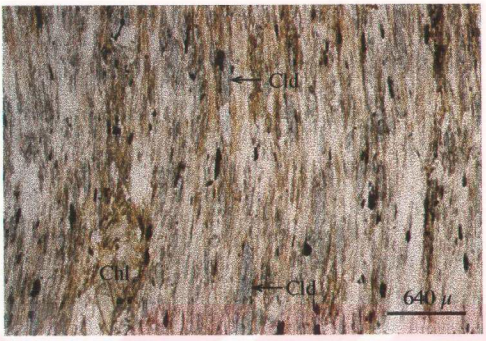
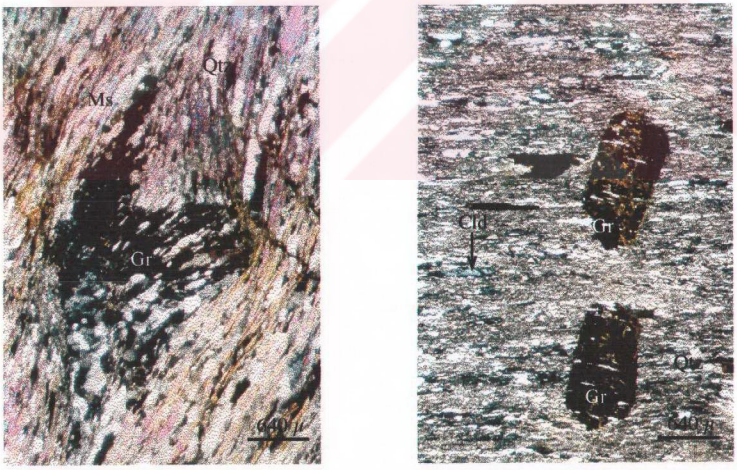


Figure 3.20. Aligned subidioblastic prismatic chloritoid crystals show remarkable parallelism with the main foliation, PPL.



a) b)

Figure 3.21. a) Syn-tectonic garnets show 45° dextral rotation with respect to external foliation during the growing, CPL, b) Euhedral post-tectonic garnet crystals overgrow the former foliation, Note that the cleavage structure trap into the garnets as passive inclusions and perfectly continue without any deflection and development of strain shadow, CPL.

Staurolites are found as small crystals within the matrix of quartz and sericite. They are produced by a reaction from chloritoid crystals (Figure 3.22). They show typical colourless to golden yellow pleochroism colour and high relief.

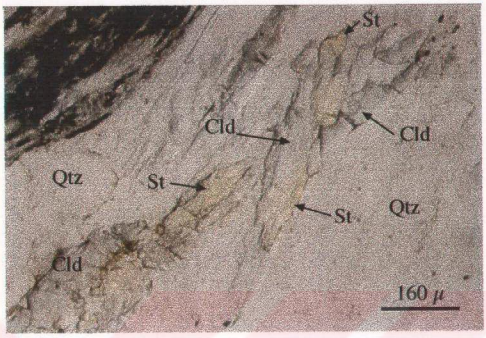


Figure 3.22. Staurolites showing remarkable yellow pleochroism colour are produced by a reaction from chloritoid crystals, PPL.

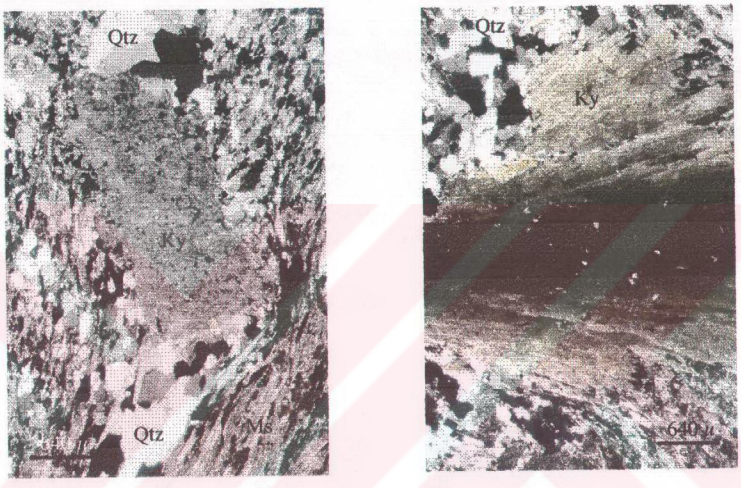
Kyanite crystals are recognised as aligned prismatic porphyroblasts (Figure 3.23.a). Some kyanite crystals are found as fascicular bundles (Figure 3.23.b). They have very distinctly high relief and show grey, yellow interference colours.

Zoisite was found only in one sample as long, lath-shaped crystals, which display preferred parallelism with the main schistosity. It is characterised by blue interference colour and high relief.

3.2.3. Marbles

Marbles in the basement schists are recognised only in middle nappe unit (Figure 3.2). They cover an area of about 1 km^2. The marbles are cropped out at over the southwestern part of Karacaali village. They are easily distinguished from the other lithologies by their grey and white colours and well developed foliation, which is consistent with the original bedding plane. The foliation is defined usually by preferentially development of muscovites along the clay rich thin horizons of the original rocks. Marbles occur as lenses bands and layers within the schists and

phyllites. The contact relationships between marble and schists are concordant and transitional. Calc-schist levels are frequently found along the contacts that represent the original transitional contact relationships between pelitic and carbonate rich rocks .



a) b)

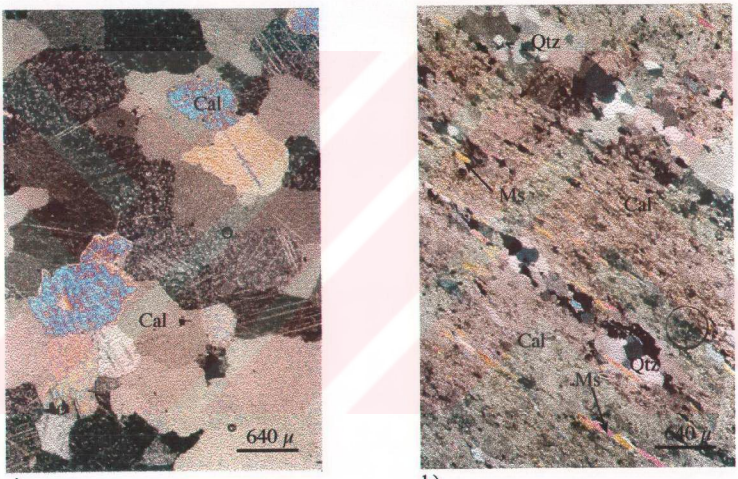
Figure 3.23. a) Prismatic kyanite porphyroblasts, and b) fascicular bundle type kyanite crystals in phyllites, CPL.

The general mineral assemblage of marble is calcite ± quartz ± muscovite ± graphite ± opaque oxide phases. Modal analyses of representative marble samples from middle nappe unit are given in Table 3.6. Marbles display granoblastic texture resulted from the common occurrence of equigranular calcite crystals (Figure 3.24.a). On the other hand, foliated marbles are characterised by a fabric defined by aligned muscovite laths alternating with calcite and quartz rich layers (Figure 3.24.b).

Table 3.6. Modal mineralogical composition and mineral percentage of the representative marble samples. t:trace

	156/A	364	440	526	541/10	96-167/B
Quartz	■	■	t	t	■	■
Muscovite	t		t		■	■
Calcite	▬	▬	▬	▬	▬	▬
Graphite	t					
Opaque oxide		t		t	t	t

■ 20 %



a) b)

Figure 3.24. a) Granoblastic texture due to the common occurrence of equigranular calcite crystals, CPL. b) Foliated marbles with a fabric defined by aligned muscovite laths alternating with calcite and quartz rich layers, CPL.

Calcite is the dominant mineral and occurs as anhedral crystals. They show high interference colours and good cleavage under crossed nicols Typical calcite twinning resulted from deformation is abundant. Furthermore, this deformation cause preferential orientation of the calcite crystals.

Muscovite defines foliation in the rock and usually occurs as aligned subidioblastic flakes. The increase of amount of muscovite produce a lepidoblastic texture (Figure 3.24.b).

Quartz usualy occurs as anhedral crystals. Some occur as crystal aggregates forming quartz ribbons.

3.2.4. Metabasites

Metabasites are divided into two main groups; metagabbros and amphibolites. **Metagabbros** crop out at the northwestern and southern parts of Eğrektaş hill which is located at the northern part of the study area (Figure 3.2). They usually occur in augen/granitic gneisses ot the upper nappe unit. Metagabbros are observed as lens-shaped bodies which reach up to 12 x 40 m in size. They are fine-grained, massive rocks and show dark green colours (Figure 3.25). Metagabbros, all over the Menderes Massif, are previously regarded to be Middle Miocene in age and post-metamorphic in character (Dora et al. 1987). In recent years, it has been documented that they are of Precambrian/Cambrian in age and are subjected to poly-phase metamorphism under granulite, eclogite and almandine-amphibolite facies conditions (Candan, 1994; 1995; Oberhänsli et al, 1997; Candan et al, 2001).

The general mineral assemblage of metagabbros is plagioclase + orthopyroxene + clinopyroxene ± olivine + hornblende ± biotite ± chlorite ± garnet ± serpentine ± clinozoisite ± calcite ± talc ± spinel + opaque oxide phases. The modal analyses of the representative metagabbro samples fiom upper nappe unit are given in Table 3.7.

Plagioclase, orthopyroxene, clinopyroxene and olivine are the relict igneous phases in metagabbros. Plagioclase is labrador (An_{60-65}) in composition (Candan, 1996). They show typical lamellar twinnig. Needle-shaped clinozoisite crystals are commonly observed in plagioclase crystals as a product of poly-phase etamorphism.

T.C. YÜKSEKÖĞRETİM KURULU
DOKÜMANTASYON MERKEZİ



Figure 3.25. General appearance of metagabbro within orthogneisses, 2 km soutwest of Eğrektaş hill (30875/32275).

Two types of pyroxene are found in metagabbros; ortho and clinopyroxene. Orthopyroxenes are usually hypersthene in composition, whereas clinopyroxenes are diopside in composition (Candan, 1996). Ortho- and clinopyroxenes are commonly replced by amphibole (hornblende) crystals as a corona structures. Some pyroxenes include very small spinel crystals which display cloudy texture. Euhedral and bigger spinel crystals are also present in metagabbros.

Furthermore, corona structures are also observed along the contacts of olivine and plagioclase. Three zones are distinguished around olivine crystals; orthopyroxene in inner part, amphibole + spinel which display symplectic growing in middle part and amphibole in outer part (Figure 3.26).

Table 3.7. Modal mineralogical composition and mineral percentage of the representative metagabbro samples. t: trace

	238/A1	238/B2	349/B1	349/B2	576/A	576/B
Plagioclase	▬	▬	▬	▬	▬	▬
Orthopyroxene	▬	▬	▬	▬	t	
Clinopyroxene	▬	▬	▬	▬	▬	▬
Olivine	▬	▬	▬			▬
Hornblende	▬	▬	▬	▬	▬	▬
Biotite	t	t	t		t	t
Chlorite	t		t		▬	▬
Garnet	t		t	t		
Serpentine	t	t	t	▬		
Zoisite	▬	▬	▬	▬	t	
Calcite		t			▬	▬
Talc	▬	▬	t	▬	▬	▬
Spinel	▬	▬	t	t		
Opaque oxide	▬	▬	▬	▬	▬	▬

▬ 10 %

Similar corona textures which is geneticaly related to the replacement of olivine by orthopyroxene are also observed between opaque oxide (ilmenite) and plagioclase. In this corona texture ilmenite crystals are rimmed by the partially developed biotite and amphibole shells.

Amphibolites are usually observed as sill and and pods in variable sizes in schists of the lower and middle nappe units of Pan-African basement (Figure 3.27). They show well-developed schistosity and have a ligh- to dark-green colours. Amphibolites have typical nematoblastic texture characterised by preferently orientation of prismatic amphibole crystals and porphyroblastic texture characterised by garnet porphyroblasts reaching up to 1 cm diameter (Figure 3.28.a). Acording to mineral composition, amphibolites can be divided into two groups; i) garnet-amphibolites and ii) epidote amphibolites.

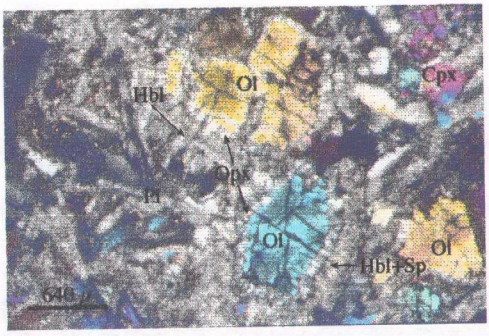


Figure 3.26. Corona structures between olivine and plagioclase in metagabbro. Three zones are distinguished around olivine crystals; orthopyroxene in inner part, amphibole + spinel which display symplectic growing in middle part and amphibole in outer part, CPL.

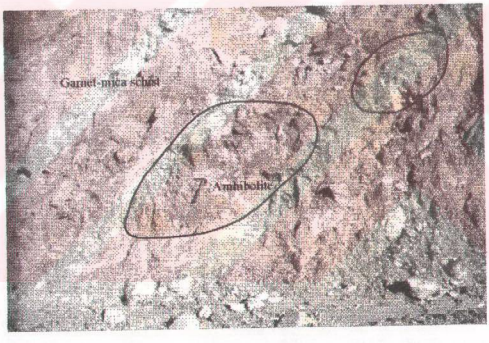


Figure 3.27. Boudinaged amphibolite sills in garnet-mica schist, 1.5 km east of Palamutcuk village, 13600:15075.

Based on the petrographical studies, the general mineralogical composition of garnet and epidote amphibolites is quartz + plagioclase + biotite ± chlorite + garnet + hornblend ± zoisite ± epidote + sphene ± zircon ± rutile ± calcite ± opaque oxide phases. The modal analyses of the representative amphibolite samples are given in Table 3.8.

Plagioclase is quite abundant in amphibolites. It forms subhedral to anhedral crystals. Although, the great majority of plagioclase lack twinning, but some small crystals in the matrix show very well lamellar twinning. Biotite occurs as subidioblastic to idioblastic lath. Chlorite is formed by the retrograde overprint of biotite and garnet. Garnet is commonly found as subhedral crystals, but some post-tectonic garnets occur as euhedral crystal (Figure 3.28.a).

Hornblende occurs as medium to large subidioblastic to idioblastic crystals which are prismatic and typical amphibole shape with two well-developed cleavages. They show parallel alingment to the main foliation with biotites. The green to brownish green pleochroism is pronounced in these minerals.

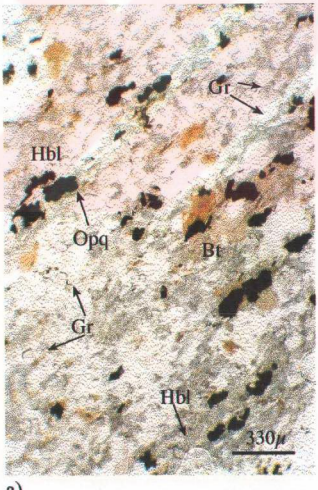
Table 3.8. Modal mineralogical composition and mineral percentage of the selected amphibolite samples. t: trace

	Lower Nappe Unit (garnet amphibolite)			Middle Nappe Unit (garnet amphibolite)		
	96-69	**96-98**	**96-101**	**575/B**	**96-28**	**97-76**
Quartz	▪	▪	▪	▪	▪	▪
Plagioclase	▬	▬	▬	▬	▪	▬
Biotite		▮	t	▪	t	
Chlorite		▮		t	t	
Garnet	▪	▪	▪	▮	▪	▮
Hornblende	▬	▬	▬	▬	▬	▬
Epidote		t		t		
Zoisite		t	t	t		t
Sphene	▮	t	▮	▪	t	▮
Zircon				t		
Rutile					▮	▮
Calcite		t				
Opaque oxide	▪	▪	▪	t	▪	

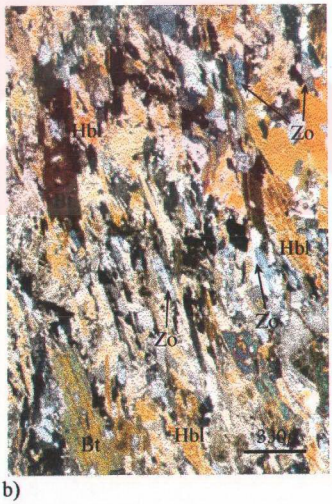
▪ 10 %

	Middle Nappe Unit (epidote amphibolite)				
	70	**463/A**	**95-38/B**	**96-182/B**	**97-63**
Quartz	■	▪	■	■	■
Plagioclase	▬	▬	▬	■	■
Biotite	▪	▬	▪	■	▬
Chlorite	t			t	t
Hornblende	▬▬	▬	▬	▬	▬▬
Epidote	t	▪	▪	▪	▪
Zoisite	▪	t	■	■	■
Sphene	▪	▪	▪		▪
Rutile				▪	
Calcite		t		▪	t
Opaque oxide			▪	t	t

■ 10 %



a)



b)

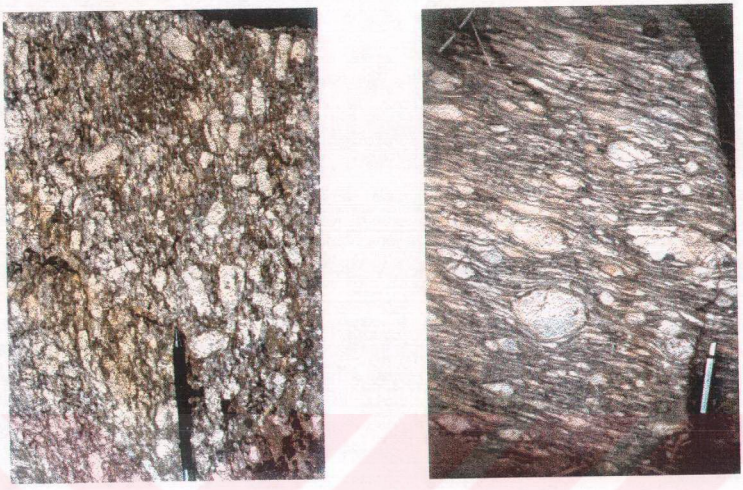
Figure 3.28. a) General appearance of garnet amphibolite showing nematoblastic texture, PPL, b) photomicrograph of epidote amphibolite. Note that, prismatic zoisite crystal are parrallel to the foliation with hornblende and biotite, CPL.

Epidote and zoisite are also common. The high relief and second order interference colours under crossed polars are typical for epidote. On the other hand, epidote display typical light yellow pleochroism colour under PPL. Zoisite usually occurs as anhedral to subhedral tabular crystals but some long lath shaped crystals show preferred orientatiton parallel to the main foliation. They are distinguished by their high relief and anomalous blue interference colour (Figure 3.28.b).

3.2.5. Orthogneiss

Orthogneisses (granitic, augen and banded gneisses) are formed by deformation and metamorphism granitoid precursor rocks (see Chapter 4). They constitute most of southern part of the middle nappe unit and eastern and northern part of the middle nappe unit and eastern and northern part of the upper nappe unit (Figure 3.2) and covers an area of about 175 km^2. Orthogneisses have usually white to dirty white colours and become darker when the rock has more biotite content. Granitic gneisses are massive and show no foliation, whereas augen and banded gneisses display pronounced penetrative foliation which are resulted from deformation under ductile conditons (Figure 3.29). In general, augen gneisses have feldspar porphyroblasts ranging from 1 to 3 cm. In some samples these orthoclase crystals most probably relict phases after granitic precorsers, and may reach up to 5-6 cm. Orthogneisses, both internaly and peripherally, include numerous xenolithes schists which are particularly common close to the margins. The smallest xenolite can be measured in centimetres and metres. Some of them are large enough to mark on map (Figure 3.2).

A huge orthogneiss body in the middle nappe unit tectonically overlies the Pan-African basement schists of lower nape unit in the southern part of the study area (Figure 3.2). The tectonic contact relationship between orthogneiss and schist is well exposed at a number of localities such as east of Aksu village and around Kahvedere village (Figure 3.30). Cataclastic rocks which are produced by the reactivation of the former ductil thrust plane are observed along the thrust fault boundary between schist and gneiss.



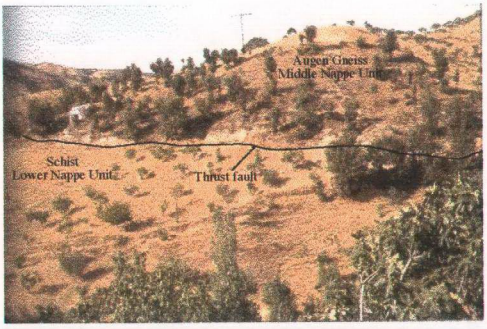
a) b)

Figure 3.29. General appearence of a) granitc gneiss and b) augen gneiss.

On the other hand, in many localities, intrusive contact relationship between schist and huge orthogneiss body is clearly observed within the middle nappe unit (Figure 3.31). Numerous sills and dykes of orthogneiss are found in schists close to the margins of orthogneiss. Some of them clearly cross cut the schistosity of schist and have sharp contacts with country rocks. Also, numerous schist xenoliths are observed in orthogneiss close to the margins. Schist xenoliths in orthogneisses and sills and dykes of orthogneiss in schists prove the original intrusive contact relationship between schist and orthogneiss.

Similar intrusive contact relationship between schist and a small orthogneiss body which is located 2 km northeast of Derbent is clearly observed. Numerous sills and dykes of orthogneiss occur in the schists close to the orthogneiss body (Figure 3.32). Furthermore, the contact between orthogneiss (granitic gneiss) and schist cross cut the main schistosity of schists in many places (Figure 3.33).

a)



b)

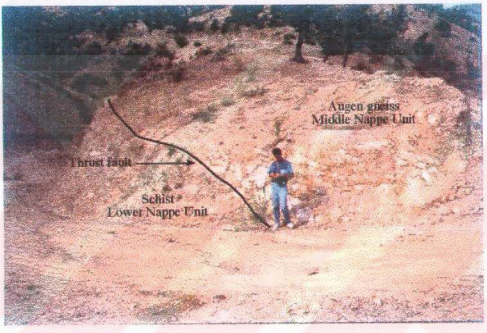


Figure 3.30. The contact relationship between orthogneiss of middle nape unit and schist of lower nappe unit, a) east of Aksu village (16925/15450), b) around Kahvedere village 28550/14075).

Orthogneisses of the upper nappe unit tectonically overlie the schists of the middle nappe unit in western part of the study area and in the northern part of the study area (around Bahadır village).

Orthogneisses consist mainly of K-feldspar (orthoclase and/or microcline), plagioclase, quartz, muscovite and biotite. They also contain small amount of garnet in some samples. Accessory minerals include apatite, zircon, epidote, sphene and tourmaline. Orthogneisses have commonly porphyroblastic and lepidoblastic texture (Figure 3.34). On the contrary, granitic gneisses show granoblastic texture.

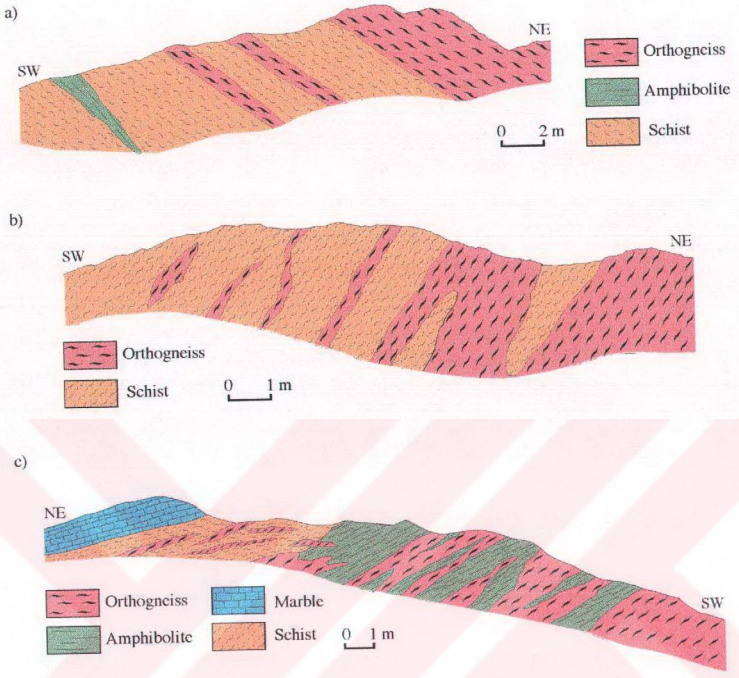


Figure 3.31. The contact relationship between orthogneiss and schist and amphibolite, a) 3 km NW of Kahvedere village, 26400/16475, b) 5 km SW of Sarıpınar village, 24650/19850 and c) 1.5 SW of Karaca Ali village, 38525/20625.

The general mineral assemblage of orthogneisses is quartz + plagioclase + orthoclase ± microcline + muscovite + biotite ± chlorite ± garnet ± tourmaline ± zoisite ± epidote ± apatite ± zircon + opaque oxides. The modal analyses of representative orthogneisses samples are given in Table 3.9.

Orthoclase is the most common constituent. It usually occur very large anhedral to subhedral megacrysts with irregular grain boundaries and comprises the great majority of the porphyroblasts in the rocks. The crystal size of orthoclase porphyroblasts usually ranges from 0.5 cm to 7 cm in diameter. They show

commonly string, rodded and beaded perthitic textures. Myrmekitic intergrowth is common along the grain boundaries of orthoclase. Microcline most probably after orthoclase shows typical crosshatched twinning.



Figure 3.32. The contact relationship between orthogneiss and schist. Sills and dykes of orthogneiss occur in the schists close to the orthogneiss bodies, 2 km norteast of Derbent.

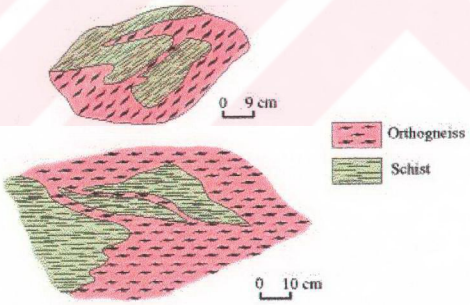


Figure 3.33. The contact relationship between orthogneiss (granitic gneiss) and schist. The boundary of orthogneiss cut across the main schistosity indicate the intrusive contact relationship, 2 km southeast of Derbent.

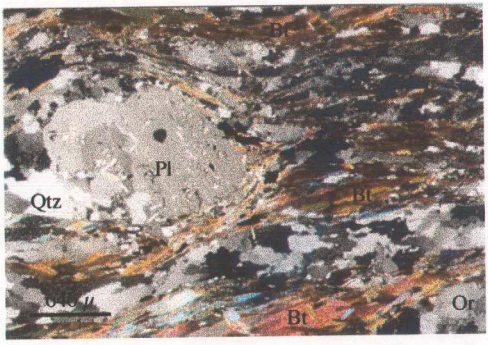


Figure 3.34. Photomicrograph showing lepidoblastic and porphyroblastic texture in orthogneisses, CPL.

Table 3.9. The modal mineralogical composition and mineral percentage of the representative orthogneiss samples. t: trace

	Middle Nappe Unit				Upper Nappe Unit			
	95-44	**95-77/A**	**96-77**	**97--66**	**232**	**386**	**97-58**	**97-59**
Quartz	▬	▬	▬	▬	▬	▬	▬	▬
Plagioclase	▬	▬	▬	▬	▬	▬	▬	▬
Orthoclase	▬	▬	▬	▬	▬	▬	▬	▬
Microcline					▬			▬
Muscovite	▬	▬	▬	▬	▬	▬	▬	▬
Biotite	▬	▬	▬	▬		▬	▬	▬
Chlorite	t							
Garnet		▬			▬	t		▬
Tourmaline					t		t	
Zoisite				t				
Epidote				t				
Apatite	t		t		t		t	t
Zircon	t	t	t	t	t	t	t	t
Opaque oxide	t	▬	t	▬			t	t

▬ 10 %

Although, it is not as common as orthoclase plagioclase also occurs as large porphyroblasts. Small anhedral plagioclase crystals associated with quartz are commonly observed. They show typical lamellar twinning as a result of ductile deformation.

Quartz is one of the major constituents of the orthogneisses. It occurs as anhedral equigranular crystals and display common ribbon structure due to the ductile deformation.

Micas, biotite and muscovite, tend to define the microstructure in the rock. They occur as aligned subidioblastic flakes and show remarkable parallelism to the foliation. Chlorite occurs as a retrogressive mineral replacing biotite and garnet.

Garnets occur mainly anhedral porphyroblasts. In some samples garnets occur as subhedral to euhedral small crystals enclosing biotite as a corona structure (Figure 3.35).

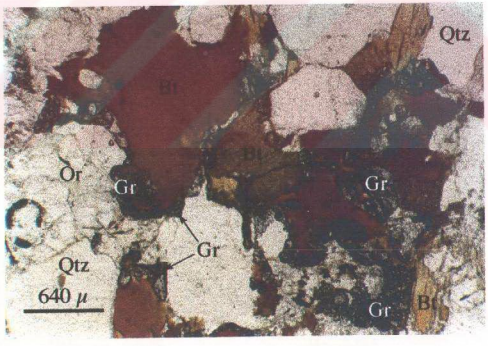


Figure 3.35. Subhedral to euhedral small garnet crystals overgrowth around biotites as a corona structure, CPL.

3.3. Paleozoic-Mesozoic cover units

In the Menderes Massif, the cover series are divided into two units; i) Paleozoic units which are made up of, from bottom to top, yellowish quartzite and phyllite - marble - black quartzite intercalation, and ii) Mesozoic-Early Tertiary sequence consisting of, in ascending order, metaconglomerate - mica schist intercalation, yellowish dolomites, platform-type thick marble with metabauxite deposites and preserved rudist fossils, red colour pelagic marble and metamorphic olistostrome (Dürr, 1975; Dora et al, 1995; Konak, et al 1987; Özer, 1998).

The contact relationship of these two units is still controversial. However, along the southern border of the Menderes Massif, it is generally regarded that this contact is characterized by a metaconglomerate level which is assumed to represent an unconformity between Paleozoic and Mesozoic series (Konak et al. 1987).

In the study area, the Pan-African units are overlain by the cover series, upper most nappe unit, with a tectonic contact. This unit is exposed in a very small place at the northwestern part of Derbent area (Figure 3.2). The lithostratigraphy of the cover units in this area can be given as follows; staurolite-garnet phyllite - quartzite - marble intercalation, amphibolites and overlying white coloured massive marbles. Based on the presence of the metabauxite lenses at the western extention of this marbles, these metacarbonates can be correlated to the Mesozoic marbles widely occuring at the southern flank of the Menderes Massif.

On the other hand, although there is no direct evidence except for the dominant black colour of the lithologies, the quartzite - phyllite - marble intercalation underlying the Mesozoic carbonates can be correlated with the Permo-Carboniferous units, Göktepe formation, of the Menderes Massif.

In the second locality, Demirhan area north of Atça, the similar black coloured lithologies are intruded by the Triassic leucocratic orthogneisses (Figure 3.1). In addition to the geochronological evidence obtained by this study the preserved bryozoa fossils which give a Permo-Carboniferous age (Dora et al., 1995), in the

western extension of this black series around Paşayaylası verify the Paleozoic age of these black units. The geological and petrographical characteristics of the main lithologies of the Paleozoic - Mesozoic units are given below.

3.3.1. Metapelites (phyllite-schist-quartzite intercalation)

In the Derbent area, metapelites are recognized in upper most nappe unit around Eğrektaş hill and west of Bahadır village, (Figure 3.2, 3.3, 3.37) Furthermore, metapelites are also recognised in the Demirhan area. They cover an area about 15 km^2 in these two study areas.

The upper nappe unit of Pan-African basement is tectonically overlain by metapelites and marble of cover series in the Derbent area (Figure 3.36). Metapelites are predominantly composed of schists and phyllites and subordinately quartzite and black marble. Quartzite and black marble are observed as thin interlayers and lenses in schist and phyllites. Schists and phyllites vary from dark from dark brown to black colours. They display pronounced schistosity and cleavage and are characterised by a well developed lepidoblastic texture due to the paralel alignment of mica flakes. At some horizons, they contain black albite spots and reddish garnet porphyroblasts embedded in a fine-grained micaceous matrix.

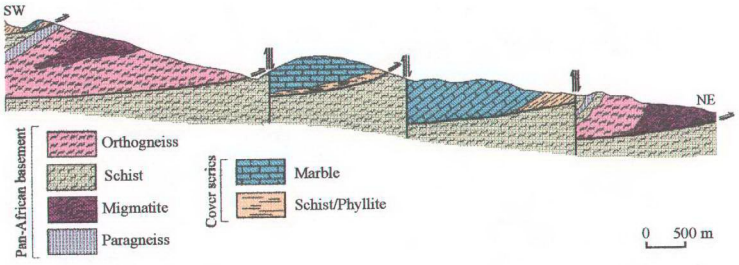


Figure 3.36. The contact relationship between cover series and Pan-African basement, west of Bahadır village (see Figure 3.3).

In the Demirhan area, metapelites are predominantly composed of black phyllite intercalating with black quartzite and subordinately schist and marble. Metapelites are overlain by Pan-African orthogneisses with a tectonic contact (Figure 3.37). Furthermore, metapelites are intruded by the Triassic leucocratic orthogneises (see Chapter 3.5, Figure 3.27).

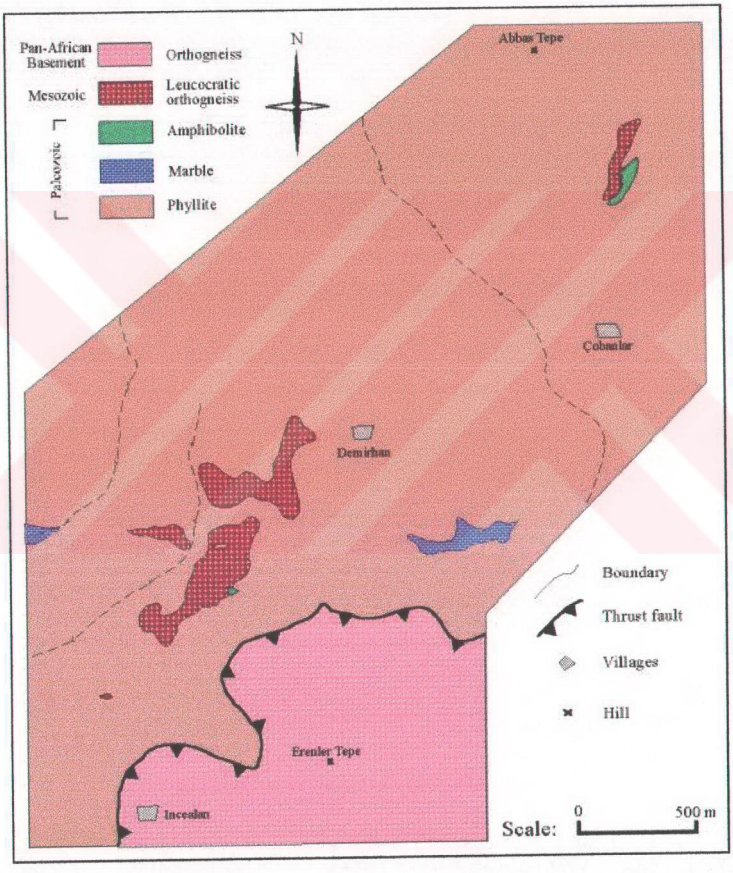


Figure 3.37. Geological map of Demirhan region located in the southern part of the Ödemiş-Kiraz Submassif of the Menderes Massif. National grid: Aydın M20-a2

Schists are composed of predominantly garnet-mica schists and subordinately mica schists and calc-schist. The following assemblages are observed with a matrix of quartz and plagioclase;

⇒ quartz - muscovite - biotite - garnet

⇒ quartz - muscovite - biotite

⇒ quartz - muscovite - calcite

The general mineral assemblage of schists is quartz + plagioclase + muscovite + biotite ± chlorite ± garnet ± tourmaline ± apatite ± zircon ± calcite + opaque oxide phases. The modal analyses of the representative schist samples are given in Table 3.10.

Table 3.10. Modal mineralogical composition and mineral percentage of the representatitve schist samples. t: trace

	garnet-mica schist		mica schist		calc schist	
	253	**96-35**	**188**	**225**	**96-39**	**96-107/C**
Quartz	▬	▬	▬	▬	▬	▬
Plagioclase	▬	▬	▬	▬		
Muscovite	▬	▬	▮	▬	▬	▬
Biotite	▬	▬	▬	▬		
Chlorite	▮	▮				t
Garnet	▮	▮				
Tourmaline	t	t		t	t	
Apatite	t	t	t	t		
Zircon	t	t	t	t	t	
Calcite					▬	▬
Opaque oxide	▮	▮	▮	t	▮	▮

▬ 10 %

Quartz is one of major constituents of the scihsts. They occur as anhedral equigranular crystals and show typical undulatory extinction. Plagioclase are found

T.C. YÜKSEKÖĞRETİM KURULU
DOKÜMANTASYON MERKEZİ

as small anhedral crystals with quartz in the matrix, and show rarely lamellar twinning and albite twinning.

Micas most commonly occur as aligned subidioblastic flakes (Figure 3.38) They show remarkable parallelism which defines a lepidoblastic texture. Biotite is generally the dominant mica phase in schist. Chlorites occur as a retrograde phase mineral replacing biotite and garnet.

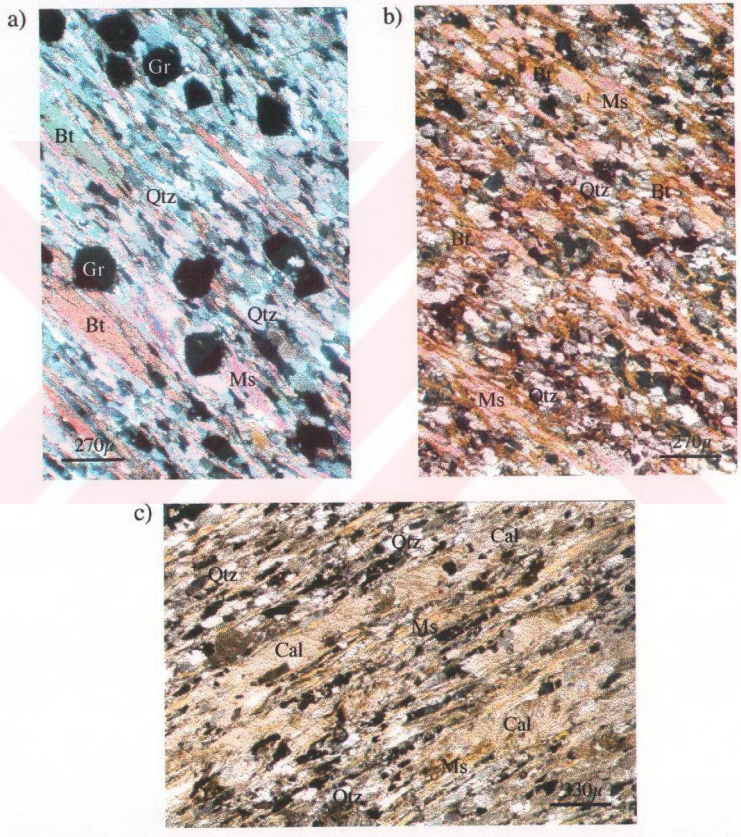


Figure 3.38. a) Photomicrograph showing lepidoblastic texture in garnet-mica schist, b) General appearance of mica schists which display parallel alignment of mica flakes, c) Photomicrograph showing lepidoblastic texture in calc-schist, CPL.

Garnet is very common and occurs as euhedral to subhedral crystals (Figure 3.38.a). Some garnets lack any inclusions. The crystal size of garnets usually ranges from 100 μ to 300 μ but may reach up to 6-7 mm. Oxidation and chlorite replacement around the edges of garnet grains are common.

Phyllites are divided into subgroups according to their mineral assemblages. The following assemblages are observed in phyllites;

⇒ quartz - sericite - garnet - staurolite
⇒ quartz - sericite - garnet - chloritoid
⇒ quartz - sericite - garnet
⇒ quartz - sericite - chloritoid

The general mineral assemblage of phyllites is quartz ± muscovite + sericite ± chlorite ± chloritoid ± garnet ± staurolite ± tourmaline ± apatite ± zircon ± graphite and opaque oxide phases. The modal analyses of the representative phyllite samples from upper most nappe unit are given in Table 3.11.

Sericite and muscovite is usually the dominant mica phases in phyllites. They occur as aligned subidioblastic small flakes which define the microstructures in the rocks. They produce an intense cleavage and some of them show remarkable crenulation cleavage.

Chloritoids are commonly found as aligned subidioblastic acicular crystals, which show remarkable parallelism with the main foliation (Figure 3.39). They display high relief, pale greenish to bluish pleochroism and dark bluish interference colours.

Garnets are very common and are observed as syn-tectonic crystal. They occur as subhedral and euhedral porphyroblasts. The crystal size of garnets reaches up to 1 cm. Syn-tectonic garnet porphyroblasts show well-developed inclusion trails (Figure 3.40).

Table 3.11. Modal mineralogical composition and mineral percentage of the representatitve phyllite samples. t: trace

	chloritoid phyllite		garnet phyllite		chloritoid-garnet phyllite	staurolite-garnet phyllite
	71	**198**	**379**	**423**	**377**	**217**
Quartz	▬	▪	▬	▪	▬	▪
Sericite	▬▬	▬▬	▬▬	▬▬	▬▬	▬▬
Muscovite		▪				▪
Chlorite			▮		t	
Chloritoid	▮	▬			▪	
Garnet			▪	▬	▬	▬
Staurolite						▮
Tourmaline			t	t	t	
Apatite		t			t	
Zircon			t		t	
Rutile				t		
Graphite	▬			▪	▪	
Opaque oxide	t	t	▮	▪	▪	▮

▬ 10 %

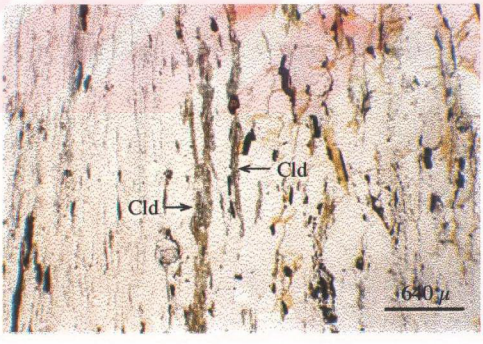


Figure 3.39. Aligned subidioblastic prismatic chloritoid crystals showing remarkable parallelism with the main foliation, PPL.

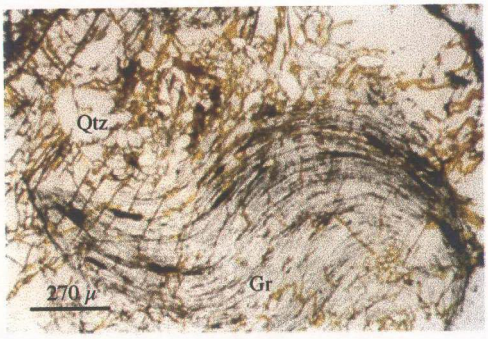


Figure 3.40. Syn-tectonic garnet crystal showing well-developed inclusion trails, PPL.

Staurolites are observed as small crystals within the matrix of sericite and as inclusions in the rim of garnet porphyroblasts (Figure 3.41). They show typical colourles to golden yellow pleochroism colours.

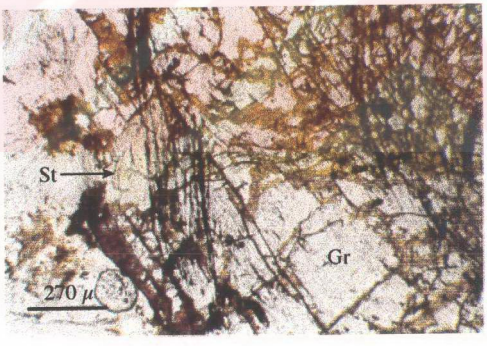


Figure 3.41. Photomicrograph showing staurolite in the rim of syn-tectonic garnet porphyroblast as inclusions. Note that, inclusions in garnets pass into staurolite and perfectly continue on the right side of the crystal, PPL.

3.3.2. Marble

Marbles in cover units are recognised only in upper part of the **???** nappe unit (Figure 3.2). They cover an area of about 7 km2. The marbles are well-exposed around Eğrektaş hill and NW of Bahadır village (Figure 3.42). They have gray and white colours and exhibit well-developed foliation. The general assemblage of marbles is calcite ± quartz ± muscovite ± graphite ± opaque oxide phases. The modal analyses of the representative marble samples are given in Table 3.12. Marbles are usually foliated and display granoblastic texture due to the common occurrence of equigranular calcite crystals.

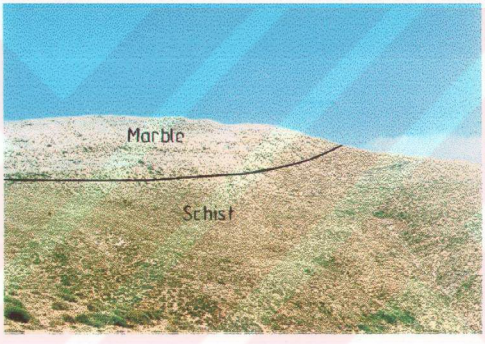


Figure 3.42. The contact relationship between schist and marble, west of Eğrektaş hill (29575/34775)

Tablo 3.12. Modal mineralogical composition and mineral percentage of the representative marble samples. t: trace

	182	195	249	577/D	96-161
Quartz	▮	▮		■	t
Muscovite	t	t		t	
Calcite	▬	▬	▬	▬	▬
Opaque oxide		t			

■ 20 %

3.3.3. Metabasites

Metabasites are observed in the schist of cover series around Derbent and Demirhan areas as sills and pods variable in size (Figure 3.43). They show usually well-developed schistosity and have nematoblastic texture characterised by alingment of prismatic amphibole crystals. Metabasites are composed of mainly amphibolites and garnet-amphibolites.

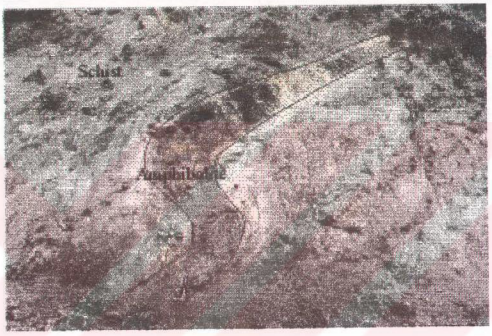


Figure 3.43. An amphibolite bodie in garnet-mica schist of cover series, 2 km southwest of Eğrektaş hill, 28975:32050.

The general mineral assemblage of metabasites is quartz + plagioclase + biotite ± chlorite ± garnet + hornblende ± zoisite ± epidote ± sphene ± apatite ± rutile ± opaque oxide phases. The modal analayses of the representative samples of metabasites in Table 3.13.

Quartz and plagioclase are quite abundant in amphibolites. They form subhedral to anhedral crystals. Biotite occurs subidioblastic laths. Chlorite occurs as a retrogresive mineral replacing biotite. Garnet is commonly found as subhedral crystals.

Hornblende occurs as medium to large subidioblastic to idioblastic crystals which are prismatic. They have typical amphibole shape with two well-developed cleavages (Figure 3.44).

Table 3.13. Modal mineralogical composition and mineral percentage of the representative amphibolite samples. t: trace

	259	97-55/A	97-55/B	97-55/C1	97-55/D
Quartz	▬	▬	▬	▬	▬
Plagioclase	▬	▬	▬	▬	▬
Biotite	▮	▬	t	▮	▬
Chlorite	▮				t
Garnet		▬	▬	▬	▮
Hornblende	▬	▬	▬	▬	▬
Epidote			t		t
Zoisite		▮			t
Sphene		t		t	▬
Apatite		t			
Rutile	t				
Opaque oxide		t		▮	t

▬ 10 %

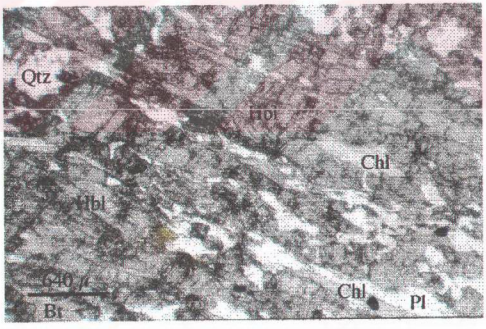


Figure 3.44. Subidioblastic to idioblastic aligned hornblende crystals defining well developed nematoblastic texture, PPL.

3.3.4. Leucocratic orthogneiss

In general, the leucocratic orthogneisses are exposed in the eastern and southern parts of the Ödemiş-Kiraz Submassif in a NNE trending zone, approximately 80 km in long (Figure 3.1). In the Derbent area, the leucocratic orthogneisses are observed only in the middle nappe unit of Pan-African basement (Figure 3.2). Leucocratic orthogneisses intruded into schist and orthogneisses of the Pan-African basement in the Derbent area (Figure 3.45). On the contrary, they intruded into the schist and phyllites of the cover series in the Demirhan area. The leucocratic orthogneisses are fine grained and more or less equigranular rocks, and generally have pronounced foliation. They are usually white and yellowish white coloured. When the rock (muscovite ± biotite leucocratic orthogneiss) have more muscovite content they become light green colour (Figure 3.46.a). Whereas, a big leucocratic orthogneiss body occuring at the western of Karacaali village and some small bodies on the same locality have dark colour resulted from high magnetite content (magnetite ± biotite ± muscovite leucocratic orthogneiss (Figure 3.46.b). The leucocratic orthogneiss include peripherally numerous schist xenolites which are particularly common close to the contact.

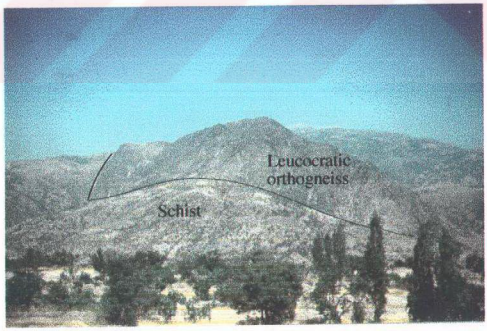
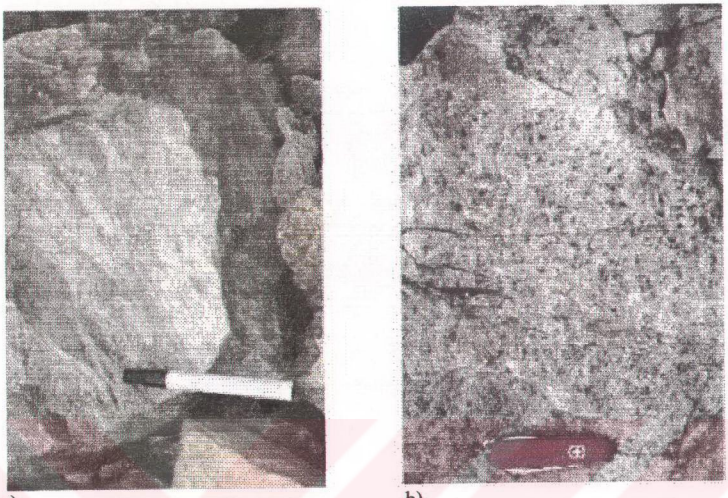


Figure 3.45. The panoramic view of leucocratic orthogneisses in the Derbent area, Dededağı, 34500:31300.



a) b)

Figure 3.46. a) General appearance of the muscovite rich leucocratic orthogneiss., b) general appearance of magnetite bearing leucocratic orthogneisses.

The contact relationship between leucocratic orthogneiss and schist is well exposed at a number of localities in the Derbent area. Intusive contact relationships between leucocratic orthogneiss and schist of Pan-African basement are observed clearly in some localities (Figure 3.47). The foliation resulted from Alpine deformation cross cut the original intrusive contact relationship between leucocratic orthogneiss and schist.

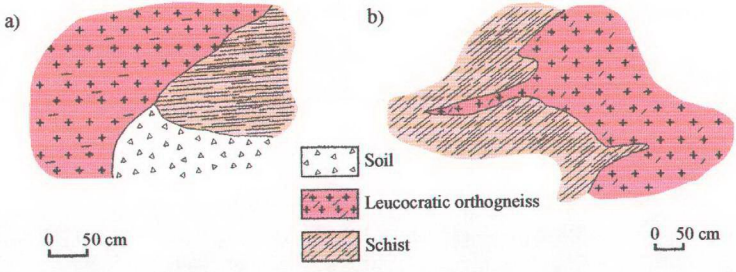


Figure 3.47. The intrusive contact relationship between leucocratic orthogneiss and schist a) 35200:29200, b) 34125:27525.

Leucocratic orthogneisses are clearly observed as dykes cutting across the foliation of the schistosity of schist and the foliation of the augen gneisses (Figure 3.48).

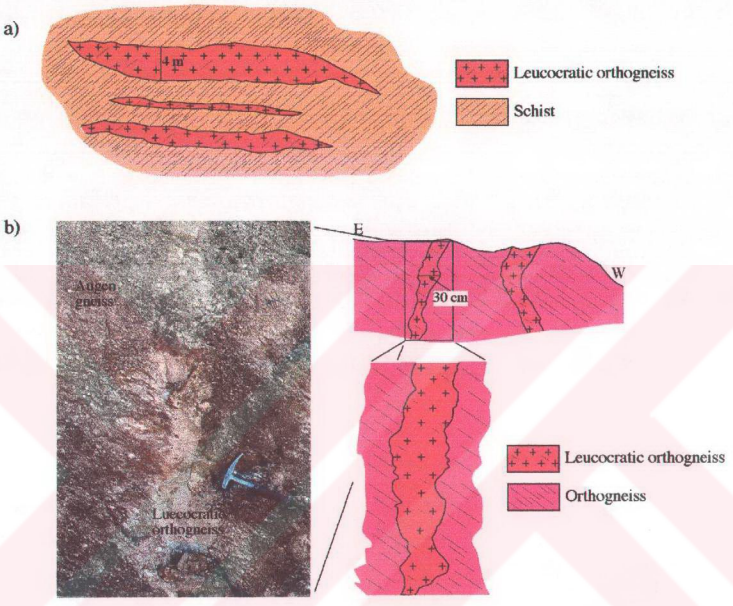


Figure 3.48. The dykes of leucocratic orthogneisses cut across the schistosity of schist (a, 22125:17125) and the foliation of the augen gneisses (b, 28400:20450).

Furthermore, the boundary of leucocratic orthogneisses are usually parallel to the main foliation of metapelites (Figure 3.49), due to the last main metamorphism of the Menderes Massif. Many sills of the leucocratic orthogneisses displaying conformable relationship with the foliation of metapelites are observed close to the contact.

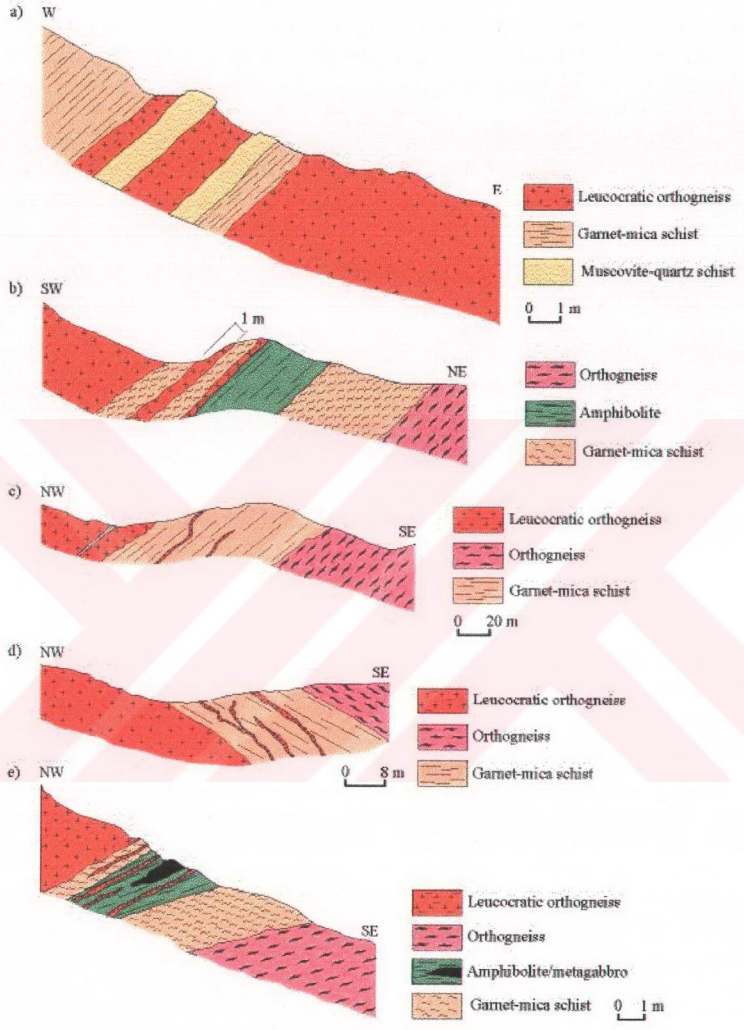


Figure 3.48. The contact relationship between leucocratic orthogneisses and schists. Sills of the leucocratic orthogneisses are observed close to the contact, a) 35125/28725, b) 29300/18650, c) 29250/18600, d) 28375/21100, e) 31100/24850.

Some sills of leucocratic orthogneisses are also observed in augen gneisses with conformable relationships with respect to the foliation of augen gneisses (Figure 3.50).

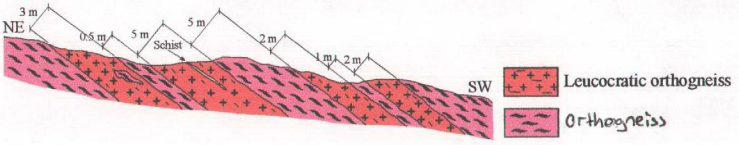


Figure 3.50. The contact relationship between sills of the leucocratic orthogneisses and the orthogneisses, 31875:17000.

In the Demirhan area, leucocratic orthogneisses intruded into the metapelites of the cover series. They occur as sills which are parallel to main schistosity of metapelites (Figure 3.51).

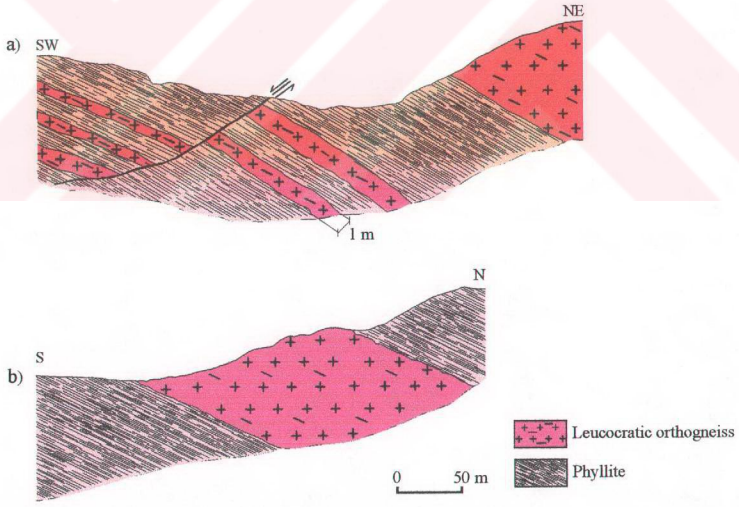


Figure 3.51. The contact relationship between leucocratic orthogneisses and phyllites of the cover series, 07175:03725.

The leucocratic orthogneisses in Demirhan area are fine grained, more or less equigranular and weakly deformed rocks. Quartz, plagioclase and K-feldspar (orthoclase + microcline) make up 88-95 vol. % of the rock, reflecting its primary granitic composition. Leucocratic orthogneisses show usually lepidoblastic and porphyroblastic textures which are characterised by the alignment of muscovites and porphyroblasts of K-feldspars and plagioclases respectively (Figure 3.52.a,b). Furthermore, in the undeformed parts of the leucocratic orthogneisses granoblastic texture is observed (Figure 3.52.c, d).

On the basis of mineralogical composition of the leucocratic orthogneiss, three different types of leucocratic orthogneiss can be distinguished;

⇒ muscovite ± biotite leucocratic orthogneiss (Derbent area)
⇒ magnetite ± biotite ± muscovite leucocratic orthogneiss (Derbent area)
⇒ biotite leucocratic orthogneiss (Demirhan area)

The general mineral assemblage of leucocratic orthogneisses is quartz + plagioclase + orthoclase ± microcline ± muscovite ± biotite ± chlorite ± epidote ± allanite ± sphene ± apatite ± zircon ± magnetite. The modal analyses of the representative samples of lecocratic orthogneisses are given in Table 3.14.

K-feldspars (orthoclase and microcline) are the major constituent of the leucocratic orthogneisses. They usually form large anhedral to subhedral crystals with irregular grain boundaries. The porphyroblasts range in size between about 250-300 μ to 6-7 mm maximum. K-Feldspars make up 10-38 vol. % of the rock and include roded, braided and interlicking type perthites (Figure 3.53). Microcline shows typical crosshatched twinning. Myrmekitic intergrowth is common along the grain boundaries of K-Feldspars.

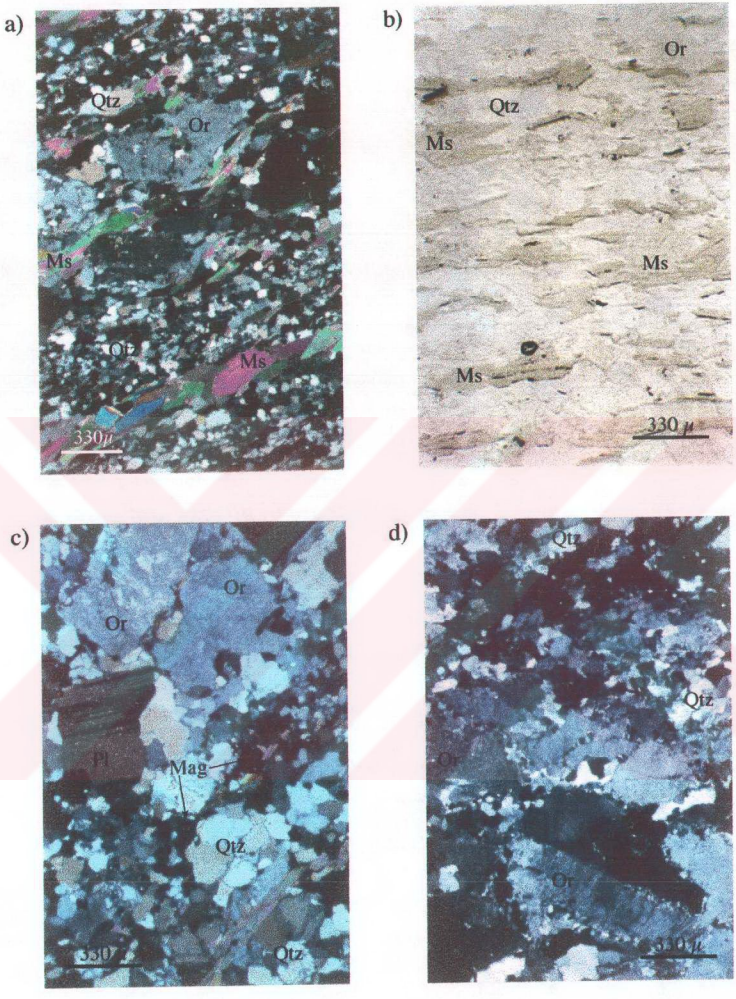


Figure 3.52. a) and b) Muscovites showing remarkable parallelism cause lepidoblastic texure in leucocratic orthogneisses. Note that, they have light green pleochroism, CPL, PPL (muscovite±biotite leucocratic orthogneiss), c) granoblastic texture in undeformed parts of the leucocratic orthogneisses, PPL (magnetite±biotite±muscovite leucocratic orthogneiss and biotite leucocratic orthogneiss respectively).

Table 3.14. Modal mineralogical composition and mineral percentages of the representative leucocratic orthogneiss samples. t:trace

	muscovite ± biotite leucocratic orthogneiss (Derbent area)					
	176	**476**	**600**	**732**	**95-75**	**97-74**
Quartz	▬	▬	▬	▬	▬	▬
Plagioclase	▬	▬	▬	▬	▬	▬
Orthoclase	▮	▬	▬	▬	▬	▬
Microcline	▬	▬	▬	▮	▮	▬
Muscovite	▮		▮	▬	▮	▬
Biotite	t		t			
Epidote		t				
Alanite			t	t	t	
Apatite			t		t	
Zircon	t	t	t	t	t	t
Opaque oxide	t	▮	t	t	t	t

▬ 10 %

	magnetite ± biotite ± muscovite leucocratic orthogneiss (Derbent area)				biotiteleucocratic orthogneiss (Derbent area)	
	531	**718/A**	**95-15**	**97-68/A**	**96-37**	**97-44**
Quartz	▬	▬	▬	▬	▬	▬
Plagioclase	▬	▬	▬	▬	▬	▬
Orthoclase	▬	▬	▬	▬	▬	▬
Microcline				▮		
Muscovite	▬	▮		▬		
Biotite		t	▮		▮	▮
Chlorite					t	
Epidote	t				t	
Sphene	t	t				
Apatite						
Zircon		t	t		t	t
Opaque oxide (magnetite)	▮	▬	▬	▬	t	t

▬ 10 %

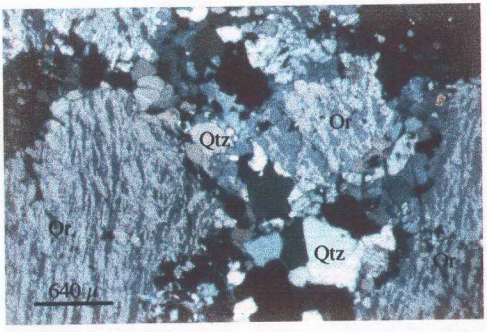


Figure 3.53. Photomicrograph of orthoclase showing common perthitic structure, mainly roded and braided type, CPL.

Plagioclase occur commonly as anhedral to subhedral crystals in variable size. It also occurs as large porphyroblasts as orthoclase. Some orthoclases rarely are mantled by plagioclase rims (Figure 3.54). Plagioclase shows typical lamellar twinning and makes up 8-25 vol. % of the rocks.

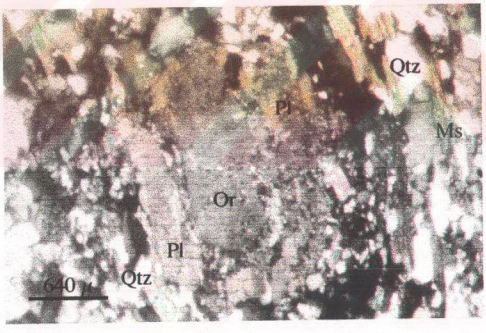


Figure 3.54. Photomicrograph showing orthoclase crystal mantled by plagioclase rims in leucocratic orthogneisses, CPL.

Muscovites are green coloured in the rock samples (Figure 3.46.a) and have pale-green pleocroism in thin sections (Figure 3.52.b). They occur as platy or tabular crystals which are parallel to the foliation. Although the muscovite contents of the muscovite ± biotite leucocratic orthogneisses in the Derbent area reach up to 20

vol.%, biotite is present as small thin platy crystals, and never exceeds 1 vol. % in the muscovite ± biotite leucocratic orthogneisses. They reach up to 5 vol. % in the magnetite ± biotite ± muscovite leucocratic orthogneisses in the Derbent area and in the biotite leucocratic orthogneisses in the Demirhan area.

Several leucocratic orthogneisses (magnetite ± biotite ± muscovite leucocratic orthogneisses) contain abundant magnetite crystals (Figure 3.46.b). Magnetite crystals reach up to 15 vol. % in the magnetite ± biotite ± muscovite leucocratic orthogneisses (Figure 3.55).

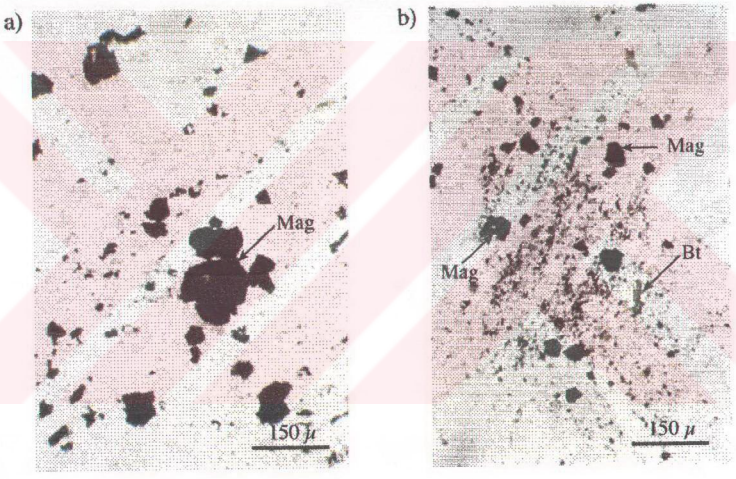


Figure 3.55. a), b) Photomicrograph showing magnetite crystals in magnetite bearing lecocratic orthogneisses, PPL.

In the Derbent area, west of Karacaali village, contact metamorphic rocks which have a wollastonite - grossular - idocrase - epidote assemblage are developed at the contact of the leucocratic orthogneisses and marbles (Figure 3.56, 3.57). Additionaly, at the leucocratic orthogneiss-marble contact similar rocks having a grossular-epidote-tremolite assemblage were detected at two locations in nortwest of Alasehir.

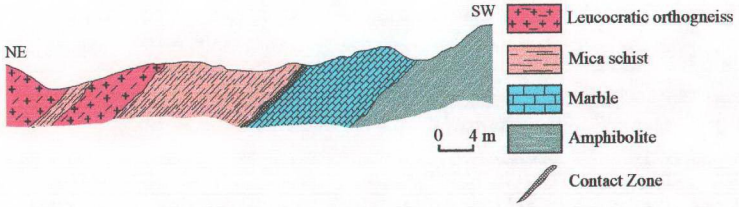


Figure 3.56. The contact relationship between leucocratic orthogneiss and marble, contact metamorphic assemblage occur in marble, 40375:20325.

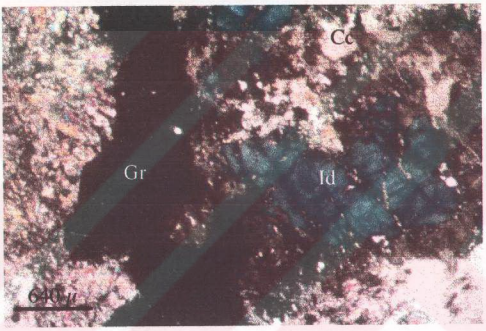


Figure 3.57. Photomicrograph showing grossular and idocrase in the contact metamorphic rocks. Note that, idocrase display typical dark blue interference colour, CPL.

3.4. The rocks of İzmir-Ankara Zone

Unmetamorphosed rocks of the İzmir-Ankara Zone are recognized around Bahadır village, northern part of the study area, in the Derbent area (Figure 3.2, 3.3). They cover an area about 1 km^2. The metamorphic rocks of the cover series are tectonicaly overlain by the unmetamorphosed rocks of İzmir-Ankara Zone (Figure 3.58). The unmetamorphosed rocks are predominantly composed of serpentinites and subordinately lateritic rocks. Candan (1988) reported that the metamorphic basement in the Demirci area is tectonicaly overlain by İzmir-Ankara Zone rocks composing of flysch, limestones and ultrabasic rocks.

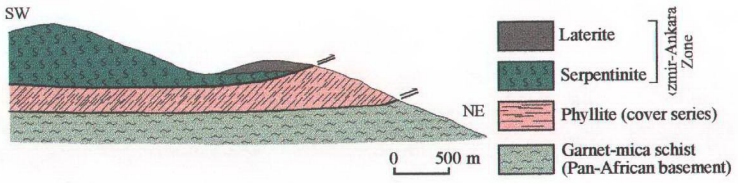


Figure 3.58. Contact relationship of İzmir-Ankara Zone rocks with phyllite of cover series, 1 km SW of Bahadır village, 37100:32750.

Along the road cuts, the fresh parts of serpentinites are usually yellowish green and pale green coloured, the altered parts of the rocks are dark brown colours. They are massive, fine to medium grained and do not show a foliation. Pyroxene crystals are visible by the naked eyes in some samples (Figure 3.59).

Based on the petrographical studies the mineralogical composition of serpentinites is determined as serpentine ± olivine ± orthopyroxene ± clinopyroxene + opaque oxide phases. Modal analyses of the representative serpentinite samples are given in Table 3.15

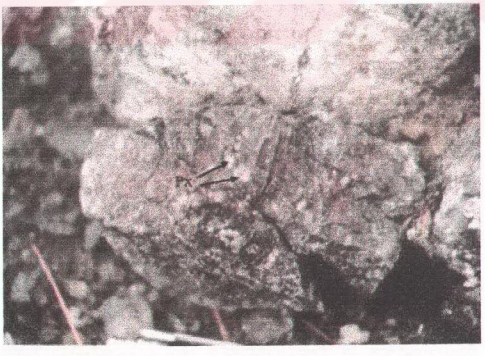


Figure 3.59. Serpentinites of İzmir-Ankara Zone rocks. Pyroxene crystal are visible in some samples.

Table 3.15. Modal mineralogical composition and mineral percentage of representative serpentinite samples. t:trace

	5/B	351	425/C
Olivine	▬		▬
Clinopyroxene	t		▬
Orthopyroxene	t		▮
Serpentinite	▬	▬	▬
Opaque oxide	▮	▬	▮

▬ 10 %

Completely serpentinized samples show characteristic mesh texture. Relict olivine, orthopyroxene and clinopyroxene are observed as primary minerals of ultrabasic rocks in thin sections (Figure 3.560). Olivines show high birefringence colours and have commonly irregular cracks. Serpentinization of olivines are very common. Olivines are of forsterite (Fo_{91}) in composition (Akkök, 1985). Orthopyroxenes show low birefringence colours and are of enstatite in composition. Clinopyroxenes display high birefringence colours and are of diopside in composition.

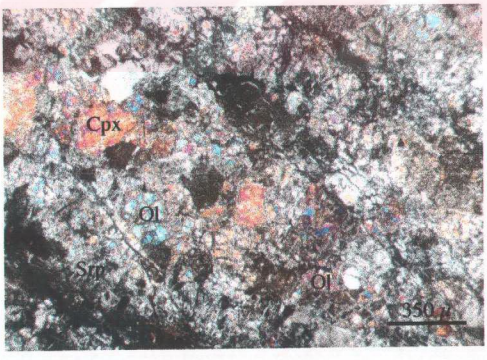


Figure 3.60. Photomicrograph illustrating the general apperance of serpentinites. Serpentinisation of the ultrabasic rock is common, CPL.

CHAPTER FOUR
GEOCHEMISTRY

4.1. Introduction

18 representative samples of augen/granitic gneisses and 35 samples of leucocratic orthogneisses from the Ödemiş-Kiraz Submassif of the Menderes Massif, south of Alaşehir, were collected for analysis (Figures 4.1, 4.20). Major oxide and trace element results and CIPW norms are presented in Table 4.1 and Table 4.2.

The samples were analysed at Dokuz Eylül University, İzmir, using a Phillips PW 1130 X-ray spectrometer and at University of Tübingen, Germany, using Siemens SRS 300 X-ray spectrometer, calibrated against both international and own standards of appropriate composition.

The principal objectives of the geochemical investigation can be given as follows:

to compare with the field recognition of a granitic igneous origin for the augen/granitic gneisses and leucocratic orthogneisses;
to establish whether the protolith is S-type or I-type;
to establish a possible source of magma generation;
to study the primary magmatic characteristics of the granitic precursor, using relatively immobile major and trace elements;
to establish the nature of any chemical variation and whether any chemical groups within the granitic protolith can be identified;
to investigate the tectonic setting of the protolith rock(s) using chemical discriminates.

4.2. Preparation of the samples for XRF

A total of 53 rock samples, 18 from the augen/granitic gneisses and 35 from the leucocratic orthogneisses, were collected to investigate the origin and geochemical characteristics of rock types. All rock specimens which were weighted at about 1.5-2 kg were prepared to analysis by the following way; a) samples were crushed into small pieces by means of hammer to remove the weathered materials at the margin of the

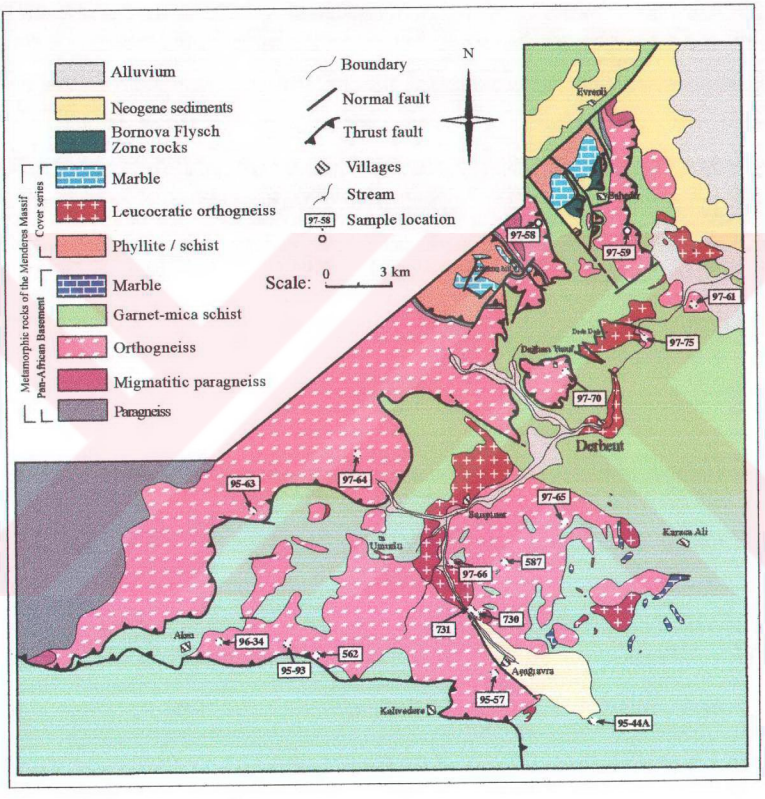


Figure 4.1. Location map of the samples for geochemical analyses of the augen/granitic gneisses, south of Alaşehir.

Table 4.1. Chemical and normative data of augen/granitic gneisses, na:not analysed)

SAMPLE	562	587	730	731	733	95-44A	95-57	95-63	95-93	96-34	97-58	97-59	97-61	97-64	97-65	97-66	97-70	97-75
Major Oxides (wt %)																		
SiO_2	67.24	69.48	71.12	71.21	72.01	68.72	68.03	69.54	66.93	69.82	66.88	73.59	68.1	74.23	70.21	69.55	69.86	71.59
TiO_2	0.73	0.36	0.41	0.36	0.36	0.49	0.47	0.63	0.73	0.57	0.71	0.21	0.79	0.21	0.41	0.54	0.71	0.32
Al_2O_3	15.87	14.73	14.26	14.5	14.03	15.1	15.61	15.04	16.32	13.07	15.03	13.63	14.82	13.94	14.45	14.7	14.71	14.67
Fe_2O_3	4.67	3.65	3.11	2.77	2.52	3.59	3.54	3.51	3.96	1.03	4.97	1.33	4.33	1.21	2.93	3.64	3.22	2.28
MnO	0.02	0.06	0.05	0.05	0.05	0.08	0.04	0.07	0.05	0.02	0.06	0.02	0.04	0.01	0.04	0.06	0.03	0.02
MgO	1.53	0.65	0.53	0.49	0.47	0.63	0.72	0.92	1.35	0.28	1.82	0.33	2.18	0.30	0.62	0.99	1.63	0.44
CaO	0.66	1.43	1.31	1.28	0.27	0.43	1.27	0.63	1.86	0.61	1.51	0.76	1.81	0.52	1.53	0.67	1.86	0.63
Na_2O	4.29	3.56	3.54	3.60	3.50	3.93	3.55	3.25	2.83	2.72	2.72	2.52	4.03	2.30	3.10	2.33	3.58	2.23
K_2O	3.35	4.65	4.56	4.80	5.15	4.33	4.29	5.41	3.86	5.04	3.15	5.04	1.78	5.06	4.72	5.49	2.31	5.19
P_2O_5	na	na	na	na	na	na	0.14	na	0.16	0.17	0.24	0.08	0.17	0.07	0.23	0.29	0.16	0.18
LOI	1.54	0.99	0.88	0.83	1.02	1.66	1.31	0.96	0.98	0.68	2.33	0.99	1.41	1.54	0.95	1.21	1.37	2.15
Total	99.9	99.56	99.77	99.89	99.38	98.96	98.97	99.96	99.73	99.66	99.42	98.49	99.45	99.38	99.18	99.47	99.42	99.71
Trace Elements (ppm)																		
Ba	806	756	669	709	731	678	860	811	808	262	586	498	437	447	944	1036	407	679
Cr	45	42	33	24	23	37	-	28	39	4	63	30	28	-	4	22	34	-
Ga	16	16	16	15	16	17	-	14	na	na	na	na	na	na	na	na	na	na
Nb	19	20	21	18	17	20	16	24	13	4	12	3	14	6	12	25	15	17
Ni	na	na	na	na	na	na	-	na	10	-	26	5	13	-	3	12	5	1
Rb	70	54	133	126	134	117	141	159	131	142	110	138	82	158	134	194	128	170
Sr	108	146	139	140	87	109	143	182	162	106	161	98	144	99	154	164	240	101
Th	20	10	7	3	2	28	-	16	na	na	na	na	na	na	na	na	na	na
V	na	na	na	na	na	na	30	59	59	11	88	6	76	8	28	42	74	23
Y	27	17	43	43	34	33	56	24	22	46	37	36	48	35	44	42	23	22
Zn	na	na	na	na	na	na	64	43	61	23	93	24	25	23	62	120	26	61
Zr	285	284	239	234	246	212	316	202	212	70	220	123	258	117	272	260	270	171
Ratios																		
A/NK	2.08	1.79	1.76	1.73	1.62	1.83	2.09	2.29	2.24	1.68	2.56	1.80	2.55	1.89	1.85	1.88	2.50	1.98
A/CNK	1.91	1.53	1.52	1.50	1.57	1.74	1.70	1.87	1.75	1.56	2.04	1.64	1.95	1.77	1.55	1.73	1.90	1.82
F/F+Mg	0.75	0.85	0.85	0.85	0.84	0.85	0.80	0.72	0.75	0.79	0.73	0.80	0.67	0.80	0.83	0.79	0.66	0.84
F/Mg	3.05	5.62	5.87	5.65	5.36	5.70	4.03	2.63	2.94	3.67	2.74	4.05	1.99	4.03	4.76	3.67	1.97	5.18
Mg/F	6.20	4.30	3.64	3.26	2.99	4.22	5.13	4.51	5.31	1.31	6.79	1.66	6.51	1.51	3.55	4.64	4.84	2.72
Mg/Ca	2.32	0.45	0.40	0.38	1.74	1.47	0.56	0.83	0.72	0.46	1.20	0.43	1.20	0.57	0.40	1.48	0.88	0.69
Na/Ca	6.50	2.49	2.70	2.81	12.96	9.14	2.06	2.6	1.52	4.43	1.81	3.32	2.22	4.41	2.03	3.47	1.92	3.52
Na/K	1.28	0.77	0.78	0.75	0.68	0.91	0.91	1.43	0.73	0.54	0.86	0.50	2.27	0.45	0.66	0.42	1.55	0.43
Nb/Y	0.70	1.17	0.48	0.42	0.51	0.6	0.39	0.42	0.59	0.09	0.32	0.08	0.29	0.17	0.27	0.6	0.65	0.77
Rb/Sr	0.64	0.37	0.96	0.9	1.54	1.07	0.66	0.57	0.81	1.34	0.68	1.41	0.57	1.60	0.87	1.18	0.53	1.68
Rb/Zr	0.24	0.19	0.56	0.54	0.55	0.55	0.38	0.51	0.62	2.03	0.5	1.12	0.32	1.35	0.49	0.75	0.47	0.99
Rb/Ba	0.09	0.07	0.20	0.18	0.18	0.17	0.11	0.21	0.16	0.54	0.19	0.28	0.19	0.35	0.14	0.19	0.31	0.25
Zr/TiO_2	0.04	0.08	0.06	0.07	0.07	0.04	0.04	0.04	0.04	0.06	0.03	0.06	0.03	0.06	0.07	0.05	0.04	0.05
K/Rb	482	855	342	380	383	369	419	261	294	355	287	365	217	320	352	283	181	305
Selective Normative Componets																		
Q	25.77	26.94	29.48	28.43	30.66	27.43	24.24	32.26	32.36	30.54	33.71	37.73	31.24	40.13	30.58	32.89	34.22	37.22
C	3.99	1.24	1.12	1.05	2.21	3.17	2.48	3.44	3.12	2.43	4.97	2.83	3.39	3.91	2.01	4.40	3.30	4.65
Or	19.80	27.48	26.95	28.37	30.43	25.59	24.17	16.05	22.79	29.78	18.62	29.78	10.50	29.91	27.86	32.41	13.66	30.68
Ab	36.30	30.12	29.95	30.46	29.62	33.25	31.48	32.81	23.95	22.97	23.04	21.33	34.06	19.45	26.25	19.72	30.28	18.90
An	3.27	7.09	6.50	6.35	1.34	2.13	8.98	6.38	8.20	1.94	5.93	3.28	7.88	2,11	6.08	1.45	8.22	1.98
An+Ab	39.57	37.21	36.00	36.81	30.96	35.38	40.46	39.19	32.15	24.91	28.97	24.61	41.94	21.56	32.33	21.17	38.5	20.88
An+Or	23.07	34.57	33.45	34.72	31.77	27.72	33.15	22.43	30.99	31.72	24.55	33.06	18.38	32.02	33.94	33.86	21.88	32.66

samples; b) samples were washed and scrubbed under the tap to remove all extraneous materials such as soils; c) the rock samples were reduced in to fragments of 2 to 6 mm diameter pieces to remove by a hardened steel jaw crusher; d) the rock chips were then homogenised by quartering; e) an approximately 100 gr rock chips were powdered by vibratory disc mill with tungsten carbide for 5 minutes. After this stage, the samples were ready to prepare for major and trace element analysis by XRF.

4.3. Geochemistry of augen/granitic gneisses

4.3.1. Whole rock analyses

All chemical analysis of augen/granitic gneisses from different localities of Çine, Ödemiş-Kiraz and Demirci-Gördes Submasifs (Kun, 1983; Kun & Candan, 1987; Bozkurt, 1994; Gezbul, 1994; Dannat, 1997; Sözer, 1997; Özkan, 2000) and from the study area are plotted on the same diagram for correlation.

4.3.1.1. Major elements

The major oxides of TiO_2, Al_2O_3, Fe_2O_3, MgO, CaO, Na_2O, K_2O and P_2O_5 of the gneisses collected from the study area as well as from the previous studies carried out in different parts of the Menderes Massif are plotted versus SiO_2. Augen/granitic gneisses of the study area characteristically have high SiO_2 content ranging from 67-76 wt% (Table 4.1). Gneiss samples from three submassifs have similar SiO_2 content ranging from 63-78 wt% (see references above). Most elements show a scattered distribution, CaO, Na_2O, K_2O and P_2O_5, against silica in Harker (1909) variation diagrams. Approximately curvilinear compositional trends are shown by decrease in TiO_2, Al_2O_3 and Fe_2O_3 with increasing SiO_2 content (Figures 4.2, 4.3). MgO shows partly scattered distribution and poor negative correlation with SiO_2 content.

4.3.1.2. Trace elements

Trace elements of Ba, Cr, Ga, Nb, Ni, Rb, Sr, V, Y, Zn, and Zr are plotted against SiO_2 (Figures 4.4, 4.5). Most of the elements such as Ba, Cr, Ga, Nb, Ni, Rb, Sr, Y, Zn, and Th, show a scattered distribution. Whereas, V and Zr contents of the samples show poor negative correlation with SiO_2 content.

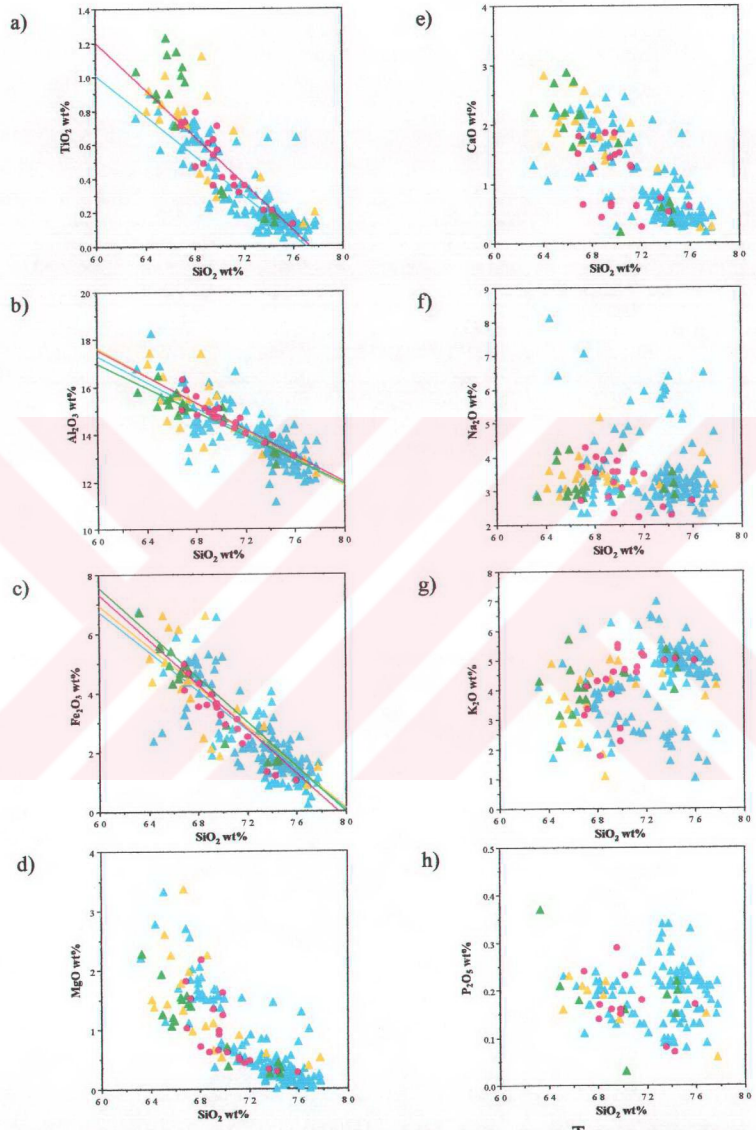


Figure 4.2. Major oxides variation diagrams (TiO_2, Al_2O_3, $Fe_2O_3^T$, MgO, CaO, Na_2O, K_2O, and P_2O_5) against SiO_2 (wt %) for augen/granitic gneiss from different submassifs of the Menderes Massif. ▲ : Çine submassif, ▲ : Ödemiş-Kiraz submassif, ▲ : Gördes submassif, ● : Study area

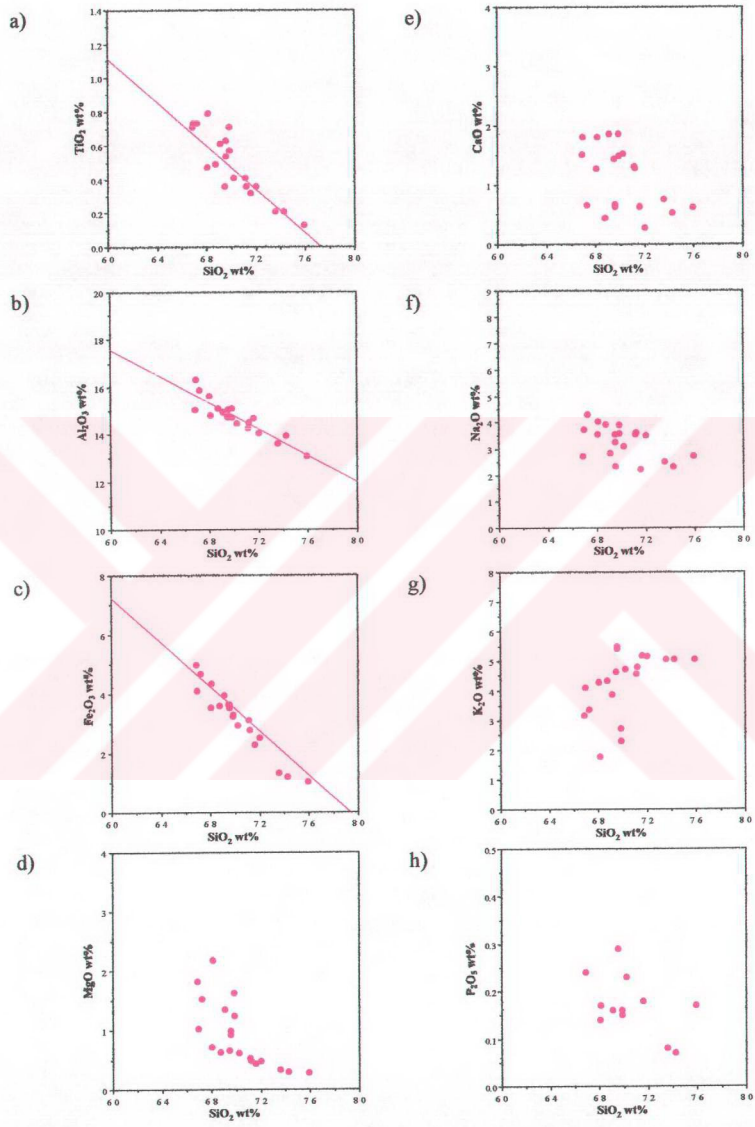


Figure 4.3. Major oxides variation diagrams, TiO_2, Al_2O_3, $Fe_2O_3^T$, MgO, CaO, Na_2O, K_2O, and P_2O_5 (ppm) against SiO_2 (wt %) for augen/granitic gneiss of the study area.

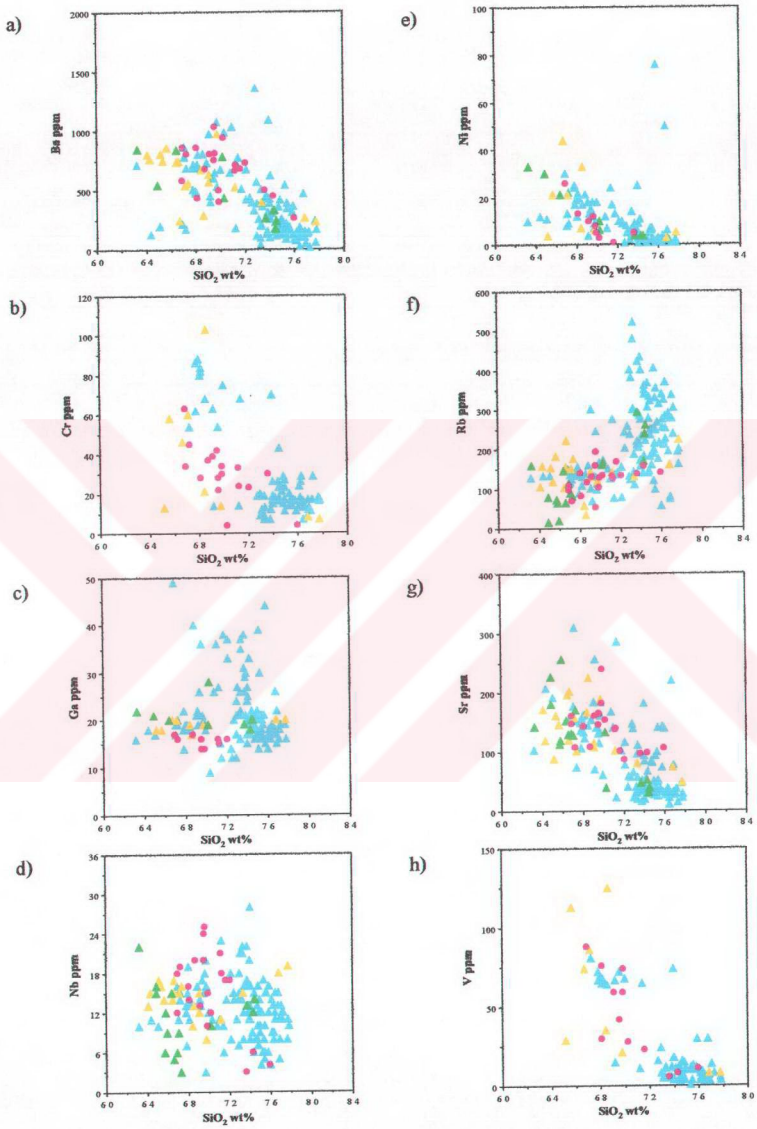


Figure 4.4. (Continue)

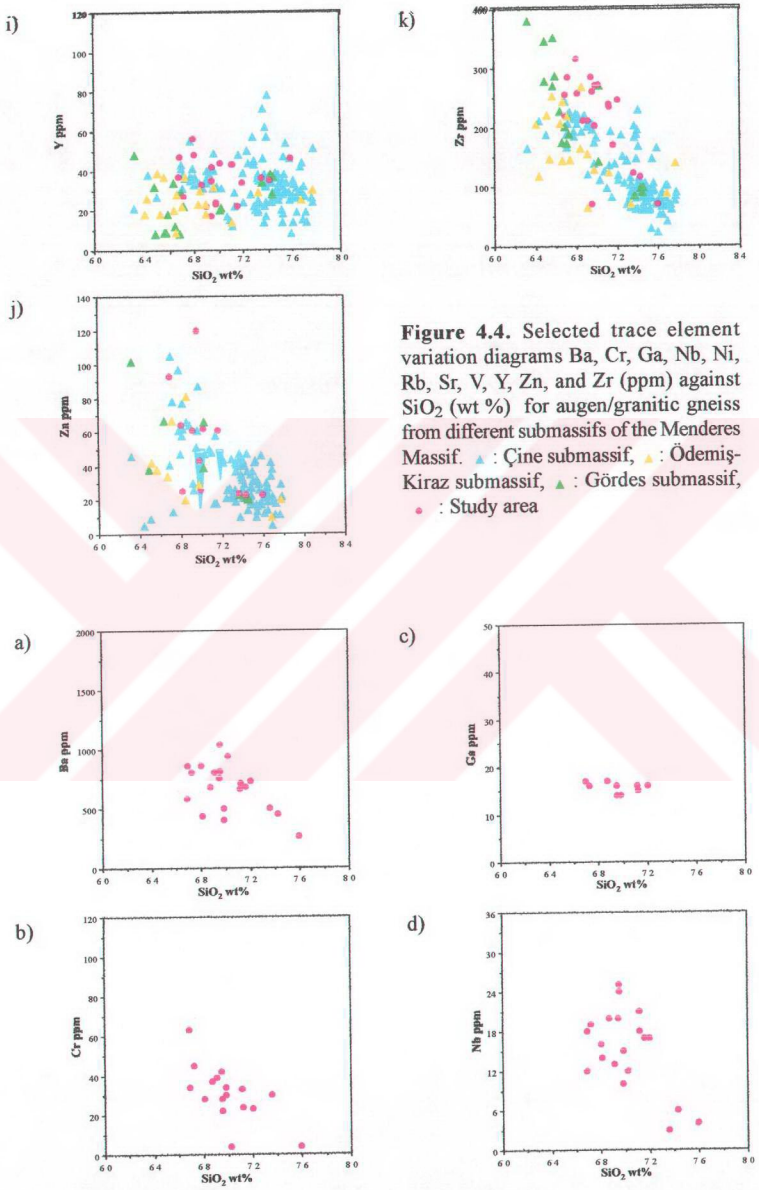


Figure 4.4. Selected trace element variation diagrams Ba, Cr, Ga, Nb, Ni, Rb, Sr, V, Y, Zn, and Zr (ppm) against SiO_2 (wt %) for augen/granitic gneiss from different submassifs of the Menderes Massif. ▲ : Çine submassif, ▲ : Ödemiş-Kiraz submassif, ▲ : Gördes submassif, ● : Study area

Figure 4.5. (Continue)

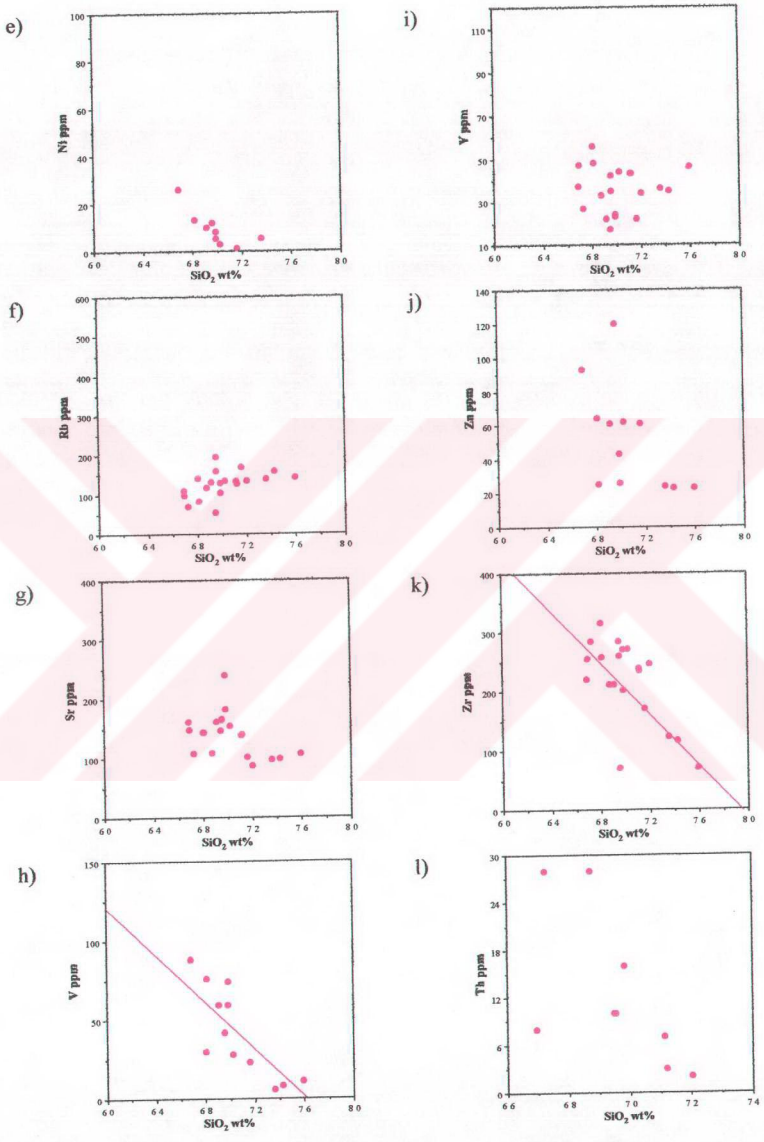


Figure 4.5. Selected trace element variation diagrams, Ba, Cr, Ga, Nb, Ni, Rb, Sr, V, Y, Zn, Zr, and Th (ppm) against SiO_2 (wt %) for augen/granitic gneiss of the study area.

4.3.2. Element Mobility

The original contents of both major and trace elements in igneous rocks may be changed substantially by element mobility during secondary alteration processes (e.g. spilitic alteration, metamorphism). Several diagrams are constructed, using combinations of elements such as Ti, Zr, Y, Nb, Ga, Ce, and Sc, to reveal both the type of alkalinity and degree of differentiation of standard magmatic rock series by Floyd and Winchester (1978). In general, these elements are regarded to be "immobile" (Cann, 1970; Field and Eliot, 1974; Winchester and Floyd, 1976, 1977; Floyd and Winchester, 1978; Winchester and Max, 1982) during the alteration and low-grade metamorphism.

The graphical comparison of major oxides versus TiO_2 may provide more reliable results to determine which of the major elements have been mobilised during metamorphism. TiO_2 versus Fe_2O_3 and MgO diagrams show positive correlation whereas, Al_2O_3 show negative correlation. On the other hand MnO, CaO, Na_2O, K_2O and P_2O_5 versus TiO_2 diagrams show scattered distribution (Figures 4.6, 4.7).

Geochemical data indicate that some high-grade rocks are severely depleted in the large incompatible elements (LIL) such as U, Th, K, Rb, and Ba (Paschier et al., 1990) during greenschist to amphibolite facies metamorphism (Condie et al., 1977; Tarney and Windley, 1977; Weaver and Tarney, 1981; Floyd and Winchester, 1983; Sheraton, 1984). Some trace elements have been plotted against TiO_2 as an immobile element. Good positive correlation is evident between TiO_2 and V. Whereas Cr, Nb, Ni, Sr, and Zr show less good or weak correlation and considerable scatter of points (Figures 4.8, 4.9). When Rb is plotted against K_2O (Figure 4.9.l), good positive correlation is evident which suggests that these elements are also immobile during metamorphism.

The trace elements, Ce, Ga, Nb, Ni, Y, Zr, seem to remain relatively "immobile" compared with other elements during secondary alteration processes such as metamorphism (Cann, 1970; Eliot, 1973; Pearce and Cann, 1973; Hermann et al., 1974; Pearce, 1975; Winchester and Floyd, 1976; Floyd and Winchester, 1978, 1983; Winchester and Max, 1982). The TiO_2-Vbinary plot (Figures 4.8, 4.9) show good correlation which suggest that only V have also remained immobile during metamorphism.

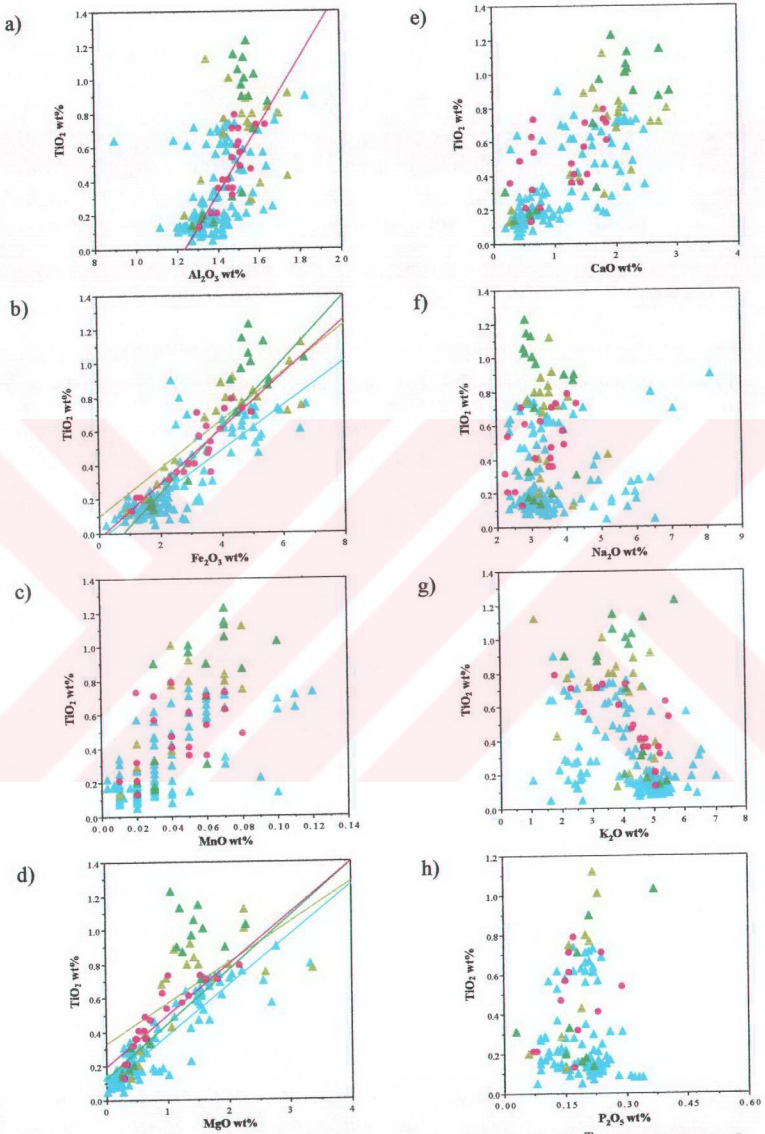


Figure 4.6. Graphical comparison of major oxides, Al_2O_3, $Fe_2O_3^T$, MgO, CaO, Na_2O, K_2O, and P_2O_5 versus TiO_2 (wt %) for augen/granitic gneiss from different submassifs of the Menderes Massif. ▲ : Çine submassif, ▲ : Ödemiş-Kiraz submassif, ▲ : Gördes submassif, ● : Study area

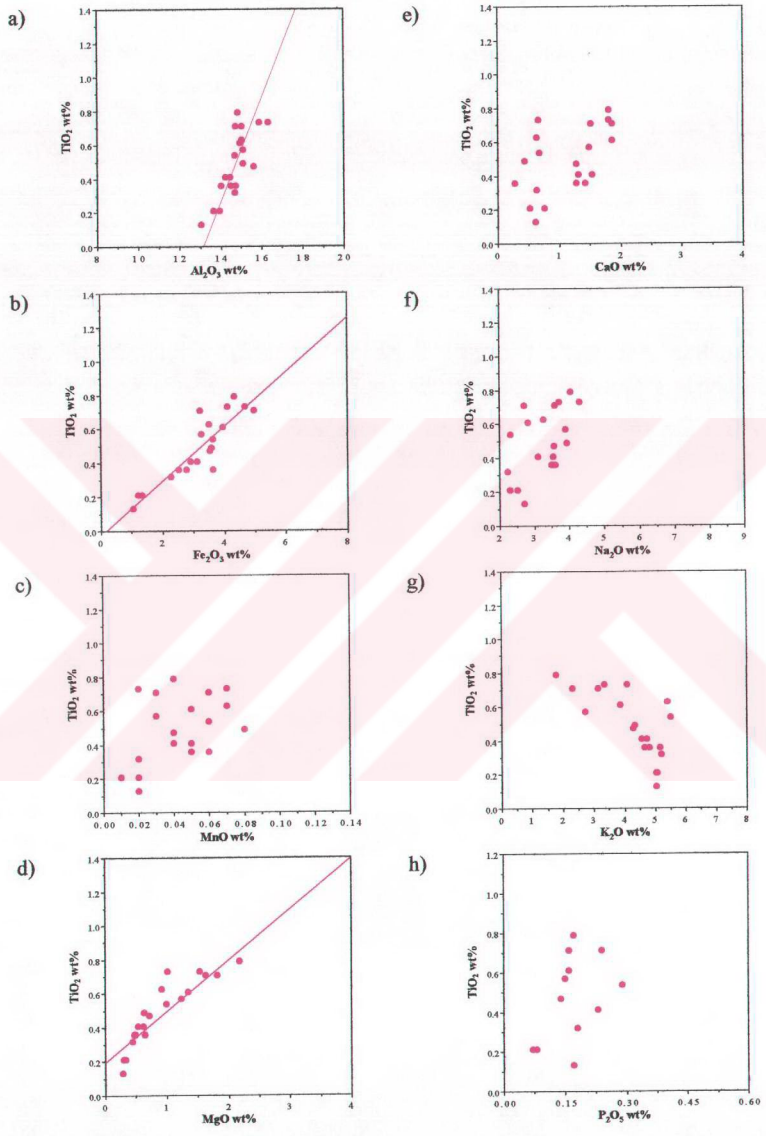


Figure 4.7. Graphical comparison of major oxides, Al_2O_3, $Fe_2O_3^T$, MgO, CaO, Na_2O, K_2O, and P_2O_5 versus TiO_2 (wt %) for augen/granitic gneiss of the study area.

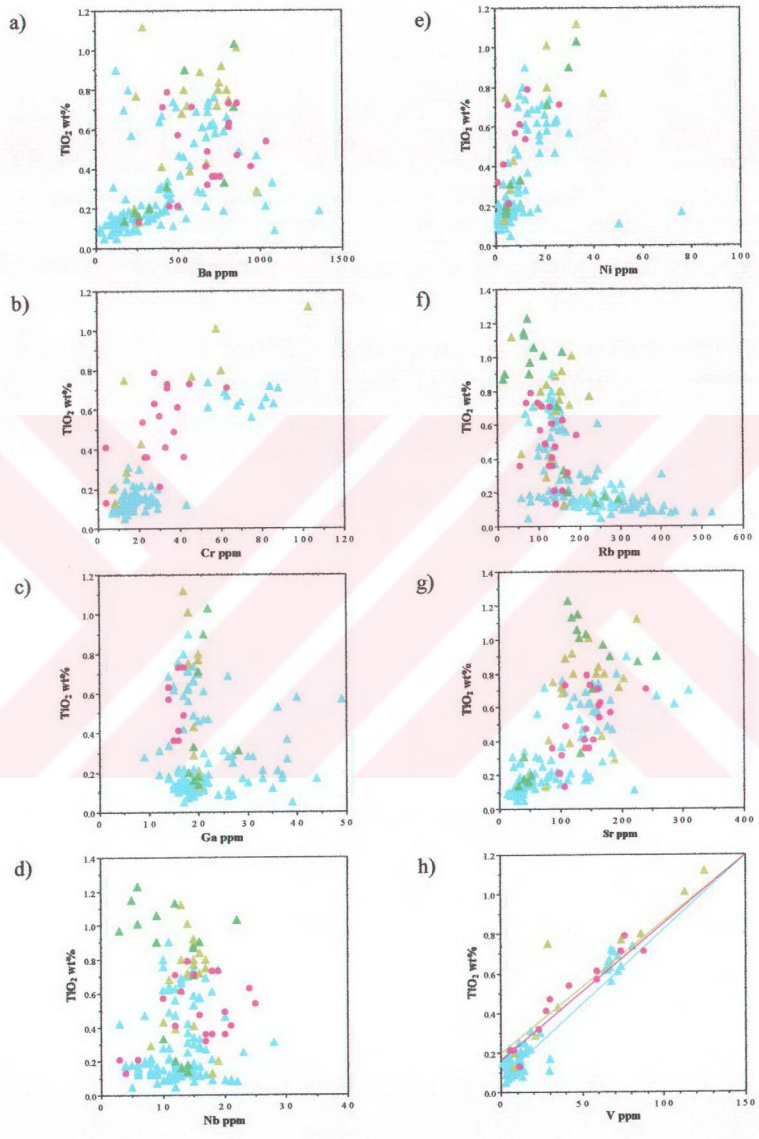


Figure 4.8. (Continue)

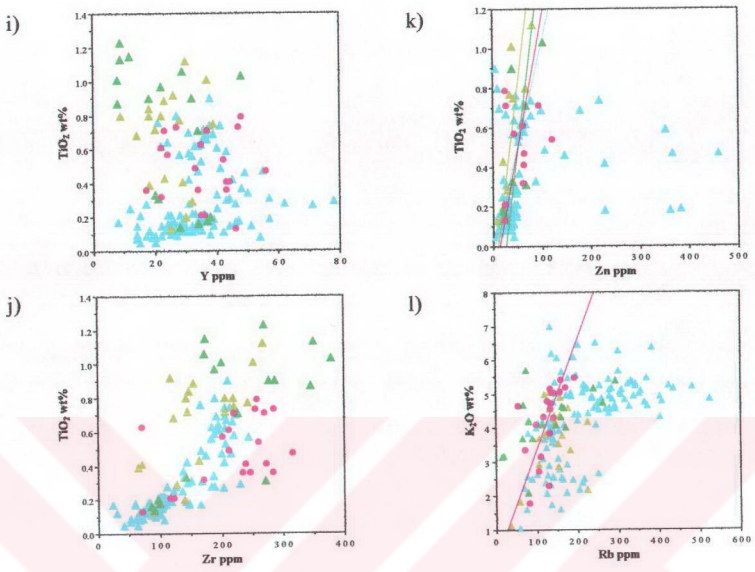


Figure 4.8. Graphical comparison of trace elements, Ba, Cr, Ga, Nb, Ni, Rb, Sr, V, Y, Zn, and Zr (ppm) versus TiO_2 (wt %) for augen/granitic gneisses from different submassifs of the Menderes Massif. ▲ : Çine submassif, ▲ : Ödemiş-Kiraz submassif, ▲ : Gördes submassif, ● : Study area

4.3.3. Protoliths of augen/granitic gneisses

Many researchers have especially debated the origins of augen/granitic gneisses, which form one of the common rock types of basement series in the metamorphic sequence. Some researchers suggest that the protoliths of the gneisses are of sedimentary in-origin and their gneissic texture results from high-grade metamorphism (see Chapter 3.2). However, especially in recent studies, the great majority of the authors suggest that protoliths of augen/granitic gneisses are of igneous origin and have a granitic composition.

Although, the field relationships provide strong supports for the granitic origin of the augen/granitic gneisses. The chemical analyses of the samples were plotted on several discrimination diagrams to reveal the origin of the rocks. Analysis of augen/granitic gneisses on the Na_2O/Al_2O_3 against K_2O/Al_2O_3 diagram suggested for the discrimination of sedimentary and igneous rocks by Garrels and Mackenzie (1971) are shown in Figure

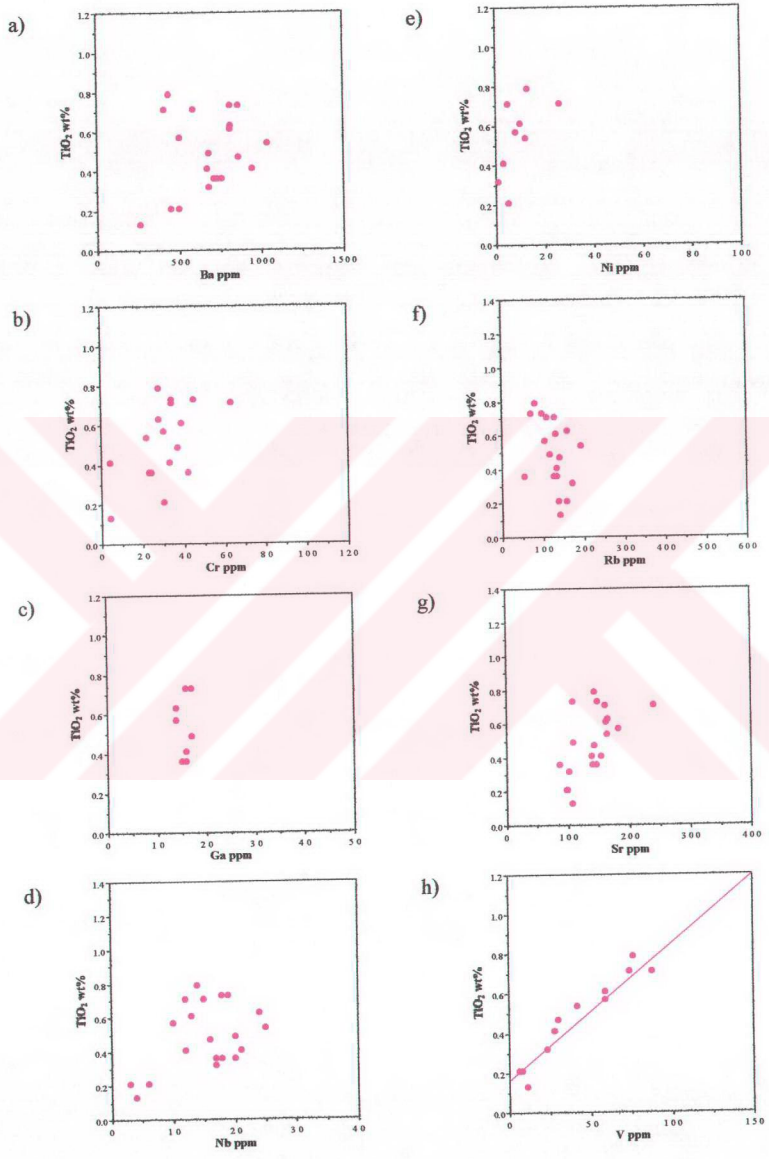


Figure 4.9. (Continue)

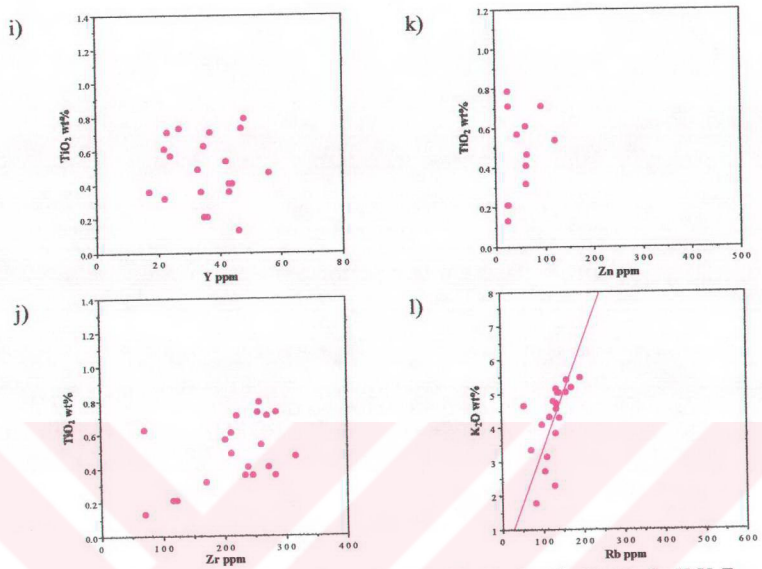


Figure 4.9. Graphical comparison of trace elements, Ba, Cr, Ga, Nb, Ni, Rb, Sr, V, Y, Zn, and Zr (ppm) versus TiO_2 (wt %)for augen/granitic gneiss of the study area

4.10.a. The great majority of the samples are concentrated within the igneous field. Similarly, most of the samples plot in the igneous field of P_2O_5/TiO_2 versus MgO/CaO after Werner (1987) (Figure 4.10.b). Also, whole samples fall within the orthogneiss field on the Al_2O_3 against MgO diagram for the discriminant of paragneiss and orthogneiss series after Marc (1992) (Figure 4.10.c). Some samples plot in sedimentary field in Figures 4.10.a and b, due to the element mobility of Na_2O, K_2O, P_2O_5 and and CaO.

4.3.4. Chemical classification

In this section it is intended to identify and classify the original igneous rocks of augen/granitic gneisses according to their normative mineral, major element and trace element compositions.

4.3.4.1. Normative classification

On the Ab-An-Or ternary diagram the great majority of the samples fall within the granite field, although one sample, which is relatively rich in albite, falls in the trondhjemite field (Figure 4.11.).

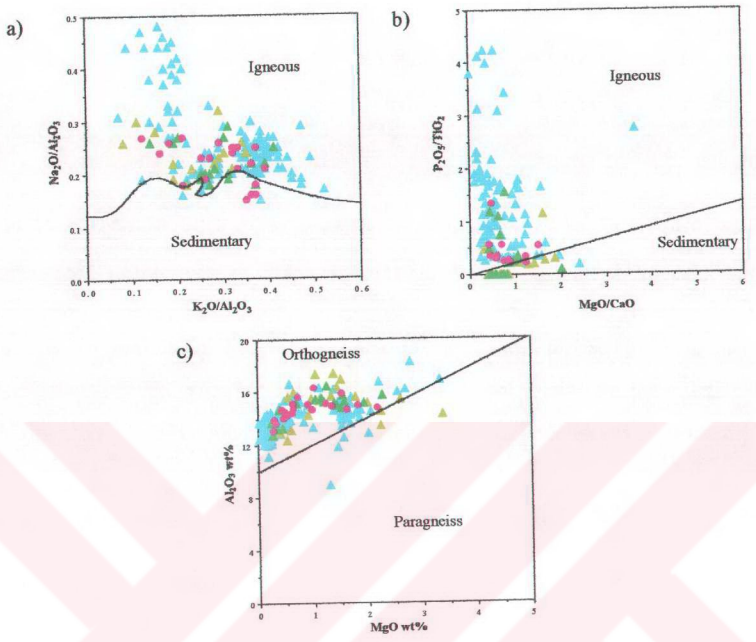


Figure 4.10. a) Na_2O/Al_2O_3 vs K_2O/Al_2O_3 (after Garrels &Mackhenzie, 1971) and b) P_2O_5/TiO_2 vs MgO/CaO (after Werner, 1987) discrimination diagrams suggesting an igneous origin for the augen/granitic gneisses of the study area. c) The samples from study area are concentrated in the orthogneiss field of the Al_2O_3 vs MgO discrimination diagram (after Marc, 1992). ▲ : Çine submassif, ▲ : Ödemiş-Kiraz submassif, ▲ : Gördes submassif, ● : Study area

4.3.4.2. Multicationic classification

Multicationic diagram after Debon and Le Fort (1983) based on the major element analysis may provides an approach to the granite classifications and interpretations. Oxide percentages are recast to milication values per 100 g (see De la Roche et al., 1980; Debon and Le Fort, 1983). In the multicationic diagram based on Q=Si/3-(K+Na+2Ca/3) versus P=K- (Na+Ca), most of gneisses from the study area plot into the granite, adamellite and granodiorite fields (Figure 4.12).

4.3.4.3. Major element classification

The chemical classification and nomenclature of plutonic rocks using the total alkalis

(Na_2O+K_2O) versus SiO_2 (TAS) diagram of Cox et al., (1979) which is adapted by Wilson (1989) for plutonic rocks. The curved solid line subdivides the alkaline and subalkaline rocks. Augen/granitic gneisses are concentrated within the granite and granodiorite fields; only two samples plotted within the alkali-granite field (Figure 4.13).

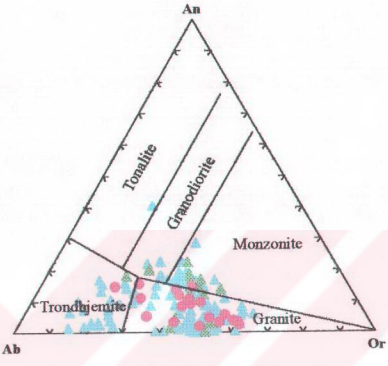


Figure 4.11. Chemical classification of the protoliths of the augen/granitic gneiss on a normative An-Ab-Or ternary diagram after Barker(1979). ▲ : Çine submassif, ▲ : Ödemiş-Kiraz submassif, ▲ : Gördes submassif, ● : Study area

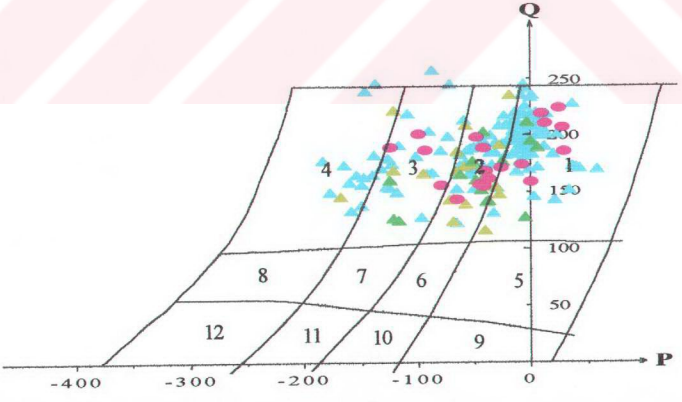


Figure 4.12. Multicationic classification of the protoliths of the augen/granitic gneiss on Q = [Si/3 - (K+Na+2Ca/3)] vs P= K-(Na+Ca), (after Debon and Le Fort, 1983). ▲ : Çine submassif, ▲ : Ödemiş-Kiraz submassif, ▲ : Gördes submassif, ● : Study area
1-Granite, 2-Adamellite, 3-Granodiorite, 4-Tonalite, 5-Syenogranite, 6-Monzogranite, 7- Monzodiorite, 8-Diorite, 9-Siyenite, 10-Monzonite, 11- Monzogabro, 12- Gabbro

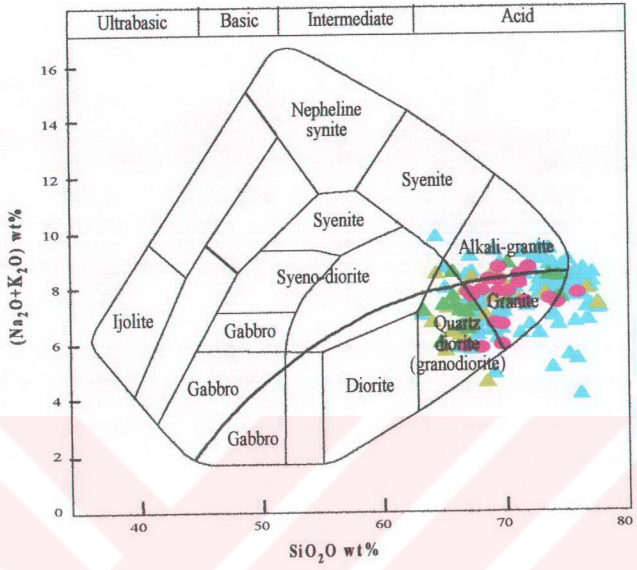


Figure 4.13. The chemical classfication and nomenclature of plutonic rocks using the total alkalis (Na_2O+K_2O) versus SiO_2 (TAS) diagram after Cox et al., (1979) adapted by Wilson (1989) for plutonic rocks. ▲ : Çine submassif, ▲ : Ödemiş-Kiraz submassif, ▲ : Gördes submassif, ● : Study area

4.3.4.4. Trace element classification

Winchester and Floyd (1977) established a chemical means of discriminating different volcanic rock types and magma series which can also be applied to metamorphosed or extensively altered rocks. In this classification, Winchester and Floyd (1977) have used minor and trace elements, such as Ti, Zr, Y, Nb, Ce, and Ga, which are generally considered to be immobile elements during metamorphism. In this section, the chemical classification scheme proposed by Winchester and Floyd (1977) has been adopted for the augen/granitic gneisses to assign a protolith rock type, using relatively immobile elements.

Samples are plotted on SiO_2 versus Nb/Y and SiO_2 versus Zr/TiO_2 diagrams (Winchester and Floyd, 1977). The majority of the samples fall within the granodiorite field; three samples which have relatively high SiO_2 content plot into the granite field (Figures 4.14.a, b).

In summary, it is apparent from the results based on the different oxides and elements which are used to determine the composition of the protoliths of the gneissic rocks that augen/granitic gneisses from the study area as well as from different part of the Menderes Massif have a granite and granodiorite compositions.

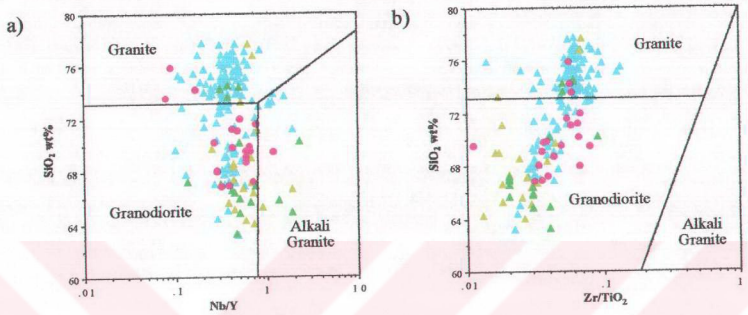


Figure 4.14. Classification of the protolith of the augen/granitic gneisses on a) SiO_2 vs Nb/Y; and b) SiO_2 vs Zr/TiO_2 binary plots (adapted from Winchester and Floyd, 1977). ▲ : Çine submassif, ▲ : Ödemiş-Kiraz submassif, ▲ : Gördes submassif, ● : Study area

4.3.5. Alkaline/Subalkaline affinity

Analyses of the augen/granitic gneisses have been plotted on a series of diagrams in order to determine the primary magmatic characteristics of rocks.

A total alkali (Na_2O+K_2O) versus silica (TAS) diagram was used for classification of volcanic rocks by Cox et al. (1979). This diagram was adapted for plutonic rocks by Wilson (1989). Samples are plotted on this diagram and great majority of the samples fall within the subalkaline field (Figure 4.15.a). Pearce and Cann (1973) have suggested that the Nb/Y ratio can be used as an index of alkalinity since rocks of alkaline affinity usually have Nb/Y ratios higher than those of tholeitic affinity. Later, Winchester and Floyd (1976) have accepted Nb/Y ratios higher than 0.67 as the discriminant value between subalkaline and alkaline basalts. Using this criterion, the augen/granitic gneisses plotted on Zr/TiO_2 versus Nb/Y diagrams (Winchester and Floyd, 1977; Floyd and Winchester, 1978) fall in the subalkaline field (Figure 4.15.b). Due to the element mobility of Na_2O, K_2O, Nb and Y some of the samples plot on alkaline field in Figure 4.15.a. b.

The K_2O versus Na_2O diagram after Middlemost (1975) used for comparative purposes shows that most of the samples fall within the high-K field, while six samples fall within the K-series field and one is Na_2O-rich (Figure 4.15.c).

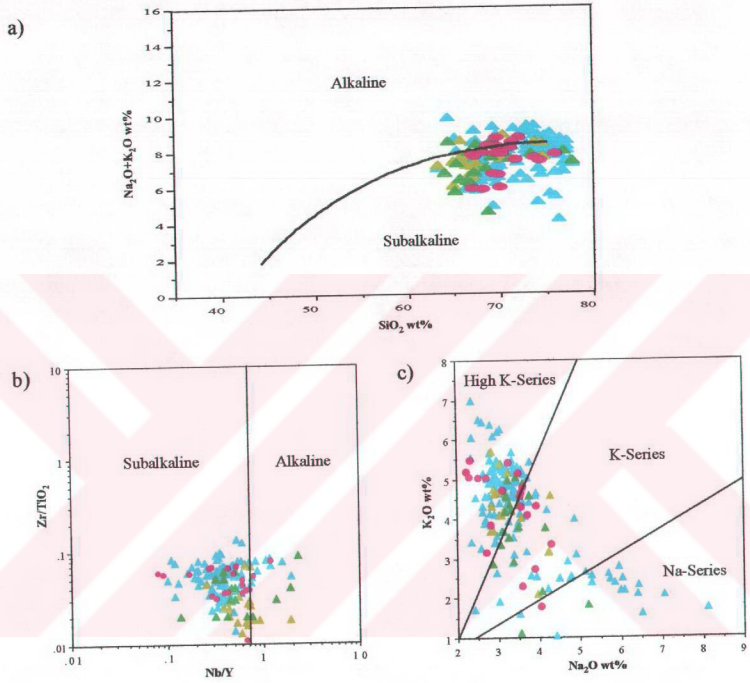


Figure 4.15. a) (Na_2O+K_2O) vs SiO_2 binary plot after Cox et al. (1979). The dividing line between alkali and subalkali granite fields is after Miyashiro (1978); b) Zr/TiO_2 vs Nb/Y binary plot after Pearce and Cann (1973), and c) K_2O vs Na_2O binary plot after Middlemost (1975) showing the subdivision of the alkaline field into high K-, K-, and Na- sub series. ▲ : Çine submassif, ▲ : Ödemiş-Kiraz submassif, ▲ : Gördes submassif, ● : Study area

4.3.6. Magmatic suite determinations

On an AFM ternary diagram with the dividing line of Kuno (1968) and Irvine and Baragar (1971) to differentiate between tholeiitic and calc-alkaline suites (Figure 4.16.a), the analyses show low Fe (Table 4.1) which characterise the calc-alkaline suite. On the

$Na_2O+K_2O-Fe_2O_3^T$-MgO ternary diagram all samples fall within the calc-alkaline series field (Figure 4.16). It has been suggested that K and Na are considerably more mobile whereas Fe and Mg remain reasonably immobile during metamorphism.

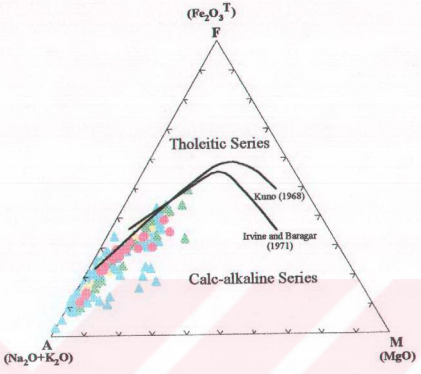


Figure 4.16. AFM ternary diagram with the dividing line after Kuno (1968) and Irvine and Baragar (1971). ▲ : Çine submassif, ▲ : Ödemiş-Kiraz submassif, ▲ : Gördes submassif, ● : Study area

4.3.7. Shand's index

An $Al_2O_3/(Na_2O+K_2O)$ versus $Al_2O_3/(CaO+Na_2O+K_2O)$ binary diagram was used to discriminate peraluminous, metaluminous and peralkaline magma series (Shand, 1943). This diagram shows that the augen/granitic gneisses are peraluminous (Figure 4.17). Since the A/CNK ratio and normative corundum for the majority of the samples are greater than 1.5 and 1.0 wt%, respectively.

4.3.8. Tectonic setting discrimination

Geochemical evidence for the tectonic setting of the augen/granitic gneisses relies on several major and trace element discrimination diagrams (Pearce et al., 1984; Harris et al., 1986; Maniar and Piccoli, 1989).

The development and application of trace elements to discriminate between the tectonic settings of granitoid rocks was pioneered by Pearce et al., (1984) with various discriminant diagrams for granitoid rocks with a modal quartz greater than 5.0 wt%.

T.C. YÜKSEKÖĞRETİM KURULU
DOKÜMANTASYON MERKEZİ

The discrimination in these diagrams is between four main groups according to their intrusive settings: ocean-ridge granites (ORG), volcanic-arc granites (VAG), within-plate granites (WPG), and collision granites (COLG). They have also further subdivided the granites within each group according to their precise settings and petrological characteristics where possible.

The chemical data were plotted on the SiO_2 variation diagrams for Y, Nb, and Rb, devised by Pearce et al., (1984). The majority of the samples fall within the VAG+COLG+ORG field on the Y versus SiO_2 diagram and Nb versus SiO_2 diagram (Figures 4.18.a, b). The augen/granitic gneiss samples classify as syn-COLG granites on the Rb against SiO_2 discriminant plot (Figure 4.18.c). Some exceptions (seven samples) may reflect Rb mobility during metamorphism.

On the Nb versus Y discrimination diagram (Pearce et al. 1984) the samples plot within the VAG+syn-COLG field with seven exceptions plotting in the WPG field (Figure 4.18.d). The samples scatter in the diagram Rb against Y+Nb near the VAG-WPG-syn-COLG triple point characterising the post-collision granites which are the most difficult to classify by geochemical constrains (Pearce 1996) (Figure 4.18.e).

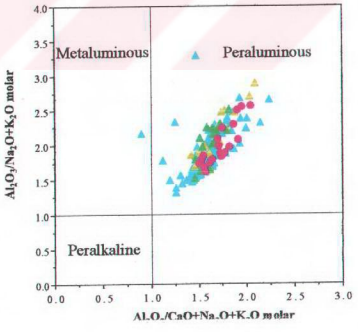


Figure 4.17. Shand's index. $Al_2O_3/(Na_2O+K_2O)$ vs $Al_2O_3/(CaO+Na_2O+K_2O)$ binary plot for the granitic protolith after Maniar and Piccoli (1989). ▲ : Çine submassif, ▲ :Ödemiş-Kiraz submassif, ▲ : Gördes submassif, ● : Study area

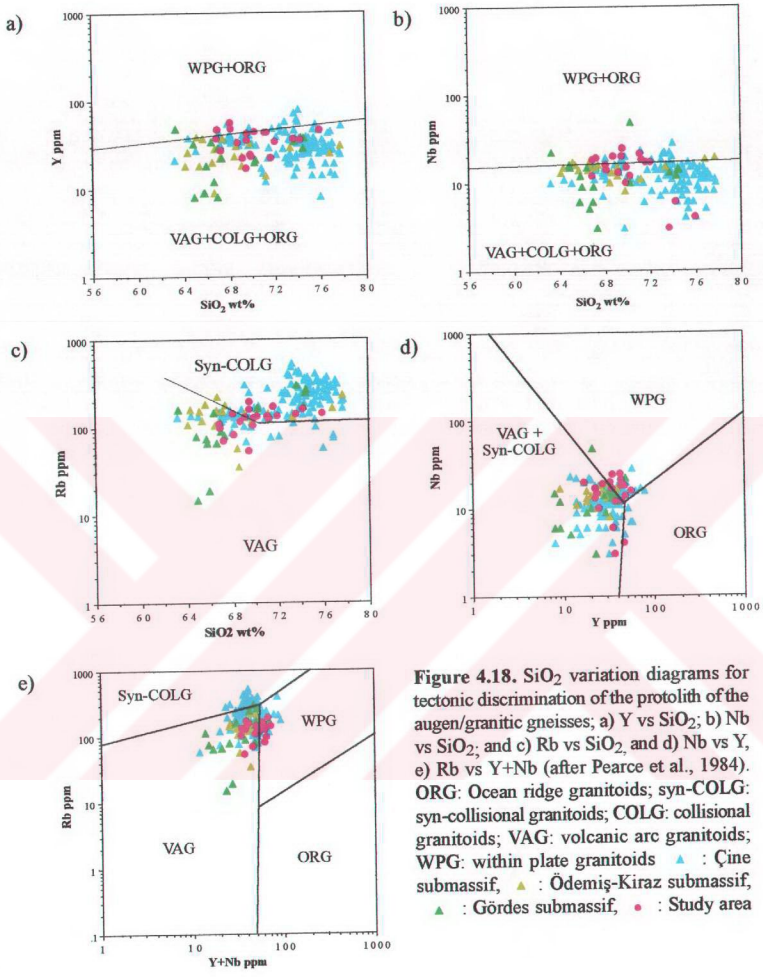


Figure 4.18. SiO_2 variation diagrams for tectonic discrimination of the protolith of the augen/granitic gneisses; a) Y vs SiO_2; b) Nb vs SiO_2; and c) Rb vs SiO_2, and d) Nb vs Y, e) Rb vs Y+Nb (after Pearce et al., 1984). **ORG**: Ocean ridge granitoids; syn-**COLG**: syn-collisional granitoids; **COLG**: collisional granitoids; **VAG**: volcanic arc granitoids; **WPG**: within plate granitoids ▲ : Çine submassif, ▲ : Ödemiş-Kiraz submassif, ▲ : Gördes submassif, ● : Study area

4.3.9. S-type affinity

The augen/granitic gneiss analyses, plotted in terms of normative corundum and molar $Al_2O_3/(CaO+Na_2O+K_2O)$, fall in the S-type field (Figure 4.19.a) (Chappell and White, 1974). Similarly, the analysis, which are plotted on the $Al_2O_3/(CaO+Na_2O+K_2O)$ versus $Fe_2O_3^T$ diagrams, fall within the S-type granites field (Figure 4.19.b) (Marc 1992).

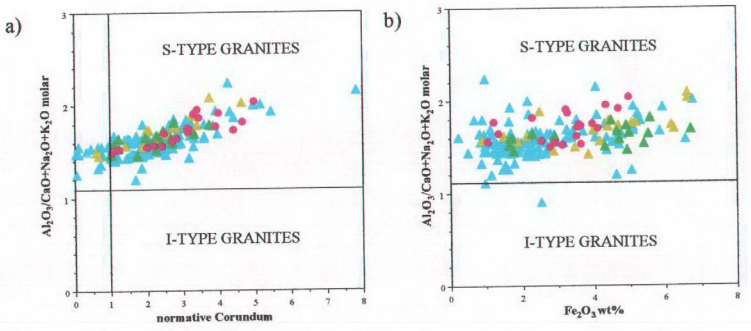


Figure 4.19. Geochemical classification of the granitic protolith on a) a normative corundum vs molar A/CNK binary plot (field boundaries are from Chappel and White (1974) and b) molar A/CNK vs $Fe_2O_3^T$ (after Marc, 1992). ▲ : Çine submassif, ▲ : Ödemiş-Kiraz submassif, ▲ : Gördes submassif, • : Study area

4.4. Geochemistry of leucocratic orthogneisses

4.4.1. Whole rock analyses

4.4.1.1. Major elements

The major elements of TiO_2, Al_2O_3, Fe_2O_3, MgO, CaO, Na_2O, K_2O and P_2O_5 are plotted against SiO_2 for all samples of the study area. Leucocratic orthogneisses of the study area characteristically have very high SiO_2 contents ranging from 71 to 84 wt% (Table 4.2). Major element distinctions among type 1, type 2 and type 3 leucocratic orthogneisses are subtle. Most of the elements show a scattered distribution with SiO_2, in Harker (1909) variation diagrams. Only K_2O show poor negative correlation with partly scatter (Figure 4.21.g). Type 2 of leucocratic orthogneiss samples shows distinct positive correlation between K_2O and SiO_2 (Figure 4.21.g). Other elements do not show any correlation. Type 2 and type 3 leucocratic orthogneisses have higher Fe_2O_3 content than type 1 of leucocratic orthogneisses (Figure 4.21.c), due to their higher biotite and iron oxide (magnetite) content. Also, they have lower P_2O_5 content than type 1 of leucocratic orthogneiss (Figure 4.21.h).

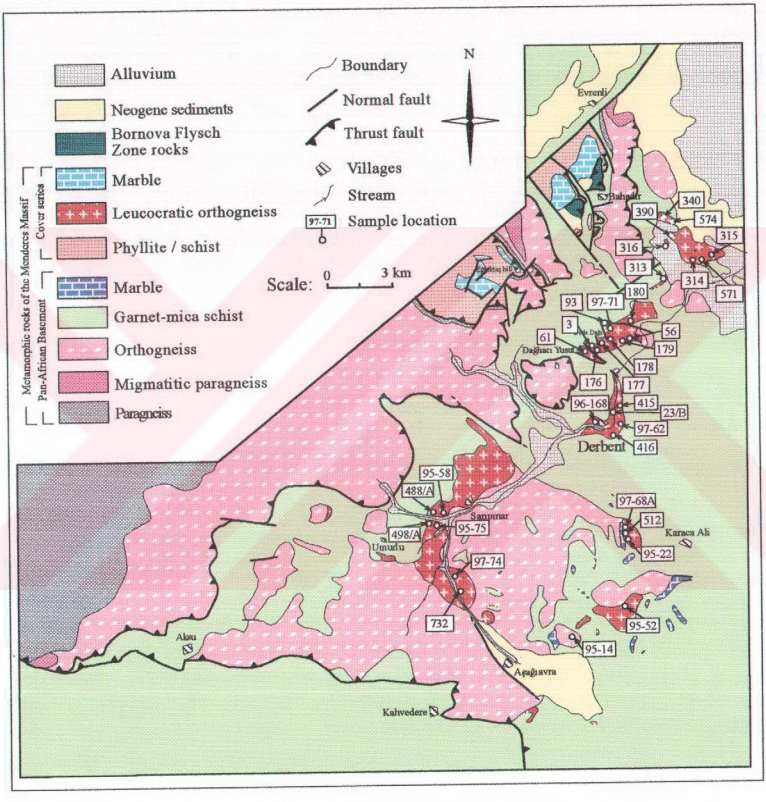


Figure 4.20.a. Sample location map for geochemical analysis of the leucocratic orthogneisses, south of Alaşehir/Manisa.

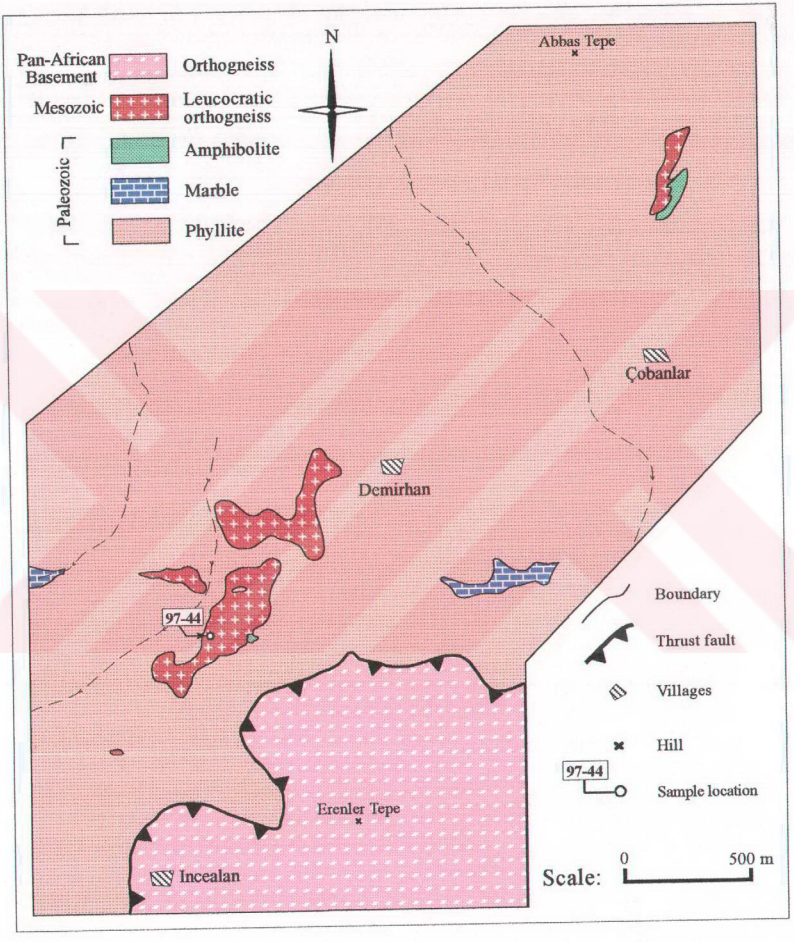


Figure 4.20.b. Sample location map for geochemical analyses of the leucocratic orthogneiss, northeast of Atça/Aydın.

Table 4.2. Chemical and normative data for leucocratic orthogneisses, na:not analysed) • muscovite±biotite leucocratic orthogneiss, ■ magnetite ± biotite±muscovite leucocratic orthogneiss, ▲ biotite leucocratic orthogneiss, continue,

SAMPLE	3	23/B	56	61	93	176	177	178	179	180	313	314	315	316	340	390	415	416
	•	•	•	•	•	•	•	•	•	•	•	•	•	•	•	•	•	•
Major Oxides (wt %)																		
SiO_2	77.09	77.43	77.09	76.15	75.79	77.27	77.34	77.16	76.15	76.86	82.54	77.87	83.77	78.53	78.98	79.09	75.76	76.32
TiO_2	0.16	0.18	0.14	0.18	0.25	0.12	0.11	0.13	0.11	0.12	0.08	0.22	0.03	0.03	0.08	0.13	0.21	0.19
Al_2O_3	12.35	13.73	12.35	13.48	14.14	12.70	12.79	12.74	11.65	12.69	10.36	12.50	9.63	13.64	12.66	12.19	13.29	13.58
Fe_2O_3	0.19	1.15	0.13	0.62	0.51	0.43	0.66	0.63	0.49	0.75	1.46	1.22	0.42	0.11	0.11	0.60	1.30	1.13
MnO	0.01	0.01	0.01	0.01	0.00	0.00	0.00	0.00	0.01	0.00	0.01	0.01	0.01	0.01	0.00	0.01	0.01	0.01
MgO	0.21	0.00	0.28	0.28	0.16	0.03	0.15	0.14	0.37	0.11	0.00	0.00	0.00	0.00	0.00	0.00	0.01	0.18
CaO	0.04	0.31	0.04	0.04	0.03	0.06	0.04	0.04	0.04	0.05	0.05	0.30	0.00	0.54	0.05	0.54	0.04	0.05
Na_2O	2.43	0.62	0.28	0.33	0.00	2.06	0.97	1.00	1.43	1.04	0.10	0.19	0.15	0.19	0.24	0.19	0.30	0.00
K_2O	5.49	5.74	5.32	5.87	5.78	5.17	5.68	5.60	5.67	6.05	3.67	4.81	3.36	4.27	4.60	4.47	6.38	5.90
P_2O_5	na	na	na	na	0.04	0.03	0.05	0.03	na	0.04	na	na	na	na	na	na	0.04	0.04
LOI	1.44	0.58	2.81	2.85	2.69	1.41	1.88	1.86	1.51	1.56	1.69	2.22	1.43	2.46	2.56	2.25	1.67	2.12
Total	99.41	99.75	98.45	99.81	99.39	99.27	99.67	99.32	97.43	99.26	99.96	99.34	98.80	99.78	99.28	99.47	99.01	99.53
Trace Elements (ppm)																		
Ba	na	na	na	na	324	136	200	184	na	220	na	na	na	na	na	na	586	436
Cr	na	na	na	na	0	0	0	0	na	0	na	na	na	na	na	na	0	70
Ga	na	na	na	na	na	na	na	na	na	na	na	na	na	na	na	na	na	na
Nb	10	38	15	10	20	32	34	34	16	34	14	14	13	17	13	10	46	48
Ni	na	na	na	na	na	3	0	2	na	3	na	na	na	na	na	na	2	0
Rb	184	147	146	167	202	152	206	198	193	212	117	203	121	129	148	197	217	194
Sr	0	0	0	16	48	50	61	59	0	52	0	0	0	0	0	0	58	42
Th	na	na	na	na	na	na	na	na	na	na	na	na	na	na	na	na	na	na
V	na	na	na	na	8	6	5	6	na	5	na	na	na	na	na	na	6	7
Y	70	98	70	58	33	22	24	23	60	22	63	73	60	73	67	67	32	35
Zn	na	na	na	na	14	12	24	22	na	21	na	na	na	na	na	na	40	23
Zr	39	147	66	83	170	128	140	138	60	135	44	98	29	44	52	38	264	226
Ratios																		
A/NK	1.24	1.89	1.98	1.95	2.25	1.41	1.65	1.65	1.37	1.53	2.50	2.26	2.47	2.76	2.35	2.36	1.79	2.12
A/CNK	1.23	1.76	1.96	1.93	2.23	1.40	1.63	1.64	1.36	1.52	2.44	2.06	2.47	2.30	2.31	1.98	1.77	2.09
F/FMg	0.48	1.00	0.32	0.69	0.76	0.93	0.82	0.82	0.57	0.87	1.00	1.00	1.00	1.00	1.00	1.00	0.99	0.86
F/Mg	0.90	-	0.46	2.21	3.14	13.31	4.54	4.67	1.32	6.83	-	-	-	-	-	-	118.55	6.13
Mg/F	1.11	-	2.15	0.45	0.32	0.08	0.22	0.21	0.76	0.15	-	-	-	-	-	-	0.01	0.16
Mg/Ca	5.25	-	7.00	7.00	4.88	0.55	3.45	3.75	9.25	2.29	-	-	-	-	-	-	0.26	3.41
Na/Ca	60.75	2.00	7.00	8.25	-	35.47	23.07	27.67	35.75	21.63	2.00	0.63	-	0.35	4.80	0.35	6.88	-
Na/K	0.44	0.11	0.05	0.06	-	0.40	0.17	0.18	0.25	0.17	0.03	0.04	0.04	0.04	0.05	0.04	0.05	-
Nb/Y	0.14	0.39	0.21	0.17	0.61	1.45	1.42	1.48	0.27	1.55	0.22	0.19	0.22	0.23	0.19	0.15	1.44	1.37
Rb/Sr	-	-	-	10	4	3	3	3	-	4	-	-	-	-	-	-	4	5
Rb/Zr	4.72	1.00	2.21	2.01	1.19	1.19	1.47	1.43	3.22	1.57	2.66	2.07	4.17	2.93	2.85	5.18	0.82	0.86
Rb/Ba	-	-	-	-	0.62	1.12	1.03	1.08	-	0.96	-	-	-	-	-	-	0.37	0.44
K/Rb	298	390	364	351	286	340	276	283	294	285	314	237	278	331	311	227	294	304
Zr/TiO2	0.02	0.08	0.05	0.05	0.07	0.11	0.12	0.11	0.05	0.11	0.06	0.04	0.10	0.15	0.07	0.03	0.12	0.12
Selective Normative Componets																		
Q	41.55	51.19	54.6	51.64	53.44	45.43	49.77	49.75	45.49	47.52	67.81	57.71	70.04	59.93	59.87	59.72	49.63	53.45
C	2.34	5.93	6.06	6.51	7.90	3.68	5.07	5.05	3.09	4.44	6.13	6.44	5.75	7.72	7.2	6.06	5.91	7.19
Or	32.44	33.92	31.44	34.69	34.18	30.54	33.59	33.08	33.51	35.74	21.69	28.43	19.86	25.23	27.18	26.42	37.71	34.88
Ab	20.56	5.25	2.37	2.79	-	17.41	8.20	8.43	12.1	8.78	0.85	1.61	1.27	1.61	2.03	1.61	2.50	-
An	0.20	1.54	0.20	0.20	-0.06	0.12	-0.09	-0.02	0.20	-0.02	0.25	1.49	-	2.68	0.25	2.68	-0.07	-0.07
An+Ab	20.76	6.79	2.57	2.99	-0.06	17.53	8.11	8.41	12.3	8.76	1.10	3.1	1.27	4.29	2.28	4.29	2.43	-0.07
An+Or	32.64	35.46	31.64	34.89	34.12	30.66	33.5	33.06	33.71	35.72	21.94	29.92	19.86	27.91	27.43	29.1	37.64	34.81

Table 4.2. Chemical and normative data for leucocratic orthogneisses, na:not analysed) • muscovite±biotite leucocratic orthogneiss, ■ magnetite ± biotite±muscovite leucocratic orthogneiss, ▲ biotite leucocratic orthogneiss, continue,

SAMPLE	488/A	498/A	571	574	732	95-52	95-58	95-75	96-168	97-62	97-71	97-74	512	95-14	95-22	97-68/A	97-44
	•	•	•	•	•	•	•	•	•	•	•	•	■	■	■	■	▲
Major Oxides (wt %)																	
SiO_2	76.56	76.23	71.23	77.49	78.49	77.36	78.23	76.62	78.35	74.86	77.62	77.81	77.14	73.91	78.28	76.40	76.22
TiO_2	0.26	0.21	0.41	0.10	0.23	0.15	0.10	0.10	0.22	0.21	0.13	0.12	0.10	0.27	0.27	0.23	0.19
Al_2O_3	12.34	12.51	14.18	11.30	11.63	13.24	11.19	11.89	12.09	12.86	13.29	11.85	10.49	11.26	9.85	11.23	12.18
Fe_2O_3	1.23	1.19	2.21	1.25	1.27	1.53	0.98	1.48	1.11	1.39	0.60	0.72	2.80	5.54	2.85	3.06	2.15
MnO	0.00	0.01	0.03	0.01	0.01	0.02	0.01	0.02	0.01	0.02	0.00	0.00	0.01	0.01	0.01	0.00	0.01
MgO	0.27	0.10	0.56	0.09	0.14	0.16	0.12	0.12	0.25	0.15	0.00	0.01	0.01	0.07	0.10	0.01	0.00
CaO	0.02	0.05	1.51	0.03	0.05	0.00	0.02	0.04	0.02	0.67	0.03	0.06	0.00	0.00	0.00	0.03	0.02
Na_2O	2.17	3.71	3.47	2.39	0.90	0.10	2.88	2.77	0.00	2.59	0.01	2.42	3.68	4.03	2.35	2.75	3.37
K_2O	5.64	5.16	4.06	5.85	5.95	4.94	5.27	5.66	5.42	5.52	5.08	5.21	5.00	4.42	5.59	4.87	4.88
P_2O_5	na	na	na	na	0.02	na	na	na	0.04	0.04	0.02	na	na	na	na	0.01	0.00
LOI	0.99	0.57	2.08	0.64	1.04	1.90	0.62	0.68	1.56	1.18	3.04	0.95	0.16	0.41	0.40	0.72	0.71
Total	99.48	99.74	99.74	99.15	99.72	99.40	99.42	99.38	99.05	99.49	99.81	99.16	99.39	99.92	99.70	99.32	99.73
Trace Elements (ppm)																	
Ba	284	301	321	16	302	117	8	40	616	362	186	108	na	27	153	60	82
Cr	23	22	19	19	0	27	18	20	0	22	0	0	20	19	28	0	0
Ga	16	18	14	15	13	16	16	20	na	na	na	na	20	20	14	na	na
Nb	26	42	29	28	21	27	42	57	39	44	37	25	59	67	81	68	125
Ni	na	na	na	na	na	na	na	na	0	4	0	0	na	na	na	3	1
Rb	210	159	186	213	201	163	177	213	162	186	206	196	141	105	141	140	126
Sr	56	42	61	42	19	33	34	18	39	62	36	34	13	18	31	8	0
Th	10	23	47	33	17	60	18	23	na	na	na	na	21	15	27	na	na
V	na	1	3	na	10	19	na	3	8	6	8	6	na	3	na	na	6
Y	41	27	22	37	32	11	42	56	30	36	20	30	45	58	56	54	100
Zn	na	na	na	na	20	na	na	na	44	32	12	10	na	na	na	30	58
Zr	15	205	153	130	166	160	116	133	248	226	150	133	368	501	475	531	858
Ratios																	
A/CNK	1.27	1.06	1.10	1.09	1.45	2.40	1.07	1.10	2.05	1.12	2.38	1.22	0.91	0.99	0.99	1.14	1.15
A/NK	1.27	1.07	1.40	1.10	1.46	2.40	1.07	1.11	2.06	1.25	2.40	1.23	0.91	0.99	0.99	1.14	1.12
F/FMg	0.82	0.92	0.80	0.93	0.90	0.91	0.89	0.93	0.82	0.90	1.00	0.99	1.00	0.99	0.97	1.00	1.00
F/Mg	4.56	11.90	3.95	13.89	9.43	9.56	8.17	12.33	4.50	9.18	-	144.80	280.00	79.14	28.50	218.50	-
Mg/F	0.22	0.08	0.25	0.07	0.11	0.10	0.12	0.08	0.22	0.11	-	0.01	-	0.01	0.04	-	-
Mg/Ca	13.50	2.00	0.37	3.00	3.00	-	6.00	3.00	15.38	0.23		0.08	-	-	-	0.48	-
Na/Ca	108.50	74.20	2.30	79.67	20.04	-	144.00	69.25	0.00	3.88	0.42	39.72	-	-	-	94.83	177.47
Na/K	0.38	0.72	0.85	0.41	0.15	0.02	0.55	0.49	0.00	0.47	-	0.46	0.74	0.91	0.42	0.56	0.69
Nb/Y	0.63	1.58	1.30	0.76	0.66	2.44	1.00	1.01	1.30	1.22	1.85	0.83	1.32	1.17	1.45	1.26	1.25
Rb/Sr	4	4	3	5	11	5	5	12	4	3	6	6	11	6	5	18	-
Rb/Zr	13.93	0.78	1.21	1.64	1.21	1.01	1.52	1.61	0.65	0.82	1.37	1.47	0.38	0.21	0.30	0.26	0.15
Rb/Ba	0.74	0.53	0.58	13.12	0.67	1.39	23.53	5.29	0.26	0.51	1.11	1.81	-	3.88	0.92	2.33	1.54
K/Rb	268	324	219	275	296	304	299	266	334	297	246	266	354	421.76	395.89	348.14	387.54
Zr/TiO_2	0.01	0.10	0.04	0.13	0.07	0.11	0.12	0.13	0.11	0.11	0.11	0.11	0.37	0.19	0.18	0.23	0.44
Selective Normative Componets																	
Q	41.91	34.65	31.44	41.00	50.24	43.15	41.09	38.58	57.33	37.1	58.08	43.63	37.73	33.63	43.15	41.70	37.91
C	2.63	0.73	1.33	0.98	3.68	-	0.71	1.13	6.29	1.50	7.73	2.11	-	-	-	1.40	1.32
Or	33.33	30.49	23.99	34.57	35.16	33.04	31.14	33.45	32.00	32.62	30.00	30.8	29.55	26.12	33.04	28.78	28.84
Ab	18.36	31.39	29.36	20.22	7.63	19.54	24.37	23.44	-	21.94	0.09	20.5	26.12	33.31	19.54	23.27	28.52
An	0.10	0.25	7.49	0.15	0.08	-	0.10	0.20	-0.16	3.06	0.12	0.30	-	-	-	0.10	0.08
An+Ab	18.46	31.64	36.85	20.37	7.71	19.54	24.47	23.64	-0.16	25.00	0.21	20.8	26.12	33.31	19.54	23.37	28.60
An+Or	33.43	30.74	36.85	34.72	35.24	33.04	31.24	33.65	31.84	35.68	30.12	31.1	29.55	26.12	33.04	28.88	28.92

4.4.1.2. Trace elements

Trace elements of Ba, Cr, Ga, Nb, Ni, Rb, Sr, V, Y, Zn, and Zr are plotted against SiO_2 (Figure 4.22). The leucocratic orthogneisses are not show linear trend on Harker variation diagrams. Type 1 of leucocratic orthogneiss samples shows weak negative correlation between Ga and SiO_2. All of the elements show scattered distribution.

4.4.2. Element Mobility

The graphical comparison of major oxides versus TiO_2 may provide more reliable results to determine which of the major elements have been mobilised during metamorphism. All of the elements show distinct scattered distribution which suggest that these elements have been mobilised relative to TiO_2 during metamorphism (Figure 4.23).

Some trace elements have been plotted against TiO_2 as an immobile element. Poor positive correlation is evident between TiO_2 and Ba of muscovite±biotite leucocratic orthogneiss (type 1) (Figures 4.24.a). Also, magnetite±biotite± muscovite (type 2) of leucocratic orthogneiss samples show distinct positive correlation between TiO_2-Y, TiO_2-Nb, TiO_2-Zr (Figures 4.24.c, f, h).

4.4.3. Protoliths of leucocratic orthogneisses

The field relationships indicate that the leucocratic orthogneisses were derived from igneous rocks. The chemistry can also be used to provide criteria for recognising the original rock type. Different types of leucocratic orthogneiss samples were plotted on several discrimination diagrams. Samples are plotted on TiO_2 versus SiO_2 diagram for the discrimination of sedimentary and igneous series; great majority of the samples fall within the igneous field (Figure 4.25.a). On the Na_2O+K_2O versus $(K_2O/K_2O+Na_2O)*100$ discrimination diagram, samples of type 2, type 3 and four samples of type 1 fall in the "igneous spectrum" of Hughes (1972) (Figure 4.25.b). Samples falling inside the funnel shaped area have magmatic Na/K ratios; those falling to the right are metasomatic. Plots of the samples on the Al_2O_3 versus MgO diagram for the discrimination of paragneiss and orthogneiss series (Marc, 1992) are shown in Figure 4.25.c. Whole of the samples fall within the orthogneiss field.

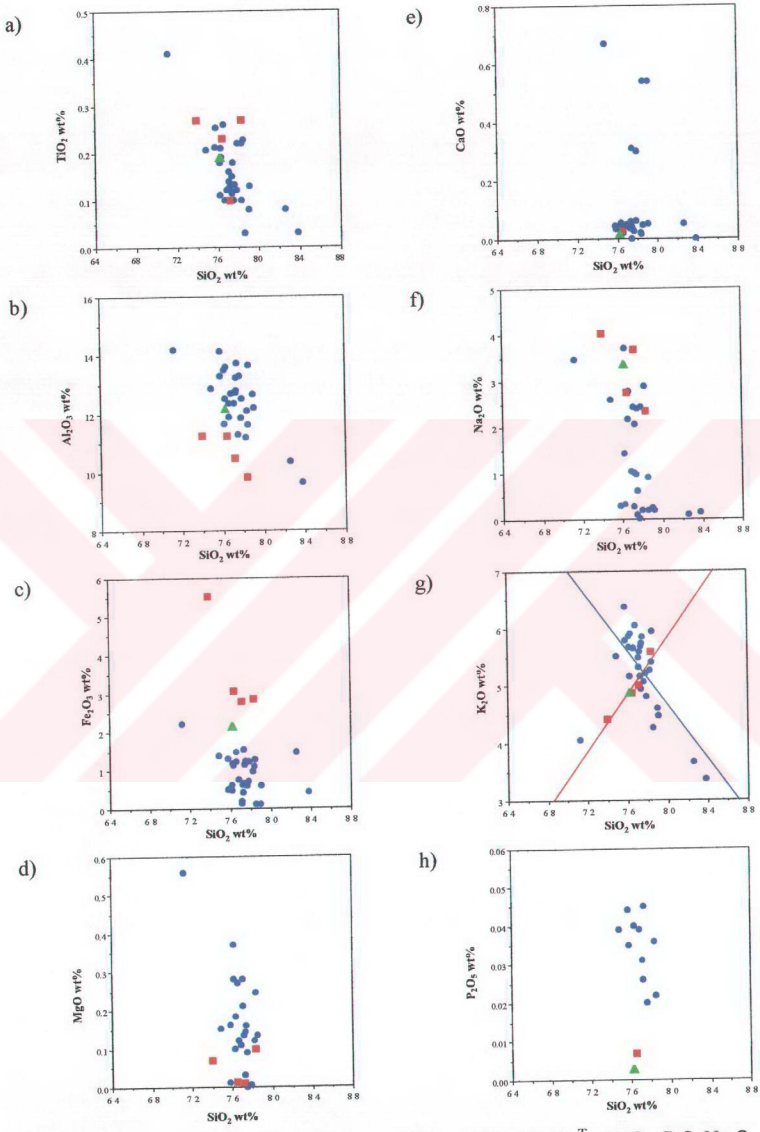


Figure 4.21. Major oxides variation diagrams of TiO_2, Al_2O_3, $Fe_2O_3^T$, MgO, CaO, Na_2O, K_2O, and P_2O_5 versus SiO_2 (wt %) for the leucocratic orthogneiss. ● muscovite±biotite leucocratic orthogneiss, ■ magnetite±biotite±muscovite leucocratic orthogneiss, ▲ biotite leucocratic orthogneiss.

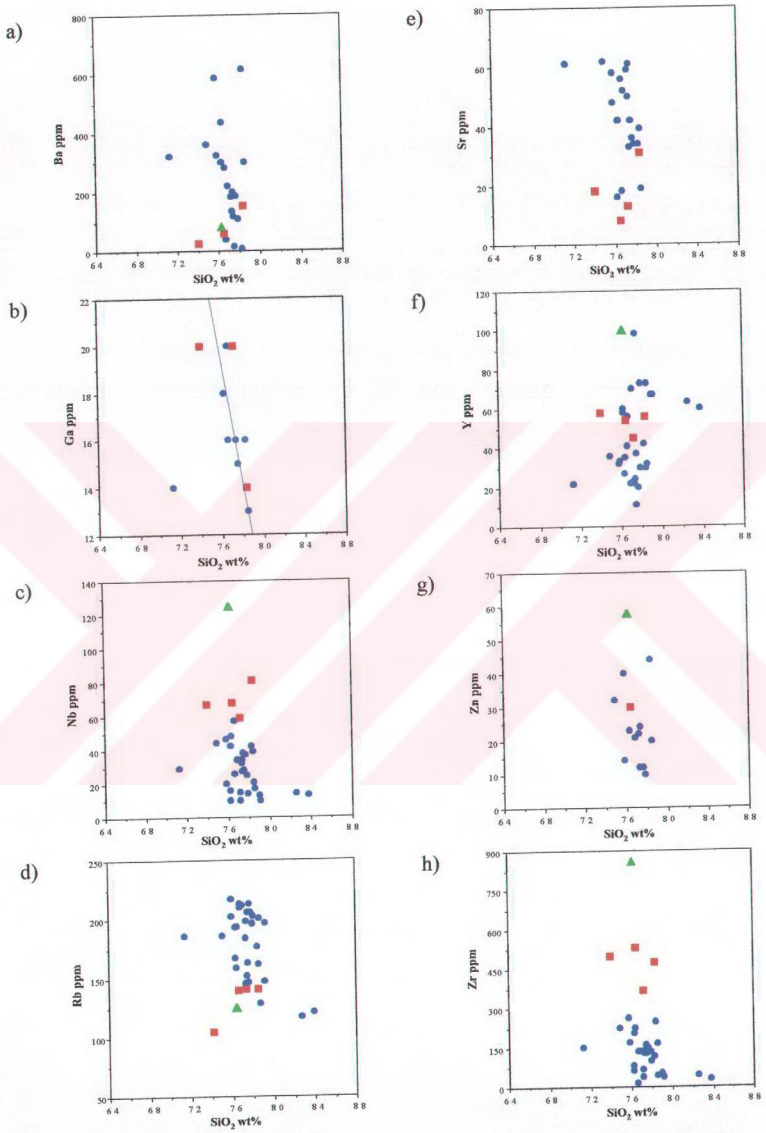


Figure 4.22. Selected trace element variation diagrams of Ba, Ga, Nb, Rb, Sr, Y, Zn and Zr (ppm) versus SiO_2 (wt %) for the leucocratic orthogneiss. • muscovite±biotite leucocratic orthogneiss, ■ magnetite±biotite±muscovite leucocratic orthogneiss, ▲ biotite leucocratic orthogneiss.

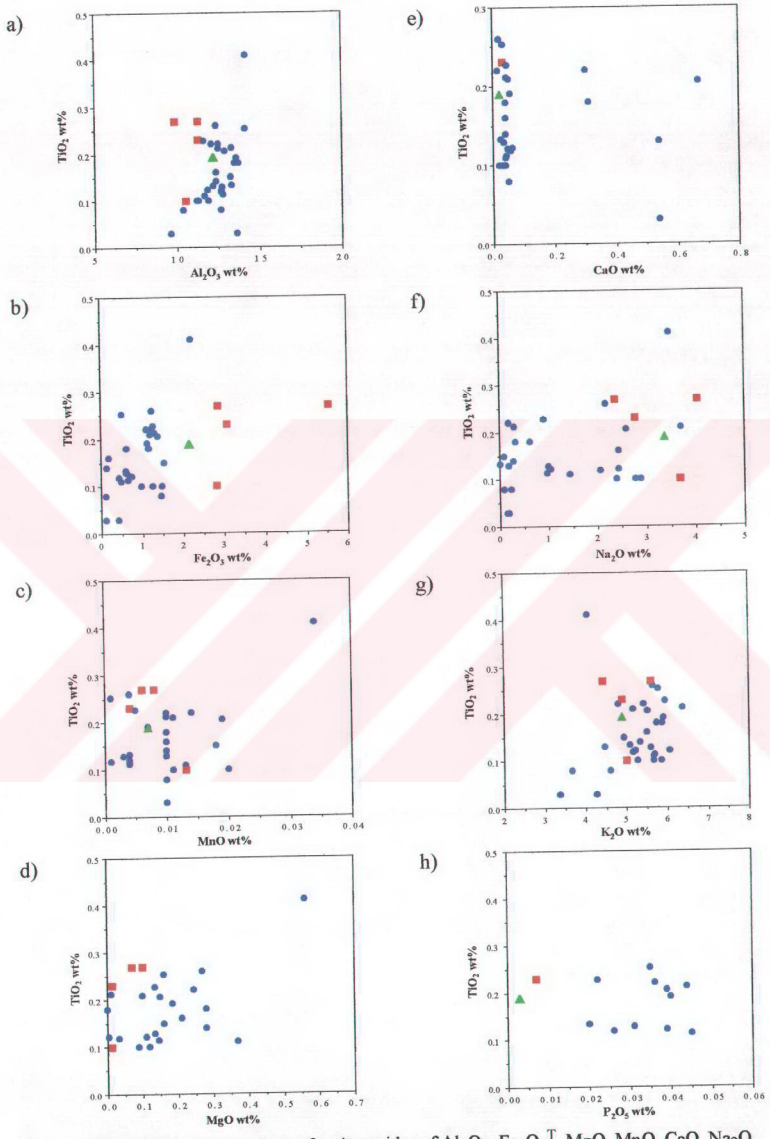


Figure 4.23. Graphical comparison of major oxides of Al_2O_3, $Fe_2O_3{}^T$, MgO, MnO, CaO, Na_2O, K_2O and P_2O_5 versus TiO_2 (wt %) for leucocratic orthogneiss. ● muscovite±biotite leucocratic orthogneiss, ■ magnetite±biotite±muscovite leucocratic orthogneiss, ▲ biotite leucocratic orthogneiss.

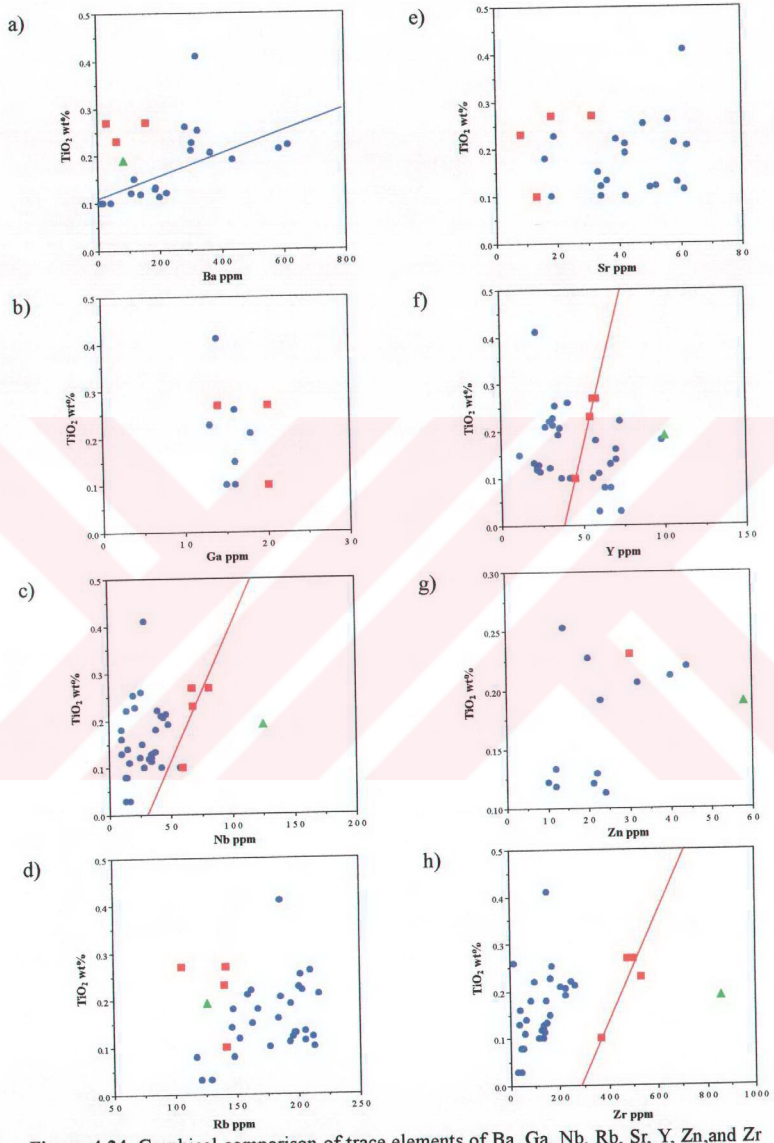


Figure 4.24. Graphical comparison of trace elements of Ba, Ga, Nb, Rb, Sr, Y, Zn,and Zr (ppm) versus TiO_2 (wt %) for leucocratic orthogneiss. • muscovite±biotite leucocratic orthogneiss, ■ magnetite±biotite±muscovite leucocratic orthogneiss, ▲ biotite leucocratic orthogneiss.

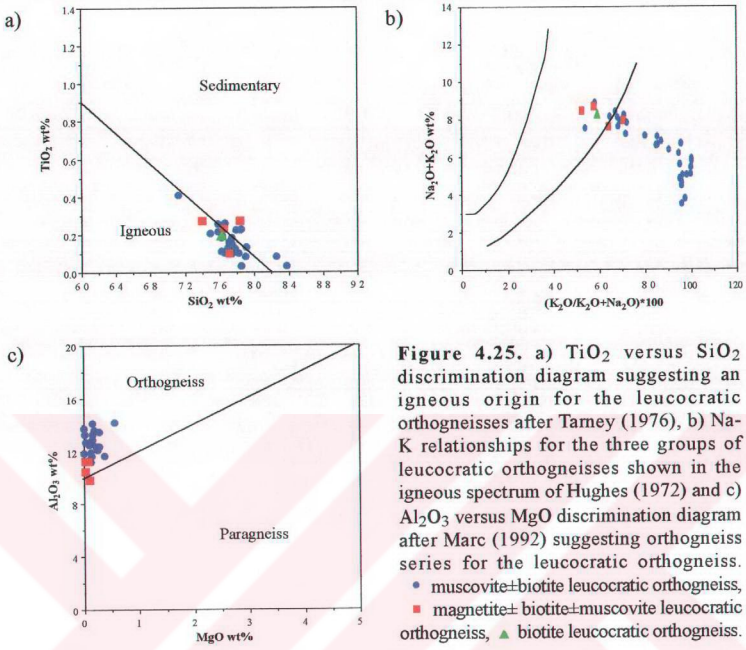


Figure 4.25. a) TiO_2 versus SiO_2 discrimination diagram suggesting an igneous origin for the leucocratic orthogneisses after Tarney (1976), b) Na-K relationships for the three groups of leucocratic orthogneisses shown in the igneous spectrum of Hughes (1972) and c) Al_2O_3 versus MgO discrimination diagram after Marc (1992) suggesting orthogneiss series for the leucocratic orthogneiss. • muscovite±biotite leucocratic orthogneiss, ■ magnetite± biotite±muscovite leucocratic orthogneiss, ▲ biotite leucocratic orthogneiss.

4.4.4. Chemical classification

In this section it is intended to identify and classify the protoliths of the leucocratic orthogneisses according to their normative mineral, major element and trace element compositions.

4.4.4.1. Normative classification

On the Ab-An-Or ternary diagram the great majority of the samples fall within the granite field, although four samples which have high Or content fall in the monzonite field (Figure 4.26).

4.4.4.2. Multicationic classification

In the multicationic diagram at Q=Si/3-(K+Na+2Ca/3) versus P=K- (Na+Ca), (Debon

and Le Fort, 1983), eight samples plot into the granite field, but only two samples fall within the adamellite field (Figure 4.27.a). Whereas, most of the samples plot on outside the diagram close to the granite field, due to the element mobility of Na and Ca.

In the "characteristic minerals" diagram of Debon and Le Fort (1982) (Figure 4.27.b), the parameters are in gram atoms x 10^3 in 100 gr of rock or mineral; A is the "aluminous index" and B is proportional to the dark mineral content (La Roche, 1964). This diagram separates peraluminous rocks or minerals with positive value of A, e.g. biotite (Bi), muscovite (Mu), from metaluminous ones, e.g. amphibole (amph), clinopyroxene (cpx). Each of its six sectors, numbered from I to VI, corresponds to a specific mineralogical composition; to a first approximation: I rocks with Mu>Bi (by volume), II=Bi>Mu, III=Bi, IV=Bi+Amph±Cpx, V=Cpx±Amph±Bi.

On the A-B diagram, most of the muscovite±biotite leucocratic orthogneiss (type 1) samples plot in the sector I (Mu>Bi), also plot in the leucogranitoids fields, and show alumino trend (Figure 4.27.b). However, magnetite±biotite±muscovite leucocratic orthogneiss (type 2) samples fall within the sector II and IV (Bi; Bi+Amph±Cpx), and

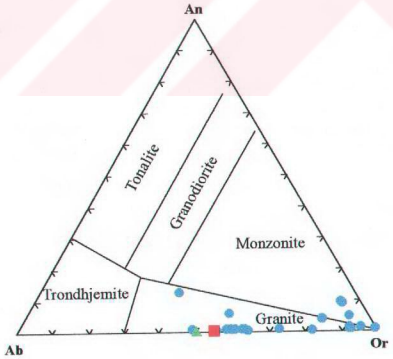


Figure 4.26. Chemical classification of the protoliths of the leucocratic orthogneiss on a normative An-Ab-Or ternary diagram after Barker (1979). • muscovite±biotite leucocratic orthogneiss, ▪ magnetite±biotite±muscovite leucocratic orthogneiss, ▲ biotite leucocratic orthogneiss.

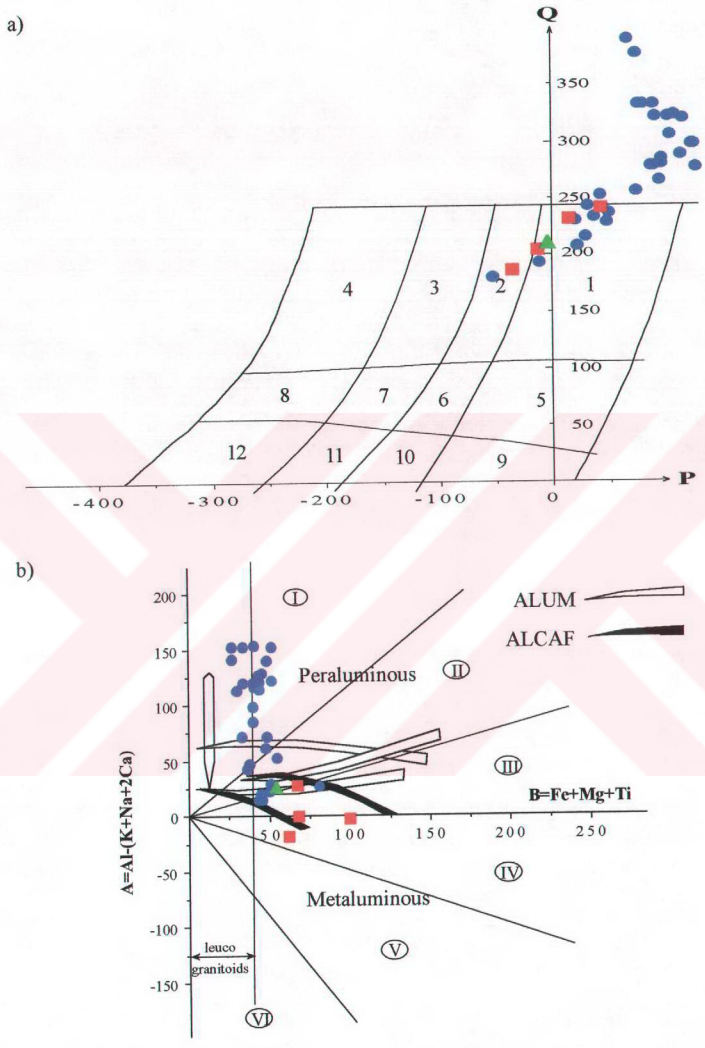


Figure 4..27. Multicationic classification of the protoliths of the leucocratic orthogneisses on a) Q = [Si/3 - (K+Na+2Ca/3)] vs P= K-(Na+Ca) and b) A=Al-(K+Na+2Ca) vs B=(Fe+Mg+Ti) after Debon and Le Fort (1983). • muscovite±biotite leucocratic orthogneiss, ■ magnetite±biotite±muscovite leucocratic orthogneiss, ▲ biotite leucocratic orthogneiss. 1- Granite, 2- Adamellite, 3- Granodiorite, 4- Tonalite, 5- Syenogranite, 6- Monzogranite, 7- Monzodiorite, 8- Diorite, 9- Siyenite, 10- Monzonite, 11- Monzogabbro, 12- Gabbro

show poor alumino-cafemic trend. Sample of type 3 falls within the sector II (Bi>Mu).

4.4.4.3. Major element classification

On the total alkalis (Na_2O+K_2O) versus SiO_2 (TAS) diagram of Cox et al., (1979) for plutonic rocks leucocratic orthogneiss samples are concentrated outside the diagram because of their high SiO_2 content (Figure 4.28). They plot close to the granite field and show a relation of decrease in total alkalis with increasing SiO_2.

4.4.4.4. Trace element classification

The geochemical data were plotted on SiO_2 versus Nb/Y and SiO_2 versus Zr/TiO_2 diagrams of Winchester and Floyd (1977). In this diagram samples fall within the granite field (Figures 4.29.a, b). In summary, it is apparent from the results that the compositions of the protoliths of the leucocratic orthogneisses are granite in composition.

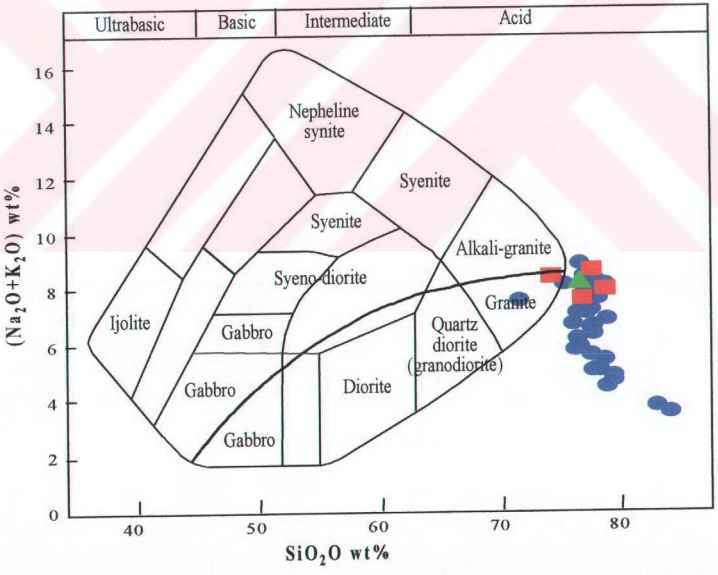


Figure 4.28. The chemical classfication and nomenclature of plutonic rocks using the total alkalis (Na_2O+K_2O) versus SiO_2 (TAS) diagram after Cox et al., (1979) adapted by Wilson (1989) for plutonic rocks. • muscovite±biotite leucocratic orthogneiss, ■ magnetite±biotite±muscovite leucocratic orthogneiss, ▲ biotite leucocratic orthogneiss.

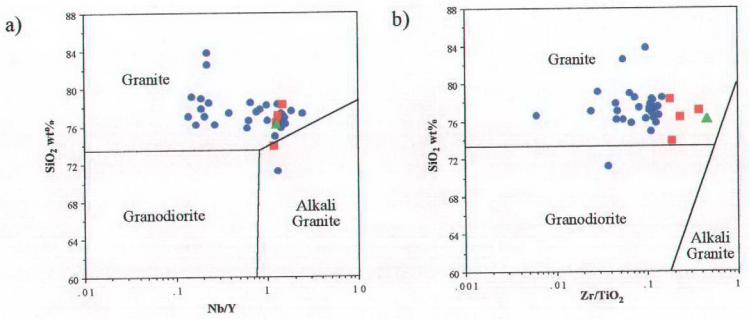


Figure 4.29. Classification of the protolith of the leucocratic orthogneisses on a) SiO_2 vs Nb/Y; and b) SiO_2 vs Zr/TiO_2 binary plots adapted from Winchester and Floyd (1977). • muscovite±biotite leucocratic orthogneiss, ■ magnetite±biotite±muscovite leucocratic orthogneiss, ▲ biotite leucocratic orthogneiss.

4.4.5. Alkaline/Subalkaline affinity

Analyses of the leucocratic orthogneisses have been plotted on diagrams in order to determine the primary magmatic characteristics of rocks. Analyses were plotted on total alkalis (Na_2O+K_2O) versus SiO_2 (TAS) diagram of Cox et al. (1979). Great majority of the samples fall within the subalkaline field (Figure 4.30.a). The same rocks are concentrated in the high-K series field on the K_2O versus Na_2O diagram of Middlemost (1975) (Figure 4.30.b).

4.4.6. Magmatic suite determinations

On the $Na_2O + K_2O - Fe_2O_3^T$ -MgO ternary diagram, all samples fall within the calc-alkaline series field according to dividing line of Irvine and Baragar (1971) (Figure 4.31). Whereas, samples of type 2 fall within the tholeitic series field according to dividing line of Kuno (1968) because of high Fe_2O_3 content of these samples.

4.4.7. Shand's index

An $Al_2O_3/(Na_2O+K_2O)$ versus $Al_2O_3/(CaO+Na_2O+K_2O)$ binary diagram was used to discriminate peraluminous, metaluminous and peralkaline magma series (Shand, 1943). It shows that the leucocratic orthogneisses are peraluminous rocks (Figure 4.32.a). On the $Al_2O_3/(CaO+Na_2O+K_2O)$ versus $(Na_2O+K_2O)/ Al_2O_3$ binary diagram all samples plot within the strongly peraluminous field (Figure 4.32.b), with the exception of two samples of type 2 which plot within the peralkaline field.

4.4.8. Tectonic setting discrimination

The geochemical data were plotted on several diagrams in order to discriminate tectonic setting of the protoliths. Most of the samples plot VAG+COLG+ORG field in the Y versus SiO_2 diagram of Pearce et al. (1984), between VAG+COLG+ORG and (Figure 4.33.a). In the Rb against SiO_2 discrimination diagram, data cluster in the syn-COLG field (Figure 4.33.b). However, in the Rb versus Y+Nb diagram, the samples are concentrated near the VAG-WPG-syn-COLG triple point which is regarded to characterise the post collisional granites, which are the most difficult to classify by geochemical constraints (Pearce, 1996) (Figure 4.33.c).

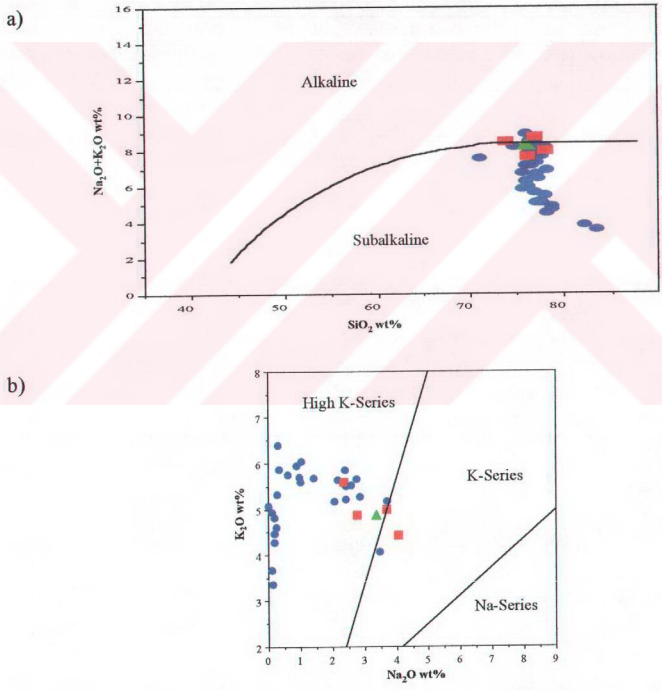


Figure 4.30. a) (Na_2O+K_2O) vs SiO_2 binary plot after Cox et al. (1979). The dividing line between alkaline and subalkaline granite fields is from Miyashiro (1978); and b) K_2O vs Na_2O binary plot after Middlemost (1975) showing the subdivision of the alkaline field into high K-, K-, and Na- sub series. ● muscovite±biotite leucocratic orthogneiss, ■ magnetite±biotite ±muscovite leucocratic orthogneiss, ▲ biotite leucocratic orthogneiss.

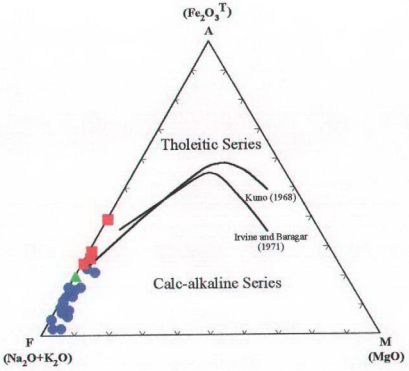


Figure 4.31. AFM ternary diagram with the dividing line of Kuno (1968) and Irvine and Baragar (1971); b) $Fe_2O_3^T$ vs Fe_2O_3/MgO,diagram after Miyashiro (1974), ● muscovite±biotite leucocratic orthogneiss, ■ magnetite±biotite±muscovite leucocratic orthogneiss, ▲ biotite leucocratic orthogneiss.

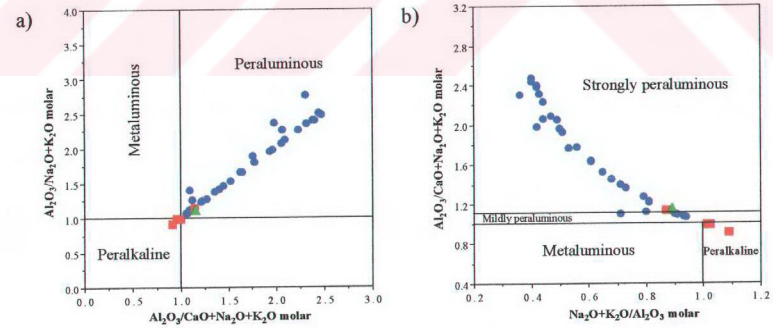


Figure 4.32. Shand's index. a) $Al_2O_3/(Na_2O+K_2O)$ vs $Al_2O_3/(CaO+Na_2O+K_2O)$ and b) $Al_2O_3/(CaO+Na_2O+K_2O)$ vs $(Na_2O+K_2O)/Al_2O_3$ binary plots for the granitic protolith of the leucocratic orthogneisses after Maniar and Piccoli (1989), ● muscovite±biotite leucocratic orthogneiss, ■ magnetite±biotite±muscovite leucocratic orthogneiss, ▲ biotite leucocratic orthogneiss.

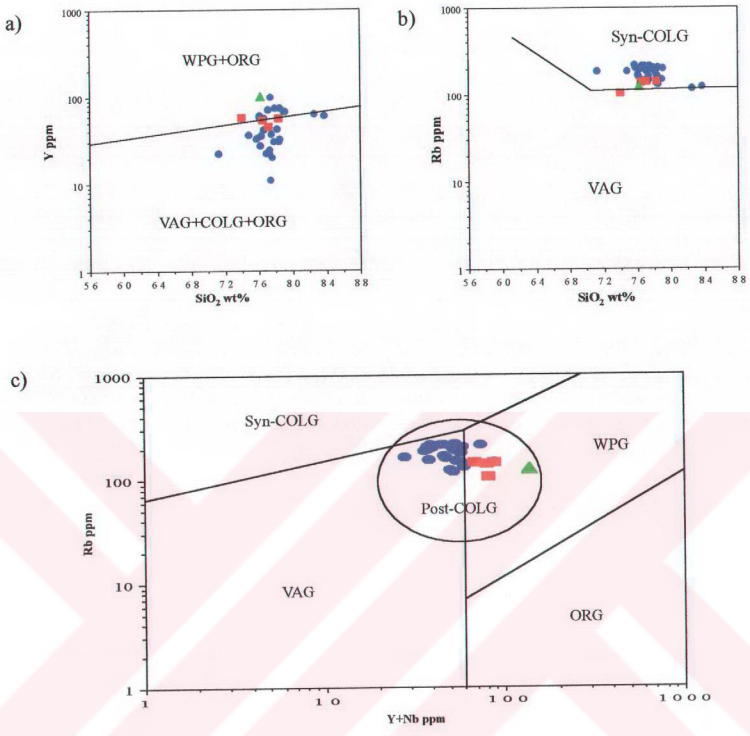


Figure 4.33. SiO_2 variation diagrams for the tectonic discrimination of the protolith of the augen/granitic gneisses; a) Y vs SiO_2 b) Rb vs SiO_2, and c) Rb vs Y+Nb after Pearce et al., (1984). ORG: Ocean ridge granitoids; syn-COLG: syn-collisional granitoids; COLG: collisional granitoids; VAG: volcanic arc granitoids; WPG: within plate granitoids. • muscovite±biotite leucocratic orthogneiss, ■ magnetite±biotite± muscovite leucocratic orthogneiss, ▲ biotite leucocratic orthogneiss.

4.4.9. S-type affinity

An S-type granite has been defined as one in which geochemical and isotopic characteristics are primarily inherited through partial melting of crustal sedimentary or metasedimentary source (Chappell and White, 1974; White and Chappell, 1977, 1983; Clemens and Wall, 1981; Clemens, 1984). In the I- and S-type granite classification of Chappell and White (1974), geochemical, mineralogical, isotopic and field characteristics

distinguish granites thought to have been derived from metasedimentary sources (S-types) and those derived from igneous source rocks (I-types).

The leucocratic orthogneiss analyses plotted in terms of molar $Al_2O_3/(CaO+Na_2O+K_2O)$ and normative corundum fall in the S-type granites field (Figure 4.34.a). The molar $Al_2O_3/(CaO+Na_2O+K_2O)$ versus $Fe_2O_3{}^T$ of Marc (1992) and molar $Al_2O_3/(CaO+Na_2O+K_2O)$ versus molar $(Na_2O+K_2O)/Al_2O_3$ diagrams of Chappell and White (1974) show that most of the samples fall within the S-type granites field (Figures 4.34.b, c). However, three samples of type 2 and type 1 fall within the I-type granites field.

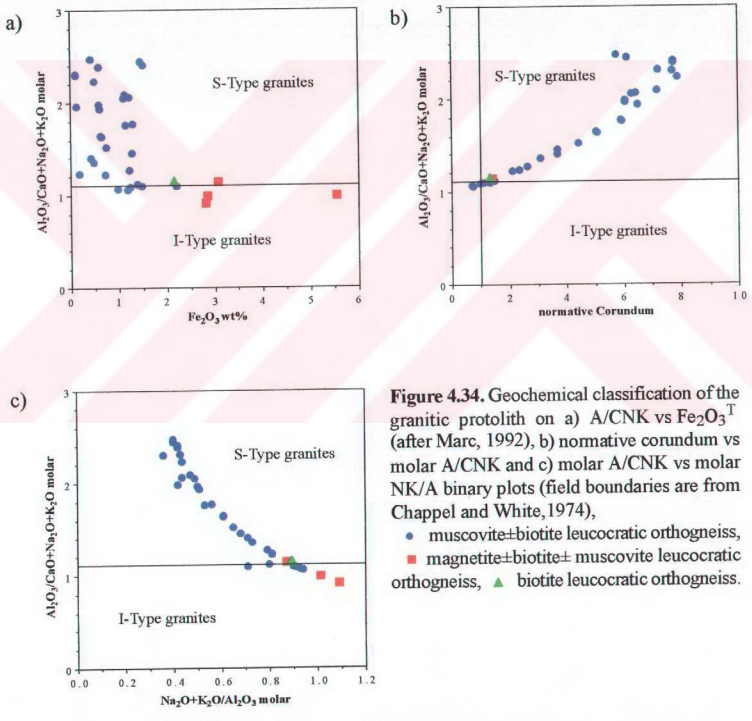


Figure 4.34. Geochemical classification of the granitic protolith on a) A/CNK vs $Fe_2O_3{}^T$ (after Marc, 1992), b) normative corundum vs molar A/CNK and c) molar A/CNK vs molar NK/A binary plots (field boundaries are from Chappel and White,1974),
• muscovite±biotite leucocratic orthogneiss,
■ magnetite±biotite± muscovite leucocratic orthogneiss, ▲ biotite leucocratic orthogneiss.

CHAPTER FIVE
GEOCHRONOLOGY

5.1. Sampling and preparation of the samples

Before sampling site and samples are selected, it must be decided whether more than one dating method should be used and whether different substances or fractions should be analyzed in order to increase the reliability of the results. The type and amount of sample depends on the method(s) to be applied. In general, rocks must be unweathered. It is advisable to select the most suitable samples for dating from a small number of "pilot" samples analyzed first. The requirements placed on the pilot samples do not necessarily have to be the same as those for the samples finally used for dating. When the results of the pilot analysis become available, the samples for the final analysis can be chosen.

After the field work, the second most important step in the dating of rocks is sample preparation (seperation of minerals and /or whole-rock preparation). An age determination can only be as good as the mineral fraction on which it is carried out: Even minute amounts of impurities increase the danger of error in the date obtained. The mineral fractions should have a purity of at least 95 %, if possible more than 99 %. Sample preparation is best done in a geochronology laboratory or at least supervised by a specialist, since it requires some experience to avoid contamination and memory effects.

A generalized scheme for the seperation of usual minerals is shown in Figure 5.1. Weathered parts are carefully removed from the fresh rock (1-30 kg), which is then broken up into pieces with a size of 5-10 mm. An aliquot is held in reserve for a whole-rock analysis. The sample is further ground to a grain size of less than about 500 μm and sieved into various grain-size fractions. To avoid contamination, it is best to use a new plastic screen for each sample for grain sizes under 150 μm. The individual grain-size fractions are seperated further on a shaking table, with high-density liquids and/or a magnetic seperator. The initial enrichment of the heavy minerals is best done on a wet shaking table; when the accessory minerals are desired, this is almost always necessary. Mica fractions must, as a final step, be ground in ethanol to remove mineral inclusions (e.g. apatite, quartz). All mineral fractions should finally be washed

in an ultrasonic bath using double-distelled water. A purity of > 99 % can be attained, almost always, only by handpicking. For the preparation the whole-rock samples, the aliquot mentioned above is divided and a split (50-100 g) is ground in an agate mortar. The pulverized rock is divided again until the aliquots have the weight necessary for each analysis.

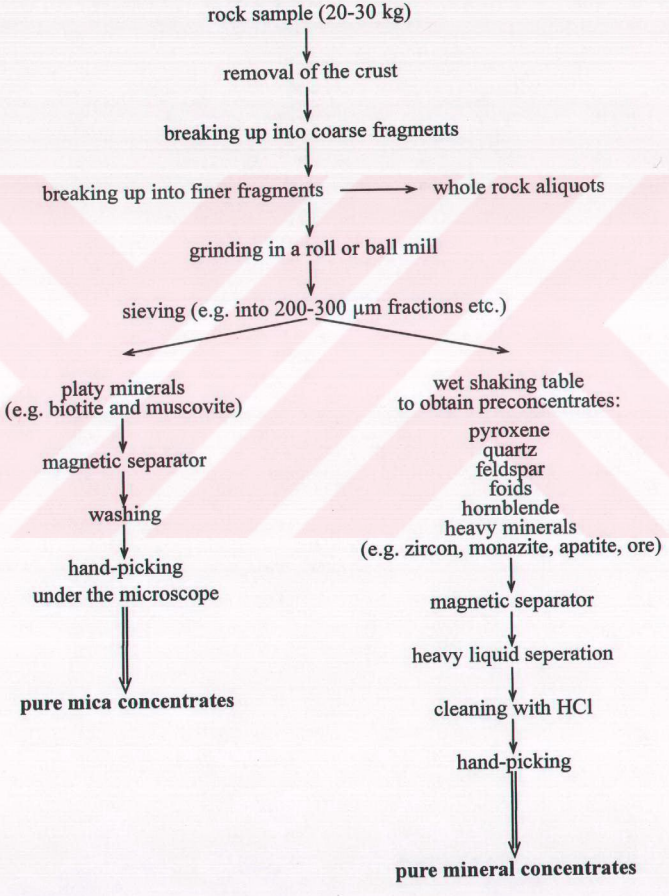


Figure 5.1. Scheme for the extraction of the common minerals from hard-rock samples.

5.2. Analytical Techniques

5.2.1. Cathodoluminescence studies of zircons

Zircon is a common accessory mineral of igneous rocks and can be easily recognized using zircon typology developed by Pupin (1980). Poldervaart (1956), in summarizing work on zircon concentrates from igneous rocks, showed that the crystallization of zircon is late in the consolidation of basaltic magma, early in dioritic or granitic magma, and may be early or late in alkaline rocks. For granitic rocks of magmatic origin, Murthy (1958) suggested that the crystallization of zircon is of short duration and is completed immediately after the emplacement of the magma from its source and prior to the crystallization of the other minerals. Considerable attention has been paid to the size and morphological characters of zircons, particularly to their length/breadth ratio, and these factors are apparently closely similar throughout a body of magmatic granite: Poldervaart (1956) postulated that lack of such a relationship may indicate that an intrusive is complex. Larsen and Poldervaart (1957) studied zircons from a magmatic batholith grading from granodiorite and tonalite and found that the zircons are uniform throughout, but are different in small bodies of granodiorite and quartz monzonite which have sharp contacts against the main batholith. They thus concluded that the batholith represents a single intrusion, which differentiated after emplacement, and that the later intrusives crystallized under different conditions. A detailed study of zircon populations from several intrusive members of the White Mountain magma series, New Hampshire, has shown that parameters such as color, single-crystal morphology, and elongation ratio vary continuously with host rock composition (Forbes, 1969); a gabbro has < 1 per cent euhedral zircons, a monzodiorite has 50 per cent euhedral, and a quartz syenite of this series has > 90 per cent of zircon population euhedral. In an autochthonous granite, Poldervaart and Eckelmann (1955) found that zircons exhibiting growth phenomena bridge the gap between the predominantly euhedral zircons of intrusive granite and the mainly rounded zircons of siliceous sediments. However, polyphase metamorphic zircons with overgrowths and evenly inherited cores (detrital cores) in zircons are often invisible under the binocular microscope (Liebetrau et al., 1995). Sharp compositional zoning in zircon is commonly observed, and is most strikingly evident in cathodoluminescence (CL) images dominated by the visible light emission from the REEs (Marfunin, 1979; Mariano, 1989; Remond et al., 1992). CL is a technique which apply to solve all internal structures of zircons, such as inherited cores, resorbed areas, magmatic zonation and inclusions, are clearly visible (Pidgeon, 1992). Both sector zoning and igneous growth or "oscillatory" zoning has been seen in various zircon populations by CL studies.

A representative split of zircons was extracted from each of the investigated gneisses. The zircons were embedded in epoxide resin with their largest prism faces oriented parallel to the surface of a mounting glass. The sample mounts were ground down and polished (Figure 5.2). The CL investigation of c-axis-parallel zircon sections was carried out on a scanning electron microscope using a 10 kV was accelerating potential. The CL detector was oriented at 30° angle towards the section plane.

The intensity of CL is related to the concentration of foreign atoms incorporated in the zircon crystal lattice (Sommerauer, 1974). Since this concentration varies during crystal growth, the CL reflects growth zoning and the boundaries between inherited cores and overgrowths, which both are not recognized under the binocular microscope.

All the CL photographs shown here made at Institute für Geologie and Paläontologie, Universität Tübingen, Germany.

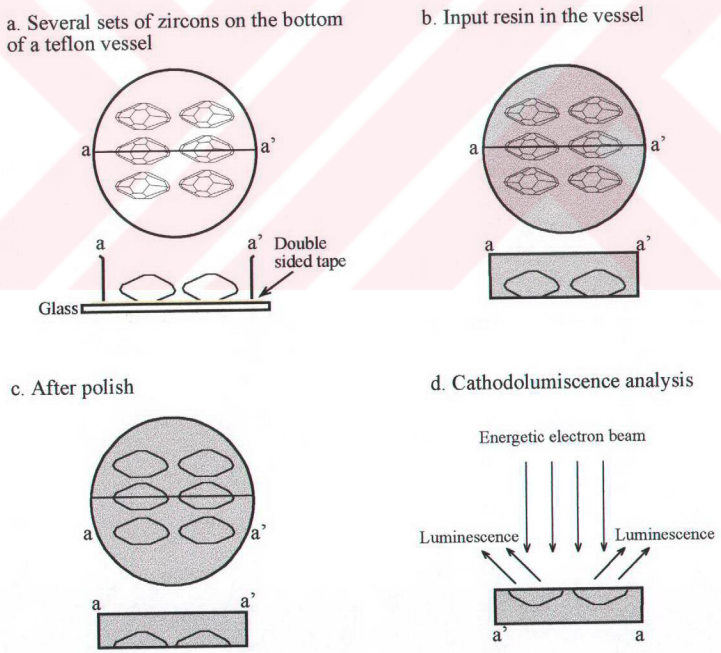


Figure 5.2. Procedure to fix zircon grains for cothodoluminescence analysis, modified after Chen (1999).

T.C. YÜKSEKÖĞRETİM KURULU DOKÜMANTASYON MERKEZİ

5.2.2. Principles of single zircon $^{207}Pb/^{206}Pb$ evaporation technique

The zircon is of great importance for investigations on the genesis, evolution, and the age of rocks. Zircons, strongly fractionating the radioactive elements U and Th from Pb during their crystallization, are widespread and prominent carriers of radioactivity. Thus they are fundemental for dating igneous and metamorphic events. The U-Pb system in zircons is very insensitive to metamorphic or tectonic events and alteration generally has no detectable effect. Geochronological determinations are made on zircons taken from a single sample, so there is no need for the existence of cogenetic relationships between different samples. For these reasons the U-Pb technique is widely used, especially for old systems. It is necessary to analyse a large number of zircons, separated into different size fractions of several milligrams each, and then dissolved in Teflon bombs. This methods was described by Krogh (1973). The analytical results were then plotted on a concordia diagram (Wetherill, 1956) to give an age. Improvement of the analytical method using magnetic seperation and air abrasion technique of the crystals yields more concordant age (Krogh, 1982a, 1982b). But they do not overcome the main disadvantage of the method. A zircon population that analysed may be mixture of zircons different ages and thus gives the mean age of the population. To avoid this problem, method of grain-by-grain zircon analysis were developed, with digestion in small Teflon bombs and very low blank levels (Lancelot et al., 1976; Bossart et al., 1986). Combination of air abrasion and single-grain dissolution can result in an accurate and precise age on a grain. But, even at this scale the zircon structure often remains complex and several crystal overgrowths may be present, or some parts of the crystal can have undergone high-level losses of radiogenic Pb. An alternative to the chemical approach is to use the sensitive high-resolution ion microprobe (SHRIMP) which developped by Hinthorne et al. (1979), Campston and Pidgeon (1986), and Campston et al. (1986). This method has the capability to date small regions within single crystals, which has been demonstrated to be especially useful for studies on zircons with complicated multi-stage magmatic and metamorphic histories. Nevertheless, the possibility of making large numbers of age determinations by this method will probally be limited by the size and cost of the equipment.

Afterwards, Kober (1986, 1987) and Kröner and Todt (1988) have developed a single zircon evaporation method using a doble Re-filament and thermal ion mass spectrometry. Single zircon evaporation method used in this study is based on the evaporation of uncrushed whole zircon grains (maximum size 300 μm). In general, dating young rocks requires the use of large zircon crystals (200-300 μm) due to the small quantities of radiogenic Pb present. The selected representative zircons are

typically 50-100 μm in width and 100-200 μm in length. Each zircon is embedded in a canoe-shaped Re-filament, known as the evaporation filament (Figure 5.3) (Kober 1986). Second, the respective grain is placed in the center of the trough, third, the rhenium metal is folded around the grain. Only a little slit remains open which faces the ionisation filament. No pretreatment of the grain before the mounting procedure is necesssary. Enveloping of the whole-grain guarantees a uniform temperature all over the crystal so that all zircon domains and all lead components are subject to equal evaporation conditions irrespective of their location within the grain. In the mass spectrometer the temperatures of both the filaments are slowly raised (ionisation filament: ~ 1930 °C, evaporation filament: ~ 1330 - ~1430 °C) until a lead ion beam on the order of 10^{-14} A is generated. A conventional multiplier is used as detector. The linearity of the amplifier system is kept under control by analyses of the NBS isotope standarts SRM 981 and SRM 983. The data is carried out by peak hopping of the scansequence 204-206-207-208-207-206. The ratio $^{204}Pb/^{206}Pb$ monitors the accessory lead components. The ratio $^{207}Pb/^{206}Pb$ derived from the average of the first and second $^{207}Pb/^{206}Pb$ ratio of each scan carries the geochronological information. The $^{208}Pb/^{206}Pb$ ratios are used for the control of fractionation trends and as an additional means for the recognition of differing radiogenic components (Kober, 1986).

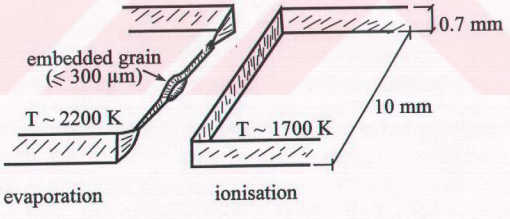


Figure 5.3. Rhenium-doble filament configuration used for Pb evaporation analysis, after Kober, (1986).

The lead ion beams generated at low to intermediate evaporation temperatures (230-1230 °C) generally turned out to be unstable and less intense. Their isotope patterns often demonstrated a rapidly varying mixture of common with radiogenic lead. The acquired data were evaluated for geochronological purposes only in the case of stable ion beams with a minimum 206/204 ratio of 5000. When a common Pb correction can be neglected.

The selected respresentative zircons were seperated at the institute für Mineralogie, Petrologie und Geochemie, Eberhard-Karls Universität, Tübingen, using standard procedures, including crushing, sieving, wilfley table, heavy liquids, electromagnetic seperation, and hand-picking using a binocular microscope. Only zircons without visible inclusions and with well-preserved crystal faces were selected and only non-magnetic zircons were evaporated as these are usually less discordant than the others (Krogh 1982a), and, therefore yield more accurate ages. The zircons typically were about 150 μm in width and 400 μm in length. Isotope measurements were carried out on a Finnigan MAT 262 mass spectrometer at University of Tübingen. The zircons were dated via the single zircon evaporation technique that measures the $^{207}Pb/^{206}Pb$ of evaporated crystals using a double Re-filament configuration. The principles of this method are described in Kober (1986, 1987), Kröner and Todt (1988) and Cocherie et al. (1992). Before use all the Re-filaments were outgassed in a bake-out device for 30 minute, using 5-A (0.7 mm-wide Re-filaments) and 6-A (1 mm filaments) currents. The outgassing took place at a pressure close to 10^{-10} bar. One or more chemically untreated zircon grains were embedded in a 0.7 mm-wide canoe-shaped Re-filament, known as the evaporation filament (Kober, 1986), and first heated to evaporate Pb components with low activation energies. Evaporation filament was placed as close as possible in front of a second 1 mm-wide Re ionization filament. Data collection started at 1430 °C, and the temperature was stepwisely increased by ca. 20 to 30 °C after each evaporation – deposition cycle. The measurement of the isotopic abundance was performed in a dynamic mode with a mass sequence 206-207-204-206-207 or 206-207-207-206-204 using an ion-counter. The ages were calculated from the $^{207}Pb/^{206}Pb$ ratios obtained on a stable ion beam, and only ratios with $^{206}Pb/^{204}Pb$ ratios > 5000 were used for further processing. A correction for common Pb was performed according to Cocherie et al. (1992) using a Pb composition with a two-stage evolution (Stacey and Kramers, 1975). Measurements of the Pb standard NBS 981 in ion counting mode yielded an average fractionation of ca. 0.1% per atomic mass unit (Chen et al., 2000). This value is considered as a suitable estimate for a correction of the mass fractionation. The errors on the ages are reported as $2\sigma_{mean}$ of the population of weighted $^{207}Pb/^{206}Pb$ ratios (Table 5.1).

5.3. Dating of metamagmatic rocks

5. 3.1. Augen gneiss

5. 3.1.1. Previous geochronological studies

Geological, petrographical, geochemical, and petrological studies in the Menderes Massif have been carried out for more than 160 years (e.g. Hamilton and Strickland, 1840; Tchihatcheff, 1869; Philippson, 1911; Önay, 1949; Nebert and Ronner, 1956; Schulling, 1958, 1962, 1973; Wippern, 1964; Graciansky, 1965; Scottford, 1969; Başarır, 1970; Dora, 1976; Dora et al., 2000). Geochronological studies have also made over three decades.

In spite of its complex tectonic structure, the Menderes Massif can be separated into two main rock assocations (Dora et al., 1995): Pan-African basement rocks and cover series. The Pan-African basement comprises partly migmatized Late Protorezoic clastic metasediments, i.e. paragneisses and mica schists, which were intruded by the protoliths of Precambrian eclogitic gabbros and syn- to post-Pan-African orthogneisses. The basement rocks were subjected to polyphase metamorphism at granulite-, eclogite-, and amphibolite-facies conditions that were related to Pan-African orogenesis at the Precambrian-Cambrian boundary (Dora et al., 1995, Oberhänsli et al., 1997; Candan and Dora, 1998; Candan et al., 2000). The most of the orthogneisses have not experienced this Pan-African metamorphism and are completely lack any mineral assemblages of this polyphase event. Although, some orthogneisses have HT mineral paragenesis, sillimanite+orthopyroxene. It is assumed that these HT orthogneises, syn-metamorphic, are older than the other orthogneisses which have not experienced Pan-African metamorphism, post-metamorphic (Candan, 1995).

The metamorphic phases that have affected the basement rocks of the Menderes Massif have been dated radiometrically. In the previous studies, this Pan-African metamorphism was dated by Rb-Sr whole-rock isochron method as 529 Ma (Schulling, 1973), 490±90 Ma (Dora, 1976), and 502±10 Ma (Şengör et al., 1984; Satır and Friedrichsen, 1986). However, monazite chemical U-Pb age of about 660±62 Ma from orthopyroxene bearing gneisses is interpreted to represent to the time of the granulite facies metamorphism of the basement units (Warkus et al., 1998). Furthermore, the migmatites and related metagranites which are regarded to be related to the latest phases of the Pan-African metamorphism, were dated of about 551±1.4 Ma by U-Pb dating of magmatic zircons (Hetzel et al., 1998). Nevertheless, the intrusion ages for the protoliths of the orthogneisses (augen/granitic gneisses) that were emplaced in the

period following Pan-African metamorphism have been found to be 546±1.2 Ma (Hetzel and Reischmann, 1996), 540-550 Ma (Dannat and Reischmann, 1998), 560-570 Ma (Koralay et al., 1998), 520-570 Ma (Loos and Reischmann, 1999). These data were obtained from magmatic zircons by the $^{207}Pb/^{206}Pb$ single-grain evaporation method. However, Şengör et al. (1984) and Satır and Friedrichsen (1986) suggest an intrusion age of 470±9 Ma based on Rb-Sr whole-rock isochron for the protoliths of the orthogneisses. On the basis of the geological evidence and Pb-Pb zircon ages of the orthogneisses, it has been suggested that polyphase metamorphic evolution of the Precambrian-Cambrian basement was related to Pan-African orogenesis (Candan and Dora, 1998).

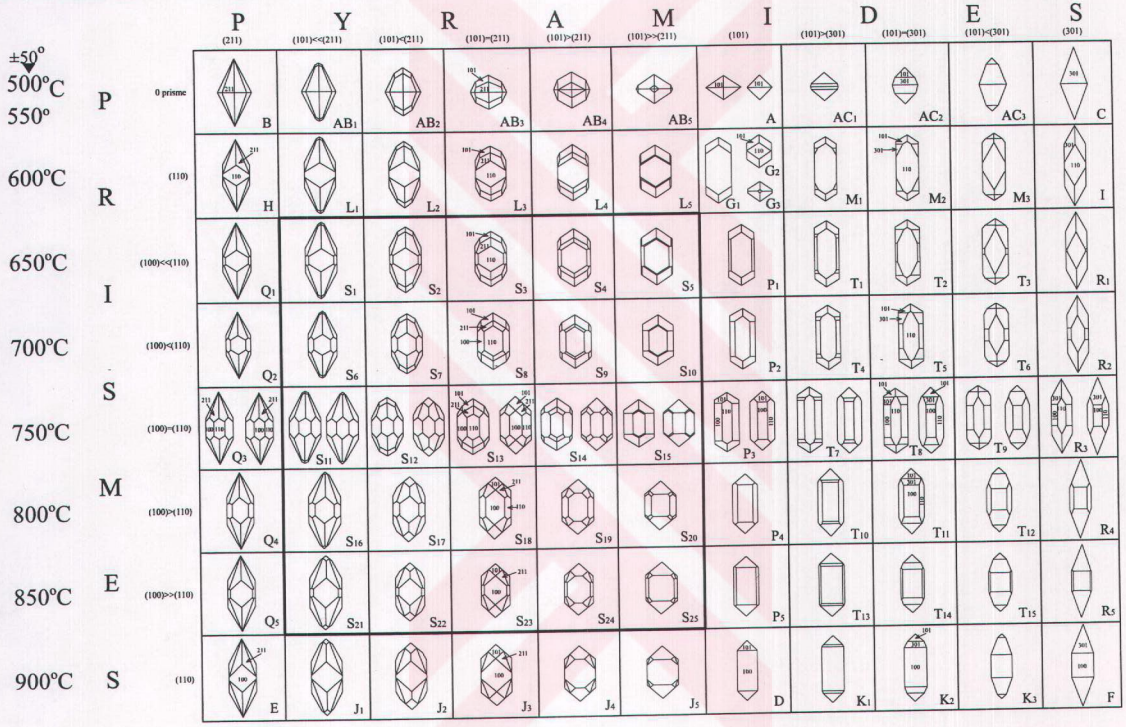
5. 3.1.2. Zircon morphology

Zircons from augen/granitic gneisses were subjected to determine under the scanning electron microscope (SEM) (Figure 5.5). Using optical microscopy the zircon concentrates are investigated and whenever possible, are divided into individual types. They selected for analysis according to differences in morphology size, color, morphology, inclusions, turbidity, abundance of cores, lack of cracks etc. 20 crystals have been chosen from each zircon type for typological investigation (Pupin, 1980) by scanning electron microscopy.

All zircons from the augen/granitic gneiss samples (95-57, 96-34 and 97-58) had very similar morphologies, which are typical of magmatic zircons (Figure 5.5). They are all euhedral sometimes asymmetric, colorless to slightly pink and brown, transparent, clear to slightly turbid, short- (2:1) and long- (3:1, 4:1) prismatic, occasionally metamict, and have few inclusions. According to the classification of Pupin and Turco (1974) (Figure 5.4) they predominantly belong to subtypes S7 and S12, and less amount of L1, S17, S13, and S2. In other words, zircons of augen/granitic gneisses are characterized by a combination of (101)<(211)-pyramids and (100)<(110) and (100)=(110)-prisms (Figure 5.5). The crystallization temperature of predominantly subtypes is about 700-750 °C. The typological analysis of the zircon populations of these samples place in the field of intrusive peraluminous crustal derived granites (Pupin 1980).

The zircons of augen/granitic gneisses (95-57, 96-34 and 97-58) are similar in respect to internal structure of cores and overgrowths. Zircon grains contain inherited (detrital) cores with highly variable sizes and multiple growth stages (Figures 5.6.a-j). The primary older growth zoning is well preserved in part of the some cores (Figures 5.6. b, c, d, f, h, i), whereas in others it is largely obliterated and apparently replaced by strongly luminescent (denoted as high-CL in Figures 5.6. e, i) and nearly homogenous

Figure 5.4. Main types and subtypes of the typologic classification and corresponding geothermometric scale, after Pupin and Turco, (1972).



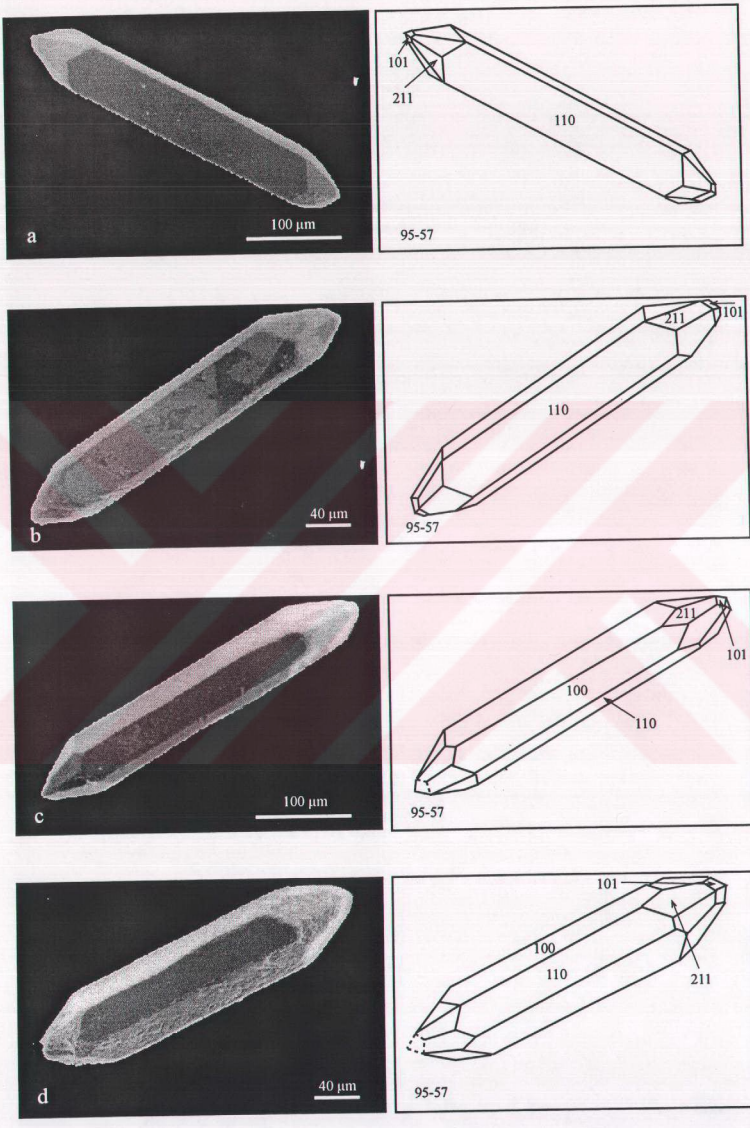


Figure 5.5. SEM images of typical zircons of augen/granitic gneisses. a and b: clear, colourless, long prismatic, clustering around L1; c and d: clear, colourless, long prismatic, clustering around S12. Continue,

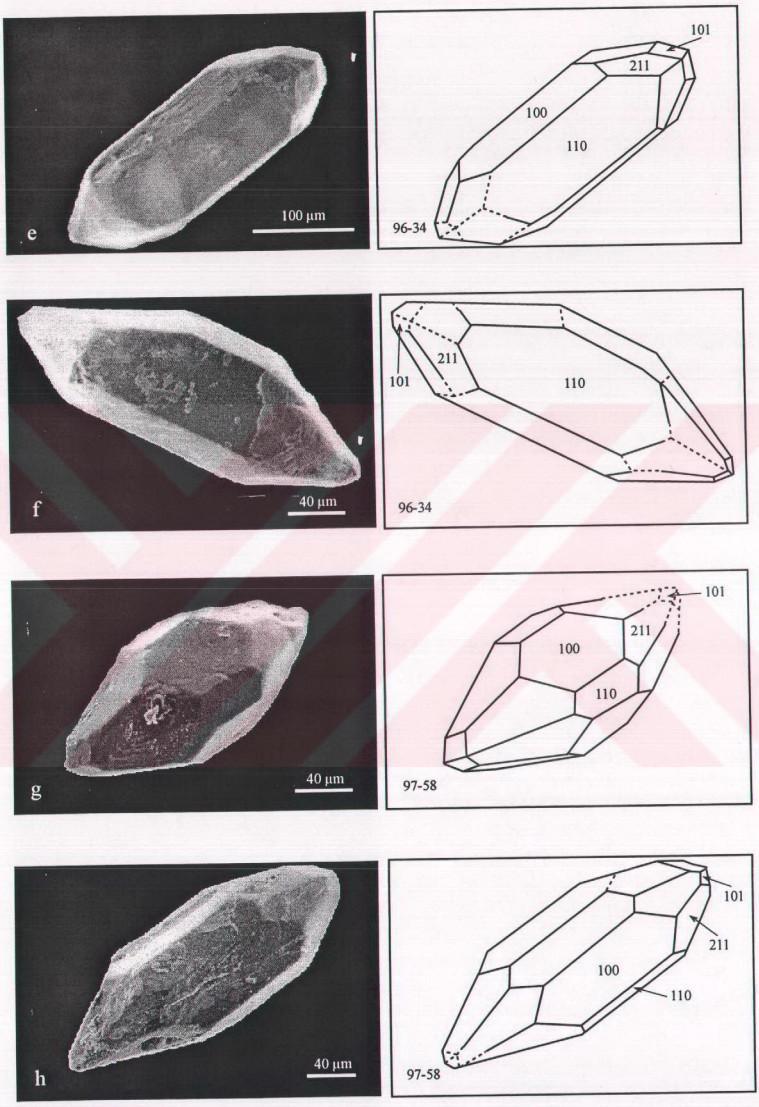


Figure 5.5. SEM images of typical zircons of augen/granitic gneisses. e and f: clear, colourless and slightly pink, long prismatic, clustering around S7; g and h: clear, colourless and slightly pink, long prismatic clustering around S17. Continue,

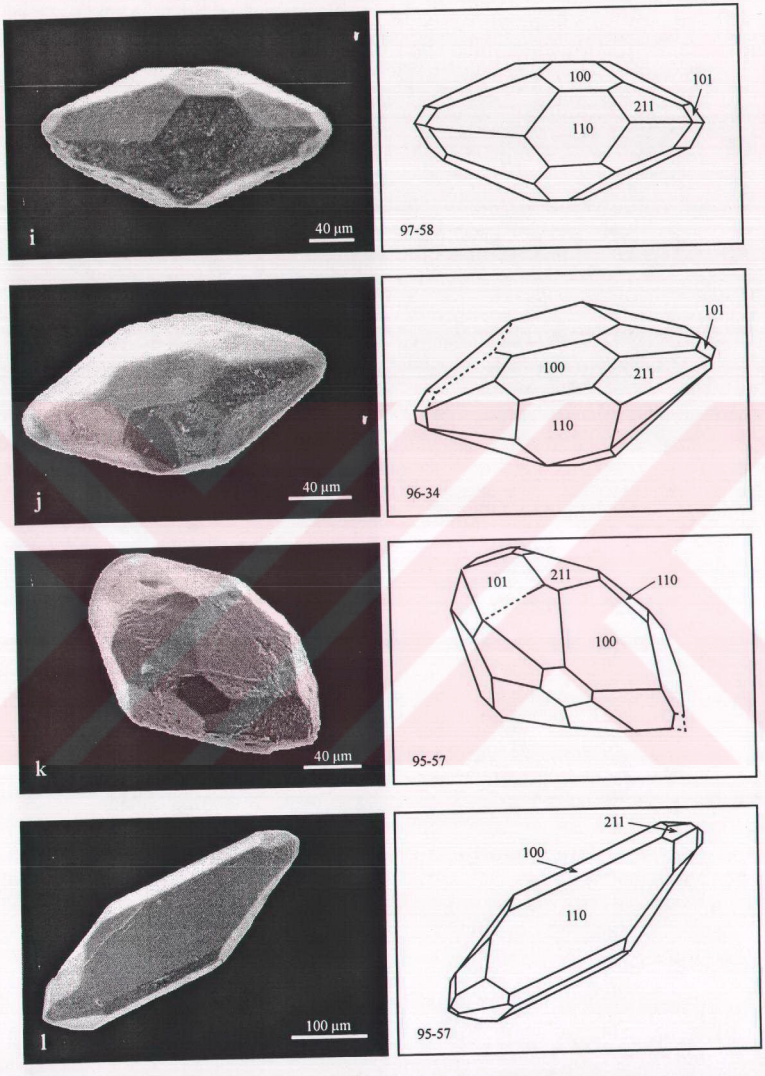
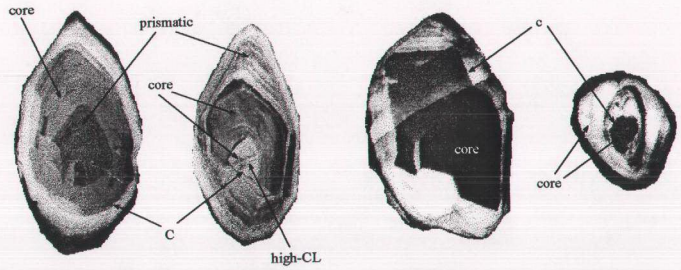
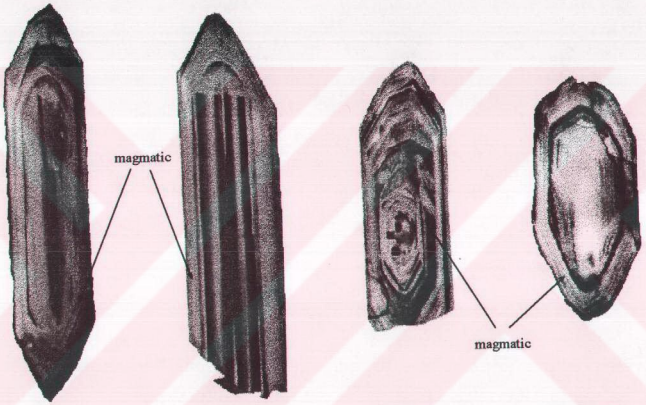


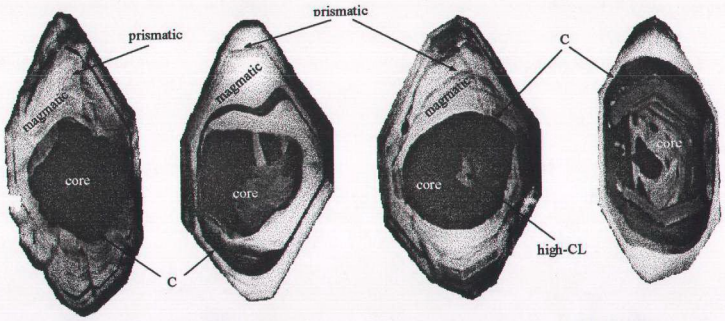
Figure 5.5. SEM images of typical zircons of augen/granitic gneisses. i and j: clear,colourless, slightly pink andbrown, short and long prismatic, clustering around S7; k: clear, colourless and slightly pink, clustering around S17; l: clear, colourless, long prismatic, clustering around S2.



a) 96-34 b) 96-34 c) 96-34 d) 96-34

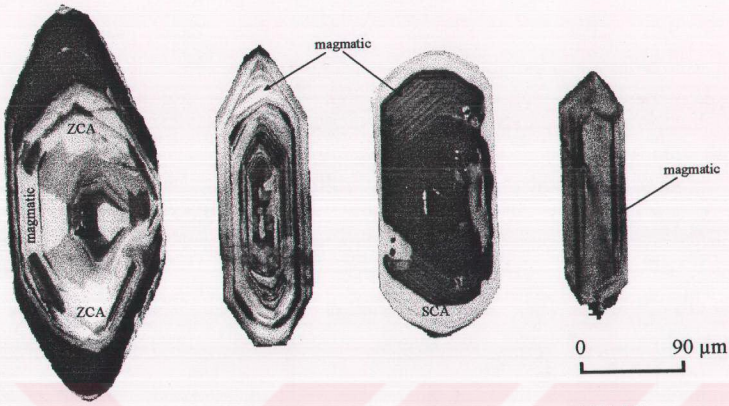


e) 96-34 f) 96-34 g) 96-34 h) 96-34



i) 97-58 j) 97-58 k) 97-58 l) 97-58

Figure 5.6. Continue.



m) 97-58 n) 97-58 o) 97-58 p) 97-58

Figure 5.6. Cathodoluminescence images of characteristic zircon populations in augen/granitic gneisses. Zircons with older core are shown from a to d and i to l. A characteristic feature for zircons is oscillatory zoning indicating a magmatic origin, e to h and m to p. ZCA zoning-controlled alteration, SCA surface-controlled alteration, C the sharp boundary (resorption surface) between cores and overgrowths.

zircon with stubby habitus. The core and overgrowths are separated by a well-preserved resorption surface marked by "C" in Figures 5.6. a to j. Most of the zircons show oscillatory zoning indicating a magmatic origin. Most of the elongated long-prismatic zircons have no cores. These grains were selected for the analysis (Figures 5.6 e-h and m-p).

5. 3.1.3. Description of the samples and $^{207}Pb/^{206}Pb$ ages

Two samples (96-34 and 97-58) from different bodies of the augen/granitic gneisses were selected for $^{207}Pb/^{206}Pb$ isotopic dating (Figure 5.7).

96-34: Sample 96-34 was collected 1.5 km east of village of Aksu (Figure 5.7). The rock is composed of quartz, orthoclase, plagioclase, muscovite, biotite, zircon, apatite and opaque oxide. The zircon grains are predominantly white, light pink, clear, translucent and short- and long-prismatic. In scanning electron microscope (SEM) images, the zircon grains were determined to be euhedral, and have morphologies strongly suggestive of an igneous origin (Figure 5.5). A cathodoluminescence (CL) study revealed magmatic zonation, inherited zircons, and new overgrowth (Figure 5.6

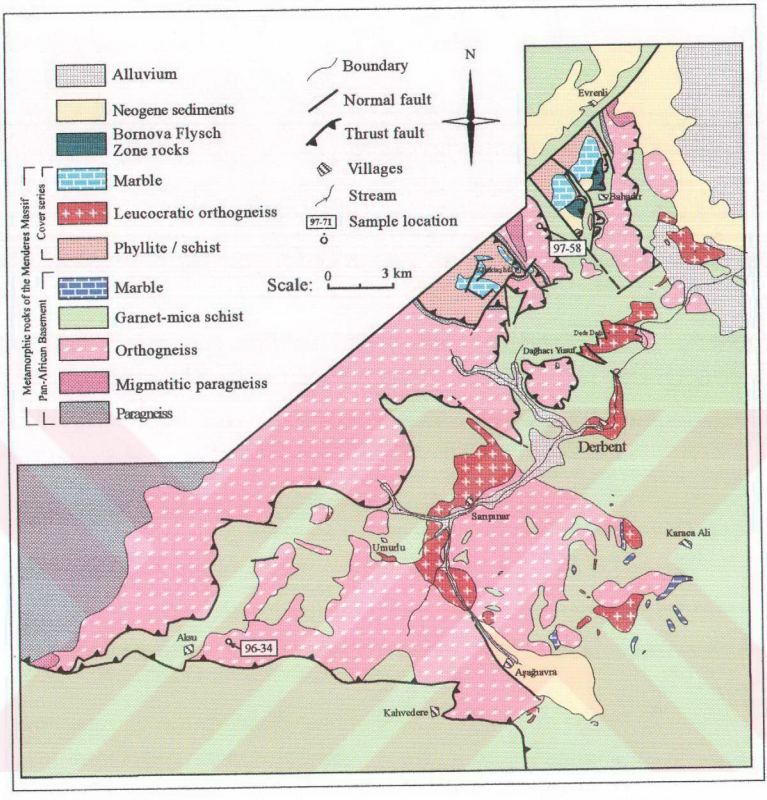


Figure 5.7. Sample location map for geochronological analysis of augen/granitic gneisses, south of Alaşehir.

a-h). Xenocrystic cores occur in zircons with stubby habitus and some show oscillatory zoning (Figre 5.6. a -d). The CL photographs indicate multiple growth stages for some zircon crytals (Figure 5.6. d and h). Four long-prismatik grains from this sample were evaporated individually and yielded ages of 550 to 564 Ma. An average value of 561.5±1.8 Ma is obtained (Table 5.1, Figure 5.7). I suggest that this age represent the intrusion age of the magmatic protolith of augen gneiss.

Table 5.1. Radiogenic $^{207}Pb/^{206}Pb$ ratios of evaporated zircon grains and corresponding ages.

Sample number	Zircon description	Grain	Number of ratio	Evaporation temperature (°C)	$^{207}Pb/^{206}Pb$ ratios (mean)	$^{207}Pb/^{206}Pb$ Age (Ma)
96-34						
	cl, c, t, lp	1	129	1460-1490	.058564±50	561.5±1.9
	cl, c, t, lp	2	88	1460-1480	.058942±93	578.5±3.4
	cl, c, t, lp	3	57	1520	.058866±24	561.6±0.9
	y, c, t, lp	4	208	1450-1490	.058592±43	551.4±1.6
	Mean		**274**		**.058564±22**	**561.5±0.8 (2σm)**
97-58						
	p, c, t, lp	1	51	1530	.063375±31	720.3±1.1
	cl, c, t, lp	2	75	1540	.059326±92	578.5±3.4
	cl, c, t, lp	3	52	1540	.059012±39	567.0±1.4
	cl, c, t, lp	4	17	1450	.058678±209	554.6±7.8
	Mean		**132**		**.059125±62**	**570.5±2.2 (2σm)**

w- white, p - pink, g – greenish, y - yellowish, cl – colourless, c – clear, t – translucent, lp - long prismatic, sp - short prismatic

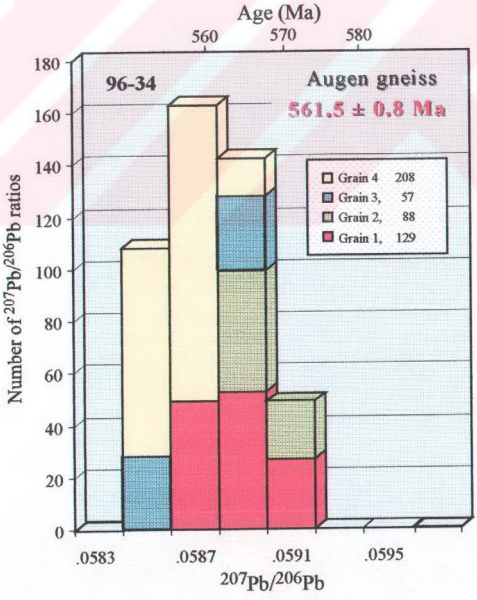


Figure 5.8 . Zircon age for augen gneiss, 96-34. Histogram of radiogenic $^{207}Pb/^{206}Pb$ ratios for evaporated zircons indicating age of 561.5±0.8 Ma (2σ mean).

97-58: This orthogneiss was sampled 2 km southwest of village of Bahadır (Figure 5.7). It shows well developed schistosity, comprises quartz, orthoclase, plagioclase, muscovite, biotite, zircon, apatite, tourmaline and opaque oxide. The zircon grains are predominantly white, pink, clear, translucent and short- and long-prismatic. SEM photographs show that zircons are euhedral, and have morphologies which are strongly suggestive of an igneous origin (Figure 5.5). A CL study revealed magmatic zonation, inherited zircons, and new overgrowth (Figure 5.6. i-o). Zircon grains often xenocrystic cores (Figure 5.6. i-l), while most zircon grains preserved their oscillatory zoning of magmatic origin (Figre 5.6. i-o). The CL images indicate multiple growth stages for some zircon crytals (Figure 5.6. m and n). Four long-prismatik grains of this sample were evaporated and yielded ages of 520 to 720 Ma. An average value of 570.5±2.2 Ma is obtained (Table 5.1, Figure 5.9). This age is interpreted the intrusion age of the magmatic protolith of the augen gneiss.

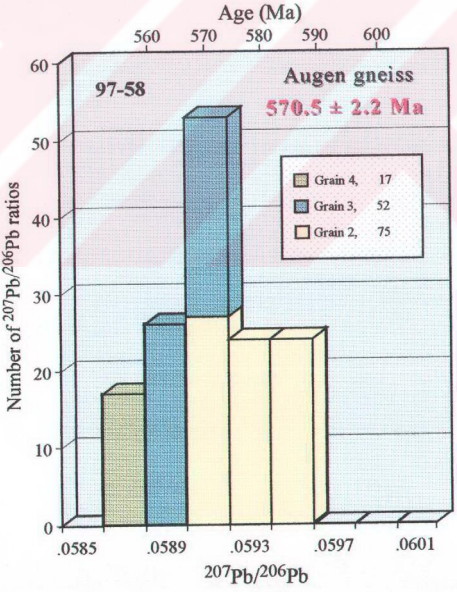


Figure 5.9. Zircon age for augen gneiss, 97-58. Histogram of radiogenic $^{207}Pb/^{206}Pb$ ratios for evaporated zircons indicating age of 570.5±2.2 Ma ($2\sigma_{mean}$).

5. 3.2. Leucocratic orthogneiss

5. 3.2.1. Previous geochronological studies

Limited number of geological and geochronological studies were carried out about the leucocratic orthogneisses. The protoliths of the leucocratic orthogneisses represent the second pulse of significant magmatic activity in the Menderes Massif, following the most common magmatic activity in Precambrian (Koralay and Dora, 1999; Koralay et al.,2001). Dannat (1997) and Dannat and Reischmann (1998) give an intrusion age of 227-240 Ma based on $^{207}Pb/^{206}Pb$ single zircon evaporation method for the protoliths of the leucocratic orthogneisses in the Ödemiş-Kiraz Submassif and Gördes Submassif. Same researchers report that the protoliths of the leucocratic orthogneisses show Nd isotopic composition $e(Nd)_t$ values from –2 to +5 and the model ages of these rocks are around 0.8-1.25 Ga. Koralay and Dora (1999) and Koralay et al., (2001) suggest that the protoliths of the leucocratic orthogneisses were metamorphosed during the Alpine orogenesis and transformed into orthogneisses. Muscovite from leucocratic orthogneisses gives a Rb-Sr mineral-whole rock age of 26.2±0.3 Ma indicate that cooling of these rocks took place between Early Oligocene and Early Miocene (Koralay et al., 1998).

5. 3.2.2. Zircon morphology

Zircon grains from the leucocratic orthogneisses were tried to determine under the scanning electron microscope (SEM) (Figure 5.10). Using optical microscopy the zircon concentrates are investigated and whenever possible, are divided into individual types. They selected for analysis according to differences in morphology size, color, morphology, inclusions, turbidity, abundance of cores, lack of cracks etc. 22 crystals have been chosen from each zircon type for typological investigation (Pupin, 1980) by scanning electron microscopy.

All zircons from the leucocratic orthogneiss samples (732, 97-71 and 97-44) had very similar morphologies, which are typical of magmatic zircons (Figure 5.10). The SEM pictures of zircons from the leucocratic orthogneisses on the other hand reveal very different morphologies compared with those from the augen/granitic gneisses (Figures 5.5, 5.10). They are all euhedral, colorless, transparent, turbid, short- (2:1) and long- (3:1, 4:1) prismatic, and have inclusions and pitted surfaces. According to the classification of Pupin and Turco (1974) (Figure 5.10) they predominantly belong to subtypes P3, P4 and P5 and less amount of P1, P2, D, S7 and S17. In other words,

zircon of the leucocratic orthogneisses are characterized by a combination of (101)-pyramids and (100)=(110), (100)>(110)-prisms (Figure 5.5). The crystallization temperature of predominantly subtypes is about 750-850 °C. The typological analysis of the zircon populations of these samples place in the field of alkaline granites derived from hybrid magmas, found in subvolcanic and/or anorogenic complexes (Pupin 1980).

The zircon grains of leucocratic orthogneisses (732, 97-71, 97-44) are mostly similar in respect to internal structure of cores and overgrowths. Zircons contain inherited cores with highly variable sizes (Figures 5.11 l-o, t). They do not show primary older growth zoning. The core and overgrowths are separated by a well preserved resorption surface marked by "C" in Figures 5.11 o. Some zircons (in Figure 5.10 e, l, f) show magmatic growth zonation only along outer-most rim of the grains (Figure 5.11 I, j, k). Most of the zircons oscillatory zoning indicating a magmatic origin (Figures 5.11 a-h, p-t). Most of the elongated long-prismatic zircons have no cores. These types of zircon grains are preferred to analysis.

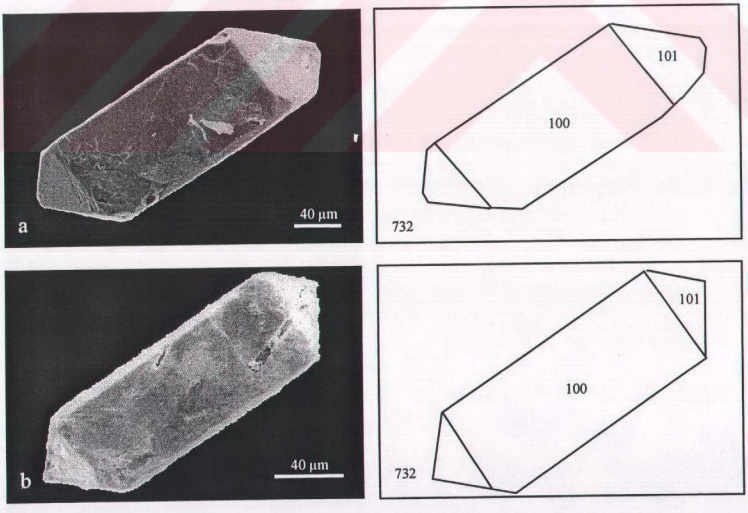


Figure 5.10. SEM images of typical zircons of leucocratic orthogneisses. a and b: colorless, turbid, short and long prismatic, clustering around D. Continue,

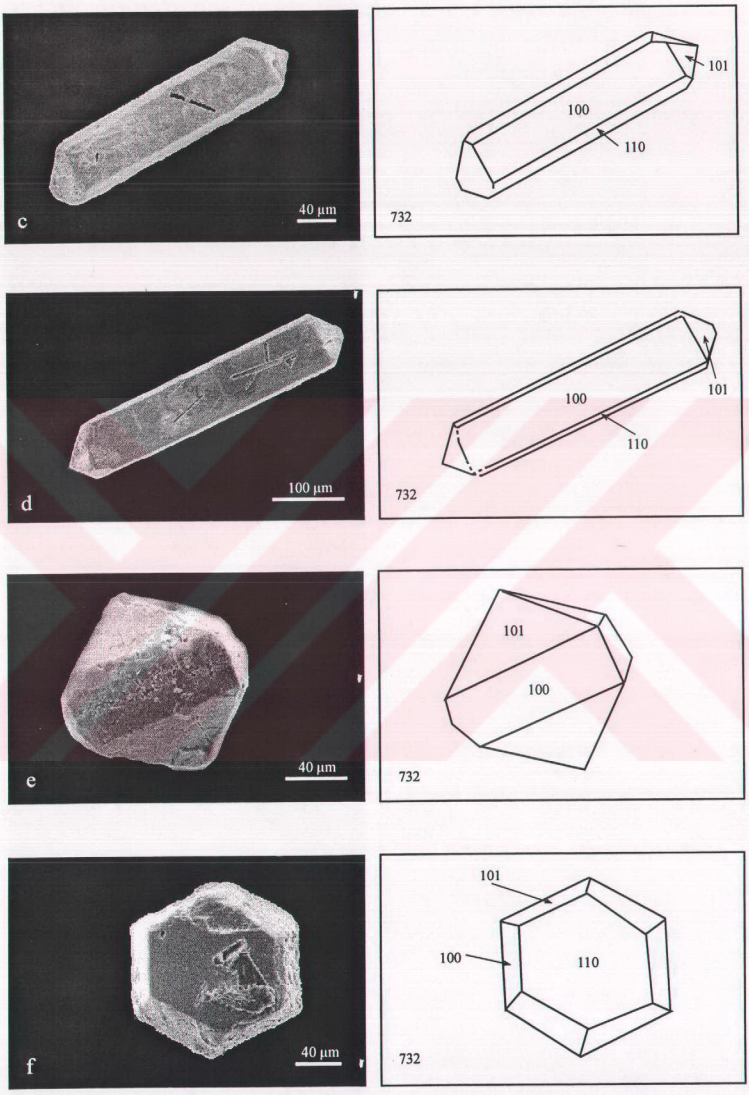


Figure 5.10. SEM images of typical zircons of leucocratic o rthogneisses. c and d: colourless, turbid, short and long prismatic, clustering around P4 and P5 respectively; e: colourless, turbid, short prismatic, clustering around D; f: colourless, clustering around P2. Continue,

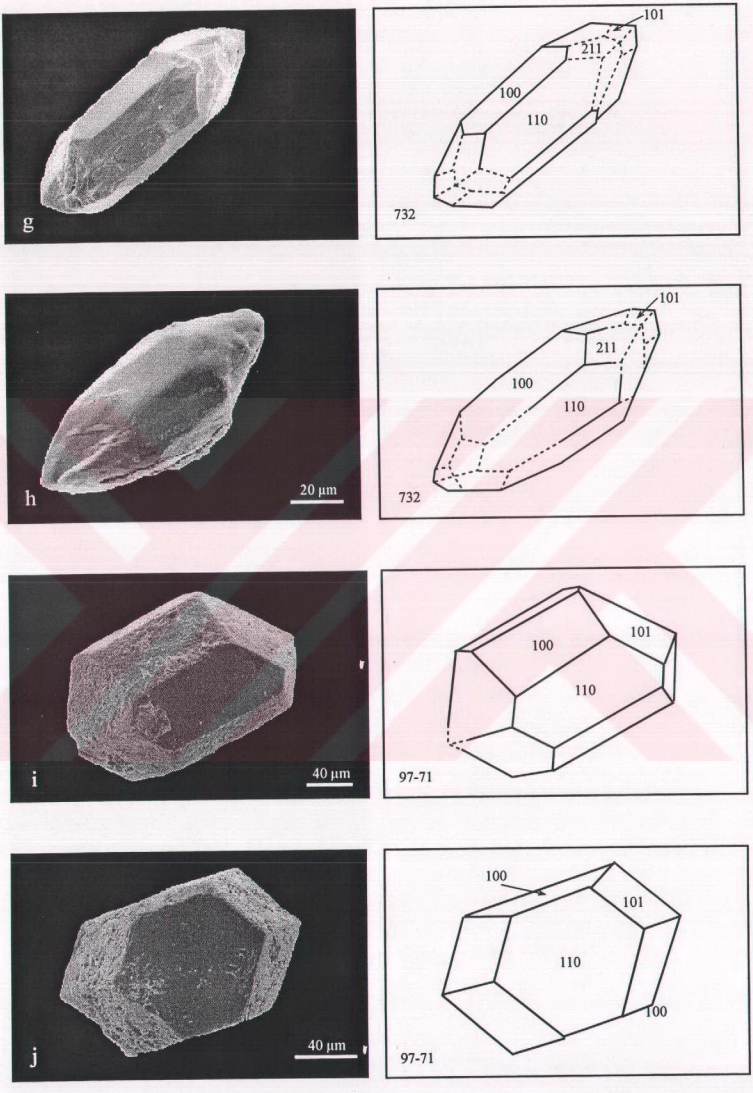


Figure 5.10. SEM images of typical zircons of leucocratic orthogneisses. g and h: clear, colourles and slightly pink, short and long prismatic, clustering around S7 and S12 respectively; i and j: colourless, turbid, short prismatic, clustering around P3 and P1 respectively. Continue,

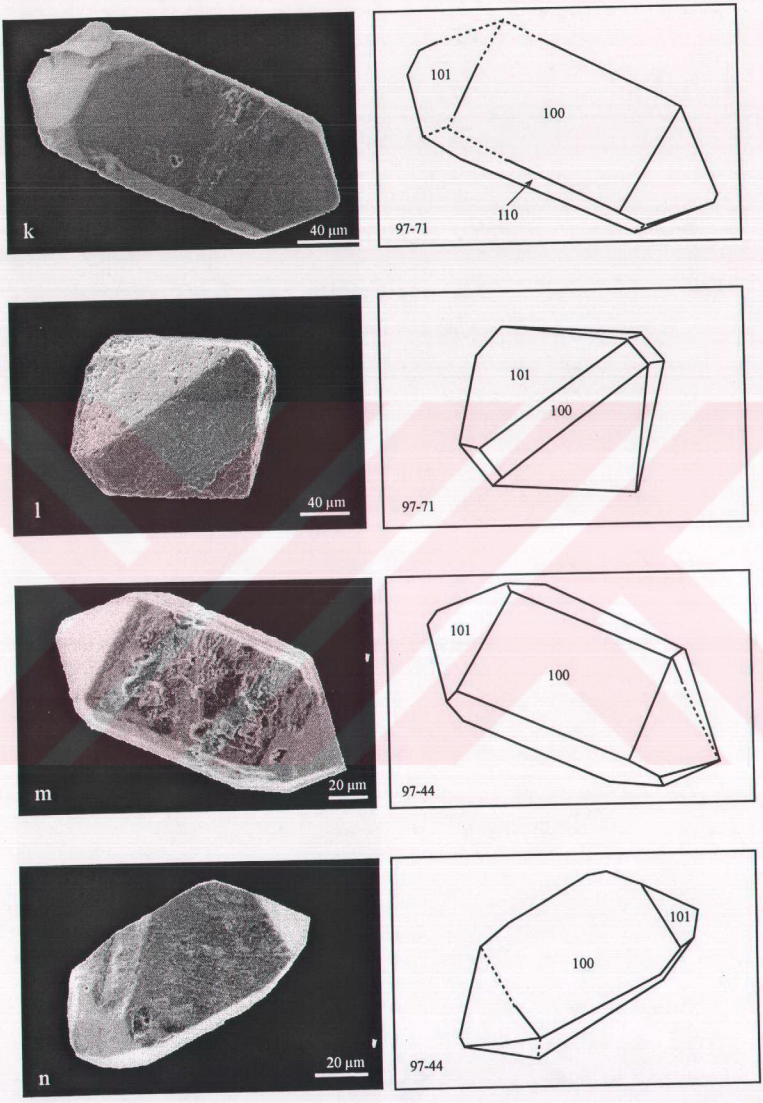


Figure 5.10. SEM images of typical zircons of leucocratic orthogneisses. k and m: colourles, pink, clear to turbid, short prismatic, clusteringaround P4; l, m and n: colourles, pink, clear to turbid, short prismatic, clustering around D. Contiune,

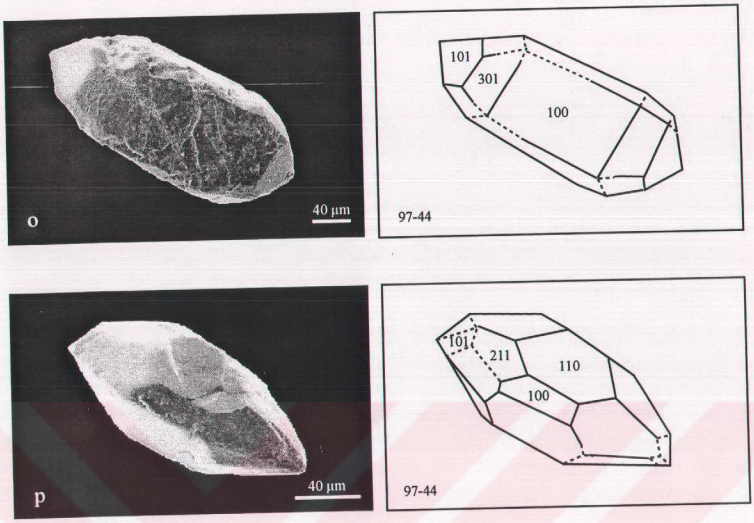


Figure 5.10. SEM images of typical zircons of leucocratic orthogneisses. o: pink, colourles, clear to turbid, long prismatic; clustering around T11, p: clear, colourless, short prismatic, clustering around S7.

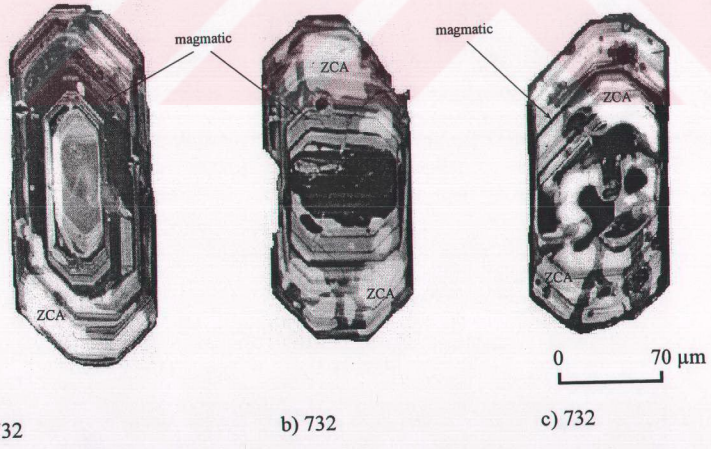


Figure 5.11. Cathodoluminescence (CL) images of characteristic zircon populations in leucocratic orthogneisses. A characteristic feature for zircons is oscillatory zoninig indicating a magmatic origin, a to c . ZCA zoning-controlled alteration, SCA surface-controlled alteration, C the sharp boundary (resorption surface) between cores and overgrowths. Continue,

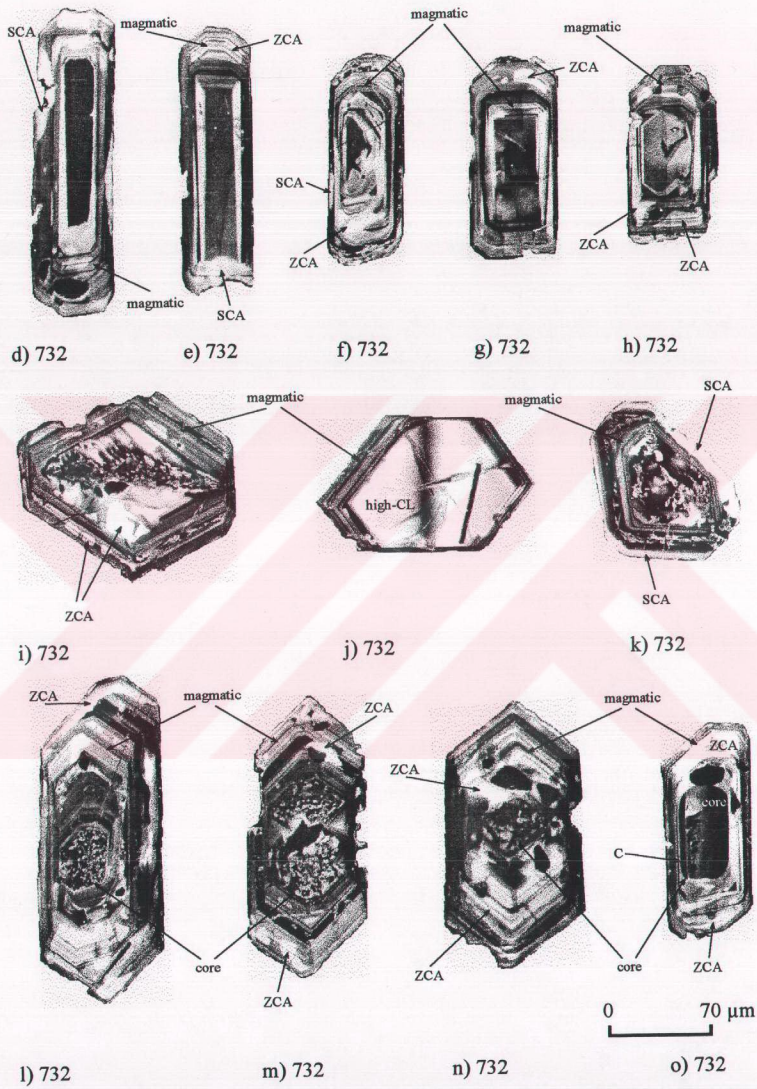
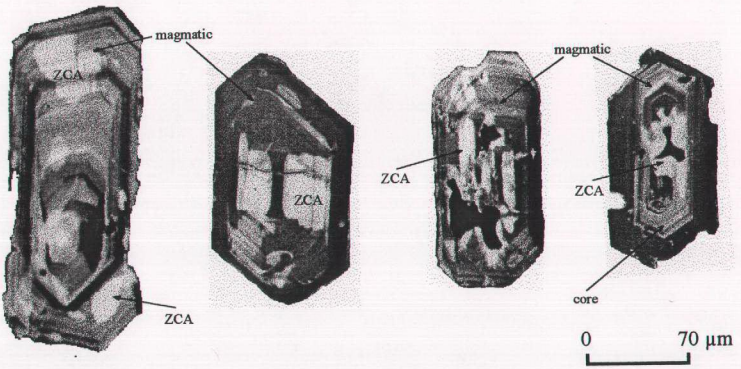


Figure 5.11. CL images of characteristic zircon populations in leucocratic orthogneisses. d to h show oscillatory zoninig indicating a magmatic origin; i to k show magmatic growth zonation only along outer-most rim of the grain; Zircons with older core are shown from l to o. ZCA zoning-controlled alteration, SCA surface-controlled alteration, C the sharp boundary (resorption surface) between cores and overgrowths. Continue,



p) 97-71 r) 97-71 s) 97-71 t) 97-71

Figure 5.11. CL images of characteristic zircon populations in leucocratic orthogneisses. p to s show oscillatory zoninig indicating a magmatic origin. Zircon with older core is shown in t. ZCA zoning-controlled alteration, SCA surface-controlled alteration, C the sharp boundary (resorption surface) between cores and overgrowths.

5. 3.2.3. Description of the samples and $^{207}Pb/^{206}Pb$ ages

Three samples (732, 97-71, and 97-44) (Figures 5.12, 5.13) from the different bodies of the leucocratic orthogneisses were selected for $^{207}Pb/^{206}Pb$ isotopic dating. The $^{207}Pb/^{206}Pb$ single zircon data are shown in Table 5.2 .

Sample 732: This sample was collected seven km south of Derbent (Figure 5.12). The leucocratic orthogneiss (type 1), with a typical granitoid appearance, has a strong schistosity and comprises quartz, plagioclase, orthoclase, microcline, muscovite ± biotite, tourmaline, zircon, and opaque oxide minerals. The zircon grains are predominantly white, translucent and long-prismatic. In the scanning electron microscope (SEM) images, the zircon grains were determined to be euhedral, and have morphologies which are strongly suggestive of an igneous origin (Figure 5.10). A cathodoluminescence (CL) study revealed magmatic zoning in all investigated crystals (Figure 5.11). Some have inherited cores that are easily detectable by CL; these cores would be difficult to identify using a binocular microscope. Five long-prismatic grains from this sample were evaporated individually and yielded ages of 240 to 250 Ma. An average value of 245.7±4.6 Ma is obtained (Table 5.2, Figures 5.14, 5.15). This age is interpreted as representing the intrusion age of the magmatic protolith of the leucocratic orthogneiss.

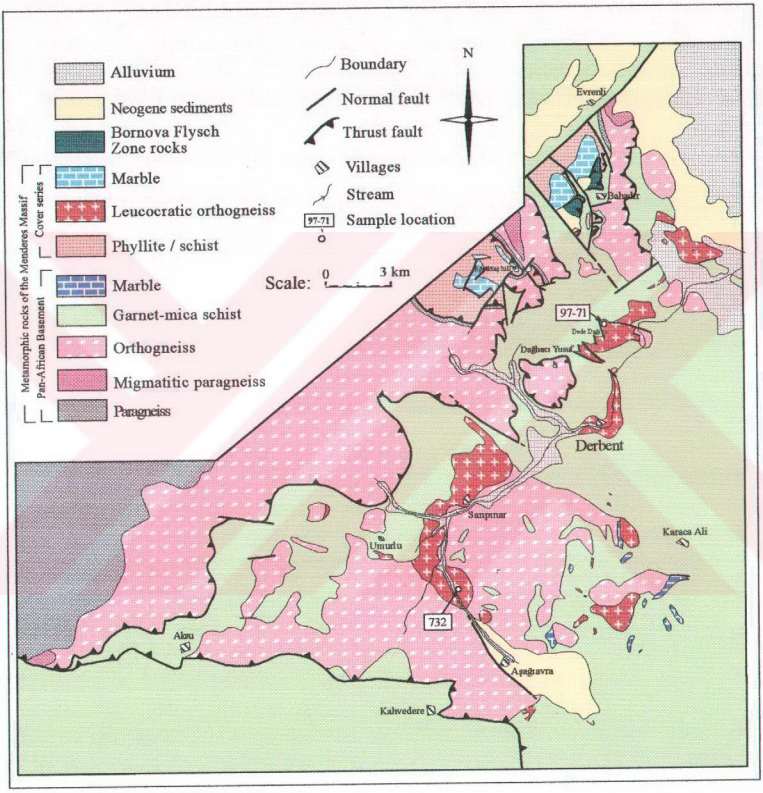


Figure 5.12. Sample location map for geochronological analyses of leucocratic orthogneisses, south of Alaşehir.

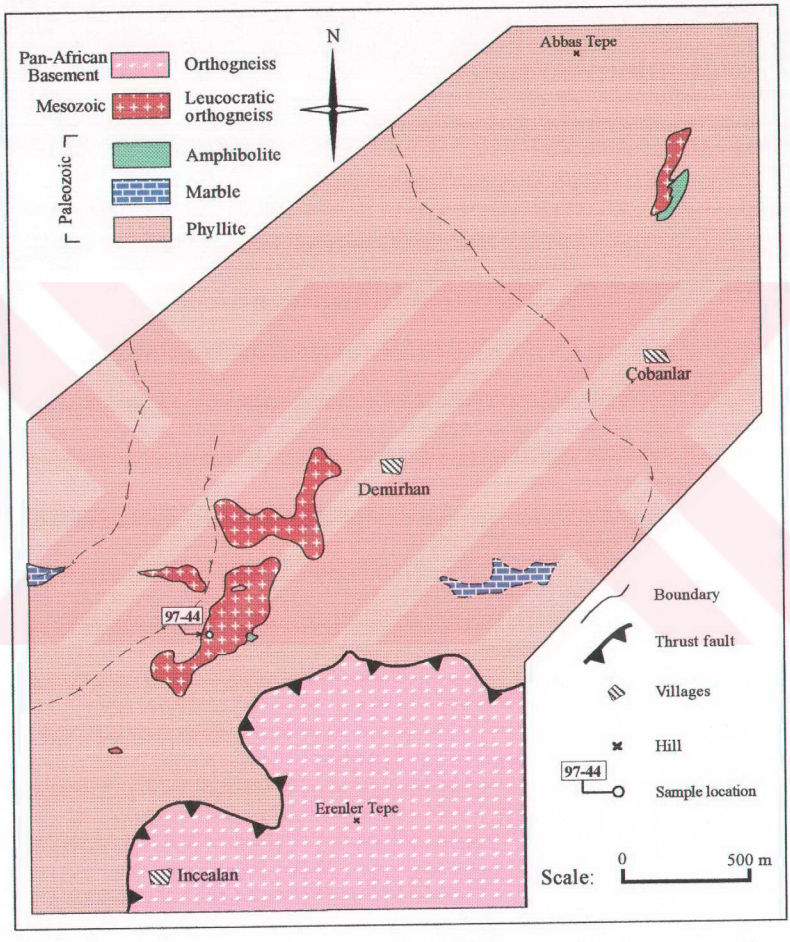


Figure 5.13. Sample location map for geochronological analysis of leucocratic orthogneisses, Demirhan village.

Table 5.2. Radiogenic $^{207}Pb/^{206}Pb$ ratios of evaporated zircon grains and corresponding ages.

Sample number	Zircon description	Grain	Number of ratio	Evaporation temperature (°C)	$^{207}Pb/^{206}Pb$ ratios (mean)	$^{207}Pb/^{206}Pb$ Age (Ma)
732						
	w, t, lp	1	47	1550	.051178±214	248.9±9.7
	w, t, lp	2	125	1430-1450	.051047±158	243.0±7.1
	w, t, lp	3	201	1430-1470	.051197±129	249.7±5.8
	w, t, lp	4	77	1450-1470	.051101±159	245.4±7.1
	w, t, lp	5	146	1430-1470	.050982±183	240.0±8.3
	Mean		**390**		**.051107±100**	**245.7±4.6 (2σm)**
97-71						
	g, t, sp	1	189	1450-1490	.051116±176	246.1±7.9
	p, c, sp	2	257	1470-1490	.050930±219	237.7±9.9
	p, c, sp	3	87	1450	.051028±237	241.1±11.0
	p, c, lp	4	191	1450-1490	.050990±146	240.4±6.6
	Mean		**472**		**.051007±115**	**241.1±5.2 (2σm)**
97-44						
	p, c, sp	1	52	1470	.050823±206	232.8±9.3
	p, c, sp	2	99	1490-1510	.050963±204	239.2±9.2
	p, c, sp	3	170	1450-1470	.050698±204	227.1±9.2
	p, c, sp	4	226	1440-1480	.050881±166	235.4±7.6
	p, c, sp	5	107	1450-1470	.051021±203	241.8±9.2
	Mean		**424**		**.050868±128**	**234.9±5.8 (2σm)**

w - white, p - pink, g – greenish, y - yellowish, cl – colourless, c – clear, t – translucent, lp – long prismatic, sp – short prismatic

Sample 97-71: This sample was collected from two km north of Derbent at Dede Da¤› (Figure 5.12). It shows distinct schistosity, comprises quartz, plagioclase, orthoclase, microcline, muscovite and opaque minerals. Zircon grains of this sample in general predominantly pink, clear and short-prismatic, with typical igneous morphologies as revealed in SEM studies (Figure 5.11). And, igneous zonation is visible in CL photomicrographs (Figure 5.12). Other zircon crystals are greenish, translucent and short-prismatic. Their length is up to 0.400 mm but the prevailing size is 0.20 mm Four grains of short- and long-prismatic habitus yielded $^{207}Pb/^{206}Pb$ ages of 238 to 246 Ma clustering at a mean value of 241.1±5.2 Ma (Table 5.2, Figures 5.16, 5.17). This age is interpreted as the time of intrusion of the magmatic protolith of this leucocratic orthogneiss.

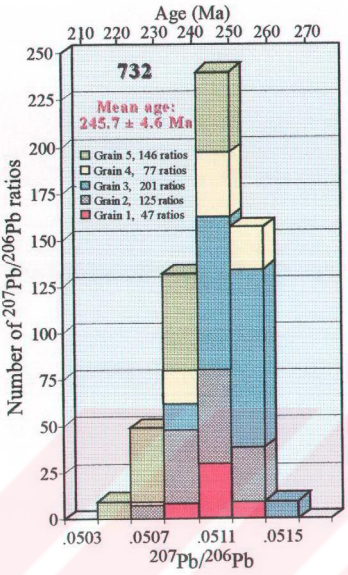


Figure 5.14. Zircon age for leucocratic orthogneiss . Histogram of radiogenic $^{207}Pb/^{206}Pb$ ratios for evaporated zircons indicating age of 245.7±4.6 Ma (2s mean).

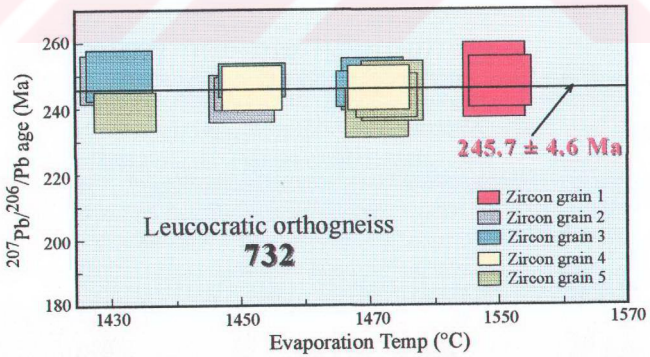


Figure 5.15. Single zircon evaporation data in a plot showing evaporation temperature versus apparent $^{207}Pb/^{206}Pb$ ages (weighted mean values). Error is 2s of the mean.

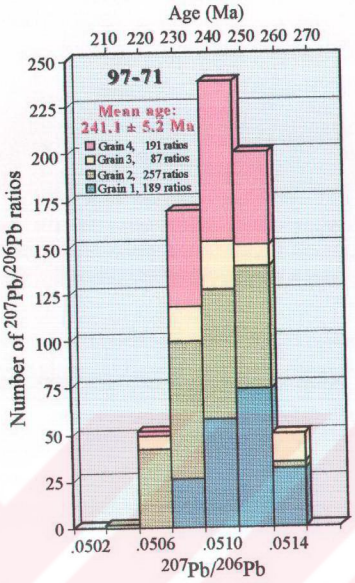


Figure 5.16. Zircon age for leucocratic orthogneiss . Histogram of radiogenic $^{207}Pb/^{206}Pb$ ratios for evaporated zircons indicating age of 241.1±5.2 Ma (2σ mean).

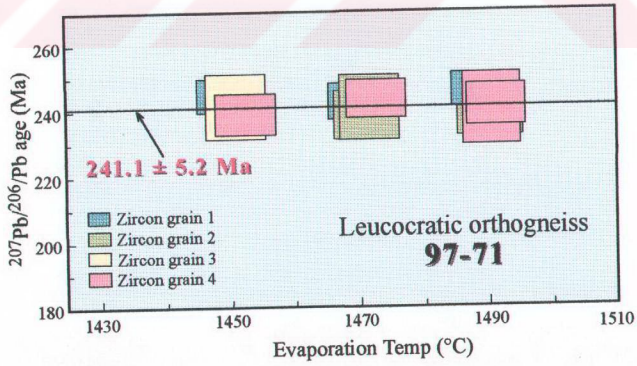


Figure 5.17. Single zircon evaporation data in a plot showing evaporation temperature versus apparent $^{207}Pb/^{206}Pb$ ages (weighted mean values). Error is 2σ of the mean.

Sample 97-44: It was taken from one km SW of the village of Demirhan (Figure 5.13). This sample is white, coarse-grained, and non-foliated, and consists of quartz, plagioclase, orthoclase, biotite ± muscovite, zircon and opaque oxide minerals. Most zircon grains of this leucocratic orthogneiss are colorless, clear and short prismatic. While some zircon grains are pink to yellowish, clear and short prismatic. The zircon morphology and the internal structure suggest that they are of igneous origin (Figures 5.11, 5.12). The ages obtained on five short-prismatic zircon crystals from this sample range from 227 to 242 Ma clustering an average value of 234.9±5.8 Ma (Table 5.2, Figures 5.18, 5.19), which is interpreted as the intrusion age of the igneous precursor of the leucocratic orthogneiss.

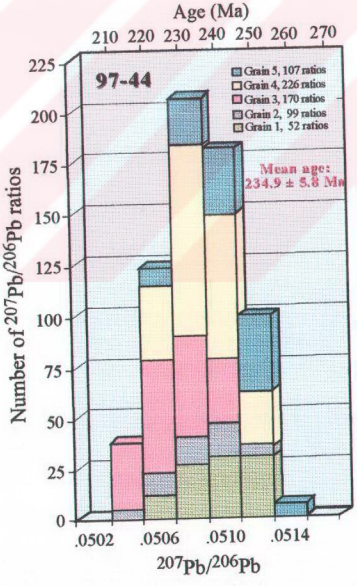


Figure 5.18. Zircon age for leucocratic orthogneiss . Histogram of radiogenic $^{207}Pb/^{206}Pb$ ratios for evaporated zircons indicating age of 234.9±5.8 Ma (2σ mean).

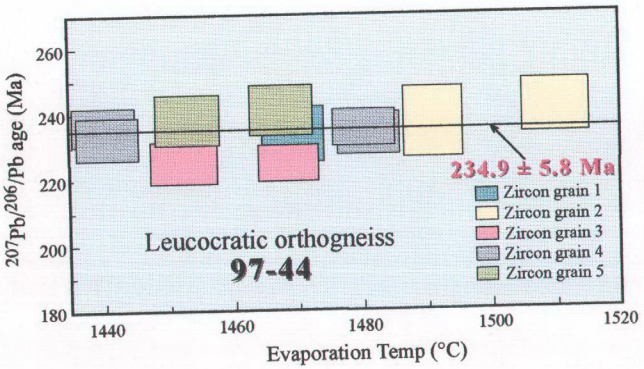


Figure 5.19. Single zircon evaporation data in a plot showing evaporation temperature versus apparent $^{207}Pb/^{206}Pb$ ages (weighted mean values). Error is 2σ of the mean.

CHAPTER SIX
DISCUSSION

Geological, geochemical and geochronological evidence of the Pan-African basement and cover series are presented in the previous chapters. In this section, the following main topics will be discussed:

- to correlation of tectonostratigraphy of the study areas with the nappe structure of the Menderes Massif on the basis of previous studies,
- distribution of the leucocratic orthogneisses in the Menderes Massif,
- geochemical characteristics, tectonic setting and origin of orthogneisses which is the products of the Pan-African magmatism forming the first phase in the Menderes Massif,
- tectonic setting and the characteristics of the precursor rocks of the leucocratic orthogneisses which is probably related to the Cimmerian magmatism, the second main magmatic event in the Menderes Massif,
- comparison of single zircon $^{207}Pb/^{206}Pb$ ages of orthogneisses and leucocratic orthogneisses with the previous studies,
- tectonic setting of the Menderes Massif during the evolution of the Paleotethys and Neotethys,

√ Tectonostratigraphy of the study areas

Until recent years, a simple internal structure model which is made up of a high-grade core, core series, and low- to medium-grade envelope, cover series, has been generally accepted for the Menderes Massif (Graciansky, 1965; Dürr, 1975; Şengör et al., 1984; Dora et al., 1990). In the previous studies, it has been regarded by şengör et al. (1984) and Satır and Friedrichsen (1986), that the core series is mostly dominated by different type gneisses such as granitic, augen and banded gneisses. Whereas, paragneisses, mica schists, migmatites and gabbroic/noritic stocks with HP relics were distinguished. It has accepted that they belong to the Pan-African basement by the recent studies (Dora et al., 1995; Candan, 1995,1996; Candan et al., 1998, 2001; Oberhänsli et al., 1997, 1998). On the other hand, the cover series consist of, in ascending order, Paleozoic metapelites with minor marble interlayers and Mesozoic series which is mainly made up of the metapelites with metaconglomerates in the lowest level and platform type thick metacarbonates with metabauxite horizons, redish pelagic marbles and overlying metaolistostrome with serpentinite and marble blocks in the upper most levels (Dürr, 1975; Konak et al., 1987; Dora et al.,1994, 1995).

Contrary to this simple dome-shaped structure model, in recent years, it has been proven by the detailed studies that the Menderes Massif displays a typical complex nappe pile structure (Konak et al., 1994; Dora et al., 1995; Partzsch et al., 1998; Ring et al., 1999; Gessner et al., 2001). According to Konak et al. (1994), Dora et al. (1995) and Partzsch et al, (1998), the central part of the Menderes Massif consists of a number of nappe slices which record different geological evolution. The last nappe stacking is regarded to be related to the Alpine orogeny by these authors. However, Ring et al. (1999) and Gessner et al. (2001) separate two stages of trusting with different age and direction based on the shear sense indicators: 1) Pre-Alpine thrusting with top to the north movement and 2) Alpine thrusting with top to the south movement.

In the field studies, it has been determined that the similar nappe stacking is also present in the study areas. In the Derbent area, the rock succession of metamorphic series can be divided into four nappe units. In ascending order, the lower, middle and upper nappes are represented by the internal imbrication of the Pan-African basement series. The uppermost nappe unit consisting of the Paleozoic-Mesozoic cover series rests tectonically upon the upper nappe units of Pan-African basement series.

Lower contact of lower nappe unit belonging to the Pan-African basement is not observed in the Derbent area. In the southwest of the Derbent area, between north of Nazilli and northeast of Germencik, it is observed that lower nappe unit rests tectonically upon the Paleozoic (Permo-Carboniferous) cover series containing the preserved Bryozoa fosills around Paşayaylazı, north of Aydın (Figure 6.1.a). Rudist bearing (Hippurites nabiensiensis, Hippurites cf. colliciatus, Hippurites sp., per. com. Prof.Dr. Sacit Özer) Upper Crateceous (Santonian-Campanian) marbles are tectonically overlain by this Permo-Carboniferous series around Eğrikavak village, northeast of Aydın (Figure 6.1.b). The schist of lower nappe unit include budins of quartz veins in different thickness. Some asymmetric quartz ribbons in lower nappe unit show the top to the SSW sense of shear (Figure 3.11).

The mica schists of the middle nappe unit show the top to south fabrics in the southern part of Derbent (Gessner et al. 2001). Gessner et al. (2001) proposed that the top to south febrics in the middle nappe unit can be fallowed across its upper nappe contact into the overlying upper nappe unit. The schists of lower and middle nappe unit consist of "quartz+muscovite+biotite+garnet" paragenesis which indicates upper green schist facies. The granulite facies conditions (735 °C) were determined in the charnockitic paragneisses belonging to the upper nappe unit which rests tectonically upon the middle nappe unit in the northern part of Bahadır village (Candan 1995; Candan et al., 1998).

The presence of common eclogite relics in the upper nappe unit also verify the contrast of the metamorphic grade between upper and middle nappe units. The upper nappe units of Pan-African basement are tectonically overlain by the upper most nappe units consisting oof Paleozoic-Mesozoic cover series. "Quartz+muscovite+garnet+staurolite" mineral paragenesis which indicate staurolite çone of almandine-amphibolite facies is determined in the metapelites of uppermost nappe unit. Furthermore, the lack of HP relics in this nappe unit show the differences of metamorphic degree between upper nappe units and uppermost nappe units.

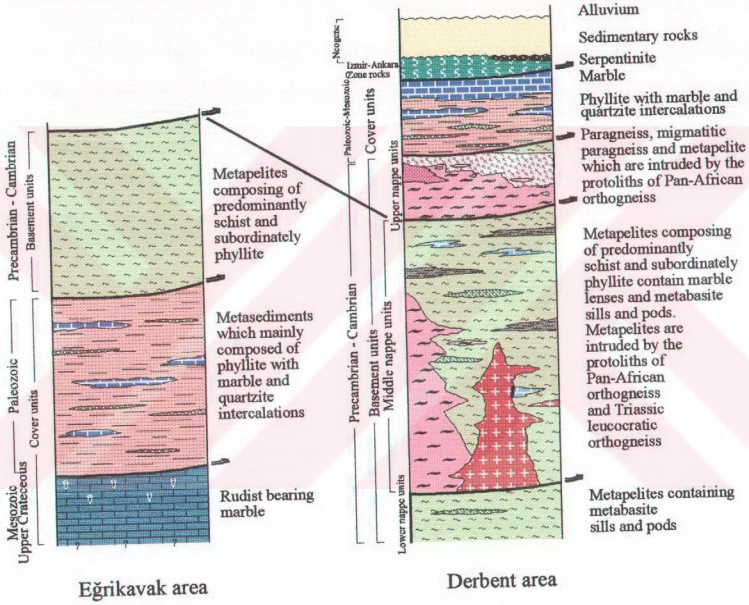


Figure 6.1. Simplified columnar section of Eğrikavak area , northeast of Aydın , and Derbent area, south of Alaşehir in the Ödemiş-Kiraz Submassif.

√ Distribution of the leucocratic orthogneisses

The leucocratic orthogneisses were first recognised around Derbent area by Akkök (1983) and called as "Dede Dağı granite". The author suggests that this Late Triassic granite intruded into the metapelites which were metamorphosed under the greenschist facies conditions which took place before the emplacement of granites. Şengör et al.

(1984) assumed that the intrusion of the granites is closely related to the closure of northern branch of Paleotethys which is called as "Karakaya Ocean". Akkök et al. (1984), Şengör et al. (1984) and Dora et al. (1994) emphasize that in Ödemiş-Kiraz and Demirci-Gördes Submassifs the distribution of the Triassic granites displays a distinct alignment along a NE-SW trending zone which is 6 km x 40 km in dimention. Similar to Derbent area, the presence of same leucocratic orthogneisse bodies which coincide roughly with this zone are also reported in north of Alaşehir and Simav, Demirci-Gördes Submassif, by Candan (1994), Dannat (1997). However, in recent years, some new leucocratic orthogneiss stocks and sills which occur outside of this zone have been recognized in Ödemiş-Kiraz Submassif. These outcrops are situated in 2 km northwest of Bayındır, 1 km southwest of Bayramlık village, southeast of Kemalpaşa and 4 km south of Allahdiyen village, south of Salihli (Figure 6.2). These new occurences disprove the assumption of a NE-SW trending alingment of Triassic orthogneisses and, on the contrary, favor the presence of a regional magmatic activity during the Early-Middle Triassic time overall the Menderes Massif.

√ Geochemistry and tectonic setting of the Pan-African orthogneisses

Based on the geochemical characteristics and ages three magmatic events can be discriminated in the Menderes Massif. These are; I) Pan-African, ii) Triassic and iii) Tertiary events. It has been determined by the geochronological methods that the oldest magmatic activity took place at the Precambrian-Cambrian boundary (Hetzel and Reischmann, 1996; Dannat, 1997; Hetzel et al., 1998; Dannat and Reischmann, 1998, Loos and Resichmann, 1999). These huge-sized batolitic granites which intruded into metadetritic sequence of the Pan-African basement were transformed to the granitic/augen and banded gneisses by multi-stage of deformations and matemorphisms. In the previous studies, different ideas for the protolihts of the gneisses have been suggested. In some studies these rocks are regarded to be derived from the sedimentary rocks (Schuling, 1962; Başarır, 1970, 1975; Akat et al., 1975; Akdeniz ve Konak, 1979; Öztürk ve Koçyiğit, 1982; Akkök, 1983; Akkök et al., 1984; şengör et al., 1984; Satır and Friedrichsen, 1986). Öztürk and Koçyiğit (1982) propose a sedimentary origin for the gneisses deu to the intercalation of these rocks with quartz arenites which show some traces interpreted as primary crosbedding. The ages scattered between 545-670 based on Rb/Sr whole rock isochron age interpreted as the sedimentation ages of the protoliths of the gneisses by Satır and Friedrichsen (1986). A granitic protolith has also been suggested for the orthogneisses by many authors (Graciansky, 1965; Konak, 1985; Erdoğan, 1992; Bozkurt et al.,1993, 1995; Dora et al.,1994, 1995; Hetzel an Reischmann, 1996; Dannat, 1997; Dannat and Reischmann, 1998; Hetzel et al., 1998; Koralay and

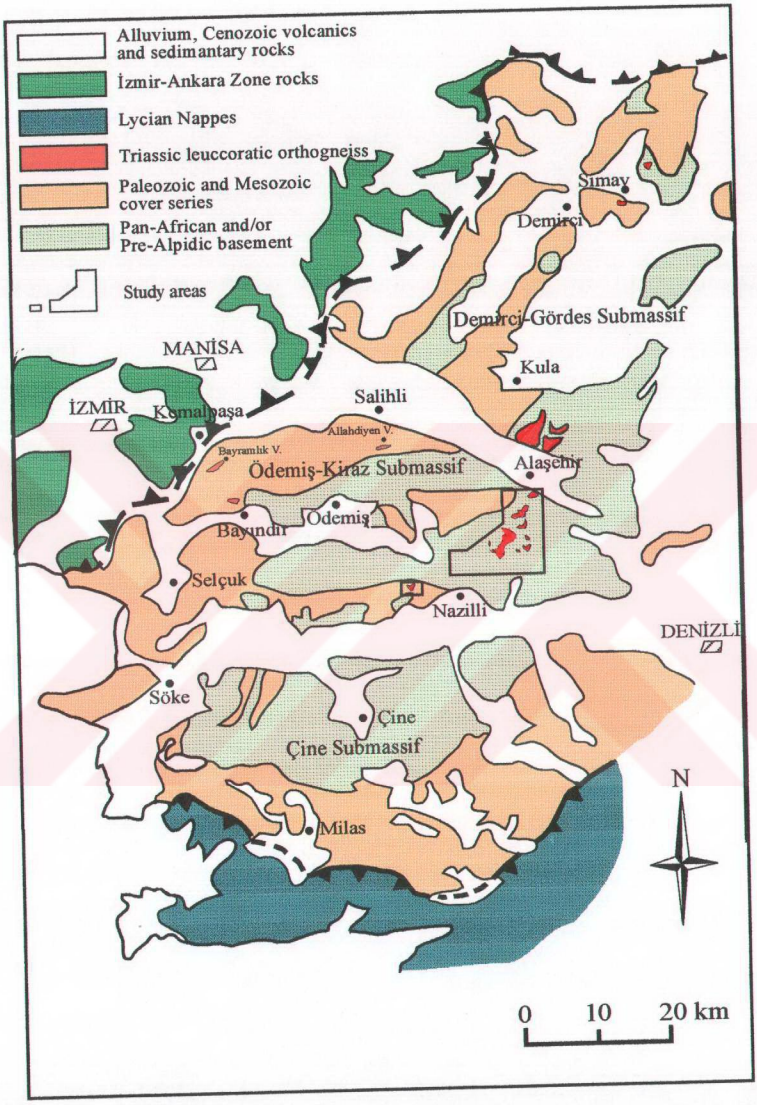


Figure 6.2. Simplified geological map of the Menderes Massif showing the distribution of leuccocratic orthogneisses, modified from Candan and Dora (1998).

Dora, 1999; Loos and Reischmann, 1999). This assumption is mainly based on the preserved primary intrusive contact relationships between augen/granitic gneisses and country rocks which dominated by schist and phyllites (Erdoğan, 1992, 1993; Bozkurt et al., 1995). Konak et al. (1987) and Dora et al. (1990) make a discrimination between augen and granitic gneisses. According to these authors, while the augen gneisses have a distinct sedimentary origin, the granitic gneisses were derived from a granitic precursor by the regional metamorphism. Whereas, Dora et al. (1994) suggests that the protoliths of all gneisses with different structures are syn- to post-metamorphic granites which intruded into the basement during the last stage of Pan-African orogeny. Based on the geochemical charactersitics, the protoliths of the augen gneisses were calc-alkaline, peraluminous, S-type, syn- to post-tectonic granites and granodiorites (Bozkurt et al., 1993, 1995; Dannat, 1997; Koralay and Dora, 1999).

The similar geological, geochemical and geochronological evidence which are described with all details in the previous chapters were obtained from Derbent area. The well preserved original intrusive contact relationships between augen/granitic gneisses and schists clearly reveal the granitic origin of these rocks. These rocks were derived from the S-type, peraluminous, syn- to post-collisional granites and granodiorites with calc-alkaline affinity. The gneisses in Derbent area can be obviously correlated with those of Çine gneisses in terms of field evidence, geochronological data and geochemical composition.

√ Geochemistry and tectonic setting of the Triassic leucocratic orthogneisses

The Early-Middle Triassic granites observed widely in the Menderes Massif characterise the second stage of regional magmatic activity. The products of this magmatic activity which is dated by single zircon evaporation method is found only as the leucocratic orthogneisses (Koralay et al., 1998; Koralay and Dora, 1999; Koralay et al., 2001). Some of the bodies coexisting in the Derbent area are described as "quartzite" and "quartzo-feldspatic gneiss" by Akkök (1981, 1983). However, Koralay (1993) emphasizes the presence of the great similarities of these rocks in terms of mineralogical, textural and geochemical characteristics and corelates them with Dede Dağı granite. These rocks which have a granitic origin display well-preserved intrusive contact relationships with schists (Akkök, 1981, 1983; Şengör et al., 1984; Koralay, 1993).

Based on the geochemical composition which is given in detail in previous chapter, these rocks are peraluminous, S-type, syn- to post-collisional granites with calc-alkaline affinity and were converted to the leucocratic orthogneisses during the Alpine

metamorphism under amphibolite facies conditions (Koralay, 1993; Dannat, 1997; Koralay and Dora, 1999; Koralay et al., 2001).

The leucocratic orthogneisses in Derbent and Demirhan areas display well-preserved intrusive contact relationship with country rocks. The most typical evidence which prove the original intrusive character can be given as follows: 1) The widespread occurences of aplitic veins in the country rocks consisting of Pan-African schists and orthogneisses, 2) the presence of numerous schist xenolites reaching up to 1 km in length along the marginal zones of the granites and 3) the cross-cut relation between granites and the schistosity of the country rocks. Thus, geological, geochemical and geochronological evidence obtained from Derbent area is consistent with the previous evidence.

√ Geochronology of the Pan-African orthogneisses

In most of the previous studies, it has been accepted that the great majority of orthogneisses were derived from syn- to post-collisional granitoids which were intruded into the Late Proterozoic clastic sediment during the latest stage of the Pan-African metamorphism (Dora et al., 1994, 1995; Hetzel and Reischmann, 1996; Dannat and Reischmann, 1998; Hetzel et al., 1998; Koralay and Dora, 1999).

These orthogneisses, augen/granitic gneisses, generally have mineral paragenesis, orthoclase, plagioclase, quartz biotite, muscovite and garnet, which is typical for metagranitic rocks. They occur mainly granitic/granodioritic in composition. On the other hand, in recent studies, it is determined that some of the orthogneisses which occur tonalitic in composition and have been experienced by HT, LP metamorphism which is characterise by the presence of sillimanite and orthopyroxene (Candan, 1995). There is no geochronological investigations on these HT orthogneisses. For this reason, the intrusion age of them is still debated. It can be concluded that the orthogneisses with HT mineral assemblage should be older than the other HT free orthogneisses which dated at about 550 Ma.

In first attemps, Rb-Sr age determinations of whole rocks on orthogneisses yielded isochron ages of 490±90 (Dora, 1975;1976) and 471±9 Ma (Şengör et al., 1984; Satır and Friedrichsen, 1986) which were interpreted as intrusion age of the protoliths. Recently, detailed geochronological investigations was carried out on orthogneisses (Table 6.1)(Figure 6.3). These data pointed out the reliable intrusion age of the

Table 6.1. Age data from orthogneissic rocks in the Menderes Massif.

Rock Type	Location	Method	Age (Ma)	Authors
Augen Gneiss	N of Selimiye Çine Submassif	$^{207}Pb/^{206}Pb$	546.0±1.6	
Augen Gneiss	N of Selimiye Çine Submassif	$^{207}Pb/^{206}Pb$	546.4±0.8	
			546.2±1.2 Ma	Hetzel and Reischmann (1996)
Augen Gneiss	NE of Kuyucak Ödemiş-Kiraz S.	$^{207}Pb/^{206}Pb$	528.0±4.3	
Augen Gneiss	W of Buldan Ödemiş-Kiraz S.	$^{207}Pb/^{206}Pb$	528.1±1.6	
Augen Gneiss	SE of Kiraz Ödemiş-Kiraz S.	$^{207}Pb/^{206}Pb$	538.1±2.6	
Augen Gneiss	SE of Simav Demirci-Gördes S.	$^{207}Pb/^{206}Pb$	541.4±2.5	
Augen Gneiss	Demirci Demirci-Gördes S.	$^{207}Pb/^{206}Pb$	537.2±2.4	
Augen Gneiss	Demirköprü Dam Demirci-Gördes S.	$^{207}Pb/^{206}Pb$	544.1±4.3	
			~ 540 Ma	Dannat (1997)
Granitic Gneiss	N of Selimiye Çine Submassif	$^{207}Pb/^{206}Pb$	563±3	
Granitic Gneiss	N of Selimiye Çine Submassif	$^{207}Pb/^{206}Pb$	536±9	
Granitic Gneiss	N of Selimiye Çine Submassif	$^{207}Pb/^{206}Pb$	572±7	
Granitic Gneiss	N of Selimiye Çine Submassif	$^{207}Pb/^{206}Pb$	521±8	
Granitic Gneiss	N of Selimiye Çine Submassif	$^{207}Pb/^{206}Pb$	556±4	
Granitic Gneiss	N of Selimiye Çine Submassif	$^{207}Pb/^{206}Pb$	546±5	
Granitic Gneiss	N of Selimiye Çine Submassif	$^{207}Pb/^{206}Pb$	551±5	
			~ 550 Ma	Loos and Reischmann (1999)
Metagranite	SW of Çine Çine Submassif	$^{207}Pb/^{206}Pb$	**547.2±1.0 Ma**	Gessner et al. (2001)
Metagranite	Birgi Ödemiş-Kiraz S.	U-Pb	**551.5±1.4 Ma**	Hetzel et al. (1998)
Augen gneiss	S of Alaşehir Ödemiş-Kiraz S.	$^{207}Pb/^{206}Pb$	**561.5±0.8 Ma**	This Study
Augen gneiss	S of Alaşehir Ödemiş-Kiraz S.	$^{207}Pb/^{206}Pb$	**570.5±2.2 Ma**	This Study

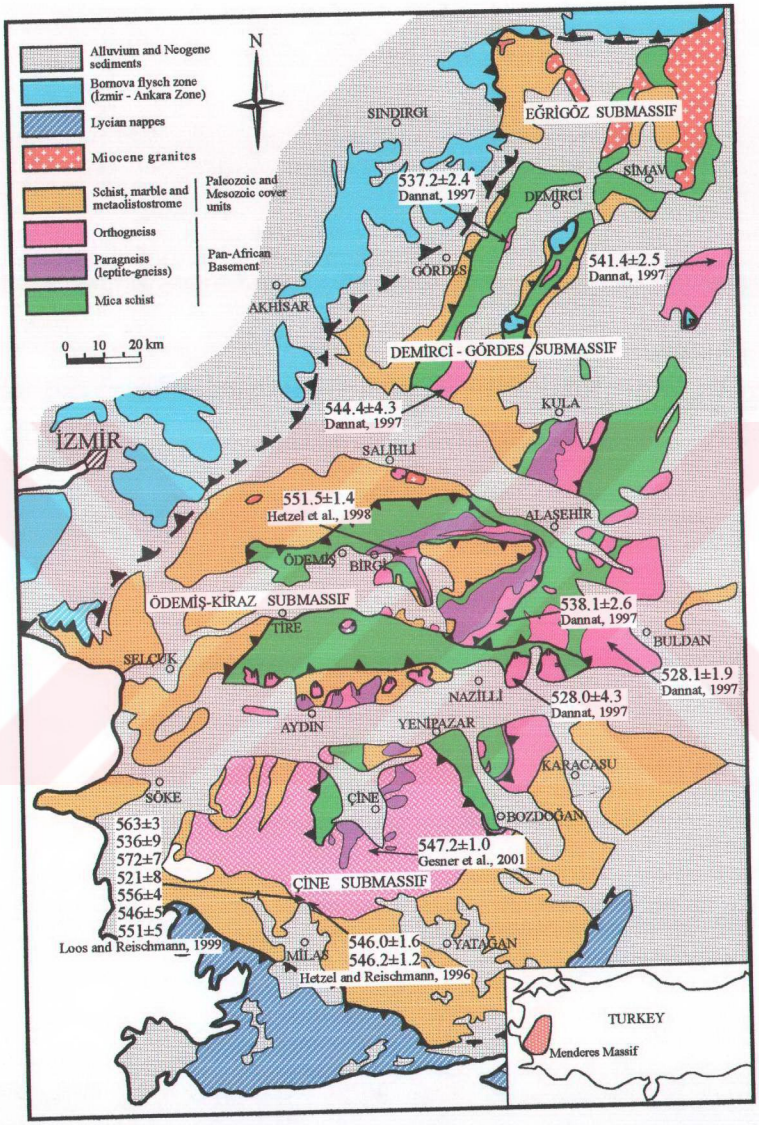


Figure 6.3. Simplified geological map of the Menderes Massif showing geochronological age data obtained from orthogneisses, after Candan and Dora (1998). Data from Hetzel and Reischmann, 1996; Dannat 1997, Hetzel et al., 1998; Loos and Reischmann, 1999, Gessner et al., 2001.

protoliths of orthogneisses. The geochronological data of the zircons from augen gneiss samples clearly indicate that the granitic precursor of augen gneisses intruded at 546.2±1.2 Ma (Latest Proterozoic) (Hetzel and Reischmann, 1996). This age is interpreted as the intrusion age of the protoliths of augen gneisses in the southern Menderes Massif. The magmatic ages yielded between 528 and 544 Ma indicate that the main igneous event of the Menderes Massif was at the Precambrian/Cambrian border (Dannat, 1997). Loos and Reischmann (1999) conclude that the intrusion ages of the granitic precursors of gneisses range from 521±8 to 572±7 Ma with an average at about 550 Ma. Gessner (2001), also reports an intrusion age 547.2±1.0 Ma from a metagranite in the Çine Submassif. These data were obtained from zircons by the $^{207}Pb/^{206}Pb$ single-grain evaporation method. Furthermore, a metagranite from the Ödemiş-Kiraz Submassif, which has been dated by conventional U-Pb dating, also revealed an age of 551.5±1.4 Ma which is interpreted as crystallization age of zircon and the granite (Hetzel et al., 1998).

The ages of these orthogneisses are concentrated mainly between the time interval of 541 to 551 Ma (Table 6.1). On the other hand, it is clear that the magmatic activity had occurred a longer period between 528 to 572 Ma. Zircon evaporation dating of two orthogneiss samples yielded mean ages of 561.5±1.8 and 570.5±2.2 Ma in this study. These ages revealed that the intrusion of the protoliths of orthogneisses occurred at the time of main magmatic phase, between 528 to 572 Ma, which took place in the Pan-African basement of the Menderes Massif. This supports that the age of the HT, LP metamorphism should be older than ~ 570 Ma.

√ Geochronology of the Triassic leucocratic orthogneisses

After the understanding of the importance of the leucocratic orthogneisses in the the Menderes Massif recent years, the geochronological and geochronological studies have been focused on these rocks (Figure 6.4). Dannat (1997) and Dannat and Reischmann (1998) give an intrusion age of 227-240 Ma based on $^{207}Pb/^{206}Pb$ single zircon evaporation method for the protoliths of the leucocratic orthogneisses in the Ödemiş-Kiraz Submassif and Gördes Submassif. Same researchers report that the protoliths of leucocratic orthogneisses show Nd isotopic composition $İ(Nd)_t$ values between –2 and +5, indicating that the protoliths of leucocratic orthogneisses originated from a hybrid magma (Dannat and Reischmann, 1998). The same authors supposed that leucocratic orthogneiss have a crustal component of ~ 10-20 %. They also proposed that the precursors of the leucocratic orthogneisses are not chemically akin to pure S-

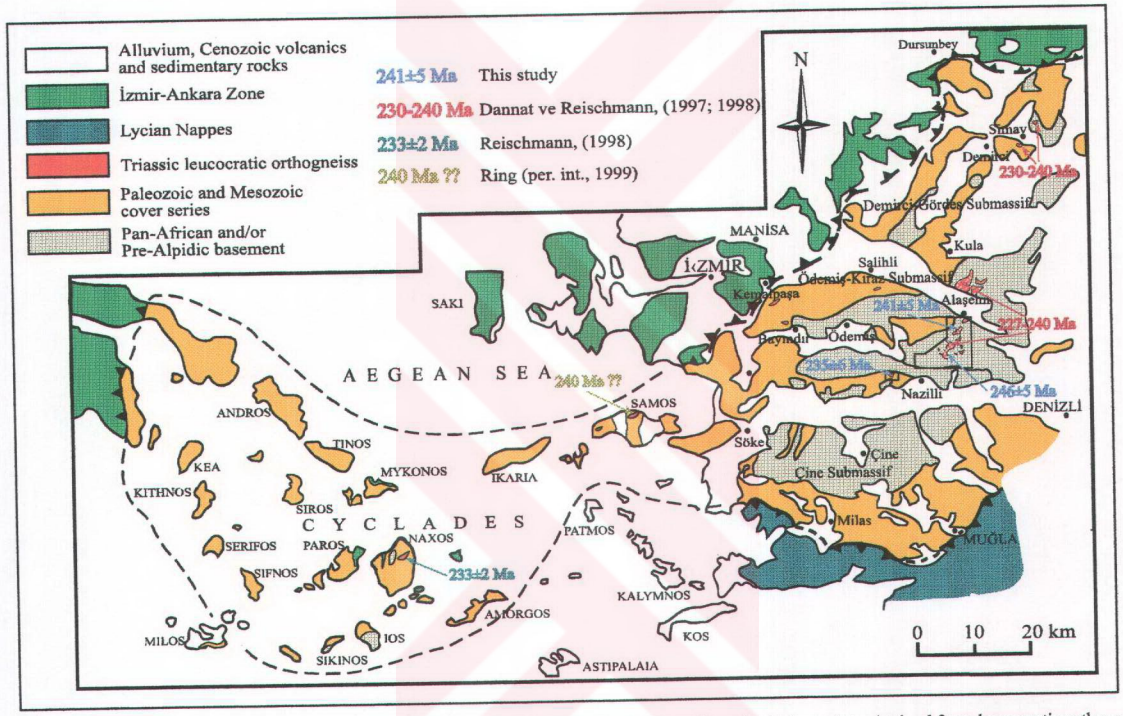


Figure 6.4. Simplified geological map of the Menderes Massif. and the Cyclades showing geochronological age data obtained from leucocratic orthogneisses, modfied after Candan and Dora (1998). Data from Dannat and Reischmann, 1996, 1997; Reischmann, 1998.

type granites but hybrid granites with a portion of sedimentary material. These type of granites show volcanic arc or continent collision environment which is typical tectonic setting for such granites is. Dannat and Reischmann (1998) also emphasize that the bimodal distribution of the magmatic events at the Precambrian/Cambrian boundary and in Triassic times obtained from the granitic precursors of gneisses of the Menderes Massif is not documented in the basement of neighboring regions such as Cycladic Complex. However, some of the leucocratic orthogneisses in Naxos island were dated at about 233±2 Ma by single zircon evporation method (Reischmann, 1998). This age is interpreted as the intrusion age of the precursor rocks of the gneisses.

The investigations of zircon grains of the leucocratic orthogneisses in the study areas yield $^{207}Pb/^{206}Pb$ ages between 235 and 246 Ma. These ages, i.e. Early-Middle Triassic (Odin, 1994; Gradstein and Ogg 1996), are interpreted as the intrusion age of the protoliths of leucocratic orthogneisses. As SEM- and CL-photographs demonstrate, the analysed zircon populations show distinct magmatic zonation and typical igneous morphologies. The ages of the leucocratic orthogneisses in the study area, central Menderes Massif, which have intrusive contact relationships with the Pan-African basement units and Paleozoic cover series are in good agreement with other Triassic ages which span a time interval between 227 Ma - 240 Ma (Dannat, 1997; Dannat and Reischmann 1998).

√ Latest Proterozoic-Early Paleozoic evolution of the Pan-African basement

Turkey is located in the eastern Mediterranean at the geological margin between the Gondwana and Laurasian continents. On a Latest Neoproterozoic-Early Cambrian reconstruction of continents around the eastern Mediterranean, the Menderes Massif forms the southern end of the Pan-African orogenic collage of northeastern Africa and Arabia (Figure 6.5). In the previous studies, Pan-African evolution spanned an interval between 1100 and 500 Ma in these regions (Al-Shanti, 1976; Greenwood et al., 1976). Although, Gass (1982) proposed that Pan-African has been divided stratigraphically into three major divisions; Lower (1200-1000 Ma ago), Middle (1000-600 Ma ago) and Upper Pan-African (600-500 Ma ago) respectively. However, Kröner (1984) pointed out that onset of "Pan-African Orogeny", at least at the northeast Africa, should be considered to have spanned only the 900 to 500 Ma interval (Kröner et al., 1983) by the recalculated ages of magmatic and metamorphic events obtained by Fleck et al. (1980). Dalziel (1991) and Hofmann (1991) suggested that the Pan-African and Brazilide ocean basins within the amalgamating cratons of Gondwana closed during the

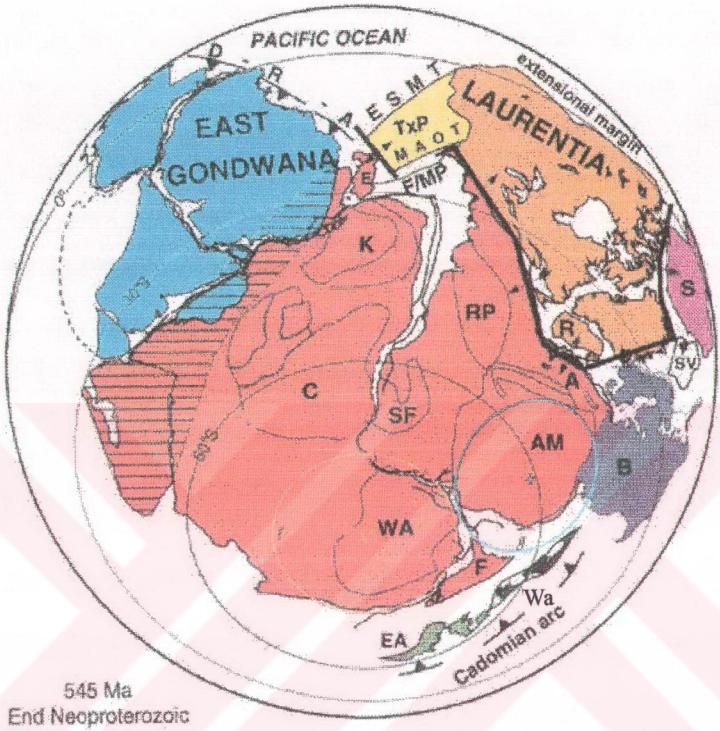


Figure 6.5. Geologically constrained reconstraction of the Pannotia supercontinent at the Precambrian-Cambrian boundary, after Dalziel (1997). Thick lines: incipient mid-Iapetus ridges; horizontal lines: East African collisional orogen involving East and West Gondwana. AM: Amazonian craton; B: Baltica (Russian craton); C: Congo craton; DRA: Delamerian Ross arc; EA: east Avalonia (southern British Isles); ESMT: hypothetical Ellsworth-Sonora-Mojave transform; F: Florida; F/MP: Falkland-Malvinas Plateau; MAOT: hypothetical Malvinas-Alabama transform; R: Rockall Plateau; RP: Rio de la Plata craton; S: Siberia (Angara craton); SF: São Francisco craton; SV: Svalbard Block; TxP: hypothetical Texas Plateau; WA: West African craton; Wa: west Avalonia.

Neoproterozoic to, at least, Cambrian time. Closure of several Pan-African – Brazilide ocean basins have resulted amalgamation of West Gondwana (Stern, 1994; Trompette, 1994; Stein and Goldstein, 1996; Unrug, 1996). The collision with Arabian terranes constituted Gondwana-Land and wrench faulting, granite plutonism and molasse sedimentation occured during 630-530 Ma (Piper, 2000).

Şengör et al. (1984), emphasize based on the age at about 500±10 Ma which is interpreted to represent the deformation and metamorphism of the core series of the Menderes Massif that the metamorphism of the Precambrian basement is related to the Pan-African orogeny. The granitic precursor of orthogneisses dated at about 550 Ma are regarded to be related to the magmatic activity subsequently following the Pan-African orogeny (Dora et al., 1994, 1995; Hetzel and Reischmann, 1996; Dannat and Reischmann, 1998; Hetzel et al., 1998; Koralay and Dora, 1999). The same common magmatic activity is also documented in NE-E Africa, forming a part of West Gondwana by Stern (1994) and Kröner et al. (1996) (Figure 6.6). Furthermore, the Pan-African granulites were recognised in numerous localities such as east of Africa, west of Madagascar, in cntral granulit belt of Sri Lanka, south of India and northwest of Antarctica along a zone extending N-S direction. Similarly, the relics of granulite facies metamorphism in the Pan-African basement of the Menderes Massif were reported by Candan (1995) and Dora et al. (2001). This evidence when combine with the reconstraction of the continents during Late Neoproterozoic-Cambrian boundary reveal that the Pan-African basement of the Menderes massif was formed as a part of West Gondwana (NNE Africa) during the Pan-African orogeny. Syn- to post- Pan-African magmatism which is characterised by the granite intrusions are commonly recognized in this orogenic belt and also in the Menderes Massif.

√ Tectonic setting of the Menderes Massif during the evolution of the Paleotethys and Neotethys

Although, there are some different views, on the presence of a mainly Paleozoic ocean north of Cimmerian continent, the Paleotethys, and a younger Late Paleozoic-Mesozoic ocean located south of this continent, Neotethys, is generally accepted by the several authors (Şengör, 1979; Şengör et al., 1980; Şengör and Yılmaz, 1981; Şengör et al., 1984; Stampfli et al., 1998). The Paleotethys was located to the north of the İstanbul Zone (Şengör et al., 1980, 1984). Robertson and Dixon (1984) and Okay (1989) have placed the Paleotethys between the Istanbul and Sakarya Zones. On the other hand, the Paleotethys have been located to the south of Sakarya Zone (Okay et al., 1996).

There are some different assumptions related to the geographical position and closure age of the Paleotethys. The Paleo-tethyan evolution was occured southward dipping subduction of Paleotethys beneath northern Turkey during the Permian-Liassic time (Şengör and Yılmaz,1981). This closure was caused by the collision of Laurasia with a Cimmerian continent or a group of continents. This rifting marked the birth of

Neotethys behind the Cimmerian continents (Şengör et al., 1980; Şengör and Yılmaz, 1981). However, the subduction of Paleotethyan ocean floor to the south resulted in the openning of Karakaya ocean during the Early Triassic, which closed shortly during the Late Triassic (Şengör and Yılmaz, 1981; Şengör et al, 1984; Tüysüz, 1990). On the other hand, Tekeli (1981) suggested that the Karakaya ocean had opened during the latest Carboniferous. But, Okay et al. (1996) suggested that the Karakaya orogeny, reflecting the closure of the Paleotethys, was caused by the collision of the oceanic volcanic arc and associated accretionary complexes with the Laurasian passive continental margin during the Latest Triassic time. This collision results to fuse of Variscan elements drifting away from the active Laurasian margin with the Cimmerian blocks derived from Gondwana (Stampfli et al., 1998).

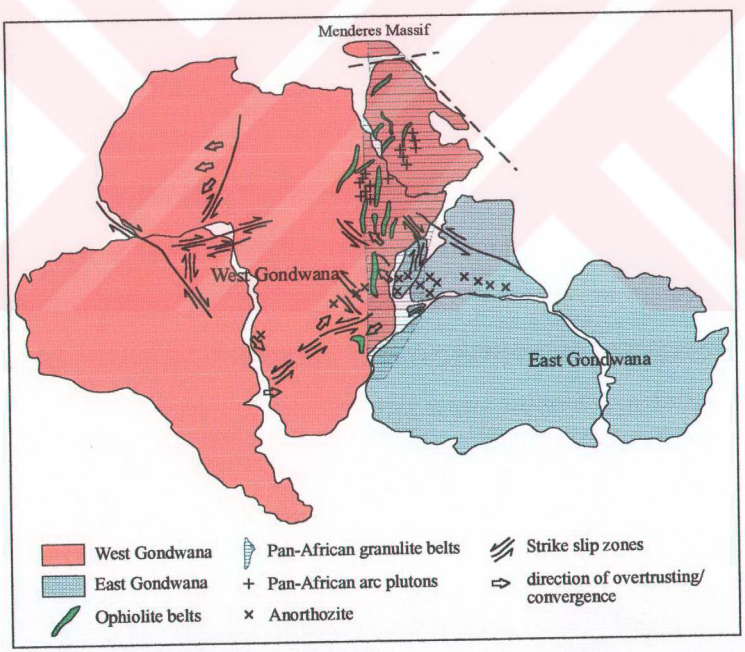


Figure 6.6. Simplified tectonic map of East and West Gondwana including Pan-African suture at Late Paleozoic time, data after Şengör et al. (1984); Dalziel (1997) and Piper (2000).

At the end of Paleozoic (Permian), the Menderes Massif was a part of Gondwana (NE Africa) and the Paleotethys was situated at the northern part of the Menderes Massif (Şengör and Yılmaz, 1981; Stampfli et al., 1998) (Figures 6.5, 6.6). During the closure of Paleotethys, a group of continents which are named as Cimmerian continents were rifted away from Gondwana land and drifted to the north (Şengör, 1979; Şengör et al., 1980; Şengör and Yılmaz, 19981; Stampfli et al., 1998). The Pan-African basement of the Menderes Massif was formed a part of these continental fragments. Although, the orthogneisses dated at about 550 Ma occur commonly in the Pan-African basement of the Menderes Massif, this magmatic activity was not recognized in the Cycladic complex. However, the contrary to the Menderes Massif, the Variscan granites, augen gneisses, are common in the Cyclades. This evidence indicate that during the Pan-African and Variscan orogenies the Menderes Massif and the Cycladic Complex were situated at different positions. The presence of the Early/Middle Triassic leucocratic orthogneisses in both of the Menderes Massif (Dannat, 1997; Dannat and Reischmann, 1998; Koralay and Dora, 1999; Koralay et al., 2001) and Cycladic complex (Reischmann, 1998) evidence that during the Permian-Triassic boundary these two crystalline complexes were close to each other and were effected by the same magmatic activity. In the tectonic model proposed by Stampfli et al. (1998) while the Menderes Massif were drifting northwards, the Cycladic complex has already collided with Pelagonian superterrane forming a part of Laurasia. The closure of the Paleotethys ocean which was located between the rifted part of Gondwana and Laurasia took place during the Early Jurassic (Sinemurian) (Stampfli et al., 1998). Okay et al. (1996) suggested that back-arc rifting occured in the Anatolide-Tauride block where carbonate sedimentatiton prevailed during the Late Permian due to the southward subduction of Paleotethys. They also claim that the collision of the volcanic arc and related acretionary complex with the continental margin of the Laurasia took place during the Late Triassic time.

Sakarya and İstanbul Zones and Variscan basement of Cyclades were situated at the north of Menderes Massif as a part of Laurasia during the Variscan orogeny (Okay et al., 1996; Stampfli et al., 1998). Whereas during this orogeny the Menderes Massif was still connected with Gondwana (Stampfli et al., 1998). In Permian time, southward subduction of the Paleotethys caused to develop back arc rifting on Gondwana. During this period, the Menderes Massif was rifted from the Gondwana and drifted towards north (Stampfli et al., 1998). In this tectonic model, it has been accepted that during this period, the Menderes Massif which is regarded to be a part of Cimmerian continents. According to Okay et al. (1996, 2001), the closure of Paleotethys took place during Late Triassic and caused blue schist to eclogite facies metamorphism in Nilüfer unit. Whereas, Stampfli et al. (1998) proposed that the closure of Paleotethys took place

during Early Jurassic time. Furthermore, the intrusion of the Cycladic complex and the Menderes Massif by Triassic leucocratic orthogneisses also supports the similar geodynamic evolution during the Triassic time. Based on the tectonic setting and intrusion ages of the protoliths of leucocratic orthogneisses the closure age of the Paleotethys around Eastern Mediterranean might be suggested as Latest Permian-Earliest Triassic (Figure 6.7). During the following stage, the protoliths of the Early/Middle Triassic leucocratic orthogneisses intruded into the Pan-African basement and Paleozoic cover series of the Menderes Massif (Figure 6.8).

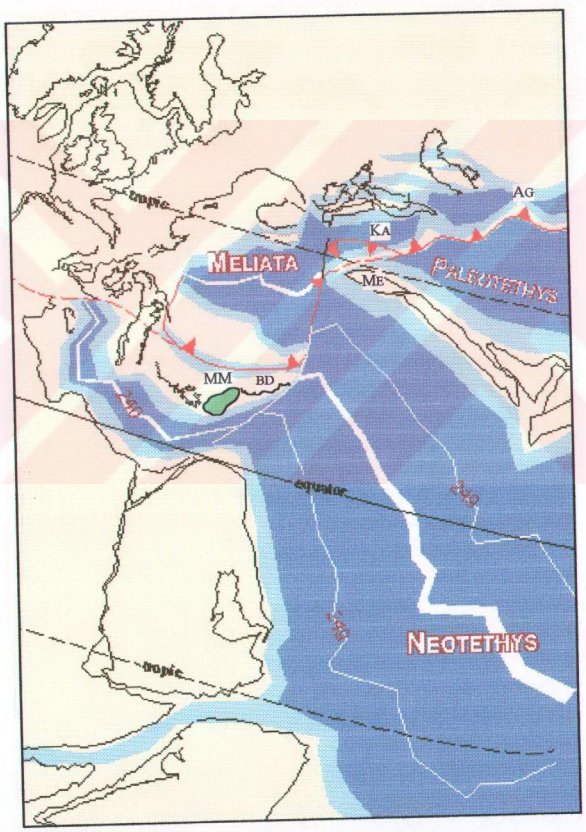
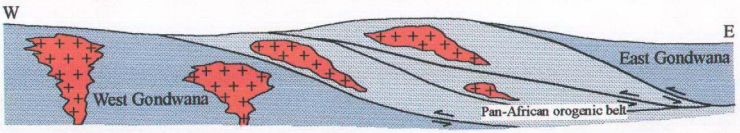


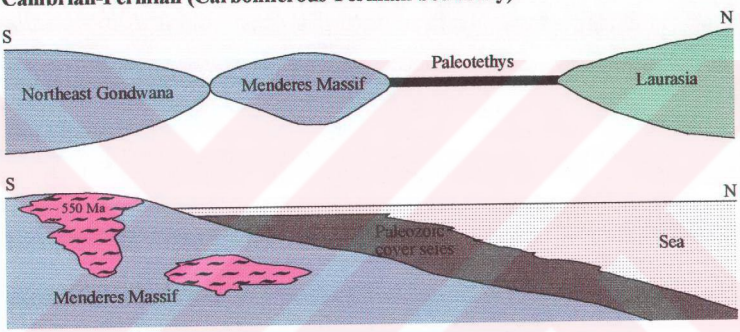
Figure 6.7. Reconstruction of Eastern Mediterranean at Latest Permian time, modified from Stampfli et al., (1998). Green coloured elipsoidal area represets the locality of the Menderes Massif proposed by this study. AG: Agh-Darband; BD: Beydağları; KA: Karakaya; ME: Menderes and Taurides; MM: Menderes Massif.

Latest Neoproterozoic-Early Paleozoic (Earliest Cambrian)



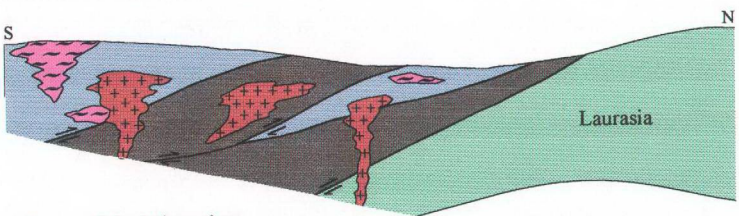
- amalgamation of East and West Gondwana
- polyphase metamorphism and deformation of the Late Proterozoic sediments during the Pan-African orogenesis
- intrusion of the ~ 550 Ma syn- to post-tectonec granitoids

Cambrian-Permian (Carboniferous-Permian boundary)



- sedimentation of Paleozoic cover sequences of the future Menderes Massif

Late Permian-Early Triassic



- closure of the Paleotethys
- tectonic juxtaposition of the Pan-African basement and the Paleozoic cover series
- metamorphism (?) of the Pan-African basement and the Paleozoic cover series
- intrusion of the Triassic granites into the Pan-African basement and Paleozoic cover series

Figure 6.8. Schematized sequential cross section showing the pre-Triassic tectonic evolution of the Menderes Massif. Discussions is in the text.

However, the closure time of the Paleotethys proposed by this study contradict with the views of the other researchers (Şengör, 1979; Şengör and Yılmaz, 1981; Okay et al., 1996; Stampfli et al., 1998) summerized above. On the other hand, the geographical position of the Menderes Massif during Late Permian-Triassic time has been reviewed on the tectonic model proposed by Stampfli et al. (1998). Although, the tectonic setting of the Triassic leuccoratic ogranites are consistent with this model. There are still some problems on the general concept of the evolution of the Paleotethys and Neotethys oceans in the western part of Turkey.

CHAPTER SEVEN
CONCLUSIONS

The result of this study are summarized as follows;

1- It is determined that the study areas consist of different nappe slices, as observed in other part of the Menderes Massif, which record different geological evolutions. The metamorphic rock succession of the Derbent area can be divided into four nappe units. In ascending order, the lower, middle and upper nappe units are represented by internal imbrication of the Pan-African basement series. The uppermost nappe units consisting of the Paleozoic-Mesozoic cover series rests tectonically upon the upper nappe units of Pan-African basement. In the Demirhan area, metapelites of cover series are overlain by a nappe unit which completely consists of Pan-African orthogneisses.

2- The precursor rocks of augen/granitic orthogneisses intruded into the protoliths of the Pan-African basement series which consist of metapelites and phyllites. Numerous sills and dykes of orthogneisses, which clearly cross cut the schistosity of schists and have sharp contacts, are found in schists close to the margins of orthogneiss. Also, numerous schist xenolites are observed in orthogneisses close to the contact. These evidence prove the granitic origin of the gneisses and the original intrusive contact relationship between schist and orthogneiss.

3- The schist and orthogneisses of the Pan-African basement and metapelites of Paleozoic cover series are intruded by the protoliths of leucocratic orthogneisses. The leucocratic orthogneisses include peripherally numerous schist xenolites which are particularly common close to the contact. Furthermore, the sills and dykes of leucocratic orthogneiss are observed in country rocks. The common presence of the xenolites in leucocratic orthogneisses and the vein rocks in country rock clearly reveal the original intrusive contact relationship between leucocratic orthogneiss and metapelites and orthogneiss.

4- The numerous leucocratic orthogneiss bodies occuring as stocks and vein rocks in the study areas and the new localities overall the Menderes Massif represent a regional scale effects of a magmatic activity in the Menderes Massif.

5- The geochemical data indicate that the protoliths of Pan-African orthogneisses were calc-alkaline, peraluminous, S-type, syn- to post-tectonic granites and granodiorites.

6- The geochemical data reveal that the protoliths of leucocratic orthogneisses were S-type granites of calc-alkaline, peralumino character, reflecting a crustully derived magma.

7- The SEM and CL photomicrographs demonstrate that the analysed zircon populations in orthogneisses have distinct magmatic zoning and typical igneous morphology. The $^{207}Pb/^{206}Pb$ ages of 561.5±1.8 and 570.5±2.2 Ma are interpreted as the intrusion ages of the protoliths of the Pan-African orthogneiss.

8- The SEM and CL photomicrographs show that the analysed zircon populations of leucocratic orthogneisses have distinct magmatic zoning and typical igneous morphology. The dating of zircon grains of leucocratic orthogneisses yields $^{207}Pb/^{206}Pb$ ages of 234.9±5.8, 241.1±5.2 and 245.7±4.6 Ma. These ages are interpreted as the intrusion age of the protoliths of leucocratic orthogneisses.

9- The geochronological and geochemical evidence indicate that the leucocratic orthogneisses were emplaced into the Pan-African basement and Paleozoic cover series during Early-Middle Triassic time most probably related to the closure of Paleotethys.

10- It can be suggested, based on the tectonic setting and ages of the syn- to post-tectonic leucocratic orthogneiss, that the closure of the Paleotethys at around Eastern Mediterranean might be taken place during Latest Permian time.

11- The intrusion of the Triassic leucocratic orthogneisses into both of the Pan-African basement and Paleozoic cover units reveals that these two units were tectonically juxtaposed prior to Triassic time.

12- The apperant presence of Triassic leucocratic orthogneisses in both of the Cycladic complex and the Menderes Massif indicates that the Pan-African basement and Paleozoic cover of the Menderes Massif was close to the Pre-Alpidic basement of the Cycladic complex prior to the intrusion of the Early/Middle Triassic granites.

REFERENCES

Akat, U., Öztürk, Z., Öztürk, E., & Çağlayan, A. (1975). Menderes Masifi güneyi – GB Toros Kuşağı ilişkisi (ön rapor), MTA Raporları, No: 5488, (unpublished).

Akdeniz, N., & Konak, N. (1979). Menderes Masifi'nin Simav dolaylarındaki kaya birimleri ve metabazik, metaultramafik kayaların konumu. Türkiye Jeol. Kur. Bült., 22, 175-183.

Akkök, R. (1981). Menderes Masifi'nin gnayslarında ve şistlerinde metamorfizma koşulları, Alaşehir/Manisa. Türkiye Jeoloji Kurumu Bülteni, C 24, 11-20.

Akkök, R. (1983). Structural and metamorphic evolution of the northern part of the Menderes Massif: New data from the Derbent area and their implication for the tectonics of the massif. J Geol, 91: 342-350.

Akkök, R. (1985). Ultramafic inclusions in the Menderes Massif, near Alaşehir, Manisa. VI. Coll. Geol. of Aegean Region, Turkey, 17-29.

Akkök, R., Satır, M., & Şengör, A.M.C. (1984). Menderes Masifi'nde tektonik olayların zamanlaması ve sonuçları. Ketin Sempozyumu, Abstracts, 93-94.

Al-Shanti, A.M.S. (1976). Geology of the Ad-Dawadimi district. Bull. Dir. Gen. Min. Res. Jeddah, 13, 57 pp.

Andriessen, P.A.M., Banga, G., & Hebeda, E.H. (1987). Isotopic age study of pre-Alpine rocks in the basal units of Naxos, Skinos and Ios, Greek Cyclades. Geol en Mijnbouw, 6, 3-14.

Aydın, Y. (1982). Geology of the Yıldız mountains (Strandja). Habilitation thesis, Istanbul Technical University, 228 p.

Barker, F., (1979), Trondhjemites: definition, environment and hypothesis of origin. In: Barker F (Ed) Trondhjemites, dacites, and related rocks. Elsevier. p 1-12.

Başarır, E. (1970). Bafa gölünün doğusunda kalan Menderes Masifi güney kanadının jeolojisi ve petrografisi. Ege Üniversitesi Fen Fakültesi İlmi Raporlar Serisi, 102,1-44.

Başarır, E. (1975). Çine güneyindeki metamorfitlerin petrografisi ve bireysel indeks minerallerin doku içerisindeki gelisimleri. DSc Thesis, Ege University, İzmir. (in Turkish with English Abstract).

Bossart, P.J., Meier, M., Oberli, F., & Steiger, R.H. (1986). Morphology versus U-Pb systematics in zircons: a high-resolution isotopic study of a zircon population from a Variscan dyke in the central Alps. Earth Planet. Sci. Lett., 78, 339-354.

Bozkurt, E. (1994). Effects of Tertiary extension in the Southern Menderes Massif, western Turkey. PhD Thesis, University of Keele, 395 p.

Bozkurt, E. (1995). Deformation during main Menderes metamorphism (MMM) and its tictonic significance: evidence from southern Menderes Massif, western Turkey. Terra Abstracts, 7:176.

Bozkurt, E., & Park, R.G. (1994). Southern Menderes Massif: An incipient metamorphic core complex in western Anatolia, Turkey. Journal of Geological Society, London, 151, 213-216.

Bozkurt, E., & Park, R.G. (1997a). Micrstructures of deformed grains in the augen gneisses of southern Menderes Massif (western Turkey) and their tectonic significance. Geol. Rundsch. 86, 103-119.

Bozkurt, E., & Park, R.G. (1997b). Evolution of a mid-Tertiary extensional shear zone in the southern Menderes Massif, western Turkey. Bull. Soc. géol. France, t. 168, 3-14.

Bozkurt, E., & Satır, M. (2000). The southern Menderes Massif (western Turkey): geochronology and exhumation history. IESCA-2000, International Earth Sciences Colloquium on the Aegean Region, İzmir, p. 135.

Bozkurt, E., Park, R.G., & Winchester, J.A. (1992). Evidence against the core/cover concept in the southern sector of the Menderes Massif. International Workshop: Work in progresss on the Geology of Turkey, Keele England, 9-10 April 1992, Abstracts, p. 22.

Bozkurt, E., Park, R.G., & Winchester, J.A. (1993). Evidence against the core/cover interpretation of the southern sector of the Menderes Massif, west Turkey. Terra Nova, 5: 445-451.

Bozkurt, E., Winchester, J.A., & Park, R.G. (1995). Geochemistry and tectonic significance of augen gneisses from the southern Menderes Massif (West Turkey). Geol. Mag., 132: 287-301.

Campston, W., & Pidgeon, R.T. (1986). Jack Hills, a further occurrence of very old detrital zircons in Western Australia. Nature (London), 321, 766-769.

Campston, W., Kinny, P.D., Williams, I.S., & Foster, J.J. (1986). The age and Pb-loss behaviour of zircons from the Isua supracrustal belts as determined by ion microprobe. Earth Planet. Sci. Lett., 80, 71-81.

Candan, O. (1988). Demirci-Borlu arasında kalan yörenin (Menderes Masifi'nin kuzey kanadı) petrografisi, petrolojisi ve mineralojisi. PhD. Thesis, Dokuz Eylül Universitesi, Fen Bilimleri Enstitüsü, İzmir, 163 p.

Candan, O. (1994). Alaşehir kuzeyinde (Menderes Masifi, Demirci-Gördes Asmasifi) gözlenen metagabroların petrografisi ve metamorfizması. Türkiye Jeoloji Bülteni, 37: 29-40, (in Turkish with English Abstract).

Candan, O. (1995). Menderes Masifi'ndeki kalıntı granulit fasiyesi metamorfizması. Tr. J. of Earth Sciences, 4, 35-55, (in Turkish with English Abstract).

Candan, O. (1996). Kiraz-Birgi çevresindeki (Menderes Masifi/Ödemiş-Kiraz Asmasifi) metagabroların petrografisi ve metamorfizması. Yerbilimleri, 18, 1-25, (in Turkish with English Abstract).

Candan, O., & Kun, N. (1991). Possible Pan-African metavolcanics in the Ödemiş Submassif of the Menderes Massif, western Turkey. Bulletin of the Mineral Research and Exploration, 112, 1-16.

Candan, O., & Dora, O.Ö. (1998). Granulite, eclogite and blueschist relics in the Menderes Massif: An approach to Pan-African and Tertiary metamorphic evolution. Geol. Bull. Turkey, 41/1, 1-36, (In Turkish with English Abstract).

Candan, O., Oberhänsli, R., Dora, O.Ö., Partzsch, J., & Çetinkaplan, M. (2000). Polyphase tectono-metamorphic evolution of the Pan-African basement of the Menderes massif: granulite, eclogite and amphibolite facies metamorphism. Abstracts, IESCA-2000, International Earth Sciences Colloquium on the Aegean Region, İzmir, p. 134.

Candan, O., Dora, O.Ö., Oberhänsli, R., Çetinkaplan, M., Partzsch, J., & Dürr, St. (1998). Pan-African high presure metamorphism in the Precambrian basement of the Menderes Massif, western Anatolia-Turkey. 3rd Int. Turkish Geol. Symp., Ankara, Abstracts, p 275.

Candan, O., Dora, O.Ö., Oberhänsli, R., Çetinkaplan, M., Partzsch, J.H., Warkus, F.C., & Dürr, S. (2001). Pan-African high-pressure metamorphism in the Precambrian basement of the Menderes Massif, western Anatolia, Turkey. Int Journ Earth Sciences, 89/4, 793-811.

Cann, J.R. (1970). Rb, Sr, Y, Zr and Nb in some ocean floor basaltic rocks. Earth and Planet. Sci. Lett., 10, 7-11.

Chappell, B.W., & White, A.J.R., (1974). Two contrasting granite types. Pacific Geology, 8: 173-174.

Chen, F., 1999, Variskan and pre-Variskan Geochronology of the Moldanubian zone of the Black Forest, Germany. PhD. Thesis, Geowissenschaftlichen Fakultaet, Eberhard-Karls Universetaet Tübingen, 121 p.

Chen, F., Hegner, E., & Todt, W. (2000). Zircon ages, Nd isotopic and chemical compositions of orthogneisses from the Black Forest, Germany – evidence for a Cambrian magmatic arc. Int. Journ. Earth. Sciences , 88, 791-802.

Clemens, J.D. (1984). Water contenets of silicic to intermediate magmas. Lithos, 17, 273-287.

Clemens, J.D., & Wall, W.J. (1981). Crystallization and origin of some peraluminous (S-type) granitic magmas. Canadian Mineralogist, 19, 111-132.

Cocherie, A., Guerrot, C., & Rossi, P. (1992). Single-zircon dating by step-wise Pb evaporation: Comparison with other geochronological techniques applied to the Hercinian granites of Corsica, France. Chem. Geol., 101: 131-141.

Condie, K.C., Viljoen, M.J., & Kable, E.J.D. (1977). Effects of alteration element distributions in Archean tholeites from the Barberton Greenstone Belt, South Africa, Contrib. Mineral. Petrol., 64, 75-89.

Cox, K.G., Bell, J.D., & Pankhurst, R.J. (1979). The interpretation of igneous rocks. George, Allen and Unwin, London.

Dalziel, I.W.D. (1997). Neoproterozoic-Paleozoic geography and tectonics: Review, hypothesis, environmental speculation. GSA Bulletin, V. 109, no:1, 16-42.

Dannat, C. (1997). Geochemie, Geochronologie und Nd-Sr-Isotopie der granitoiden Kerngneise des Menderes Massivs, SW-Türkei. Dissertation zur Erlangung des Grades, Doktor der Naturwissenschaften, Johannes Gutenberg-Universität, Tübingen, 120 p.

Dannat, C., & Reischmann, T. (1998). Geochronological, geochemical and isotopic data on granitic gneisses from the Menderes Massif, SW Turkey. 3rd Int. Turkish Geol. Symp., Ankara, Abstracts, p 275.

Debon, F., & Le Fort, P. (1982) A chemical-meneralogical classification of common plutonic rocks and association. Transaction of the royal society of Edinburg, Earth Science, 73, 135-149.

De la Roche, H., Leterrier, J., Grande Claude , P., & Marchal, M. (1980). A classification of volcanic and plutonic rocks using R1-R2 diagrams and major element analyses – its relationships and current nomenclature. Chemical Geology., 29, 183-210.

Dora, O.Ö. (1975). Menderes Masifi'nde alkali feldspatların yapısal durumları ve bunların petrojenetik yorumlarda kullanılması. Türkiye Jeoloji Kurumu Bülteni, 24, 91-94.

Dora, O.Ö. (1976). Die Feldspäte als petrogenetischer Indikator im Menderes Massiv / Westanatolien. N. Jb. Miner. Abh., 127, 3, 289-310.

Dora, O.Ö., Kun, N., & Candan, O. (1988). Metavolcanics (leptites) in the Menderes Massif: a possible paleoarc volcanism. METU Journal of Pure and Applied Sciences, V. 21/1-2, 413-445.

Dora, O.Ö., Kun, N., & Candan, O. (1990). Metamorphic history and geotectonic evolution of the Menderes Massif. Proceedings of International Earth Sciences Congress on Aegean Regions, İzmir/Turkey, V. 2, 102-115.

Dora, O.Ö., Kun. N., & Candan, O. (1990). Menderes Masifi'nin metamorfik tarihçesi ve jeotektonik konumu. (in Turkish with English Abstract) Türkiye Jeoloji Bülteni, 35/1, 1-14.

Dora, O.Ö., Savaşçın, Y., Kun. N., & Candan, O. (1987). Menderse Masifi'ndeki post-metamorfik plütonlar. (in Turkish with English Abstract) Yerbilimleri, 14, 79-89.

Dora, O.Ö., Candan, O., Oberhänsli, R., & Dürr, St. (1995). New evidence on the geotectonic evolution of the Menderes Massif. In: O Piskin, M Ergün, MY Savascın, G Tarcan (Eds), Proceedings of International Earth Sciences Colloquim on the Aegean Region, Izmir, 1: 53-72.

Dora, O.Ö., Candan, O., Kaya, O., & Koralay, E. (2000). New data relating to the origin and polymetamorphism of the paragneisses in the Menderes Massif. Abstracts, IESCA-2000, International Earth Sciences Colloquium on the Aegean Region, İzmir, p. 133.

Dora, O.Ö., Candan, O., Kun, N., Koralay, E., & Akal, C. (1994). Ödemiş-Kiraz Asmasifi'ndeki yeni jeolojik bulgular ve sorunlar. 47. Türkiye Jeoloji Kurultayı, 32-33.

Dora, O.Ö., Candan, O., Kaya, O., Koralay, E., & Dürr, S. (2001). Revision of "Leptite-gneisses" in the Menderes Massif: a supracrustal metasedimentary origin. Int Journ Earth Sciences, 89 / 4, 836-851.

Dürr, S., (1975). Über Alter und geotektonische Stellung des Menderes Kristallins / SW-Anatolien und seine Equivalente in der Mittleren Aegeis. Habilitation thesis University of Marburg, 107 p.

Dürr, S., Alther, R., Keller, J., Okrusch, M., & Seidel, E., (1978). The median Aegean crystalline belt: Stratigraphy, structure, metamorphism, magmatism. Closs, H., Roeder, D.R., Schmidt, E., (Eds), Alps, Apennines, Hellenides. Schweizerbart, Stuttgart, 445-477.

Elliot, R.B. (1973). The chemistry of gabbro/amhibolite transitions in south Norway. Contrib. Mineral. Petrol., 38, 71-79.

Erdoğan, B. (1992). Problem of core-mantle boundary of Menderes Massif. 1st International Syposium on Eastern Mediterranean Geology, Adana, Geosound, Special Issue, 314-315.

Erdoğan, B. (1993). Menderes Masifi'nin kuzey kanadının stratigrafisi ve çekirdek örtü ilişkisi. Abstracts, Geol. Congr. Turkey, Ankara, Turkey, p. 56.

Erdoğan, B., & Güngör, T. (1992).Menderes Masifi'nin kuzey kanadının stratigrafisi ve tektonik evrimi. TPJD Bülteni, C. 4/1, 9-34.

Field, D., & Elliot, R.B. (1974). The chemistry of gabbro/amhibolite transitions in south Norway. Contrib. Mineral. Petrol., 47, 63-76.

Fleck, R.J., Greenwood, W.R., Hardley, D.G., Anderson, R.E., & Schmidt, D.L. (1980). Rubidium-strontium geochronology and plate-tectonic evolution of the southern part of the Arabian shield. U.S. Geol. Surv. Prof. Pap., 1131, 38 p.

Floyd, P.A., & Winchester, J.A. (1978). Identification and discrimination of altered and metamorphosed rocks using immobile elements. Chem. Geol., 21, 291-306.

Floyd, P.A., & Winchester, J.A. (1983). Element mobility associated with metashear zones within the Ben Hope amphibolite suite, Scotland. Chem. Geol., 39, 1-15.

Forbes, W.C. (1969). Zircons of the White Mountain magma series: Belknap Mountain complex. Amer. Min., 54, 787-795.

Garrels, R.M., & Mackenzie, F.T. (1971). Evolution of sedimentary rocks. W. W. Norten New York, NY.

Gass, I.G. (1982). Upper Proterozoic (Pan-African) calc-alkaline mamgmatism in north-eastarn Africa and Arabia. (Ed) R.S. Thorpe, In: Andesites, 591-608.

Gessner, K., Passchier, C.W., Ring, U., & Güngör, T. (1998). A conspicious change of shear-sense in the granitoid augen gneiss of the Pan-African basement unit of the Menderes Massif, SW-Turkey. 3rd Int Turkish Geol Symp., Ankara, Abstracts, p 265.

Gessner, K., Piazolo, S., Güngör, T., Ring, U., Kröner, A., & Passchier, C.W., (2001). Tectonic significance of deformation patterns in granitoid rocks of the Menderes nappes, Anatolide belt, southwest Turkey, Int Journ Earth Sciences , 89, 4, 766-780.

Gezbul, T. (1994). The origin of gneisses in the Çine Submassif (MenderesMassif). MSc Thesis, Fen Bil. Ens., DEU, Izmir, 50 p.

Graciansky, P. (1965). Menderes Masifi'nin güney kıyısı boyunca (Türkiye'nin GB'sı) görülen metamorfizma hakkında açıklamalar. MTA Dergisi., 64, 8-22.

Gradstein, F.M., & Ogg, J.G.A .(1996). Phanerozoic Time Scale. Episodes 19: 1-2.

Greenwood, W.R., Hadley, D.G., Anderson, R.E., Fleck, R.J., & Schmidt, D.L. (1976). Proterozoic Crantonization in southwestern Arabia, Philos. Trans. R. Soc. London, Ser.A, A 280, 517-527.

Hamilton, W.J., & Stricland, H.E. (1840). On geology of the western part of Asia Minor. Trans. Geol. Soc. London, VI, Second series, 1-39.

Harker, A. (1909). The natural history of igneous rocks. Methuen, London.

Harris, N.B.W., Pearce, J.A., & Tindle, A.G. (1986). Geochemical characteristics of collision-zone magmatism. In: Coward, M.P., & Ries, A.C. (Eds), Collision tectonics. Geol.Soc. London, Special Publication, 19, 67-81.

Hermann, A.G., Potts, M.J., & Knake, D. (1974) Geochemistry of rare earth elements in spilites from the oceanic and continental crust. Contrib. Mineral. Petrol., 44, 1-16.

Hetzel, R., & Reischmann, T. (1996). Intrusion age of Pan-African augen gneiss in the southern Menderes Massif and the age of cooling after Alpine ductile extensional deformation. Geol. Mag., 133: 565-572

Hetzel, R., Romer, R.L., Candan, O., & Passchier, C.W. (1998). Geology of the Bozdağ area, central Menderes Massif, SW Turkey: Pan-African basement and Alpine deformation. Int. Journ. Earth Sciences, 87: 394-406

Hinthorne, J.R., Anderson, C.A., Conrad, R.L., & Lovering, J.F. (1979). Sigle-grain $^{207}Pb/^{206}Pb$ and U/Pb age determinations with a 10-μm spatial resolution using the ion-microprobe mass analyser (IMMA). Chem. Geol., 25, 271-303.

Hoffmann, P.F. (1991). Did the brakeout of Laurentia turn Gondwana inside out? Science, 252, 1409-1412.

Hughes, C.J. (1972). Spilites, keratophyres and the igneous spectrum. Geol. Mag., 109, 513-527.

Irvine, T.N., & Baragar, W.R.A. (1971). A guide of to the geochemical classification of the common volcanic rocks. Canadian Journal of Earth Sciences, 8, 523-548.

Jacobshagen, V. (1985). Geologie von Griechenland. Berlin: Gebrüder Borntraeger.

Kober, B. (1986). Whole-grain evaporation for $^{207}Pb/^{206}Pb$-age-investigations on single zircons using a double-filament thermal ion source. Contrib. Mineral. Petrol., 93, 482-490.

Kober, B. (1987). Single-zircon evaporation combined with Pb^+ emitter bedding for $^{207}Pb/^{206}Pb$-age investigations using thermal ion mass spectrometry and implications for zirconology. Contrib. Mineral. Petrol., 96, 63-71.

Konak, N. (1985). A discussion on the core-cover relationships on the basisf of recent observations (Menders Massif). Geol. Congr. Turkey., Abstracts, Ankara, p. 33.

Konak, N., Akdeniz, N., & Öztürk, E.M. (1987). Geology of the south of Menderes Massif. IGCP project no:5 Correlation of Variscan and pre-Variscan events of the alpinemediterranean mountain belt, Field meeting, Turkey, pp 42-53

Konak, N., Çakmakoğlu. A., Elibol, E., Havzaoğlu, T., Hepşen, N., Karamanderesi, I.H., Keskin, H., Sarıkaya, H., Sav, H., & Yusufoğlu, H. (1994). Development of thrusting in the median part of the Menderes Massif. 47th Geol. Cong. Ankara, Abstracts, p 34.

Koralay, O.E. (1993). Geological and petrographical investigation in the northern part of Derbent area, Ödemiş-Kiraz submassif of the Menderes Massif. MSc. Thesis, Dokuz Eylül Univ., Graduate School of Natural and Applied Sciences, İzmir, 122p.

Koralay, O.E., & Dora, O.Ö. (1999). Menderes Masifi'nde Derbent (Alaşehir) yöresinin jeolojisi ve olasılı Kimmeriyen metamorfizması. Geosound (Yerbilimleri), 34, 151-172.

Koralay, O.E., Satır, M., & Dora, O.Ö. (1998). Geochronologic evidence of Triassic and Precambrian magmatism in the Menderes Massif, west Turkey. 3rd Int. Turkish Geol. Symp., Ankara, Abstracts, p 285.

Koralay, O.E., Satır, M., & Dora, O.Ö. (2001). Geochemical and geochronological evidence for Early Triassic calc-alkaline magmatism in the Menderes Massif, western Turkey. Int. Journ. of Earth Sciences, 89 /4, 822-835.

Krogh, T.E. (1973). A low contamination method for hydrothermal decomposition of zircon and extraction of U and Pb for isotopic age determinations. Geochim. Cosmochim. Acta, 37, 485-494.

Krogh, T.E. (1982a). Improved accuracy of U-Pb zircon dating by selection of more concordant fractions using a high gradient magnetic seperation technique. Geochim. Cosmochim. Acta, 46, 631-635.

Krogh, T.E. (1982b). Improved accuracy of U-Pb zircon dating by the creation of more concordant systems using an air abrasion technique. Geochim. Cosmochim. Acta, 46, 637-649.

Kröner, A. (1984) Late Precambrian plate tectonics and orogeny: a need to redefine the term Pan-African. In: L. Cahen Memorial Volume, Museum Royal Africa Centre, Tervuren, Belgium.

Kröner, A. & Todt, W. (1988). Single zircon dating constraining the maximum age of the Barberton Greenstone Belt, South Africa. J. Geophys. Res., 93, 15329-15337.

Kröner, A., Stern, R.J., & Fleck, R.J. (1983). Chronology and mecanism of Pan-African crustal accreation in northeastAfrica and Arabia, 12th Colloquium on African Geology, Tervuren, Belgium.

Kröner, A., Braun, I., & Jaekel, P. (1996). Zircon geochronology of anatectic melts and residues from a high-grade pelitic assemblage at Ihosy, southern Madagascar: evidence for Pan-African granulite metamorphism. Geol. Mag., 133(3), 311-323.

Kun, N. (1983). Çine dolayının petrografisi ve Menderes Masifi'nin güney kesimine ait petrolojik bulgular. PhD. Thesis, Dokuz Eylül University, İzmir, 130 pp.

Kun, N., & Candan, O. (1987). Ödemiş-Kiraz Asmasifi'ndeki leptitlerin dağılımı, konumları ve oluşum koşulları. TÜBİTAK Projesi, Proje No: TBAG 688, 133 p.

Kuno, H. (1968). Differantiation of basalt magmas. In: Hess, H.H. & Poldervaart, A., (eds), Basalts: The poldervaart treasite on rocks of basaltic composition, Interscience, New York, 2, 623-688

Lancelot, J., Vitrac, A., & Allegre, C.J. (1976). Uranium and lead isotopic dating with grain by grain zircon analysis: a study of complex geological history with a single rock. Earth Planet. Sci. Lett., 29, 357-366.

Larsen, L.H., & Poldervaart, A. (1957). Measurement and distribution of zircons in some granitic rocks of magmatic origin. Min. Mag., 31, 544-564.

Liebetrau, V., Poller, U., Nägler, T.F., Frei, R., & Sergeev, S.A. (1995). The problem of zircon-dating and geochemical discrimination of S-type granitoids in consideration of cathodoluminescence studies and Sm/Nd data: a case study from the Silvretta nappe/Central Alps. Beih. Eur. J. Mineral., 7: 153.

Loos, S., & Reischmann, T. (1999). The evolution of the southern Menderes Massif in SW Turkey as revealed by zircon dating. Geol. Soc. London., 156: 1021-1030

Maniar, P.D., & Piccoli, P.M. (1989). Tectonic discrimination of granitoids. Geol. Soc. of America Bull., 101, 635-643.

Marc, D. (1992) Granites and rhylithes from the northwestern USA: temporal variation in magmatic processes and relations to tectonic setting. In transactions of the Royal Society of Edinburg, Earth Sciences, 83, 51-64.

Marfunin, A.S. (1979). Spectroscopy, Luminescence and Radiation Centers in minerals. Springer, Berlin, 352 pp.

Mariano, A.N. (1989). Cathodoluminescence emission spectra of rare earth element activators in minerals. In: B.R. Lipin & G.A. McKay (Eds), Geochemistry and Mineralogy of Rare Earth Elements, Mineral. Soc. Am., Rev. Mineral., 21: 339-348.

Middlemost, E.A.K. (1975). The basalt clan. Earth Science Reviews, 11, 337-364.

Miyashiro, A. (1974). Volcanic rock series in island arcs and active continental margins. American Journal of Earth Science, 274, 321-355.

Murthy, M.V.N. (1958). On the crystallization of accessory zircon in granitic rocks of magmatic origin. Can. Min., 6, 260-263.

Nebert, K., & Ronner, F. (1956) Menderes Masifi içinde ve çevresinde alpidik ilbitizasyon olayları. MTA Bülteni, 48, 83-97.

Oberhänsli, R., Candan, O., Dora, O.Ö., & Dürr, S. (1997). Eclogites within the Menderes Massif / western Turkey. Lithos, 41, 135-150.

Oberhänsli. R, Monie, P., Candan, O., Warkus, F., Partzsch, J.H., & Dora, O.Ö. (1998). The age of blue schist metamorphism in the Mesozoic cover series of the Menderes Massif,. Schweiz. Mineral. Petrogr. Mitt., 78, 309-316.

Odin, G.S. (1994). Geological Time Scale. C R Acad Sci Paris, 318: serie II: 59-71.

Okay, A.I. (1989). Tectonic units and sutures in the Pontides, northern Turkey. In: Tectonic Evolution of the Tethyan Region, (ed) A.M.C. Şengör, 109-113, Dordrecht: Kluwer.

Okay, A.I., Monod, O., Monie, p. (2001). Triassic blueschists and eclogites from northwest Turkey: vestiges of Paleo-Tethyan subduction. 4th International Turkish Geol. Symp., Ankara, Abstracts, p 285.

Okay, A.I. Satır, M. Maluski, H. Siyako, M. Monie, P. Metzger, R. &Akyüz, S. (1996). Paleo- and Neo-Tethyan events in northwestern Turkey: Geologic and Geochronologic constraints. In: Yın A, Harrison M (eds) The tectonic evolution of Asia. Cambridge University Press, pp 420-441.

Önay, T.S. (1949). Uber die Smirgelgesteine Sudwest-Anatolien. Schweiz. Min. Pet. Mitt., 29, 359-391.

Özer, S. (1998). Rudist bearing Upper Crateceous metamorphic sequences of the Menderes Massif (western Turkey). Geobios, M.S.n. 22, 235-249.

Özkan, S. (2000). Kuşcami Köyü (Karpuzlu/Aydın) güneybatısındaki rutilli albit pegmatoidlerinin mineralojik-petrografik incelenmesi. MsC Thesis, Fen Bil. Ens., DEU, İzmir, 108 p.

Öztürk, A., Koçyiğit, A. (1982). Selimiye-beşparmak bölgesi metamorfitlerinin tektoniği. TÜBİTAK Projesi , Matematek Fiziki ve Biyolojik Bilimler Araştırma Grubu, Proje No: TBAG-137, (unpublished).

Partzsch, J., Oberhänsli, R., Candan, O., &Warkus, F. (1998) The Menderes Massif, W Turkey: a complex nappe pile recording 1.0 Ga of geological history. 3rd Int Turkish Geol Symp., Ankara, Abstracts, p 281.

Passchier, C.W., Myres, J.S. & Kröner, A. (1990). Field geology of high-grade gneiss terranes. Springer-Verlag, Berlin, 150 p.

Pearce, J.A. (1975). Basalt geochemistry used to investigate post tectonic environments on Cyprus. Tectonophysics, 25, 41-68.

Pearce, J.A. (1996). Sources and settings of granitic rocks. Episodes, International Geoscience Newsmagazine, 19/4, 120-125.

Pearce, J.A., & Cann. J.R. (1973). Tectonic setting of basic volcanic rocks determined using trace element analyses. Earth Planetary Scienci Letters, 19, 290-300.

Pearce, J.A., Harris, N.B.W. & Tindle, A.G. (1984). Trace element discrimination diagrams for the tectonic interpretation of granitic rocks. Journal of Petrology, 25, 956-983.

Philippson, A. (1911). Reisen und forschunggen im Westlichen Kleinasien. Petermanns Mitt., Erganzungs heft 172.

Pidgeon, R.T. (1992). Recrystallisation of oscillatory zoned zircon: some geochronological and petrological implications. Contrib. Mineral. Petrol. 110: 463-472.

Piper, J.D.A. (2000). The Neoproterozoic Supercontinent: Rodinia or Paleopangea. Earth and Planetary Science Letters, 176, 131-146.

Poldervaart, A. (1956). Zircon in rocks. 2. Igneous rocks. Amer. J. Sci., 254, 521-554.

Poldervaart, A., & Eckelmann, F.D. (1955). Growth phenomena in zircon of autochthonous granites. Bull. Geol. Soc. America, 66, 947-948.

Pupin, J.P. (1980). Zircon and granite petrology. Contrib. Mineral. Petrol., 73: 207-220

Pupin, J.P., & Turco, G. (1974). Application à quelques roches endogènes du massif franco-italien de l'Argentera-Mercantour, d'une typologie originale du zircon accessoire. Étude comparative avec la méthode des R.M.A. Bull. Soc. fr. Minéral. Cristallogr. 97, 59-69.

Reischmann, T. (1998). Pre-Alpine origin of tectonic units from the metamorphic complex of Naxos, Greece, identified by single zircon Pb/Pb dating. Bull of the Geol Soc of Greece Proceedings, 8th In.t Cong . Patras, XXXII/3: 101-111.

Remond, G., Cesbron, F., Chapoulie, R., Ohnenstetter, D., Roques-Carmes, C., & Schvoerer, M. (1992). Cathodoluminescence applied to the microcharacterization of mineral materials: a present status in experimentation and interpretation. Scanning Microsc., 6: 23-68.

Ring, U., (1999). (Personal interview).

Ring, U., Gessner, K., Güngör, T., & Passchier, C.W. (1999). The Menderes Massif of western Turkey and the Cycladic Massif in the Aegean-do they really correlate? Geological Society of London, 156: 3-6.

Robertson, A.H.F., & Dixon, J.E. (1984). Introduction: aspects of the geological evolution of the Eastern Mediterranean. In: Dixon, J.E. Robertson, A.H.F. (eds) Geological Evolution of the Eastern Mediterranean, Geological Society of London, Special Publications, 17, 1-75.

Satır, M., & Friedrichsen, H. (1986). The origin and evolution of the Menderes Massif, W-Turkey: A rubidium /strontium and oxygen isotope study. Geol. Rund., 75, 703-714.

Schulling, R.D. (1958). Menderes Masifi'ne ait bir gözlü gnays üzerinde zirkon etüdü. MTA Dergisi, 37-41.

Schulling, R.D. (1962). Petrology, age and structure of Menderes Migmatite Complex in Southwest Turkey. Bull. of the Min. Res. Exp., 58, 71-84.

Schulling, R.D. (1973). Active role of continents in tectonic evolution, geothermal models. In: De Jong, K.A. & Scholten, R. (Eds), Gravite and tectonics. New York, 37-41.

Scotford, D.M. (1969). Metasomatic augen gneiss in greenschist facies, western Turkey. Geol. Soc. Amer. Bull., 80, 1079-1094.

Shand, S.J. (1943). Eruptive rocks: Their genesis composition, classification, and their relations to ore deposites. John Wiley, New York.

Sheraton, J.W. (1984). Chemical changes associated with high-grade metamorphism of mafic rocks in the east Antarctic Shield. Chemical Geology, 47, 135-157.

Sözer, K. (1997). Mineralogy of the adularia occurences in the vicinity of Ovacık and Yeniköy / Çine area (Menderes Massif). MsC Thesis, Fen Bil. Ens., DEU, İzmir, 112 p.

Sommerauer, J. (1974). Trace element distribution patterns and the mineralogical stability of zircon – an application for combined electron microprobe techniques. Proc. Electron Microscopy Society of Southern Africa, 4, 71-72.

Stacey, J.S., & Kramers, J.D. (1975). Approximation of terrestrial lead isotope evolution by a two stage model. Earth Planet Sci. Lett., 26: 207-221.

Stampfli, G.M., Mosar, J., De Bono, A., & Vavais, I. (1996). Late Paleozoic, Early Mesozoic plate tectonics of the Western Tethys. Bull. Geol. Soc. Greece, 8th Internat. Congress Geol. Soc. Greece, Patras 1998, vol. XXXII/1, 113-120.

Stein, M., & Goldstein, S.L. (1996). From plume head to continental lithospherein the Arabian-Nubian shield. Nature, 382, 773-778.

Stern, R.J. (1994). Arc assembly and continental collision in the Neoproterozoic East African orogen – implications for the consolidation of Gondwana. Annual Review of Earth and Planetary Sciences, 22, 319-351.

Şengö,r A.M.C. (1979). Mid-mesozoic closure of Permo-Triassic Tethys and its implications. Nature, 279, 590-593.

Şengör, A.M.C., & Yılmaz, Y. (1981) Tethyan evolution of Turkey: a plate tectonic approach. Tectonophysics, 75: 181-241.

Şengör, A.M.C., Yılmaz, Y., & Ketin, İ. (1980). Remnants of a pre-Late Jurassic ocean in northern Turkey: Fragments of Permian-Triassic Paleo-Tethys. Geological Society of America Bulletin, Part 1, 91, 699-609.

Şengör, A.M.C., Satır, M., & Akkök, R. (1984). Timing of tectonic events in the Menderes Massif, western Turkey: Implications for tectonic evolution and evidence for Pan-African basement in Turkey. Tectonics, 3/7: 693-707.

Tarney, J. (1976). Geochemistry of Archaean high-grade gneisses, with implications as to the origin and evolution of the Precambrian crust. In: Windley, B.F. (Ed), The early history of the earth. Wiley, New York, 405-418.

Tarney, J., & Windley, B.F. (1977). Chemical thermal gradients and the evolution of the lower continental crust. Journal of the Geological Society, London, 134, 153-172.

Tchihatcheff, P.D. (1869). Asie Mineure. Description Physique, Quatrime Partie Geologie, III, 552 p.

Tekeli, O. (1981). Subduction complex of pre-Jurassic age, northern Anatolia. Geology, 9, 68-72.

Trompette, R. (1994). Geology of western Gondwana, Rotterdam, A.A. Balkema, 350 p.

Tüysüz, O. (1990). Tectonic evolution of a part of the Tethyside orogenic collage: The Kargı Massif, northern Turkey. Tectonics, 9/1, 141-160.

Unrug, R. (1996), The assembly of Gondwana. Episodes, 19, 11-20.

Warkus, F., Partzsch, J.H., Candan, O., & Oberhänsli, R. (1998). The tectono-metamorphic evolution of the Birgi-Tire nappe in the Menderese Massif, SW-Turkey. 7th Syposium tektonik strukturgeologie-kristallingeologie, Freiberger Forschungsheft, C-471, 237-238.

Weaver, B.L. & Tarney, J. (1981). Chemical changes during dyke metamorphism in high grade basement terranes, Nature, 289, 47-49.

Werner, C.D. (1987). Saxonian granulites–igneous or lithogenous. Contribution to the geochemical diagnosis of the original rocks in High-metamorphic complexs. In: Gerstenberger, H., (Ed) Contributions to the geology of the Saxonian granulite massif (Sächsisches Granulitegebirge), Zfl-Mitteilungen Nr 133, 221-250.

Wetheril, G.W. (1956). Discordant uranium-lead ages. Trans. Am. Geophys. Union, 37, 320-326.

White, A.J.R., & Chappell, B.W. (1977). Ultrametamorphism and granitoid genesis. Tectonophysics, 43, 7-22.

Wilson, M. (1989). Igneous petrogenesis. Unwin Hyman, London.

Winchester, J.A & Floyd, P.A. (1976). Geochemical magma type discrimination and application to altered and metamorphosed basic igneous rocks. Earth and Planet. Sci. Lett., 28, 459-463.

Winchester, J.A & Floyd, P.A. (1977). Geochemical discrimination of different magma series and their differentiation products using immobile elements. Chemical Geology, 20, 325-343.

Winchester, J.A & Max, M.D. (1982). The geochemistry and origins of the Precambrian rocks of the Rosslare Complex, SE Ireland. Journal of the Geological Society, London, 139, 309-319.

Wippern, J. (1964). Menderes Masifi'nin Alpidik dağ oluşumu içindeki durumu. MTA Dergisi, 62, 80-87.

T.C. YÜKSEKÖĞRETİM KURULU DOKÜMANTASYON MERKEZİ